Measurements and Modeling of Moisture Diffusion Processes in Transformer Insulation Using Interdigital Dielectrometry Sensors

by

Yanqing Du

B.S., Northwestern Polytechnical University, Xi'an, China, 1993
M.S., Northwestern Polytechnical University, Xi'an, China, 1994
M.S., Massachusetts Institute of Technology, 1999
E.E., Massachusetts Institute of Technology, 1999

Submitted to the Department of Electrical Engineering and Computer Science
in Partial Fulfillment of the Requirements for the Degree of
Doctor of Philosophy in Electrical Engineering and Computer Science

at the

Massachusetts Institute of Technology
May 1999

Signature of Author .....
Department of Electrical Engineering and Computer Science
May 19, 1999

Certified by .....
Markus Zahn
Professor of Electrical Engineering
Thesis Supervisor

Certified by .....
Bernard C. Lesieutre
Associate Professor of Electrical Engineering
Thesis Co-Supervisor

Accepted by .....
Arthur C. Smith
Chairman, Committee on Graduate Students
Department of Electrical Engineering and Computer Science

To my parents:

Du Zhonghai

and

Ye Liane

Measurements and Modeling of Moisture Diffusion Processes in Transformer Insulation Using Interdigital Dielectrometry Sensors

by
Yanqing Du

Submitted to the Department of Electrical Engineering and Computer Science on May 12, 1999 in partial fulfillment of the requirements for the Degree of Doctor of Philosophy.

Abstract

The presence of moisture in a transformer deteriorates the transformer insulation by decreasing its electrical, mechanical, and thermal strength. Therefore, it is important to monitor the moisture condition in both liquid and solid insulation to assure transformer performance. There are commercially available sensors to measure the moisture in oil. When the transformer system is in equilibrium, moisture partitioning curves for the oil-paper system can be used to find the moisture in paper from the oil measurement. A comprehensive study of the classic moisture equilibrium curves is given, historical mistakes are corrected, and all relevant concepts are clarified. This research serves as a useful tool to utilities and manufacturers. A new set of moisture equilibrium curves is constructed for moisture in oil up to the saturation moisture content.

A measurement technique exploiting the linearity between the relative humidity of the oil and the moisture content of the oil to indirectly measure the oil solubility is developed. Solubility tests are performed for differently conditioned oils: Fresh Shell Diala AX oil, lab-aged Shell Diala A oil, used oil from Ramapo Substation, and used oil from Texas Utilities. Results show that aging under normal operation at service temperature is not very likely to significantly change the water solubility.

When the system is not in equilibrium, the equilibrium moisture curves are not applicable and the three-wavelength interdigital dielectrometry sensor developed at the MIT Laboratory for Electromagnetic and Electronic Systems provides a unique way to measure the spatial profile of the moisture distribution in transformer pressboard. Preliminary measurements of oil-free and oil-impregnated pressboard are given in this thesis. A joint research group effort led to development of an improved design of the three-wavelength sensor and interface box circuitry which reduces the problems associated with the previous design and simplifies the inversion algorithm to convert the sensor signal to dielectric properties. The thesis focuses on the design and implementation of experimental studies based on interdigital dielectrometry using the new three-wavelength sensor.

As a first step to relate measurable dielectric properties to absorbed moisture, the moisture and temperature effects on the dielectric spectrum of oil-free pressboard are

measured using a parallel-plate electrode sensor for nine moisture levels and five temperature levels. A dielectric model for biological tissue is adopted here for cellulose structured pressboard. A universal curve is found relating dielectric properties to moisture concentration and temperature by fitting the data to the model. Preliminary measurements of oil-impregnated pressboard show similar characteristics.

The moisture diffusion process in oil-free transformer pressboard is monitored using the new interdigital dielectrometry three-wavelength sensor in a specially constructed bench-top apparatus. Experiments are performed for five different temperatures at various moisture levels. The time evolution of the moisture spatial profile in transformer pressboard is non-destructively estimated. Experimental results show good agreement with theoretical analysis of the moisture diffusion equation on the effects of moisture level, pressboard thickness, and temperature on the diffusion process.

The diffusion coefficient for oil-free pressboard as a function of temperature and moisture concentration is estimated. Numerical algorithms for solving the non-linear diffusion equation are derived. Literature results of the diffusion coefficient for cellulose insulation are compared and analyzed.

The interdigital sensor setup is also combined in a transformer oil Couette Facility that simulates the transformer environment for studying temperature and moisture transients in pressboard. The understanding of moisture-related processes in power transformers can be enhanced with this methodology.

Finally, a newly promoted in-situ time-domain measurement technique is implemented using the Tettex Recovery Voltage Meter. Time domain measurements are performed for oil-impregnated pressboard in both parallel-plate and coaxial cylinder electrode geometries (the Couette Facility). The results for temperature and aging effects show good agreement with theory.

Thesis Supervisor: Markus Zahn
Title: Professor of Electrical Engineering

Thesis Co-Supervisor: Bernard C. Lesieutre
Title: Associate Professor of Electrical Engineering

Acknowledgments

It has been a great joy and privilege to have Professor Markus Zahn as my primary research advisor. His insight and love for research have been a great inspiration to me. His encouragement and kindness have meant so much to me, especially during hard times at MIT. I am grateful for all his support and guidance to me, not only in research, but also in other aspects of graduate life.

I am grateful to my co-supervisor, Professor Bernard C. Lesieutre, who has made important contributions to the project, especially in the modeling and numerical sections. The Doctoral Area Exam under his supervision was truly a learning experience.

I want to thank Prof. Jeffrey H. Lang for participating in my thesis committee and providing valuable discussions and suggestions. Thanks also to my academic advisor Prof. Jin Au Kong for his encouragement and support from my first day at MIT. I am fortunate to have had the opportunity to experience their exciting and stimulating teaching.

The research projects covered in this thesis were mainly supported by the Electric Power Research Institute, grant no. WO 8619-01, managed by Mr. Stan Lindgren, and the National Science Foundation, grant no. ECS-9523128. I want to thank Mr. Lindgren not only for the financial support, but also for his support for woman engineers. My first year of study at MIT was supported by a Wang Tiwu Fellowship sponsored by the late Mr. Wang Tiwu. I thank him for his generosity and vision to support education. I am also thankful for the financial support from the American Public Power Association through three Demonstration of Energy-Efficient Developments Scholarships, sponsored by Belmont Utility managed by Mr. Timothy McCarthy.

My colleagues at the MIT High Voltage Research Lab are a wonderful group of people who are more than extra hands for the experiments: Tza-Jing Gung, Robert Lyons, Afsin Ustundag, Albert Lu, and Julio Castrillon. Darrell Schlicker deserves special thanks for always being there to help me and share with me his great ideas without any reservation, without which my path to completion would have been much longer and more difficult. I thank my major collaborator for the project, Alexander Mamishev, for his constructive criticism of my professional approach, from touch-typing to Taguchi method, which greatly stimulated me to strive for perfection; and for his great help with this thesis writing. Yanko Sheiretov and Dr. Philip von Guggenberg provided much help in the early stages of the research.

Some of the experiments analyzed in this thesis were performed under my supervision by undergraduate students Madhu Sarda and Noemi Altamirano, and visiting Professor Seong-Hwa Kang from Korea. I thank them for their contributions and credit them individually in the thesis.

I want to thank Mr. Wayne Ryan who made all the tough and heavy experimental efforts possible. His numerous everyday contributions were essential to the completion of this thesis research. Thanks to Dr. Karen Walrath for computer maintenance, David Otten for hardware troubleshooting, and Rocco Albano for excellent machine

work. Donation of Maxwell software by Ansoft Corp. and GC-CAM by GraphiCode, Inc. is gratefully appreciated.

Thanks to LEES secretaries Kathy McCue, Sara Wolfson, and Karin Janson-Strasswimmer, for providing valuable assistance, and to Vivian Mizuno for her friendship. Also, I would like to thank the departmental administrative officers Peggy Carney and Marilyn Pierce, for their encouragement and support toward my graduate study at MIT, and Monica Bell for her effective and systematic work.

I want to thank Mr. Paul Griffin of Doble Engineering Company for his instruction in oil chemistry, numerous technical discussions, and free technical services. Thanks also to the following scientists for valuable discussions, inputs, encouragement, and document and material supply: Dr. Chathan Cooke of MIT; Dr. T. V. Oommen of ABB-ETI; Prof. Steven A. Boggs of University of Connecticut; Mr. Noah Tai of Consolidated Edison; Dr. Giuessepie Urbani of Haefely Trench AG, Switzerland; Prof. Len Dissado of Leicester University, U.K.; Dr. Stephen D. Foss of Dynamic Rating Systems; and Prof. Stanislaw Gubanski of Chalmers University of Technology, Sweden. Special thanks to Mr. Thomas Prevost of EHV-Weidmann, for technical support and the generous supply of large quantities of transformer board; and to Tettex Instruments for the loan of a Tettex Recovery Voltage Meter.

Thanks to all my teachers in China at the Northwestern Polytechnic University, in particular my former advisors Professors Junfeng Ma, Lao Ji, and Xiaobin Zhang who built my foundations for research and prepared my way to the US. Thanks to Prof. Pei C. Hu for being my mentor over the years.

I want to thank my friends in the MIT Chinese Bible Study Group and the MIT Graduate Christian Fellowship: Paul & Betty, Guangyu & Weiran, Leslie, Jeff, and many others, for their prayers and friendship. I thank Haiyan & Jiyong, Yinan & Pei, and Marilyn for their sustaining care, help, and prayers, and for being there when I needed them. I am grateful for the staff and friends at the Cambridge Salvation Army. Thanks to Robert for the joy, encouragement, and help during this thesis writing.

My thanks also go to my host family, Alberta and Roger Lipson, for the wonderful time they spent with me and the moral support they gave to me.

I am deeply grateful to Yanwu for all the unforgettable teaching, support, and love.

I want to thank all my family and relatives in China. My deep memory and gratitude go to my late grandmother who had almost no education but taught me to be a better person through diligence and kindness. I am blessed with the persevering and sacrificial love of my parents Du Zhonghai and Ye Liane, and my sister Qian, who made this all worthwhile. I thank Mom and Dad for their patience for a lifetime with a troublesome daughter. I thank my sister for her sacrifices to give me all the best opportunities, and for all the lovely cards and letters. This thesis is dedicated to them!

Contents

Abstract **3**

Acknowledgments **5**

Contents **7**

List of Figures **12**

List of Tables **23**

1 Introduction **27**
1.1 Background of Thesis 27
1.2 Monitoring of Transformer Insulation 28
1.3 Scope of Thesis 31
1.4 Outline of Thesis 32

2 Theoretical Background **35**
2.1 Interdigital Dielectrometry 35
2.2 Moisture Measurement for Transformer Insulation 37
2.3 Dielectric Properties of Insulating Materials 37
2.4 Frequency and Time Domain Measurements 39

3 Moisture Equilibrium in Transformer Oil-Paper Systems **41**
3.1 Background 42
3.1.1 Transformer Oil 42
3.1.2 Water in Oil 42
3.1.3 Relative Humidity 43
3.1.4 Paper 43
3.1.5 Water in Paper 44
3.1.6 Water Vapor Pressure 44
3.2 Moisture Effects on Transformer Oil-Paper Systems 44
3.2.1 Moisture Effects on Oil 45
3.2.2 Moisture Effects on Paper 45
3.3 Off-line Methods to Measure Moisture in Transformer Insulation 45

3.4 On-line Methods to Measure Moisture in Transformer Insulation 46
3.5 Moisture Equilibrium Curves 47
3.5.1 Overview 48
Fabre-Pichon Curves 48
Oommen Curves 49
Equilibrium Curves for Water Vapor Pressure and Moisture Content 54
Griffin Curves 57
MIT Curves 58
3.5.2 Comparison 59
Direct Measurement versus Indirect Measurement 59
Water Solubility in Oil 61
3.5.3 Curve Comparison 62
3.5.4 Case Study 65
3.6 Measurements of Moisture Solubility for Differently Conditioned Oils . 68
3.6.1 Introduction 68
3.6.2 Water Solubility and Relative Humidity Meter 68
3.6.3 Differently Conditioned Oils 73
3.6.4 Measurement Results 80
3.6.5 Discussion 80
3.7 Summary 81

4 Universal Curves **83**
4.1 Introduction 83
4.2 Measurements for Oil-Free Pressboard 84
4.2.1 Measurement Technique 84
4.2.2 Measurement Results 85
4.3 Effective Dielectric Constant of Pressboard 94
4.3.1 Wiener Limits 94
4.3.2 Mixed Model 97
4.3.3 Estimated Dielectric Constant with Different Models 98
4.4 Error Analysis 104
4.5 Universal Curve Model and Fitting 109
4.6 Measurements for Oil-Impregnated Pressboard 117
4.6.1 Measurement Technique 117
4.6.2 Measurement Results 118
4.7 Summary 119

5 Early Design Sensor Measurements **123**
5.1 Measurement Setup 123
5.2 Multi-wavelength Sensor 123
5.3 Lumped Circuit Model 128
5.4 Experimental Verification of the Penetration Depth 134

5.5 Moisture Dynamics Experiments . . . 138
5.5.1 Oil-Free Pressboard . . . 138
5.5.2 Oil-Impregnated Pressboard . . . 139
5.6 Antistatic Additive Measurements . . . 143
5.7 Non-idealness of the Sensor . . . 144
5.8 Summary . . . 145

6 Measurements of Pressboard Using Improved Sensor 147
6.1 New Sensor Design . . . 147
6.2 New Interface Box . . . 149
6.2.1 Feedback Capacitor . . . 150
6.2.2 Cross-coupling . . . 155
6.3 Experimental Setup . . . 157
6.4 Experiment Description . . . 162
6.5 Effects of Pressboard Thickness . . . 162
6.6 Temperature Effects . . . 167
6.7 Negative Conductance . . . 170
6.8 Summary . . . 170

7 Diffusion Analysis 173
7.1 Introduction . . . 173
7.2 Boundary Conditions . . . 173
7.3 Moisture Spatial Profile . . . 174
7.3.1 Distribution of Dielectric Properties . . . 174
7.3.2 Moisture Profiles . . . 175
7.4 Calculation of Diffusion Coefficient as a Function of Temperature and Moisture Concentration . . . 180
7.4.1 Solving the Non-linear Diffusion Equation . . . 180
7.4.2 Discussion . . . 182
7.5 Forward Simulation of the Sensor Response with Established Mapping . 185
7.5.1 Simulation Procedures and Results . . . 185
7.5.2 Error Sources . . . 185
7.6 Summary and Analysis of Literature Study on the Diffusion Coefficient 193
7.7 Summary . . . 198

8 Couette Experiments 201
8.1 Couette Facility . . . 201
8.2 Modified Sensor for the Couette Facility . . . 206
8.3 Moisture Diffusion Experiments . . . 208
8.4 Measurement Results for Oil-Free Pressboard . . . 209
8.4.1 Wetting Process in Couette . . . 209
8.4.2 Drying Process in the Couette Facility . . . 213
8.5 Measurement Results for Oil-Impregnated Pressboard . . . 218
8.5.1 Measurements of Temperature Transient . . . 218

8.5.2 Simulation of Temperature Transient 224
8.6 Summary 225

9 Recovery Voltage Measurements 227
9.1 Introduction 227
9.2 Measurements with Parallel-Plate Electrodes 229
9.2.1 Tests in the Frequency Domain 232
9.2.2 Tests in Time Domain 238
9.3 Couette Facility Measurements 241
9.3.1 Excitation Voltage 241
9.3.2 Charging Characteristics 241
9.3.3 Temperature Effects 241
9.4 Summary 242

10 Conclusions 247

A Instructions for Using the Bench-Top Apparatus 251

B New Interface Box 255
B.1 Interface Box Circuitry 255
B.2 Interface Box Assembly 265
B.2.1 Materials to Begin with 265
B.2.2 Board Preparation 269
B.2.3 Interface Board Assembly 269
B.2.4 Interface Box Assembly 270
B.2.5 Wiring 276

C Moisture Content in Wood Pulp 281

D Couette Experiment Check List 283
D.1 Pre-Check 283
D.2 Manual Operation before Starting the Computer Controlled Experiment 284
D.3 To Fill Oil in Couette Charger 285
D.4 To Push Oil from Couette Charger to Reservoir 286
D.5 To Vacuum Couette Charger 286
D.6 To Wet Oil in Couette 286

E Data Processing Code 289
E.1 Diffusion Analysis 289
E.2 General Three-Wavelength Sensor Data Processing 295
E.3 Reconstruction of Jeffries' Curves 300
E.4 Couette Facility Data Processing 301

F Forward Simulation Input File 305

Bibliography **307**

List of Figures

1.1 A typical surface tracking discharge pattern on pressboard due to flow electrification in a failed transformer. 29
1.2 The author in front of one phase of the Ramapo Substation Westinghouse 500/345kV, 333 MVA auto transformer. 30

2.1 Imposed $\omega - k$ interdigital dielectrometry 36

3.1 Fabre-Pichon Curves for moisture equilibrium of the air-oil-paper complex as a function of the air and oil surrounding the paper. 49
3.2 Curves redrawn by EHV-Weidmann for moisture equilibrium of the air-oil-paper complex as a function of the oil moisture and temperature surrounding the paper. 50
3.3 Oommen's Curves for various temperatures for moisture equilibrium in a paper-oil system 52
3.4 Moisture in wood pulp as a function of relative humidity of the ambient by Jeffries 53
3.5 Oommen Curves for low moisture region of moisture equilibrium for a paper-oil system 54
3.6 Vapor pressure versus moisture in paper comparing the erroneous formula of Equation (3.4) (dashed line) and the correct formula of Equation (3.5) (solid line). 57
3.7 Moisture in Paper versus ambient Relative Humidity curves comparing erroneous Equation (3.4) (dashed line) and correct Equation (3.5) (solid line). 58
3.8 Griffin Curves for water equilibrium in cellulose/mineral oil systems . 59
3.9 Regenerated curves following Griffin's procedure comparing erroneous Equation (3.4) (dashed line) and correct Equation (3.5) (solid line). . 63
3.10 MIT developed curves for water equilibrium in cellulose/mineral oil systems for a wide range of moisture concentrations. 64
3.11 The relative humidity of the oil at 70°C decreases as the moisture diffuses from oil into pressboard. 66
3.12 System equilibrium operating point found using the moisture equilibrium curves for oil and paper system and (3.11). 67

3.13 Harley CT-800 moisture sensor. The sensing element is at the bottom of the long rod. 71
3.14 Harley Moisture Sensor calibrated in Shell Diala AX oil at 35°C when first arrived in 1995 (calibrated by D. E. Schlicker at MIT High Voltage Research Lab.) The dashed line is the ideal output and the solid line is the linear regression of measured output. 72
3.15 Harley Moisture Sensor calibrated in Shell Diala AX oil at 35°C in 1997 after two years in service. The dashed line is the ideal output and the solid line is the linear regression of measured output. 72
3.16 Infrared scan for the tested Ramapo oil with 1-mm cell path and new oil as reference beam. Little to none of oxidation inhibitor was detected at 3660 cm^{-1}. Carbonyl compounds detection region at 1700-1730 cm^{-1} shows more absorbance than that of TU oil in Figure 3.17. 76
3.17 Infrared scan for the tested TU oil with 1-mm cell path and new oil as reference beam. Little to none of oxidation inhibitor was detected at 3660 cm^{-1}. Carbonyl compounds detection region at 1700-1730 cm^{-1} shows less absorbance than that of Ramapo oil in Figure 3.16. 77
3.18 Infrared scan for the tested Ramapo oil with 0.2 mm-cell path and air as reference beam. The absorbance difference in signature band around 700-1200 cm^{-1} shows that the Ramapo and Texas Utility oils are different products. 78
3.19 Infrared scan for the tested TU oil with 0.2 mm-cell path and air as reference beam. The absorbance difference in signature band around 700-1200 cm^{-1} shows that the Ramapo and Texas Utility oils are different products. 79
3.20 Measurements of moisture concentration versus the relative humidity for differently conditioned oils at 35°C. 81

4.1 Nettelblad's results for (a) ε' for humid paper at high temperatures as a function of frequency. (b) Master curve of ε'' for humid paper (c) ε'' of dry pressboard and insulation paper at 130°C. 87
4.2 Parallel-plate sensor used for dielectrometry measurements of pressboard as a function of moisture and temperature. 88
4.3 Test vessel used for oil-free pressboard measurements. 88
4.4 A full spectrum of ε' obtained for nine moisture levels and five temperatures. 89
4.5 A full spectrum of ε'' obtained for nine moisture levels and five temperatures. 90
4.6 Dielectric spectrum of oil-free pressboard at 2.0% moisture content for five temperatures. 91
4.7 Discrete frequency shifting of all forty five measured oil-free pressboard data sets to minimize least square differences suggests the existence of a universal curve. 93

4.8 The (a) equivalent circuit elements and (b) equivalent structure for the parallel limiting model for pressboard composed of fiber with relative dielectric constant ε_F and filling material (air or oil) with relative dielectric constant ε_X. 95
4.9 The (a) equivalent circuit elements and (b) equivalent structure for the series limiting model for pressboard composed of fiber with relative dielectric constant ε_F and filling material (air or oil) with relative dielectric constant ε_X. 96
4.10 Diagram of oil (ε_{oil}) embedded in solid fiber (ε_F) in idealized cube form; example with edge ratio K=50%. 100
4.11 Equivalent circuit for the partial capacitances of an oil-impregnated fiber matrix. 101
4.12 The calculated relative dielectric constant of oil-impregnated pressboard as a function of oil-free pressboard density for the three different models given in Figure 4.8, Figure 4.9, and Figure 4.11. 102
4.13 The relative dielectric constant of oil-free pressboard as a function of oil-free pressboard density with three different models given in Figure 4.8, Figure 4.9, and Figure 4.11. 103
4.14 The estimated error bars for the complex dielectric permittivity in Figure 4.6 measured for oil-free pressboard at 70°C and 2.0% moisture content. 107
4.15 The estimated error percentage for the complex dielectric permittivity in Figure 4.6 measured for oil-free pressboard at 70°C and 2.0% moisture content. 108
4.16 Different types of dielectric response functions f(t) for dielectric materials in the time domain. 110
4.17 The real and imaginary parts of the complex susceptibility for different models of a dielectric material in the frequency domain. 112
4.18 The measured frequency dependence of the real, $\varepsilon'(\omega)$, and the imaginary, $\varepsilon''(\omega)$, parts of the complex dielectric permittivity of samples of leaves from the Jade (Crassula Portulacaceae) plant. The curves through the data points have been obtained using the model circuit shown in Figure 4.19. The three data sets at low, mid, and high frequencies are indicated by cross, circular, and plus symbols, respectively. The individual sets of data are shown with their scales and have been reconstructed to give the single characteristic. 114
4.19 Equivalent circuit model for determining the Universal Curve described by (4.43) and (4.44). 115
4.20 Universal curve for oil-free pressboard. The solid line is the curve calculated from the model. The dotted lines are the data points of Figure 4.4 and Figure 4.5 shifted in frequency according to the parameters in Table 4.6 with (4.45). 116

4.21 Dielectric properties of oil-impregnated pressboard at moisture content 1.5% at five temperatures. 120
4.22 Dielectric properties of oil-impregnated pressboard at 70°C for four moisture levels. 121

5.1 General measurement setup using an interdigital sensor. 125
5.2 Earlier design of the Kapton three-wavelength interdigital sensor. . . 126
5.3 Detailed drawing of the Kapton three-wavelength interdigital sensor head. 126
5.4 The Kapton 1 mm single-wavelength interdigital sensor. 127
5.5 The equivalent circuit of the floating-voltage measurement of an interdigital sensor with a parylene coating resulting in capacitances C_P and with known load capacitor C_L. 128
5.6 Gain and phase measurement in air showing flat gain curves with near zero phase using a clean Kapton three-wavelength interdigital sensor like that in Figure 5.2. 130
5.7 Simulated response for the sensor circuitry with $C_p = 110pF$, $C_L = 3pF$, $C_{12} = 4pF$, $G_{12} = 500pS$, and $C_{20} = 100pF$. 131
5.8 (a) Measured sensor response in Shell Diala A oil at room temperature. (b) Estimated dielectric properties of Shell Diala A oil from measurements of (a) using a continuum model algorithm. 132
5.9 Equipotential lines in the half-cell geometry of a 1 mm interdigital sensor with lossless dielectrics. Relative permittivity of parylene coating is ε_r=3.05 with thickness of 5 μm. The driven electrode (right) is at 1 V peak potential, the sensing electrode (left) is at 0.2 V potential, and the ground plane is at 0 V. The interelectrode spacing a is 0.32λ. 133
5.10 The cross-section of the interdigital sensor with two layers of materials above it. The relative permittivities of the polycarbonate Lexan sheet and the vinyl film have been estimated to be 2.6 and 3.8 respectively. 134
5.11 High frequency (f = 1 kHz) experimental estimation of the effective penetration depth of a three-wavelength sensor by varying the thickness of the vinyl layer adjacent to the sensor of Figure 5.10. 137
5.12 Measured response of the 5 mm wavelength sensor's gain to the movement of the interlayer boundary, d_v, in Figure 5.10. 138
5.13 Response of the 5 mm wavelength sensor's phase to the movement of the interlayer boundary, d_v, in Figure 5.10. 139
5.14 Comparison of the measured (1) and theoretical ($\varepsilon_r = 2.6$ for Lexan and $\varepsilon_r = 3.8$ for vinyl) (2) response of the interdigital sensor ($\lambda = 5$ mm) at 10 kHz. 140
5.15 The measured response of the 5.0 mm wavelength when the moisture leaves the pressboard due to vacuum. As the moisture is reduced, the pressboard is more insulating and the curves shift to the left. 141

5.16 Dielectric spectra for 2 mm thick oil-impregnated EHV-Weidmann Hi-Val pressboard at ambient air in equilibrium at 70°C. The slope of $\log \varepsilon''$ vs. $\log f$ is about -0.7 indicating a frequency dispersive conductivity. 142

5.17 Microscope picture of the 1 mm wavelength electrodes of a three-wavelength Kapton sensor. The spacing between the drive and sense electrodes is about $a = 0.30\lambda$. 144

6.1 The improved design of the Teflon three-wavelength sensor 148

6.2 The new short-circuit interface box with the cable to the controller box connected at the back. 150

6.3 Equivalent circuit for short-circuit measurement. 151

6.4 Feedback capacitance tests for the new interface box with test capacitance of 80.6 pF, 56.1 pF, and 47.0 pF respectively for the three channels corresponding to 1.0 mm, 2.5 mm, and 5.0 mm wavelengths for the interdigital sensor. The effective feedback capacitances are: 1317 pF, 809 pF, and 1370 pF. 152

6.5 The new Teflon sensor measurement in air with new interface box with feedback capacitance of 1317 pF, 809 pF, and 1370 pF respectively for the 1.0 mm, 2.5 mm, and 5.0 mm wavelengths. 154

6.6 The effects of cross-coupling in oil-free pressboard measurements are demonstrated by comparing measurements with all wavelengths simultaneously excited (solid line) or each wavelength individually excited (dash-dotted line) over the frequency range of 0.005-10 kHz. 156

6.7 Schematic of the bench-top apparatus for moisture and additive diffusion experiments using dielectrometry measurements. 158

6.8 The bench-top apparatus for moisture and additive diffusion experiments using dielectrometry measurements. 159

6.9 Test structure simultaneously using a pair of three-wavelength sensors in laboratory bench-top measurements. 160

6.10 New fixture for holding the connecting wires from the sensor. 161

6.11 The measured Gain and Phase change of the three-wavelength sensor at 10 Hz for 1.0 mm thick oil-free pressboard under wetting process at 30°C. 164

6.12 The relative humidity of the test chamber during the moisture diffusion process. (a) 1.0 mm pressboard at 30°C (b) 1.5 mm pressboard at 30°C. The periodic change of the relative humidity for (b) is due to the 24-hour ambient temperature change. 165

6.13 The transcapacitance and transconductance of the three-wavelength sensor oil-free pressboard under wetting process at f=10 Hz and 30°C. (a) 1.0 mm pressboard; (b) 1.5 mm pressboard. 166

6.14 The measured transconductance of the Teflon three-wavelength sensor measurements for 1.5 mm oil-free pressboard under wetting process at $f = 0.1Hz$ for various temperatures. 168
6.15 The air relative humidity of the test chamber at various temperatures. 169
6.16 The distributed element circuit model for possible negative transconductance. 171
6.17 Another distributed element circuit model for possible negative transconductance. 171

7.1 A schematic representation of the experimental arrangement. The 1.5 mm thick oil-free pressboard is modeled as a three-layer medium with distinct properties for each layer related to the quantity of moisture in each layer. 175
7.2 Measured relative humidity of the ambient at 70°C. 177
7.3 Measured capacitance at 10 Hz between each electrode pair throughout the moisture diffusion experiment in 1.5 mm thick oil-free pressboard for each sensor wavelength at 70°C. 177
7.4 Average moisture level measured by each wavelength: region 1 (1 mm), regions 1 and 2 (2.5 mm), and regions 1, 2, and 3 (5 mm). . . . 178
7.5 Calculated spatial profiles of moisture concentration across the thickness of the oil-free pressboard from dielectrometry measurements. Numbers next to the curves correspond to the time in hours at which the profile was measured. 178
7.6 Theoretical spatial profiles of moisture concentration across the thickness of oil-free pressboard using a constant diffusion coefficient of $D = 2.3 \times 10^{-11}$ m/s^2. Numbers next to the curves correspond to the time in hours after the moisture was stepped on to 1.8% at $x = 0$. 179
7.7 1 mm wavelength sensor detects changes near the pressboard-sensor surface at $x = l$ while the moisture diffuses from the ambient at $x = 0$. 182
7.8 Calculated moisture profile in the pressboard at 60°C for moisture diffusion coefficient as a function of concentration using estimated parameters and as a constant $D = 2.4 \times 10^{-11}$ m^2/s, an average of D at $C = 0\%$ and $C = 3.0\%$, the measured boundary condition at 60°C. 184
7.9 Calculated moisture profile in the pressboard at 70°C for moisture diffusion coefficient as a function of concentration using estimated parameters listed in Table 7.1. 186
7.10 Calculated relative permittivity profile in the pressboard at 70°C and f=10 Hz for the moisture diffusion process of Figure 7.9 using the universal curve described by Tables 4.5 and 4.6. 187
7.11 Calculated relative conductivity profile in the pressboard at 70°C and f=10 Hz for the moisture diffusion process of Figure 7.9 using the universal curve described by Tables 4.5 and 4.6. 188

7.12 Calculated transcapacitance and transconductance at 70°C and f=10 Hz for the moisture diffusion process of Figure 7.9 using the universal curve described by Tables 4.5 and 4.6. 189
7.13 Measured transcapacitance and transconductance at 70°C and f=10 Hz for the moisture diffusion process with ambient relative humidity of Figure 7.2. 190
7.14 Calculated gain and phase at 70°C and f=10 Hz for the moisture diffusion process of Figure 7.9 using the universal curve described by Tables 4.5 and 4.6. 191
7.15 Measured gain and phase at 70°C and f=10 Hz for the moisture diffusion process with ambient relative humidity of Figure 7.2. 192
7.16 Comparison of the moisture profiles for a constant diffusion coefficient with linear concentration distribution (dash-dot lines) and diffusion coefficient as a function of concentration at 30°C with a nonlinear concentration distribution (solid lines). The top curves are for Ast's test 2 with sample thickness of 0.0518 cm and the lower curves are for Ast's test 7 with sample thickness of 0.126 cm as listed in Table 7.3. 200

8.1 Couette Facility for monitoring moisture diffusion in oil and pressboard and to determine its effect on flow electrification 203
8.2 The Couette Facility inside the stainless steel hood. 204
8.3 Flow electrification hazard condition analysis due to moisture diffusion as a step change in temperature from 20°C to 70°C moves the initial moisture equilibrium at A instantaneously to B, and then over many diffusion time constants the system reaches the new equilibrium point C at 70°C. 205
8.4 The modified design of the three-wavelength sensor to fit the Couette Facility. 206
8.5 The 1 mm wavelength sensor response to the adjustment of the compression device at $f = 10^{3.796}$=6252 Hz. Each adjustment corresponds to an equal turning torque. As the sensor gets closer to the pressboard with increasing torque, the transcapacitance increases and so does the gain. 207
8.6 The air relative humidity of the Couette Charger during the wetting process at 60°C. 210
8.7 The calculated transcapacitance and transconductance at f=0.1 Hz for oil-free pressboard at 60°C. 211
8.8 The moisture profile obtained from sensor measurements (top) and simulated (bottom) for the wetting process of oil-free pressboard at 60°C with time t in hours. 212
8.9 The frequency sweep of oil-free pressboard in equilibrium with ambient air at 17.8% relative humidity and 70°C prior to drying. 214

8.10 The air temperature and relative humidity of the Couette Charger during the drying process. 215

8.11 The measured gain and phase at $f = 0.1$ Hz of the three-wavelength sensor in the Couette Charger for oil-free pressboard during the drying process. 217

8.12 The oil temperature, relative humidity, and moisture concentration conditions in the Couette Charger when the temperature controller was set to 70°C. The cooling system was turned off, thereby causing the ripple in the controlled temperature. 220

8.13 The measured gain and phase of the oil-impregnated pressboard at f=0.1 Hz when the temperature controller was set from 30°C to 70°C. 221

8.14 The transcapacitance and transconductance of the oil-impregnated pressboard from measurements at f=0.1 Hz when the temperature controller was set from 30°C to 70°C. 222

8.15 The temperature and gain of the 5 mm wavelength for oil-impregnated pressboard at f=0.1 Hz when the temperature controller was set from 30°C to 70°C. The overlap of the period of two "sinusoids" clearly demonstrates that the interdigital sensor instantaneously detects the dielectric property change due to the temperature change. 223

8.16 The simulated and measured gain and phase of the 5 mm wavelength for oil-impregnated pressboard at f=0.1 Hz when the temperature controller was set from 30°C to 70°C. 226

9.1 The Tettex Recovery Voltage Meter RVM 5461. 229

9.2 The Tettex Recovery Voltage Meter (RVM) measurement schematic: (a) The principle circuit of voltage recovery measurement. (b) Time diagram of the RVM procedure. (c) Recovery voltage V_{max} as a function of charging time t_c. 231

9.3 The dielectric spectrum of fresh Shell Diala A oil at room temperature calculated from parallel-plate electrode measurements using fringing field and non-fringing field formulas of (9.1)–(9.4). 233

9.4 The dielectric spectrum measured by general impedance measurement techniques for new and aged oil and pressboard: (a) oil; (b) pressboard. 235

9.5 The test structure for the layered oil and pressboard. 236

9.6 The equivalent circuit for the test structure of Figure 9.5 with pressboard and oil in series. 236

9.7 The calculated (from (9.5)) and measured effective dielectric spectrum by general admittance measurement techniques for a series layer of 1.0 mm thick oil-soaked pressboard and 0.7 mm thick oil: (a) Aged test sample; (b) New test sample. 237

9.8 The measured maximum recovery voltage as a function of charging time t_c for lab-aged and new oil-soaked pressboard at room temperature with V_c=200 V, $t_c/t_d = 2$. Due to a smaller dielectric relaxation time constant, the aged pressboard has a peak closer to the time origin. 239
9.9 The measured recovery voltage with V_c=200 V as a function of open circuit time with $t_c/t_d = 2$ for a lab-aged pressboard and oil layered structure for various charging times at room temperature. With the increase of the charging time, the time at which the recovery voltage reaches maximum shifts to the right because the fast polarization components have decayed away during the longer discharge period. . 240
9.10 Measured return voltage measurements using the Tettex Recovery Voltage Meter with the Couette Facility for various charging voltages with layered oil and pressboard insulation at 70°C. The charging time is t_c=0.02 s and the discharging time is t_d =0.01 s. 242
9.11 Replot of the measured recovery voltage of Figure 9.10 as a ratio of return voltage over the charging voltage. 243
9.12 Measured recovery voltage for layered oil and paper insulation in the Couette Facility as a function of open circuit time for different charging times at 70°C with $V_c = 200$ V and $t_c = 2t_d$. 244
9.13 Measured return voltage measurements using the Tettex Recovery Voltage meter in the Couette Facility for various temperatures with layered oil and pressboard insulation with $V_c = 200$ V, t_c=0.2 s, and $t_d = 0.1$ s. 245
9.14 Measured charging characteristics for (a) aged oil and pressboard in a parallel-plate electrode structure at room temperature, (b) oil and pressboard in the Couette Facility at 70°C, and (c) layered oil and pressboard in the Couette Facility at 30°C with $V_c = 200$ V and $t_c = 2t_d$. 246

B.1 Schematic of the digital expansion board of the interface box circuitry, mainly laid out by D. E. Schlicker at MIT. 257
B.2 Component side of the digital expansion board of the interface box circuitry. 258
B.3 Solder side of the digital expansion board of the interface box circuitry. 259
B.4 Schematic of the drive board of the interface box circuitry. 260
B.5 Component side of the drive board of the interface box circuitry. . . 261
B.6 Solder side of the drive board of the interface box circuitry. 262
B.7 Schematic of the sense board of the interface box circuitry. 263
B.8 Component side of the sense board of the interface box circuitry. . . 264
B.9 Solder side of the sense board of the interface box circuitry. 264
B.10 SMA connections for the drive board. 269
B.11 Connectors for the digital board. 270
B.12 Machine template for the top of the box for LED connections. 271

B.13 Machine template for DB 15 connector on the back of the box. . . . 272
B.14 Machine template for DB 25 connector on the left side of the box. . . 273
B.15 Machine template for SMA connectors on the front of the box. 274
B.16 Machine template for the shielding and separating aluminum plates. 275
B.17 Numbering and positioning of the four-pole double-throw C&K switch for the relay signal. 275

C.1 Moisture in wood pulp as a function of ambient relative humidity curves reconstructed from the 6-th order polynomial fit to Jeffries' data. 282

D.1 The instrument rack of the Couette Facility. 284

List of Tables

3.1 Diffusion coefficient parameters estimated by Foss. 60
3.2 Comparison of diffusion coefficients by Foss and double sided diffusion time for 1 mm thick oil-free and oil-impregnated pressboard using (3.6) and (3.7) with C=0.5%. 60
3.3 Comparison of estimated parameters for the Arrhenius form in (3.9) of the solubility of water in transformer oil as a function of temperature. . 61
3.4 Water saturation solubility in oil by different investigators calculated using Table 3.3 values in (3.9). 61
3.5 Equilibrium moisture in paper under various oil moisture and temperature conditions as reported by different authors. 62
3.6 Quantitative calculation of moisture transfer from oil to pressboard using Method 1. 65
3.7 Typical properties of Shell Diala Oils 74
3.8 Testing results of the measured oils by Doble Engineering before use in thesis experiments. 74
3.9 Additional testing results of the measured oils after thesis experiments and later received non-mixed Ramapo oil by Doble Engineering. 75
3.10 Comparison of measured water solubility at 35°C and conductivity in differently conditioned oils. 80

4.1 Moisture and temperature levels for measurements performed for oil-free pressboard. 85
4.2 The calculated dielectric constant of oil-impregnated and oil-free pressboard as a function of oil-free pressboard density for three different models given in (4.2), (4.4), and (4.12). 98
4.3 Calculated sensitivity of the dielectric constant to the density of the pressboard using the mixed model of (4.12) for oil and air filler materials. 99
4.4 The average values of measured gain and phase in air over 64 frequencies and the estimated relative dielectric constant of air. 105
4.5 The parameters of the universal curve model by a least squares fit of the experimental data to the model in Figure 4.19 described by (4.43) and (4.44). 113
4.6 The parameters of the logarithmic shifting for the experimental data to fit to the universal curve in Figure 4.19. 114

4.7 Moisture content and temperature levels at which oil-impregnated measurements were conducted. 117

5.1 Comparison of the conductivity of pressboard and oil before and after injection of Anti-Static Additive ASA-3 at 70°C using parallel-plate sensor. 143
5.2 Measured interelectrode spacing ratio (a/λ) for five Kapton sensors. The designed value is a/λ=0.25. 145

6.1 The measured gain of the Teflon sensor in air and theoretically predicted gain using different programs. Sheiretov's program takes the sensor electrodes to have zero height whereas Lesieutre's program allows finite height electrodes, here taken to be 14 μm. 153
6.2 The capacitance and relative permittivity for the 1 mm wavelength sensor in air estimated using Lesieutre's program for 0.6 dB variation on the gain measurement. Error bars due to the deviation are given in parentheses. 153

7.1 Diffusion coefficient parameters obtained from measurements using a least squares fit for oil-free pressboard. 182
7.2 A comparison of measured diffusion coefficient (m^2/s) and literature reported values at 60°C. 184
7.3 Ast's original measured data and estimated concentration independent diffusion coefficient for various levels of moisture concentration and temperature. 196
7.4 Estimated coefficients for formula (7.5) from Ast's data and those of Foss and this thesis work. 197
7.5 Ast's original data converted to SI units. 198
7.6 Comparison of the diffusion coefficient $D(\times 10^{-10}$ $m^2/s)$ for the tested conditions by different investigators. Ast1 are those values obtained by Ast using a linear concentration distribution. Ast2 is estimated from Ast's original data in this thesis using the empirical diffusion coefficient formula (7.5) with temperature and moisture dependence listed in Table 7.4. Foss' is estimated using (7.5) with temperature and moisture dependence listed in Table 7.4. $\bar{D} = (D(C_0) + D(C_1))/2$ is an average diffusion coefficient. 199

B.1 Components list for the drive board. 265
B.2 Components list for digital board. 266
B.3 Components list for the sense board. 267
B.4 Additional parts of the interface box 268
B.5 Connection from one end of the multi-conductor cable to DB-15 connector of the interface box. 276
B.6 Connection from the other end of the multi-conductor cable to 9-pin CPC connector of the controller box 276

B.7 Connection from the other end of the multi-conductor cable to 16-pin connector mate with the controller box 16-pin connector. 277
B.8 Connections for the LEDs on the top of the interface box to the digital board. 278
B.9 Board wiring for DB-15 connectors to board headers and switch. 279

C.1 Polynomial fitting parameters for partition curves for ambient air relative humidity and moisture in paper for various temperatures. 281

Chapter 1

Introduction

1.1 Background of Thesis

This thesis presents continuing research on interdigital dielectrometry and its application to measurements of the dynamics of moisture diffusion in transformer insulation materials, extending previous studies by degree candidates at the MIT Laboratory for Electromagnetic and Electronic Systems [1–3].

According to the concepts of frequency-wavenumber dielectrometry, commonly denoted as "$\omega - k$" dielectrometry, application of a spatially periodic potential with fundamental wavelength $\lambda = 2\pi/k$ and angular frequency $\omega = 2\pi f$ to the surface of a test dielectric generates an electric field which penetrates into the volume of the test material to a depth proportional to λ [1]. Consequently, the conduction and displacement currents, which flow into the sensing electrodes, depend on the dielectric properties of the sample.

The measured dielectric properties can be directly related via a calibrated mapping to other physical properties of the material, such as moisture content and temperature. This thesis focuses on the application of "$\omega - k$" dielectrometry for monitoring the moisture content and spatial profile in transformer insulation.

Moisture dynamics between oil and transformer pressboard as a function of temperature is very important in power transformer operation. For example, if there is

too much moisture in the system, dielectric losses cause heating and power dissipation, thereby decreasing transformer efficiency. Furthermore, if the temperature were to drop too quickly before the moisture in the oil could diffuse into pressboard, oil moisture would exceed the saturation value at this temperature, resulting in free water in the oil. Such free water in the high voltage region of the transformer could result in catastrophic electric breakdown and transformer failure. Another transformer failure mode dependent on moisture dynamics is flow electrification, which often arises when a transformer that has been out of service is being recommissioned. A plausible scenario is that as the transformer heats up, moisture is driven out of the pressboard insulation into the oil. The moisture first comes from near the pressboard interface, leaving a very dry interface that is also highly insulating. Any accumulating surface charge has no leakage path and thus the surface charge density can increase until spark tracking discharges occur. These sparks cause gas formation, which can rise into the high electric field region causing a high-energy discharge that causes transformer failure. If failure does not occur during the early times of the recommissioning process, the moisture deeper in the pressboard diffuses to the surface reaching equilibrium with the oil moisture. The moisture diffusion time can easily be a few weeks, but once there is no longer an interfacial dry zone, there is a leakage path for interfacial surface charge so that the surface charge density cannot rise to electric field strengths beyond the breakdown strength of oil and pressboard. Thus, once the transformer is in moisture equilibrium, this flow electrification hazard is minimized. A typical pressboard surface tracking discharge pattern from a failed transformer is shown in Figure 1.1.

1.2 Monitoring of Transformer Insulation

Electrical power engineering was one of the first fields of electrical engineering. The first Technical Committee of the American Institute of Electrical Engineers, an ancestor of today's Institute of Electrical and Electronics Engineers, was the High Voltage Transmission Committee formed in 1903 [4]. Because of the long developing history,

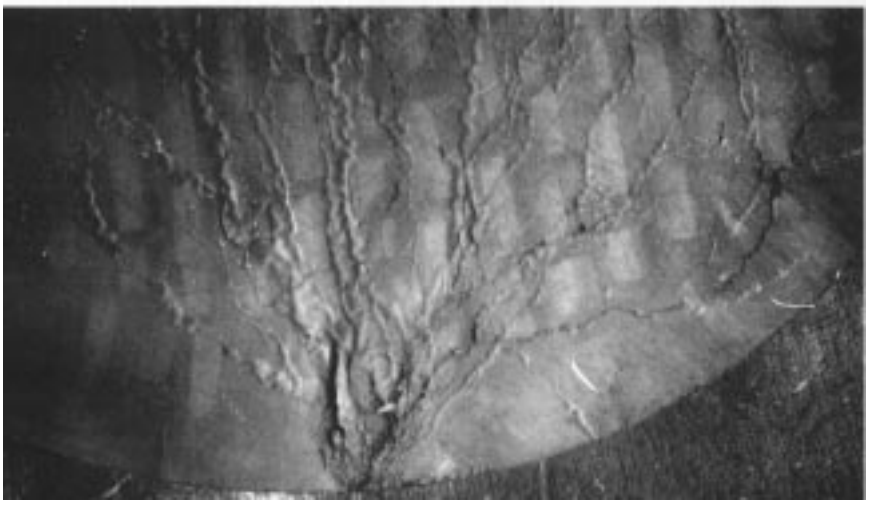

Figure 1.1: A typical surface tracking discharge pattern on pressboard due to flow electrification in a failed transformer.

the number of transformers in service which have now reached a "very respectable" age is steadily increasing [5]. Economical and environmental concerns no longer permit us to replace them at will. A large power transformer can cost more than $1 million and requires about one year to manufacture. A single phase unit of a Westinghouse 500/345kV, 333 MVA auto transformer is shown in Figure 1.2. The huge size of the transformer is demonstrated by contrast with the people around it. Disposal of such a unit is also expensive in addition to the cost of the new unit and the cost of the interruption of the power service. Insulation diagnostics are therefore becoming increasingly important.

Besides the classical insulation testing methods of resistance, power frequency dissipation factor and polarization index measurements, in recent years additional methods to assess insulation systems have been promoted. They include relaxation currents, recovery voltage, and complex capacitance (dielectric spectrum) measurements. A good study of existing methods can be found in [6, 7].

This thesis focuses on the moisture dynamics in power transformer insulation systems and a new non-destructive testing method using an interdigital dielectrometry sensor. As will be discussed in Chapter 3, moisture has detrimental effects on the

Figure 1.2: The author in front of one phase of the Ramapo Substation Westinghouse 500/345kV, 333 MVA auto transformer.

performance of transformer insulation. Therefore close monitoring of the moisture in insulation is important for transformers both during the manufacturing process and during service. One of the major stages in the manufacture of transformers is the processing or drying of the insulation. This thesis work, in developing the interdigital dielectrometry sensor to measure the moisture in pressboard, gives the manufacturers a tool to control and monitor this important stage in the manufacturing process. Through the use of on-line measurement techniques the dryout stage can be optimized reducing the time required. A savings of one half to three days in processing time can be translated to millions of dollars in additional throughput for the transformer manufacturer [8].

1.3 Scope of Thesis

The scope of this thesis work is twofold: to continue the development of sensors and methodologies for the continuous on-line measurement of the moisture dynamics of transformer insulation materials; and to provide a theoretical understanding and modeling of the relationships involved in these measurements. Early degree candidates have developed the multiple wavelength sensor concept, first generation sensor design, computer algorithms based on continuum model, and preliminary measurements to demonstrate the sensor capability. The main objectives of this thesis research are as follows:

1. To design and perform experiments in a bench-top apparatus using a three-wavelength interdigital dielectrometry sensor; and to improve the hardware design including sensor, experimental setup, feed-through for the sensor signal, and electronics for the interface circuitry, for precise experiments.

2. To understand the physics of moisture partitioning in air-paper-oil systems and survey available methods for transformer moisture monitoring.

3. To experimentally determine the correlation between moisture and temperature on complex permittivity in tested materials.

4. To perform moisture diffusion measurements in a bench-top apparatus with the improved sensor design at various temperature and moisture levels.

5. To study the mathematics of nonlinear diffusion processes, and analyze the measured data from the moisture diffusion process to reach quantitative conclusions.

6. To incorporate the three-wavelength sensor into the Couette Facility to do continuous on-line measurements of a simulated transformer environment along with other monitoring instrumentation.

7. To perform time domain measurements using the Tettex Return Voltage Meter and to compare with frequency domain measurements.

1.4 Outline of Thesis

Many of the thesis sections have been presented in the author's publications [9–20].

Chapter 2 gives the basic theoretical background of this research, in particular interdigital dielectrometry. Chapter 3 covers the comprehensive theory and analysis of literature results of moisture dynamics in transformer oil and paper systems. It presents the research of the moisture equilibrium curves for oil-paper systems which have been widely used by utilities and transformer and other test equipment manufacturers, corrects historical mistakes, and clarifies all relevant concepts. A new set of curves was constructed for moisture in oil more than 100 PPM based on the best method.

Chapter 4 experimentally establishes a mapping from moisture and temperature to the dielectric properties of oil-free pressboard. It is the bridge for using interdigital sensors to monitor the moisture content of pressboard. A dielectric model for biological tissue is adopted for the cellulose-structured pressboard. The universal curve is found by fitting the data to the model. Preliminary measurements with the oil-impregnated pressboard show similar trends.

Chapter 5 reports the results and associated problems using a previously designed three-wavelength sensor. The multi-wavelength interdigital sensor is shown to be capable of monitoring the moisture diffusion process in pressboard.

Chapter 6 presents a new sensor and interface circuitry design. Qualitative results on temperature and thickness effects on moisture diffusion are discussed. Chapter 7 gives quantitative analysis of the measured moisture diffusion coefficient as a function of moisture and temperature in a bench-top apparatus. Literature results are also analyzed to provide comparison with this thesis work.

Chapter 8 reports the results of a specially designed three-wavelength sensor for the Couette Facility, a laboratory system that simulates a transformer environment. Moisture diffusion measurements are performed and system dynamics with a step change in temperature are also given. Chapter 9 presents a newly promoted time-domain mea-

surement technique: recovery voltage measurements using the Tettex Recovery Voltage Meter. Time domain measurements of aging and temperature effects are studied for both a parallel-plate electrode geometry and a coaxial cylinder electrode geometry (the Couette Facility). The results qualitatively show good agreement with theory.

A series of appendices serves both to provide complementary information for hardware design and experiments, and as a handy reference for future researchers.

Chapter 2

Theoretical Background

2.1 Interdigital Dielectrometry

The generic schematic of an interdigital dielectrometry sensor below a lossy dielectric medium of semi-infinite extent is shown in Figure 2.1. This electroquasistatic system has an electric scalar potential Φ obeying Laplace's equation. Neglecting variations in the y direction, the solution for each wavelength can be written as an infinite series of sinusoidal Fourier modes of fundamental spatial wavelength λ in the x direction that decays exponentially in the z direction:

$$\Phi(x,z) = \sum_{n=0}^{\infty} \Phi_n e^{-k_n z}(A_n \sin k_n x + B_n \cos k_n x), \tag{2.1}$$

where $k_n = 2\pi n/\lambda$ is the wavenumber of each spatial mode. As extensively studied in [1,3], the electric field distribution for a multi-layer dielectric system can be solved by defining a complex surface capacitance density $\hat{C}_n$, which relates $\varepsilon^* \hat{E}_{zn}$ at each planar interface at $z = constant$ to the potential $\hat{\Phi}_n$ at that surface for every Fourier mode n as:

$$\hat{C}_n = \frac{\varepsilon^* \hat{E}_{zn}}{\hat{\Phi}_n} \tag{2.2}$$

where the complex permittivity ε^* in (2.2) is defined as

$$\varepsilon^* = \varepsilon' - j\varepsilon'' = \varepsilon' - j\frac{\sigma}{\omega}, \tag{2.3}$$

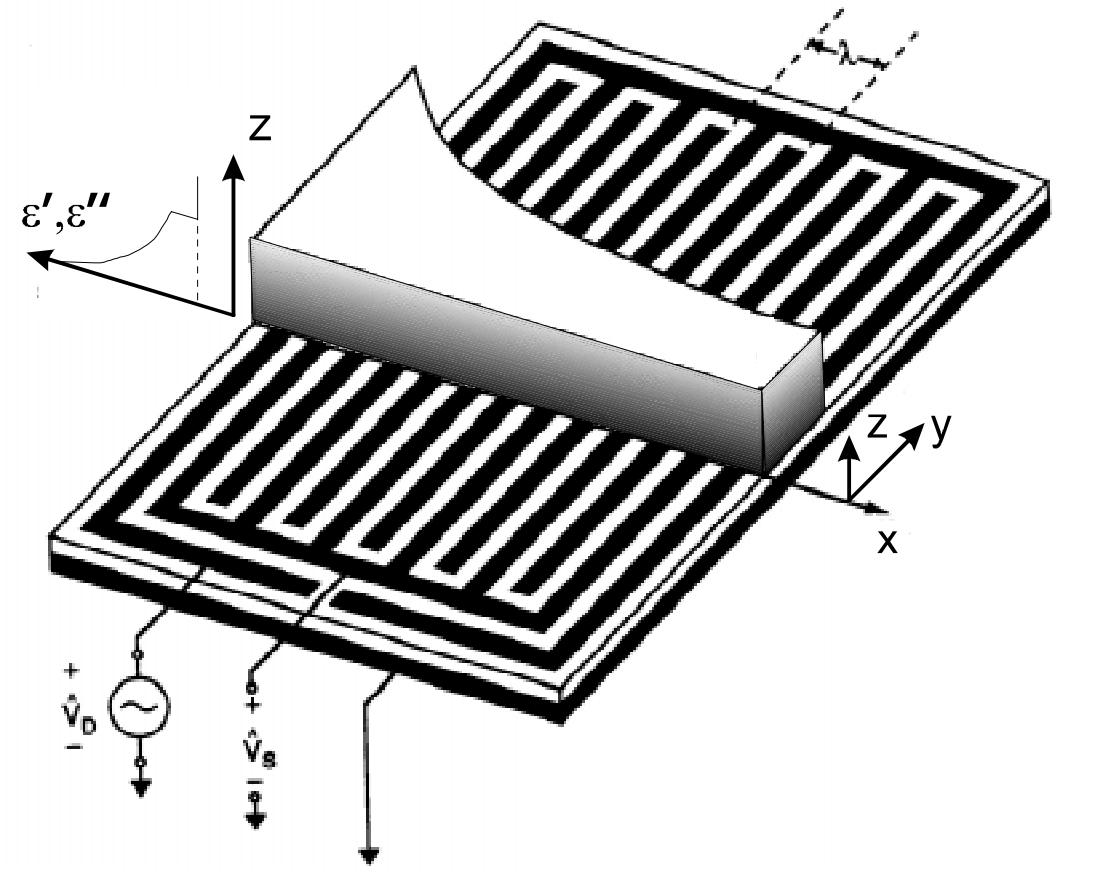

Figure 2.1: Imposed $\omega - k$ interdigital dielectrometry [21].

where ε' is the real part of the complex permittivity, ε'' is the magnitude of the imaginary part of the complex permittivity, and σ is the conductivity of the media. Knowing $\hat{C}_n$ at the electrode surface allows us to calculate the terminal currents due to the sum of conduction and displacement currents from the potential distribution at that surface, which is practically equivalent to forward-solving (2.1).

For heterogeneous media, spatial profiles of dielectric properties can be determined using multiple-wavelength sensors with each wavelength having a different penetration depth into the dielectric in contact with the sensor. Equation (2.1) shows that the electric field decays away in the z direction with penetration depth proportional to the spatial wavelength λ, i.e. the longer the wavelength, the farther the field can penetrate into the material, and the farther the dielectric properties can be measured. This

concept is the key ingredient of the profiling technology.

2.2 Moisture Measurement for Transformer Insulation

The presence of moisture in transformer insulation directly affects the system performance, so it is desirable to monitor insulation moisture content. For the oil, there are commercially available sensors to measure the moisture directly, and in equilibrium, the moisture content in the pressboard can be obtained using the partitioning curves relating moisture in oil to moisture in paper [22–24]. Those curves have been widely used by many utilities and transformer and test equipment manufacturers, and a thorough study of this topic is helpful to use this tool correctly and effectively.

For solids there are no commercially available instruments to continuously monitor the moisture distribution under non-equilibrium conditions. The multiple-wavelength interdigital dielectrometry sensor developed at the Laboratory for Electromagnetic and Electronic Systems, Massachusetts Institute of Technology, is a unique way to monitor the moisture profile in transformer board in real time.

The sensor measures the change of the dielectric properties during the moisture diffusion process and by a calibrated mapping that relates the dielectric properties to the moisture content, the spatial profile of moisture can be resolved using an inverse algorithm.

2.3 Dielectric Properties of Insulating Materials

Since the quantities that the interdigital sensor directly measures are dielectric properties of the test material, this section gives the basic background about the dielectric properties of insulating materials and their significance. Most of this section is from references [25, 26]. Dissipation factor (or power factor) D is a measure of the dielectric losses in an electrical insulating material when used in an alternating electric field

where the energy is dissipated as heat. From

$$Y = j\omega C^* = j\omega g\varepsilon^* = G + j\omega C = j\omega g(\varepsilon' - j\varepsilon''), \tag{2.4}$$

where Y is the complex admittance, ω is the angular frequency, G is the equivalent AC conductance, C is the capacitance, and g is the geometric parameter for the test cell shape and size, we obtain

$$\varepsilon' = C/g, \varepsilon'' = G/(\omega g). \tag{2.5}$$

For a parallel-plate capacitor, g is the ratio of area A to gap d.

The dissipation factor is defined as

$$D = \varepsilon''/\varepsilon' = \tan\delta = \cot\theta = G/\omega C, \tag{2.6}$$

where δ is the loss angle, and θ is the complementary phase angle (δ+θ=$\pi/2$). A low dissipation factor indicates low dielectric losses. The dissipation factor may be useful as a means of quality control, and as an indication of changes in quality resulting from contamination, deterioration in service, or as a result of handling.

Power factor PF is the ratio of the power dissipated in a material to the product of the rms sinusoidal voltage and current,

$$PF = G/\sqrt{G^2 + (\omega C)^2} = \sin\delta = \cos\theta, \tag{2.7}$$

therefore,

$$PF = D/\sqrt{1 + D^2}. \tag{2.8}$$

When the dissipation factor is less than 0.1, the power factor differs from the dissipation factor by less than 0.5%.

Insulating dielectric materials are generally used in two distinct ways: (1) to support and insulate components of an electrical network from each other and from ground; (2) and to function as the energy storage medium of a capacitor. For the first use, a low value of relative permittivity is often desirable in order to minimize the capacitance, while maintaining acceptable mechanical, chemical, and heat transfer properties. When

used as the dielectric in a capacitor, it is desirable to have a higher value of relative permittivity so the physical size of the capacitor may be as small as possible. However, an intermediate value of relative permittivity may sometimes be advantageous in achieving a better voltage distribution between the liquid and solid insulating materials with which the liquid may be in series. Intermediate values of permittivity are also sometimes used for grading stresses at the edge or end of conductors to minimize a-c corona.

Factors affecting permittivity and loss characteristics include: frequency, temperature, voltage, humidity, water immersion, weathering, deterioration, and conditioning. When adequate correlating data are available, permittivity and loss factor can be used to indicate the characteristics of a material in other respects such as dielectric breakdown, moisture content, degree of cure, and deterioration from any cause. This is the underlying basis for applying the interdigital dielectrometry sensing technique.

2.4 Frequency and Time Domain Measurements

The thesis research is mainly focused on frequency domain measurements since the interdigital dielectrometry technique is currently applied in the frequency domain. For linear systems, because the time-dependence of the current response to a step-function field and the frequency dependence of the dielectric susceptibility in response to a sinusoidal excitation are related by a Fourier transformation, measurements in one domain provide information in the other domain.

Measurements of permittivity and dielectric loss as a function of frequency are an important technique for investigating dielectric materials. Measurements in the frequency domain can be carried out by applying a sinusoidal voltage with known frequency and amplitude across the test dielectric. From the amplitude and phase of the current through the material and the geometry of the object, the complex permittivity can be estimated. To obtain the spectrum of the complex permittivity this procedure is repeated at each frequency in the desired spectrum. The typical frequency range

that is of interest in high voltage insulation is from 0.001-10 kHz. The advantages of doing frequency measurements are the availability of precise commercial equipment, high precision due to the narrow band of frequency at any single measurement, and the availability of high frequency signals up to even the terahertz region.

The time-domain measurements have the advantage of requiring a single time signal to determine a wide band frequency response. To detect aging or moisture content, it is necessary to analyze the low frequency part of the polarization spectrum. However it is very difficult to generate a 1 kV sinusoidal signal at 0.001 Hz [27]. The time-domain technique has its advantages over frequency-domain measurements for materials having very slow relaxations [28], for specimens that are unstable in time, or too small to fit in a regular dielectric cell [29]. Therefore some study is also performed in this thesis work using a time domain measurement technique. For a more thorough investigation of measurement techniques in both time and frequency domains, refer to [6, 7].

Chapter 3

Moisture Equilibrium in Transformer Oil-Paper Systems

The presence of moisture in transformers deteriorates transformer insulation by decreasing both the electrical and mechanical strength. The importance of moisture presence in paper and oil systems has been recognized since the 1920's.

It is useful to know the moisture partitioning curves between oil and paper under equilibrium conditions. When the transformer is in equilibrium operation, this provides a quick way of examining the moisture content in paper to predict future failure by measuring the moisture in oil. Over the years, many scientists have reported such a set of curves, but there has not been a comprehensive review and comparison for different curve sets. The research spans over several decades and is an important resource for electric utilities and insulation and testing equipment manufacturers. This chapter gives an overview of the classic moisture equilibrium curves and their history, and provides useful information on the relationships among them and their validity.

These curves are also used for moisture diffusion analysis using interdigital sensors in Chapter 7 and Chapter 8.

3.1 Background

An excellent review of the basic concepts that are used in this chapter is given in [30]. A brief introduction is given here.

3.1.1 Transformer Oil

Transformer oil is made by refining crude oil. It is mainly a mixture of hydrocarbon compounds of three classes: alkanes, naphthenes, and aromatic hydrocarbons. These molecules have little or no polarity. A minor part of the constituents is that of polar and ionic species, which may greatly influence the chemical and electrical properties of the oil. "Polar compounds found in transformer oil usually contain oxygen, nitrogen, or sulfur. Ionic compounds would typically be organic salts found only in trace quantities" [30]. For a more complete review on transformer oil, refer to [31].

3.1.2 Water in Oil

Insulating oils, such as transformer oil, have a low affinity for water. However, the solubility increases markedly with temperature for normally refined naphthenic transformer oil. This will be discussed more quantitatively later in this chapter. Water can exist in transformer oil in three states: (1) in practical cases, most water in oil is found in the dissolved state; (2) certain discrepancies in examining the moisture content using different measurement techniques suggests that water also exists in the oil tightly bound to oil molecules, especially in deteriorated oil; and (3) when moisture in oil exceeds the saturation value, there will be free water precipitated from oil in suspension or drops. Moisture in oil is measured in parts per million (PPM) using the weight of moisture divided by the weight of oil (μg/g).

3.1.3 Relative Humidity

Relative humidity can be defined in terms of the moisture mixing ratio r versus the saturation mixing ratio r_s, $R.H.\% = 100r/r_s$, which is a dimensionless percentage. Relative humidity for air is the water vapor content of the air relative to its content at saturation. Relative humidity for oil is the dissolved water content of the oil relative to the maximum capacity of moisture that the oil can hold at that temperature. Because the saturation mixing ratio is a function of pressure, and especially of temperature, the relative humidity is a combined index of the environment and reflects more than water content [32].

3.1.4 Paper

The following four terms are often used interchangeably in the context of solid transformer insulation: pressboard, paper (or Kraft paper), Transformerboard, and cellulose. Although in the context of particular transformer insulation, they may indicate different parts, e.g. paper tape, paper cylinders, transformerboard cylinders, angle rings, blocks, etc., in the context of moisture equilibrium, they all in general refer to electrical grade paper insulation manufactured from unbleached sulfate cellulose, consisting of a more or less long chain of glucose rings. Pressboard has been well known in the textile and paper processing industries for more than a hundred years and was used in the first electric machines. Transformerboard resulting from the efforts of Hans Tschudi-Faude of H. Weidmann Limited in the late 1920's [33] is a better type of pressboard meeting the requirements of large power transformers. It is made with high-grade sulfate cellulose, and consists solely of pure cellulose fibers without any binder. It can be completely dried, degassed, and oil impregnated. Insulation paper can be manufactured to different density, shape, and other properties for different applications.

3.1.5 Water in Paper

Water in paper may be found in four states: be adsorbed to surfaces, as vapor, as free water in capillaries, and as bound water. The paper can contain much more moisture than oil. For example, a 150 MVA, 400 kV transformer with about 7 tons of paper can contain as much as 223 kg of water [34]. The oil volume in a typical power transformer is about 80,000 liters with mass approximately 70,000 kg. Assuming a 20 PPM moisture concentration in oil, the total mass of moisture is about 1.4 kg, much less than in the paper. The unit for moisture concentration in paper is typically expressed in %, which is the weight of the moisture divided by the weight of the dry oil-free pressboard. Thus, for very dry pressboard with 0.5% moisture, the moisture mass in a typical power transformer is about 35 kg.

3.1.6 Water Vapor Pressure

Water vapor pressure is the partial pressure exerted by water vapor. When a gas is in contact with a reservoir of water, in equilibrium it reaches the saturation water vapor pressure. Saturation vapor pressure is a measure of the tendency of a material to change into the gaseous or vapor state, and it increases with temperature. At the boiling point of water, the saturation water vapor pressure at the surface of water becomes equal to atmospheric pressure.

3.2 Moisture Effects on Transformer Oil-Paper Systems

An overview of literature reported effects are summarised in this section.

3.2.1 Moisture Effects on Oil

In general, water has little effect on transformer oil. For example, a pure hydrocarbon oil exposed to humid air shows a loss angle δ lower than 0.0002 radians at frequencies up to 10 MHZ [35]. Measurements have shown that the oil conductivity is essentially independent of the moisture content [11,36]. The effects of moisture would be increased by trace amounts of salts, acids, alkalis, alcohols or any substance which ionizes in water solutions [35]. Water in mineral oil transformers increases the risk of bubble formation when desorption of water from the cellulose increases the local concentration of gases in the oil [37].

3.2.2 Moisture Effects on Paper

In general, the mechanical life of pressboard insulation is reduced by half for each doubling in water content [38]; the rate of thermal deterioration of the paper is proportional to its water content [22]. Electrical discharges can occur in a high voltage region due to a disturbance of the moisture equilibrium causing a low partial discharge inception voltage and higher partial discharge intensity [33]. Moisture has a strong effect on increasing paper conductivity. The migration of a small amount of moisture has been associated with flow electrification at paper/oil interfaces and is presumed to be due to charge accumulation on highly insulating interfacial dry zones where moisture has been desorbed [39, 40].

3.3 Off-line Methods to Measure Moisture in Transformer Insulation

There are two types of off-line methods: the Karl Fischer reaction method and the pressure gauge method.

The standard test method for measuring water in transformer oil is the ASTM D 1533 test [41] known as the Karl Fischer reaction test. It is based on the reaction of

halogens with water in the presence of anhydrous sulphur dioxide. It is widely used because of its high selectivity and sensitivity. There are commercial instruments such as the Mitsubishi Moisture Meter to accomplish the Karl Fischer titration automatically. With these instruments, an oil sample can be directly injected into the reaction unit and the moisture content will be given at the end of the reaction. In the case that the liquid samples contain interfering substances reacting with the reagents, the oil samples are placed in a water vaporizer and then the water vapor is circulated to the reaction unit to be measured.

The standard test method for moisture content of oil-impregnated cellulosic insulation is described in ASTM D 3277 [42]. The major difference is that the moisture needs to be first extracted from the cellulose. It can be done by solvent extraction or by vaporizing. In order to thoroughly extract the moisture in the paper, the paper insulation needs to be delaminated. After extraction the Karl Fischer reaction instruments can then be used the same way as for the oil to give the moisture content.

The pressure gauge method "consists of degassing and dehydrating, by extraction in a vacuum, a known quantity from the studied body, oil, paper impregnated or non-impregnated, then to separate the different volatile compounds collected either by condensation on a cold point, or by combustion." [43]. The extracted water is then heated to vapor and the vapor pressure, measured by a mercury pressure gauge, is proportional to the quantity of water content.

These direct methods require removing the moisture, so they are not practical for on-line monitoring of the transformer insulation.

3.4 On-line Methods to Measure Moisture in Transformer Insulation

For oil, there are commercially available meters that measure the relative humidity of the transformer oil in real time such as the Harley moisture sensor from J. W. Harley

Inc., and Aquaoil 100 A from Syprotech. The relative humidity can be converted to absolute moisture content by multiplying the relative humidity with the saturation moisture (solubility) of transformer oil at the measured temperature.

The recovery voltage method has been used for transformer diagnostics for years. It is based on the observation that the dielectric polarization spectrum of the paper insulation is directly related to conditions like aging and moisture content. A voltage pulse is first applied to the test specimen, which is then short circuited for a certain period of time. Then the specimen is open-circuited and the return voltage is measured which can be related to the polarization spectrum. With a calibration, it can non-destructively provide the moisture content. One such commercial product is the Tettex Automatic Recovery Voltage Meter from the Tettex Instruments Division of the Haefely Trench AG. An application of this method is given in [44].

The recovery voltage time-domain measurement is currently a unique way to measure moisture on-line. However it only gives the average moisture content of the measured paper insulation. The three-wavelength frequency-domain interdigital dielectrometry sensor investigated in this project uses the same principle that the dielectric properties of the insulating material are directly related to the moisture content, but by having multiple wavelengths, the sensor can also measure the moisture spatial profile. Since the moisture distribution can cause a DC charge redistribution due to flow electrification induced charge separation of the electrical double layer by greatly affecting electrical leakage through the pressboard, knowledge of pressboard moisture profiles is very critical to study the mechanism of flow electrification induced transformer failure.

3.5 Moisture Equilibrium Curves

It is necessary to know the moisture partitioning curves between oil and paper under equilibrium conditions. When the transformer is in equilibrium operation, this provides a quick way of examining the moisture content in paper to predict future life by measuring the moisture in oil. Over the years, many scientists have reported such

a set of curves, but there has not been a comprehensive review and comparison for different curve sets. The research spans over several decades and is an important resource for electric utilities and insulation and testing equipment manufacturers. This chapter gives an overview of the classic moisture equilibrium curves and their history, and provides useful information on the relationships among them and their validity.

3.5.1 Overview

Fabre-Pichon Curves

The moisture-equilibrium curve for an oil-paper complex was first reported by Fabre and Pichon [22] in 1960 and is shown in Figure 3.1. It is the most widely cited set of curves. The paper used was Kraft paper and an air-paper-oil complex was studied. A later summary of the work carried out at the same laboratory by Fallou [43], states that the moisture content of the oil and oil-impregnated pressboard were directly measured by the Karl Fischer reaction method.

The paper emphasized the equilibrium law which is similar to the principle that Oommen used in [23] to indirectly obtain the moisture equilibrium curves for oil-paper systems: "The relative humidity (that is to say referred to saturation value) is the same in the oil and in the air in contact with one another at the same temperature [45]." This was proved to be true within the limits of the experimental procedures by General Electric in 1960 [46].

In 1963, Norris referred to the Fabre-Pichon curves in Figure 8 of his paper [47]. Thus these curves became "affectionately" known as the "Norris Curves" even though they were originally published in Fabre-Pichon's paper [22]. EHV-Weidmann Industries, Inc., St. Johnsbury, Vt., a company specializing in Transformerboard manufacturing, redrew the curves shown in Figure 3.2 and credited Norris by noting data from [47]. Similarly, they are noted as "Norris Curves" in Figure 3 of [48], and Figure 5.4 of [49].

One possible reason for these historical mistakes is that Norris was perhaps the

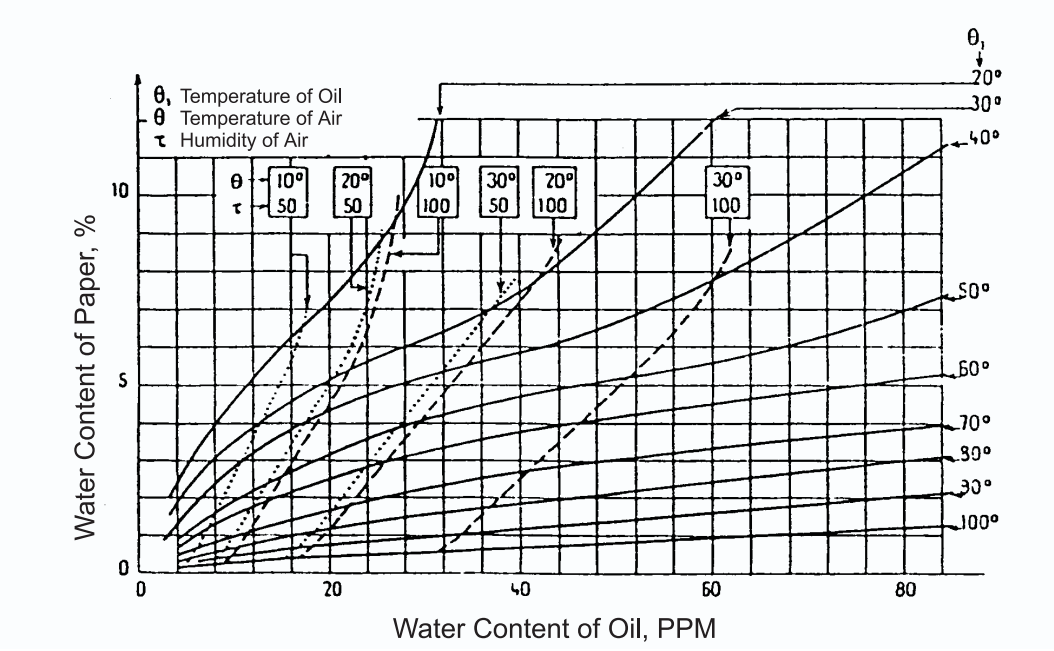

Figure 3.1: Fabre-Pichon Curves for moisture equilibrium of the air-oil-paper complex as a function of the air and oil surrounding the paper. Figure is taken from [22] except labels are translated into English.

earliest proponent of studying moisture transient processes in transformers. The other cause might be that Fabre-Pichon's paper [22] was published in CIGRE which is not a document that can be easily publicly accessed, and the original paper was in French—even the English translated paper still has French labels in all the figures. Many other people redrew the curves in a different format and the original source was lost.

Oommen Curves

In 1983 Oommen developed a set of moisture equilibrium curves, published in [23] and shown in Figure 3.3. Oommen's method is based on the principle that the equilibrium curves represent the same relative saturation for the oil and for the paper at the same temperature. He combined the Moisture in Oil versus Relative Humidity Curves in air with Moisture in Paper versus Relative Humidity curves in air to make the Moisture in Paper versus Moisture in Oil equilibrium curves.

The Moisture in Oil versus Relative Humidity curves are straight lines with the

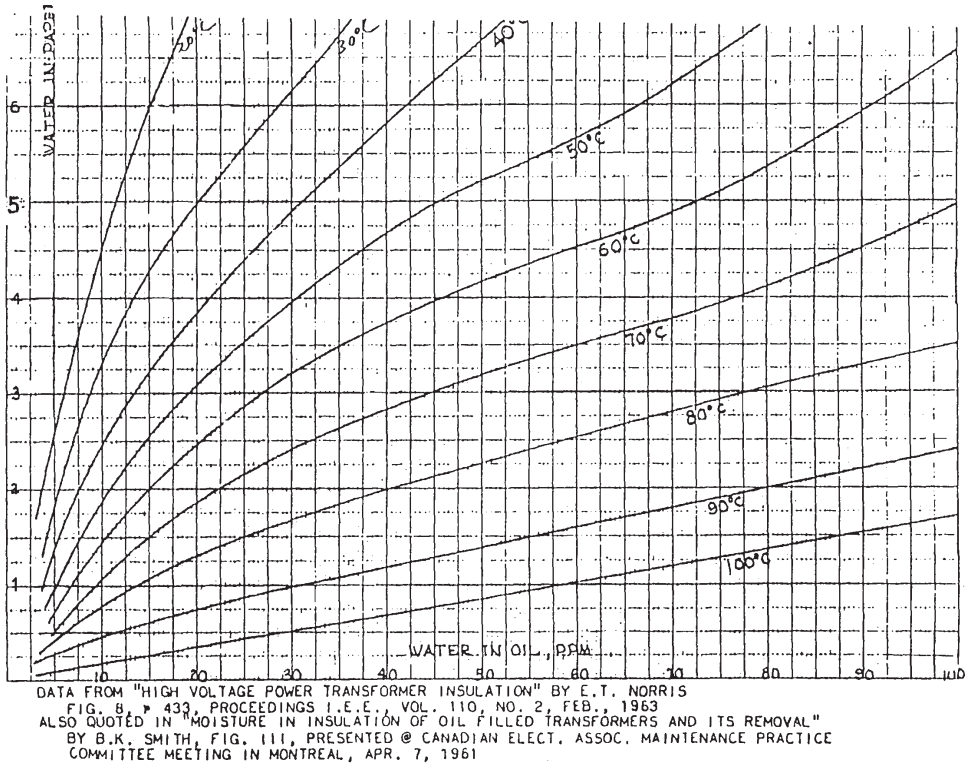

Figure 3.2: Curves redrawn by EHV-Weidmann for moisture equilibrium of the air-oil-paper complex as a function of the oil moisture and temperature surrounding the paper.

relationship

$$x_w = x_w^s \times R.H., \tag{3.1}$$

where x_w is the moisture in oil in PPM, x_w^s is the water solubility in oil in PPM, and $R.H.$ is the relative humidity of oil.

Oommen used the oil equilibrium curves along with the Moisture in Wood Pulp versus Relative Humidity Curves made from Jeffries' Data [50] shown in Figure 3.4 and generated the moisture equilibrium curves for a paper-oil system shown in Figure 3.3. The dashed lines indicate desorption curves, whereas the solid lines indicate the adsorption curves. For the same relative humidity, the moisture content of the desorption curves is slightly higher than that of the adsorption curves.

As pointed out by Reason in [51], if the relative humidity of the oil is measured

by commercially available sensors, Jeffries' data in Figure 3.4 can be directly used to estimate the equilibrium moisture concentration in the pressboard.

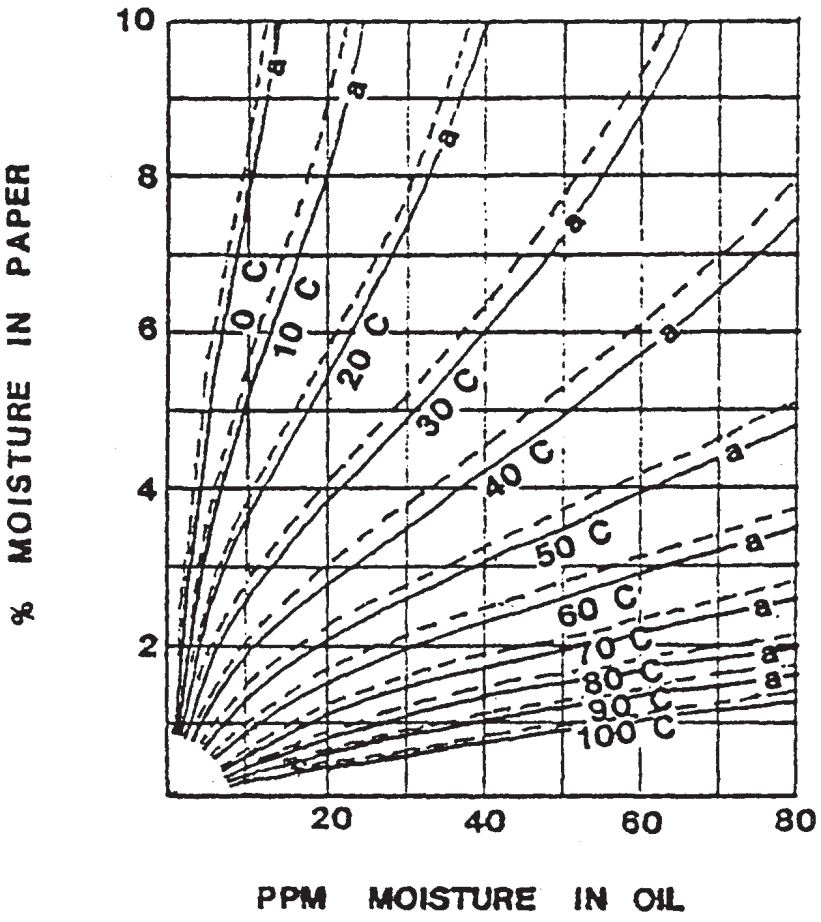

Figure 3.3: Oommen's Curves for various temperatures for moisture equilibrium in a paper-oil system [23]. Solid lines are for adsorption and dashed lines are for desorption.

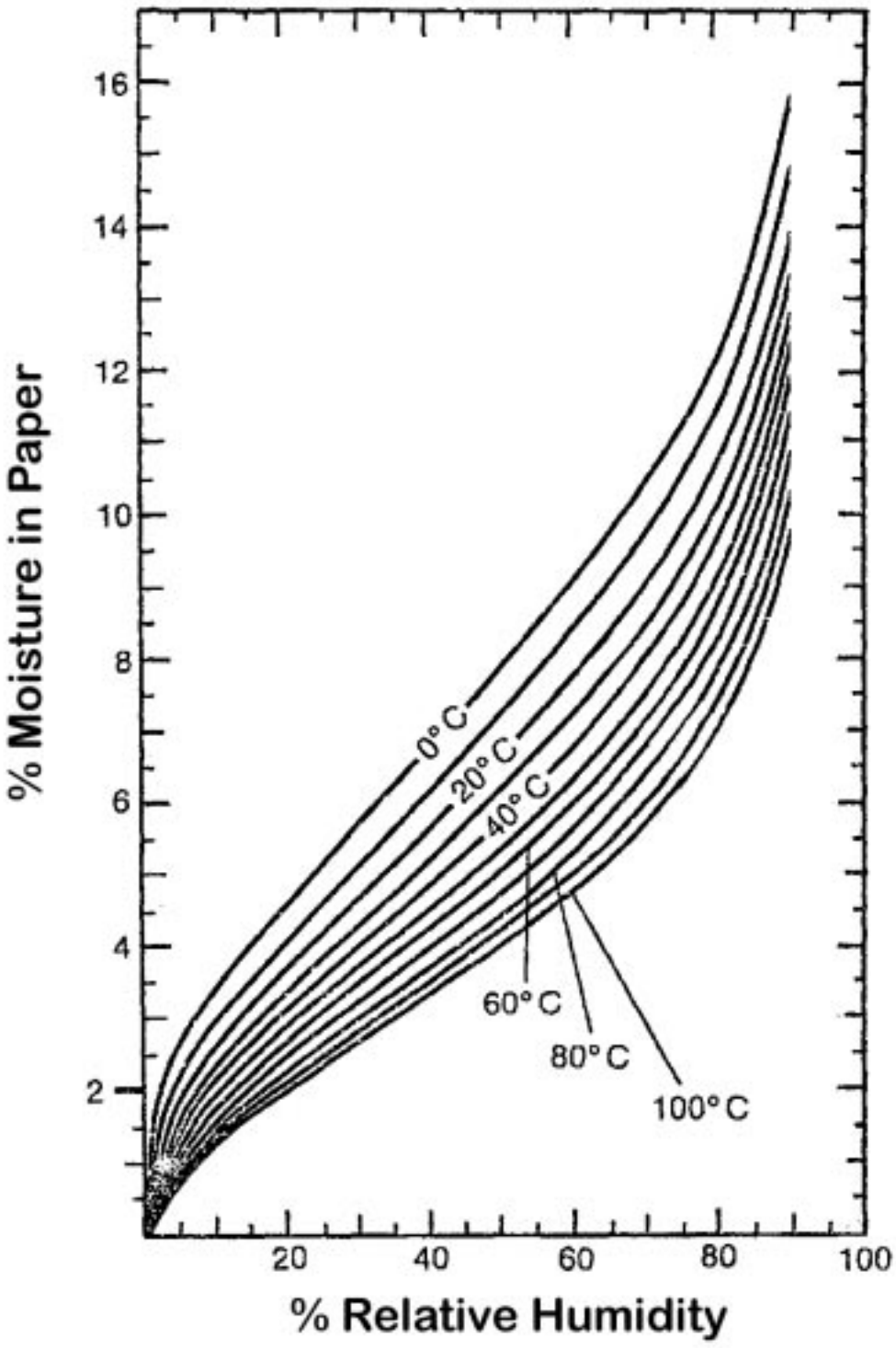

Figure 3.4: Moisture in wood pulp as a function of relative humidity of the ambient by Jeffries [50]. Figure supplied by Oommen at ABB-ETI who redrew Jeffries' data.

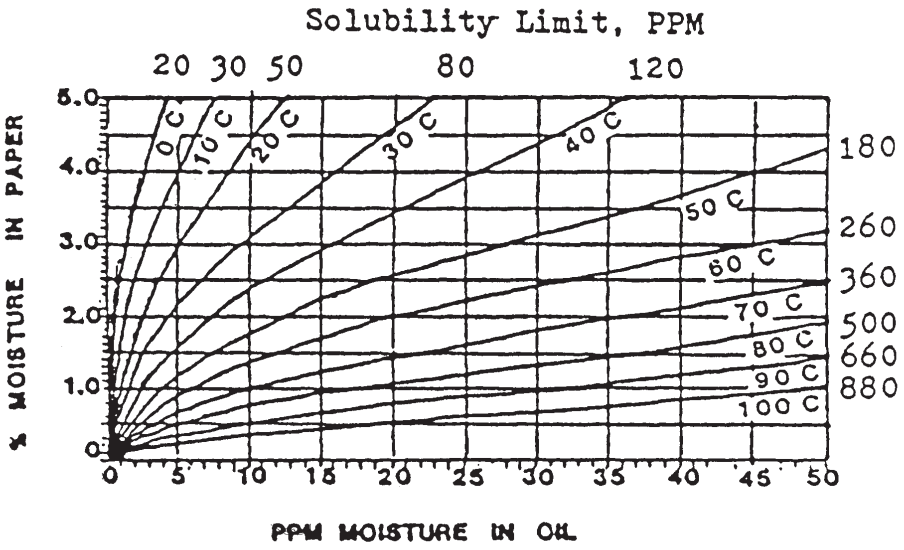

Figure 3.5: Oommen Curves for low moisture region of moisture equilibrium for a paper-oil system [23].

Figure 3.3 is not very reliable in the low moisture range due to the impractical conditioning of paper below 10% relative humidity. Hence, Oommen used the data of the vapor pressure of water in the gas space above the sample in a sealed system reported by Beer et. al. in 1966 [34] and converted to relative humidity by the relationship

$$\%R.H. = \left(\frac{p}{p_0}\right) \times 100, \tag{3.2}$$

where p_0 is the saturated water vapor pressure [52] and p is the water vapor pressure.

Combining the sorption curves for paper and oil again, Oommen constructed the sorption curves for the low moisture region as shown in Figure 3.5.

Equilibrium Curves for Water Vapor Pressure and Moisture Content

From both Fabre-Pichon and Oommen's statements, we see that the equilibrium curves for water vapor pressure and moisture content in paper can be used to derive the partition curves between oil and paper. Thus it is worthwhile to look at the evolution of this set of curves.

Piper (1946)

Among the families of equilibrium curves for water vapor pressure and moisture concentration of oil-free paper curves, the early and most widely used by manufacturers and utilities was reported by Piper [53] in 1946. Piper combined four groups of data from the literature to get a full set of curves: 1) data for cotton in high moisture concentration from Urquhart and Williams [54]; 2) data for cotton of low moisture content from Neale and Stringfellow [55]; 3) data for Kraft paper of low moisture content at elevated temperatures from Houtz and McLean [56]; and 4) data for spruce wood of high moisture content from Pidgeon and Maass [57]. By interpolation and extrapolation of experimental data, Piper derived that for the same vapor pressure, the moisture in Kraft paper is 1.7 times that of cotton.

Jeffries (1960)

This factor of 1.7 was then considered to be too high by Jeffries in 1960 compared with his data [50].

Beer et. al. (1966)

In 1966, Beer et. al. measured the water vapor adsorption curves for Kraft paper by a modified Edwards' apparatus [34]. In the sense of completeness, Beer's curve is apparently improved over Piper's because all Beer's data were obtained for Kraft paper directly.

Ewart (1974)

A paper by Guidi and Fullerton [58] covered the work performed by Ewart. Ewart's data also suggested that the paper water contents derived from cotton by Piper are too high.

Oommen (1984)

Beer's charts were not widely adopted, partly because it is not in a form that can be conveniently used. Oommen in 1984 [59] reconstructed similar charts using the data from Beer et. al. By comparison, he found the new charts will give slightly lower estimates of the moisture content for a given vapor pressure and temperature than the Piper chart.

Fessler et. al. (1987)

Fessler et. al. needed an accurate formula to build a model for bubble formation in transformers. Noticing the differences in the literature, they directly measured the moisture in paper and the moisture vapor pressure and did a comparison with existing reports [37]. Their results showed that the Piper database tends to be higher than any of the other databases and all of the other data is in reasonably good agreement. Fessler et. al. combined the data from Houtz, Ewart, Oommen and their own experiments and determined a water-paper equilibrium formula:

$$C = 2.173 \times 10^{-7} \times P_v^{0.6685} \times e^{(4725.6/T)}, \tag{3.3}$$

where P_v is the vapor pressure of water in atmospheres, C is the concentration of water in paper ($gH_2O/gPaper$), and T is the absolute temperature in °Kelvin. The water vapor pressure as a function of water concentration and temperature is also given in the report:

$$P_v = 5.8869 \times 10^9 \times C^{1.4495} \times e^{(-6996.7/T)}. \tag{3.4}$$

However, from algebraic inversion of (3.3), the correct pressure relation is:

$$P_v = 9.2683 \times 10^9 \times C^{1.4959} \times e^{(-7069.0/T)}, \tag{3.5}$$

which differs from (3.4). It appears that the derivation of (3.4) from (3.3) had an algebraic error. The difference between the two types of curves is shown in Figure 3.6. Figure 3.6 further demonstrates that (3.4) is not the inverse of (3.3) because the calculated P_v at the highest concentration at 100°C should be one atmosphere.

Using (3.2), we can also construct curves for Moisture in Paper versus Relative Humidity shown in Figure 3.7 for formulas (3.4) and (3.5). There are large differences for the high relative humidity levels between the experimental data in Figure 3.4 and the fitted data in Figure 3.7. Oommen in [23] pointed out that the sorption curves cannot be fitted exactly by any mathematical relationship for the entire range. A multi-layer adsorption model predicts a sharp rise in moisture adsorption after 50% RH [60]. Both Jeffries' curves in Figure 3.4 and the Moisture in Paper versus Relative

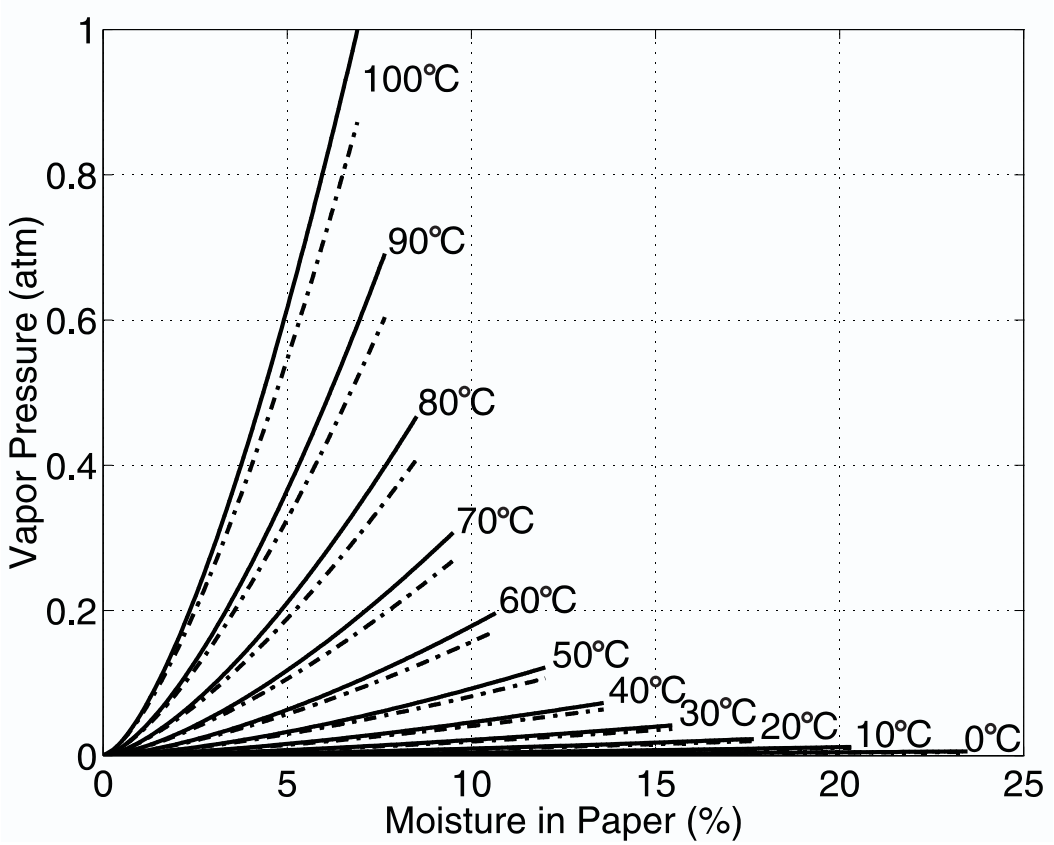

Figure 3.6: Vapor pressure versus moisture in paper comparing the erroneous formula of Equation (3.4) (dashed line) and the correct formula of Equation (3.5) (solid line).

Humidity curve in Figure 1 of Ewart's report [46] show that the slope increases at high relative humidity levels. Fessler et al's curves flatten out at the high end, which indicates possible error of the model for the high relative humidity region.

Oommen [61] also found out that the prediction of bubble evolution temperature using the mathematical model developed in [37] is off by 50 degrees in gas saturated systems. His study [61] gave the correct experimental results.

Griffin Curves

Griffin et al. at Doble Engineering in 1988 made similar curves for mineral oil and paper using Oommen's method [24]. The mineral oil refers to a typical naphthenic-based electrical insulating mineral oil.

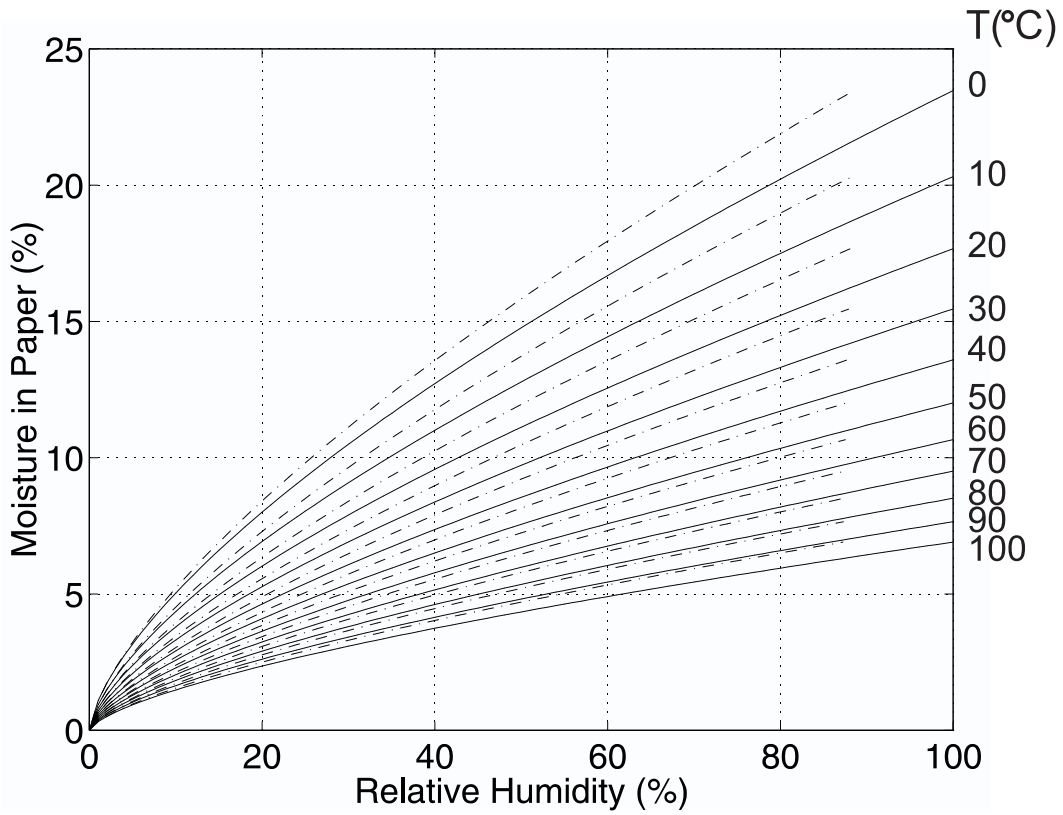

Figure 3.7: Moisture in Paper versus ambient Relative Humidity curves comparing erroneous Equation (3.4) (dashed line) and correct Equation (3.5) (solid line).

They used Fessler's formula (3.4) for vapor pressure and then converted to relative humidity using (3.2). Their original curves are shown in Figure 3.8. A comparison is given in Figure 3.9 replacing erroneous (3.4) with correct (3.5).

MIT Curves

All of the above curves available in the literature are up to at most 100 PPM moisture in oil because the primary concern of moisture concentration in the transformer environment is within that range. However, our laboratory experiments that operate at high moisture concentrations require the curves to cover a wider range. Using Oommen's method and Jeffries' curves, we generated a wider range of equilibrium curves from 0°C to 100°C and moisture in oil up to 800 PPM shown in Figure 3.10. For water in paper below 1%, we use Oommen's curves in Figure 3.5.

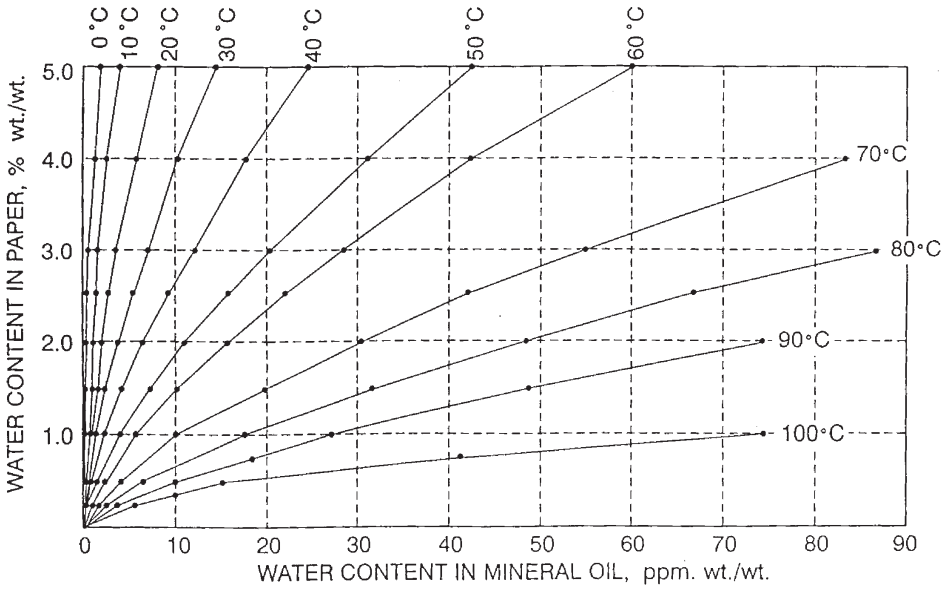

Figure 3.8: Griffin Curves for water equilibrium in cellulose/mineral oil systems [24].

3.5.2 Comparison

Direct Measurement versus Indirect Measurement

The advantage of Oommen's method is that it is much easier to determine the water equilibrium between the gas space and paper without the presence of the liquid insulation, as the moisture diffusion coefficients of oil-impregnated pressboard are about two orders of magnitude smaller than those of oil-free pressboard.

In 1974 Guidi and Fullerton in their paper [58] gave an empirical fit for diffusion coefficients of oil-impregnated Kraft paper from data studied by Ewart:

$$D(C,T) = D_0 e^{kC + E_a(1/T_0 - 1/T)}, \tag{3.6}$$

where $D_0 = 6.44 \times 10^{-14}$ m^2/s , $k = 0.5$, C is the moisture concentration in weight percent per unit weight dry cellulose, $E_a = 7700$°K, and T is the absolute Kelvin temperature. They did not specify T_0; however, from Foss' work in 1987 [62], it appears that $T_0 = 298$°K.

	D_0	E_a
Oil-free	2.62×10^{-11} m^2/s	8140°K
Oil-impregnated	1.34×10^{-13} m^2/s	8074°K

Table 3.1: Diffusion coefficient parameters estimated by Foss [62].

	Oil-Free Pressboard		**Oil-Impregnated Pressboard**	
T	20°C	70°C	20°C	70°C
$D(m^2/s)$	2.1×10^{-11}	1.2×10^{-9}	1.1×10^{-13}	6.0×10^{-12}
$\tau = d^2/(\pi^2 D)$ (hours)	1.3	0.02	261	4.7

Table 3.2: Comparison of diffusion coefficients by Foss [62] and double sided diffusion time for 1 mm thick oil-free and oil-impregnated pressboard using (3.6) and (3.7) with C=0.5%.

Foss in 1987 [62] generalized the empirical work by Ast [63] and Steele [64] at General Electric and fitted a diffusion coefficient for both oil-free and oil-impregnated paper into the same form as Guidi and Fullerton in (3.6) with $T_0 = 298$°K, $k = 0.5$, and moisture concentration C in percent by weight, and D_0 and E_a are listed in Table 3.1.

A comparison of diffusion coefficients D and the diffusion time τ for a piece of 1 mm thick pressboard with typical moisture concentration after drying of 0.5% are given in Table 3.2 using Foss' coefficients for (3.6). The diffusion time constant for moisture diffusing from both sides is calculated as

$$\tau = \frac{d^2}{\pi^2 D}, \tag{3.7}$$

where d is the thickness of pressboard. The diffusion time constant for moisture diffusing from one side is

$$\tau = \frac{4d^2}{\pi^2 D}. \tag{3.8}$$

This shows that the measurement for oil-impregnated pressboard with very small diffusion coefficient is much more susceptible to be in a non-equilibrium condition than that of oil-free pressboard with much larger diffusion coefficient, particularly at low temperatures. That is why the direct measurement of the moisture partitioning of the oil-paper system is not practical.

	Oommen [23]	**Griffin [24]**	**Shell [65]**
A	7.42	7.09	7.3
B	1670	1567	1630

Table 3.3: Comparison of estimated parameters for the Arrhenius form in (3.9) of the solubility of water in transformer oil as a function of temperature.

$T(^\circ\text{C})$	Oommen	Griffin	Shell
0	20	23	22
10	33	36	35
20	53	56	55
30	82	83	84
40	122	122	124
50	179	174	180
60	255	243	255
70	358	334	355
80	491	450	484
90	663	596	648
100	880	777	855

Table 3.4: Water saturation solubility in oil by different investigators calculated using Table 3.3 values in (3.9).

Water Solubility in Oil

The water solubility for oil can be expressed in Arrhenius form as

$$\log x_w^s = A - \frac{B}{T}, \tag{3.9}$$

where x_w^s is the saturation solubility of water in oil in PPM and T is the temperature in °Kelvin. Different coefficients A and B by different authors are shown in Table 3.3, and the calculated oil solubility at different temperatures is given in Table 3.4.

The Shell and Oommen's data agree very well over the entire temperature range. Griffin's data differs from the Shell and Oommen data at high temperatures, perhaps due to difficulty of achieving saturation at high temperature with moist bubbles.

Authors	Fabre-Pichon [22]	Oommen [23]	Griffin [24]
10 PPM 70°C	1.1 %	1.0 %	1.0 %
10 PPM 30°C	3.4 %	3.1 %	4.0 %
60 PPM 60°C	4.5 %	2.9 %	5.0 %
80 PPM 70°C	3.8 %	2.7 %	3.8 %

Table 3.5: Equilibrium moisture in paper under various oil moisture and temperature conditions as reported by different authors.

3.5.3 Curve Comparison

Due to the differences in the moisture solubility of oil, the moisture in paper versus relative humidity, and measurement accuracy, the curves generated by different investigators show differences. A comparison for different moisture and temperature levels is shown in Table 3.5. Oommen curves and MIT's curves are generated from the same source.

The curves are close to each other at low moisture concentration levels in paper. The moisture content in paper in the Oommen curves [23] is consistently lower than that of Fabre-Pichon [22] and Griffin [24]'s for the same moisture concentration in oil. The major differences occur at low temperature and at high moisture concentration levels in paper with high temperature.

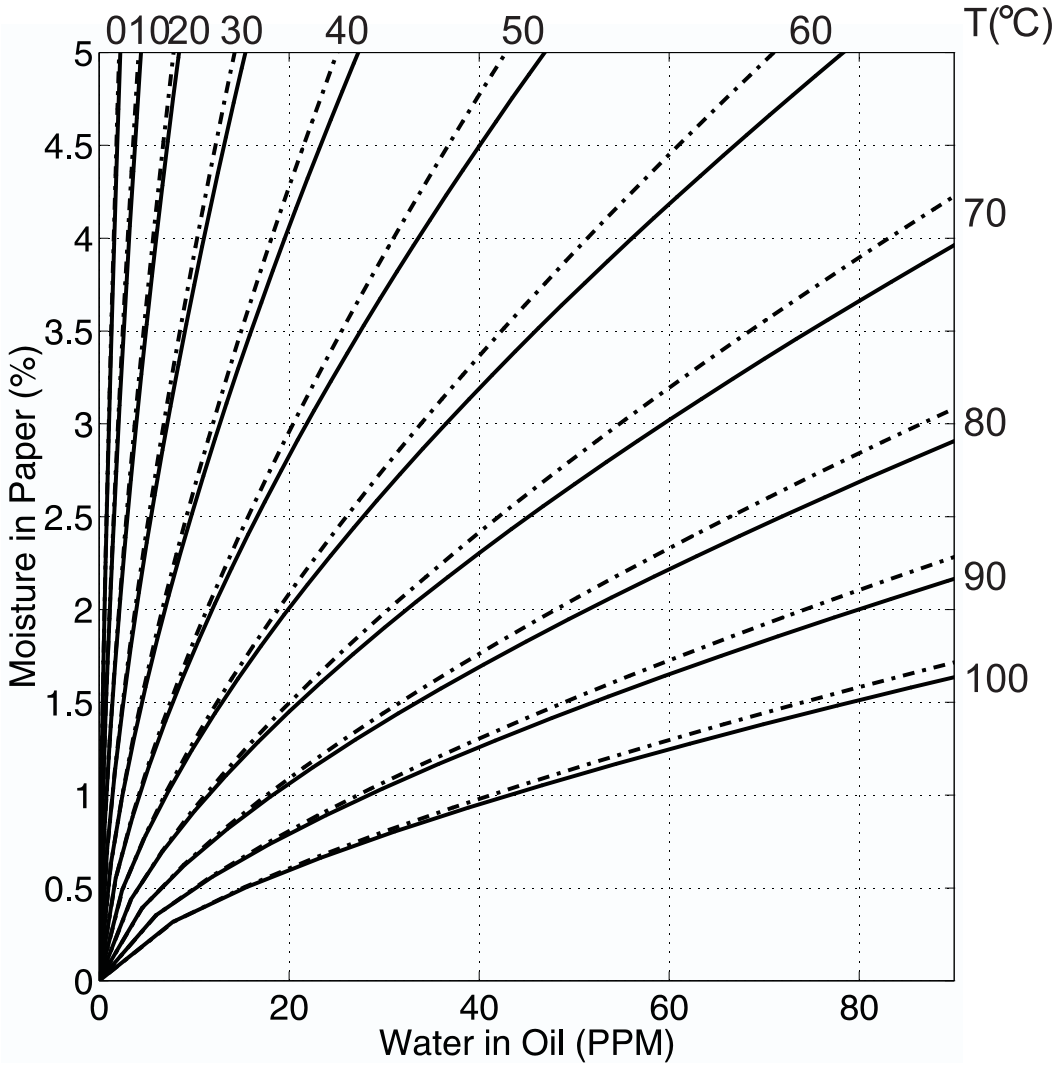

Figure 3.9: Regenerated curves following Griffin's procedure comparing erroneous Equation (3.4) (dashed line) and correct Equation (3.5) (solid line).

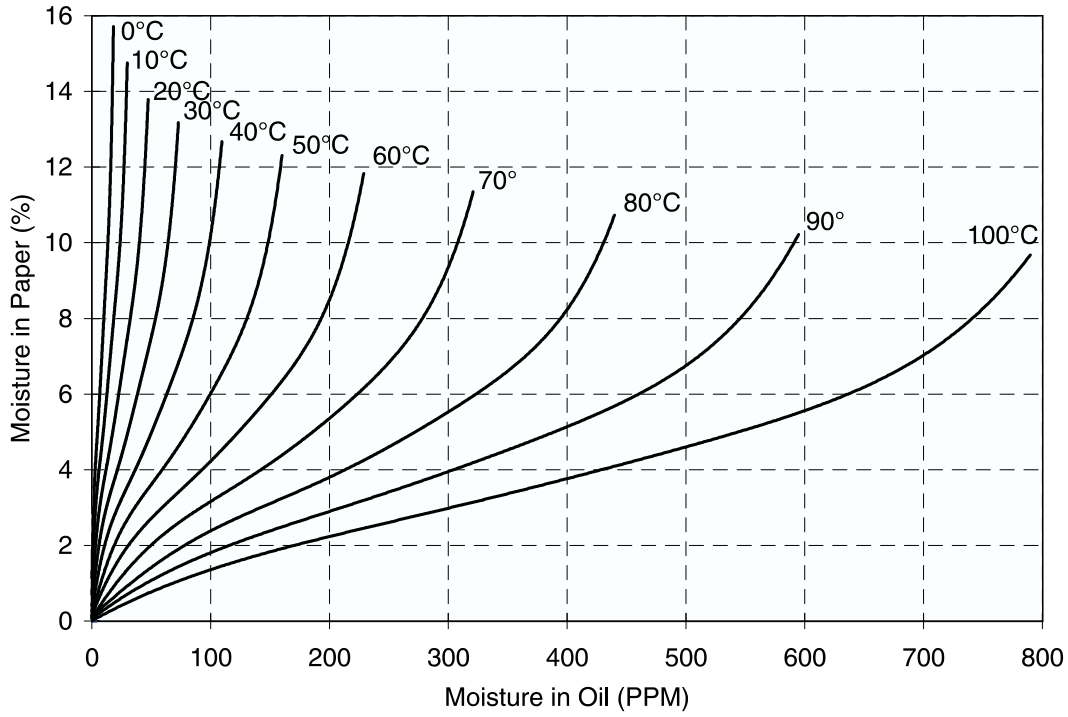

Figure 3.10: MIT developed curves for water equilibrium in cellulose/mineral oil systems for a wide range of moisture concentrations.

RH of oil at beginning(after T stabilized at 70°C)	43%
RH of oil at equilibrium:	32%
Saturated mass fraction x_s (PPM) at 70°C	$x_s = 353PPM$
PPM moisture in oil at beginning	$P_b = RH \times 353PPM = 152PPM$
PPM moisture in oil in equilibrium	$P_e = RH \times 353PPM = 113PPM$
PPM moisture diffuses to pressboard	$\triangle P_w = P_b - P_e \approx 39PPM$
Total mass of oil	$M_{oil} \approx 5300g$
Total moisture diffused into pressboard	$\triangle M_w = M_{oil} \cdot \triangle P_w \approx 0.2g$
Total mass of dry pressboard	$M_{paper} = 5.7g$
% change of moisture in pressboard	$P_{paper} = \triangle M_w / M_{paper} \times 100 \approx 3.5\%$

Table 3.6: Quantitative calculation of moisture transfer from oil to pressboard using Method 1.

3.5.4 Case Study

An examination of the moisture equilibrium curves was carried out using experimental data. The paper-oil system is initially dried under vacuum and then the dry oil is removed and moist oil is introduced to the system. A three-wavelength interdigital sensor is used to monitor the moisture diffusion process [10, 12]. The final moisture content in the pressboard and oil can be calculated using mass balance either from measurement or calculation using the oil-paper equilibrium moisture curves.

Method 1: The moisture diffusion from oil to pressboard at 70°C is monitored in the oil using a Harley moisture meter as shown in Figure 3.11. Since the system is sealed, the total moisture in the system is a fixed quantity, divided between oil and pressboard. By knowing the moisture in the oil at the beginning and at the end, the final moisture concentration in pressboard can be determined. Quantitative calculations are given in Table 3.6.

Method 2: We could not directly determine the amount of moisture in the pressboard in equilibrium for our test from any of the published curves, since none of them gives moisture concentration in oil greater than 100 PPM while the equilibrium concentration is 113 PPM. However, by inspection, we find the Fabre-Pichon and Griffin curves will not fit the data, because even at 80 PPM those curves already indicate about 4% moisture in paper; the value that corresponds to 113 PPM will be more than

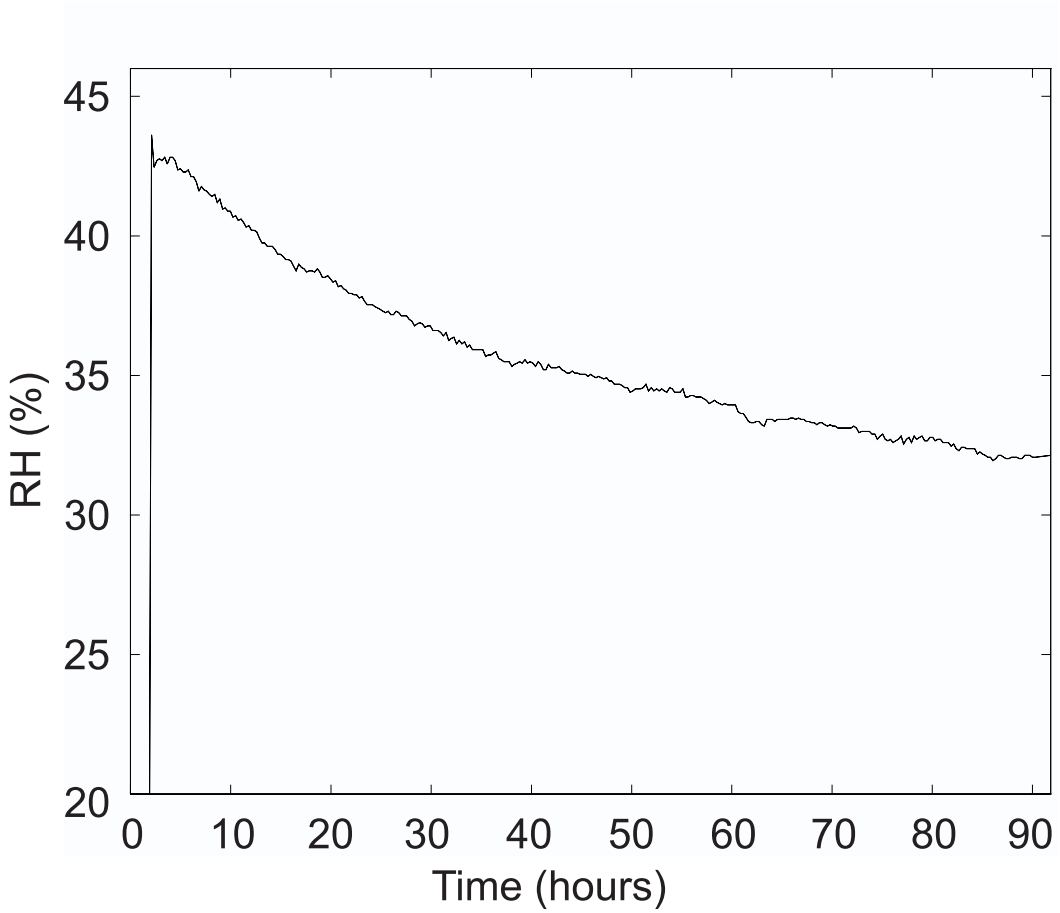

Figure 3.11: The relative humidity of the oil at 70° C decreases as the moisture diffuses from oil into pressboard.

3.5% as estimated in Method 1. Using the MIT curves of Figure 3.10, we get consistent values as illustrated in Figure 3.12.

The straight line is the mass conservation curve based on the equation:

$$P_{paper}(\%) = \frac{M^w_{total} - M^w_{oil}}{M_{paper}} \times 100, \tag{3.10}$$

where M^w_{total} (g) is the total moisture mass in the system, which is also the moisture in the oil at the beginning since we start with very dry pressboard ($P_{paper} = 0\%$); M^w_{oil} (g) is the moisture mass in oil during the experiment, which equals the water concentration in oil times the total oil mass; M_{paper} (g) is the mass of the pressboard, and P_{paper} (%) is the percentage of water in pressboard. Substituting our numbers in Table 3.6 to

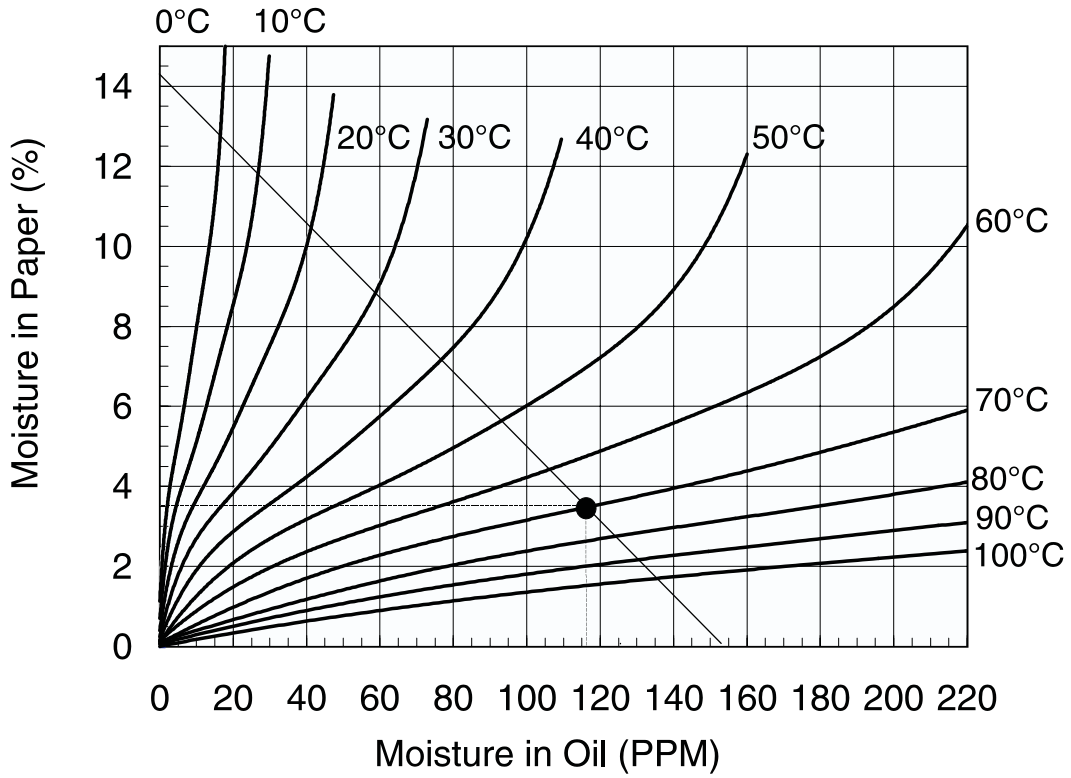

Figure 3.12: System equilibrium operating point found using the moisture equilibrium curves for oil and paper system and (3.11).

(3.10) gives:

$$P_{paper}(\%) = 14.1 - 0.093 \times M^{w}_{oil}(PPM). \tag{3.11}$$

The line is completely defined by the initial condition and the system configuration, i.e. independent of the final moisture measurement. The intersection of the mass conservation line with the moisture partition curves at 70°C indicates the equilibrium value for the system. From this curve, the final moisture in oil is about 116 PPM and the moisture in paper is about 3.5%. This is consistent with the result derived from Method 1.

3.6 Measurements of Moisture Solubility for Differently Conditioned Oils

3.6.1 Introduction

Almost all transformers in electric power delivery systems around the world are filled with liquid dielectric. The liquid functions both as electrical insulation and as a heat transfer agent. Newer liquids such as silicone and esters have their applications in special-purpose transformers, and with more environmental concerns, there are new alternatives such as edible seed-oil-based fluid [66]. However, the liquid in the majority of transformers is petroleum-based insulating mineral oil. Conventional transformer oil is made "by refining a fraction of the hydrocarbons collected during the distillation of a petroleum crude stock" [31].

It is well recognized that moisture in oil has detrimental effects on transformer performance. One important criterion is the water solubility in oil. When the moisture in oil exceeds the solubility for that temperature, free water will form and can cause electrical breakdown in a high field stressed region. The conventional way to measure water solubility is to make a saturated oil sample and then test the absolute moisture content. To achieve full saturation in transformer oil is difficult, especially at high temperature because of the high solubility. This thesis proposes an alternative method of measuring the solubility using a relative humidity sensor.

There is a general perception that oil under different aging conditions has different solubility. It is important to know the level of accuracy of this general claim, which in turn determines if extra precautions are necessary. Verification was carried out for four differently conditioned oils.

3.6.2 Water Solubility and Relative Humidity Meter

One way of determining water solubility is by the use of the new ASTM Standard Test Method D 4056-92 [67]. This method estimates the solubility of water in hydrocar-

bons at different temperatures based on calculations from values for density, refractive index, and molecular weight. This is not a very practical way to measure the water solubility. A more conventional way is to make a saturated oil sample and then measure the absolute moisture content using the standard test method for measuring water in transformer oil, the ASTM D 1533 test method known as the Karl Fischer reaction method [41]. To achieve full saturation in transformer oil is not a trivial task, especially at high temperature because of the increasing solubility.

Two ways have been generally adopted for making saturated solutions: 1. Bubble moist air through the oil. We found it difficult to achieve saturation at high temperature using this method without a well designed system like that shown in the Appendix of [24]. 2. Directly add free water. One improper practice is simply adding an excess amount of water to a sample, shake it up, let stand overnight and then measure water concentration. It is not an acceptable way of measuring the solubility because the diffusion process in the oil is very slow, and letting the solution stand overnight does not guarantee full dissolution. Also, excess free water in the oil will cause an erroneous measurement of water solubility, i.e. the free water might be sampled and measured as water dissolved in oil. Even though water is heavier than the oil, small water bubbles can still exist near the upper body of the oil by surface tension. The measurement results of such samples are non-repeatable and inconsistent. The proper implementation of this method is to add water and mix well until free water is observed. The mixture should be centrifuged to remove any entrained water and then decanted. The correct implementation of both methods requires extra equipment and care.

To avoid the error caused by taking the moisture value of a non-saturated solution as solubility, or solution with excessive free water, an alternative easily implemented method is proposed for measuring moisture solubility in transformer oil. The linearity between the relative humidity of the oil and the moisture content of the oil is utilized to find the solubility:

$$W_c = W_s \times R.H.(\%)/100, \tag{3.12}$$

where W_c is the water concentration in ppm at temperature T, and W_s is the water

solubility in ppm at the same temperature T. By measuring the slope of the curve of *Moisture Concentration* versus *Relative Humidity*, or the intercept of the curve at R.H.=100%, one can find the water solubility instead of trying to directly measure the moisture content at 100% relative humidity.

The Mitsubishi Moisture Meter Model CA-05, based on microprocessor controlled Coulometric Karl Fischer titrimetry, is used to measure the absolute moisture content in oil. The commercially available Harley Moisture Sensor is used to measure the relative humidity of transformer oil. Figure 3.13 shows the Harley CT-880-S moisture sensor used in this investigation. It consists of a dual sensor [68]- a full range (0-100% RH) thin-film capacitive humidity sensor and a thin-film platinum RTD temperature sensor, combined with a linearized 4 to 20 mA, two-wire current transmitter. The unit transmits a 4-20 mA current signal for a moisture range of 0-100% saturation. The temperature corrected current output is converted into equivalent DC voltage output across an externally connected load resistor. The newly shipped sensor was calibrated in fresh Shell Diala AX oil as shown in Figure 3.14. The titration results are obtained by dividing the moisture content by the solubility of the Shell Diala AX oil at that temperature. The reported solubility value of Shell Diala AX oil [65] is used for calibration. The ideal relative humidity is obtained by converting the output voltage by ideal transfer function $R.H.(\%) = [(V - I_{min} * R)/4] * 100\%$, where I_{min} is $4 \times 10^{-3} A$ and R is 250 Ω. After two years of use in hot transformer oil in our laboratory apparatus, the sensor was recalibrated as shown in Figure 3.15. By calibration, the relative humidity of the oil is related to the measured sensor output voltage by

$$R.H.(\%) = 22.005 \times (V - V_{\min}) - 1.308, \tag{3.13}$$

where V_{min} is 1.06V for the calibrated sensor. The calibration indicates a very good linear relationship between sensor output and the relative humidity.

Figure 3.13: Harley CT-800 moisture sensor. The sensing element is at the bottom of the long rod.

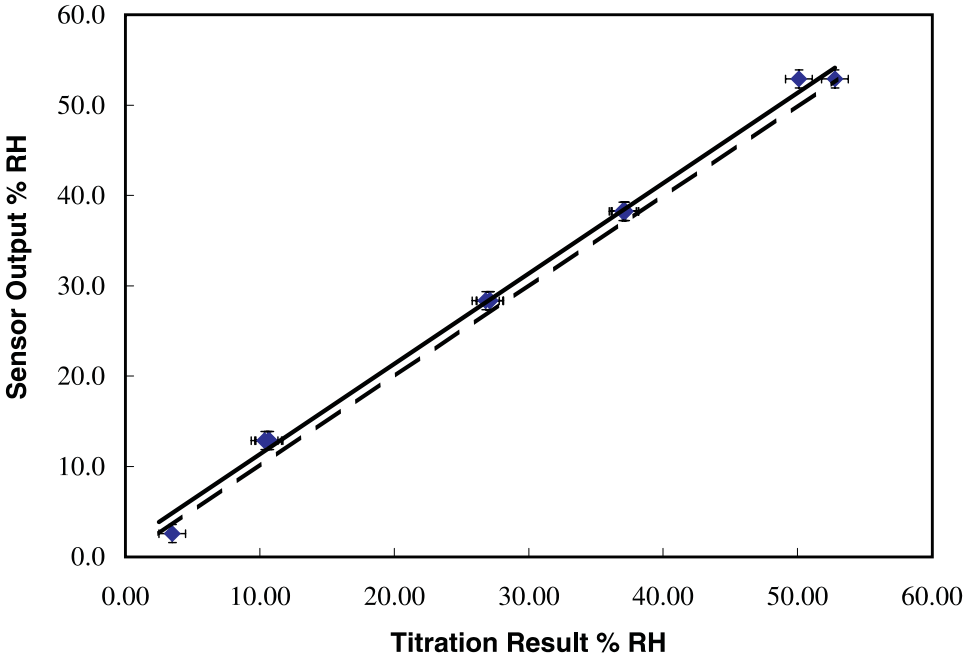

Figure 3.14: Harley Moisture Sensor calibrated in Shell Diala AX oil at 35°C when first arrived in 1995 (calibrated by D. E. Schlicker at MIT High Voltage Research Lab.) The dashed line is the ideal output and the solid line is the linear regression of measured output.

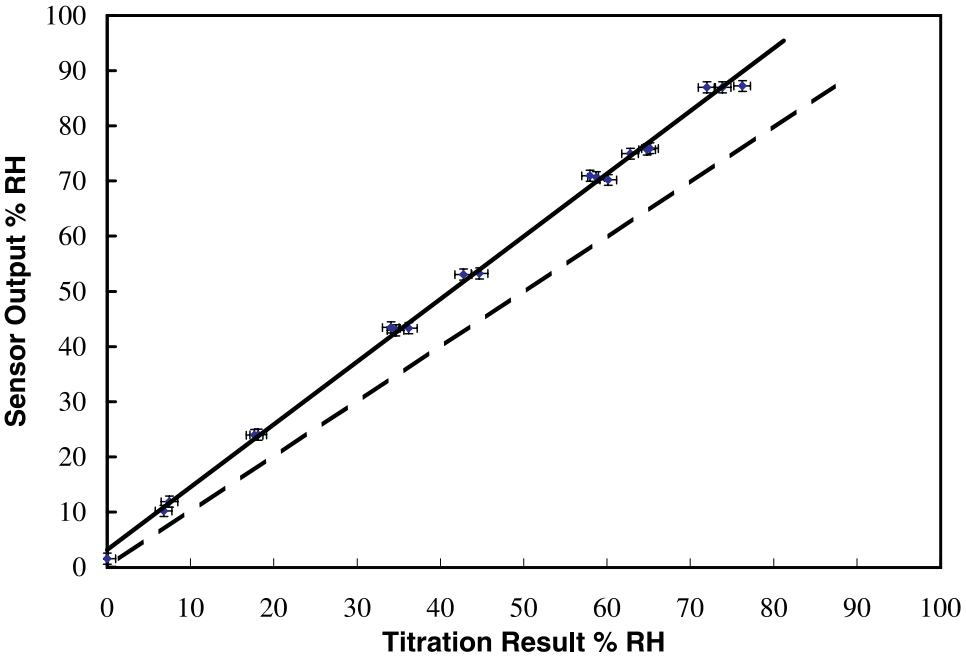

Figure 3.15: Harley Moisture Sensor calibrated in Shell Diala AX oil at 35°C in 1997 after two years in service. The dashed line is the ideal output and the solid line is the linear regression of measured output.

3.6.3 Differently Conditioned Oils

The measurements are taken for four types of differently conditioned oils at 35°C: Fresh Shell Diala AX oil, Lab-Aged Shell Diala A oil, Texas Utility used transformer oil, and Ramapo Substation used transformer oil. The Shell Diala A oil is Type I oil which is intended for use where normal oxidation resistance is required. Shell Diala AX oil is Type II oil, for more severe service applications requiring greater oxidation resistance. It contains approximately 0.2%w (2000 ppm) of oxidation inhibitor. Some typical properties of Shell Diala oils are shown in Table 3.7 [65]. The lab-aged oil is prepared by heating new oil at 70°C for two weeks with a mixture of moisture and oxygen as heat, moisture and oxygen are the major aging factors. The oil is circulated within an open vessel by a pump for thorough mixing. The Texas Utility oil was taken from a transformer that was in service at Texas Utilities. The Ramapo oil was taken from a single phase of a 500/345kV, 333 MVA (per phase) transformer at the Ramapo Substation that experienced failure due to static electrification. Because of the small quantity of the oil availability, the tested Ramapo oil is a mixture of 80% Ramapo original oil and 20% of new Shell Diala A oil.

Three of the tested oils were analyzed by Doble Engineering Company. Representative results are listed in Table 3.8 [69]. The interfacial tension (IFT) and the neutralization number (mg KOH/g) of the oil provide an indication of the degree of aging and contamination. In general, the more aged the oil, the lower the IFT and the larger the neutralization number.

Additional Doble tests were performed later for the tested Ramapo and TU oils and later shipped non-mixed Ramapo oil. The results are summarized in Table 3.9. Although the color of Ramapo is darker than TU, they do not differ much in the color scale defined by ASTM standard D1500 [70].

The infrared scans are also performed for the oils. The infrared analysis is used by organic chemists for qualitatively determining the presence or absence of specific functional groups in a mixture [72]. One infrared scan was done with a 1-mm cell

Properties	ASTM Method	Diala A/AX Oils Typical Values
Specific Gravity, 15/15°C	D1298	0.885
Visual Examination	D1524	Clear&Bright
Dielectric Breakdown Voltage		
@60 Hz, Disc electrodes, 2.5 mm gap, kV	D877	> 35
@60 Hz, VDE electrodes, kV	D1816	
1.02 mm gap		> 28
2.03 mm gap		> 56
Power Factor, 60 Hz:	D924	
@25°C, %		0.002
@100°C, %		0.01
Resistivity, Ω-cm	D1169	
@25°C		2000×10^{12}
@100°C		50×10^{12}
Relative Permittivity @25°C	D924	2.2-2.3
Water Solubility, ppm		
0°C (32°F)		20
15°C (60°F)		45
38°C (100°F)		115
66°C (150°F)		295
82°C (180°F)		500

Table 3.7: Typical properties of Shell Diala Oils [65].

path and with new oil in the path of the reference beam. This type of test for the tested Ramapo oil and TU oil is shown in Figure 3.16 and Figure 3.17. This allows for detection of oxidation inhibitor at 3660 cm^{-1} and for carbonyl compounds at 1700-1730 cm^{-1}. Little to none of oxidation inhibitor was detected for all oils. Carbonyl

	Fresh Shell Diala A	Texas Utility	Ramapo
Total PCB Content	< 2	< 2	< 2
Carbon Monoxide (CO)	0	22	66
Carbon Dioxide (CO_2)	252	748	484
Ethylene (C_2H_4)	0	11	6
Water (PPM)	20	40	21
Neutralization No. mg KOH/g	< 0.01	0.01	< 0.01
IFT, dynes/cm, 25°C	42	32	37

Table 3.8: Testing results of the measured oils by Doble Engineering [69] before use in thesis experiments.

Screen Test	ASTM Method	Non-mixed Ramapo	Tested Ramapo	Tested TU	Fresh Shell [65]
Color	D 1500	$L1.5$	$L1.5$	$L1.5$	$< L0.5$
IFT, dynes/cm, 25°C	D 971	38	36	32	47
Neutralization No. mg KOH/g	D 974	< 0.01	< 0.01	< 0.01	< 0.01
Power Factor, % at 25°C	D 924	0.201(erratic)	0.025	0.024	0.02

Table 3.9: Additional testing results of the measured oils after thesis experiments and later received non-mixed Ramapo oil by Doble Engineering [71].

compounds are mostly from oxidation of insulating materials. Both non-mixed Ramapo oil and tested mixed Ramapo oil have a little more absorbance in this region suggesting that they contain a higher amount of (non-acid) carbonyl compounds than the other two oils.

Another infrared scan was performed using a 0.2-mm cell path and air as the reference, which provides a fingerprint of the oil. Shown in Figure 3.18 and Figure 3.19 are the test results for the tested Ramapo oil and TU oil. The signature band is mostly around 700-1200 cm^{-1}. It shows that the Ramapo and Texas Utility oils are different products.

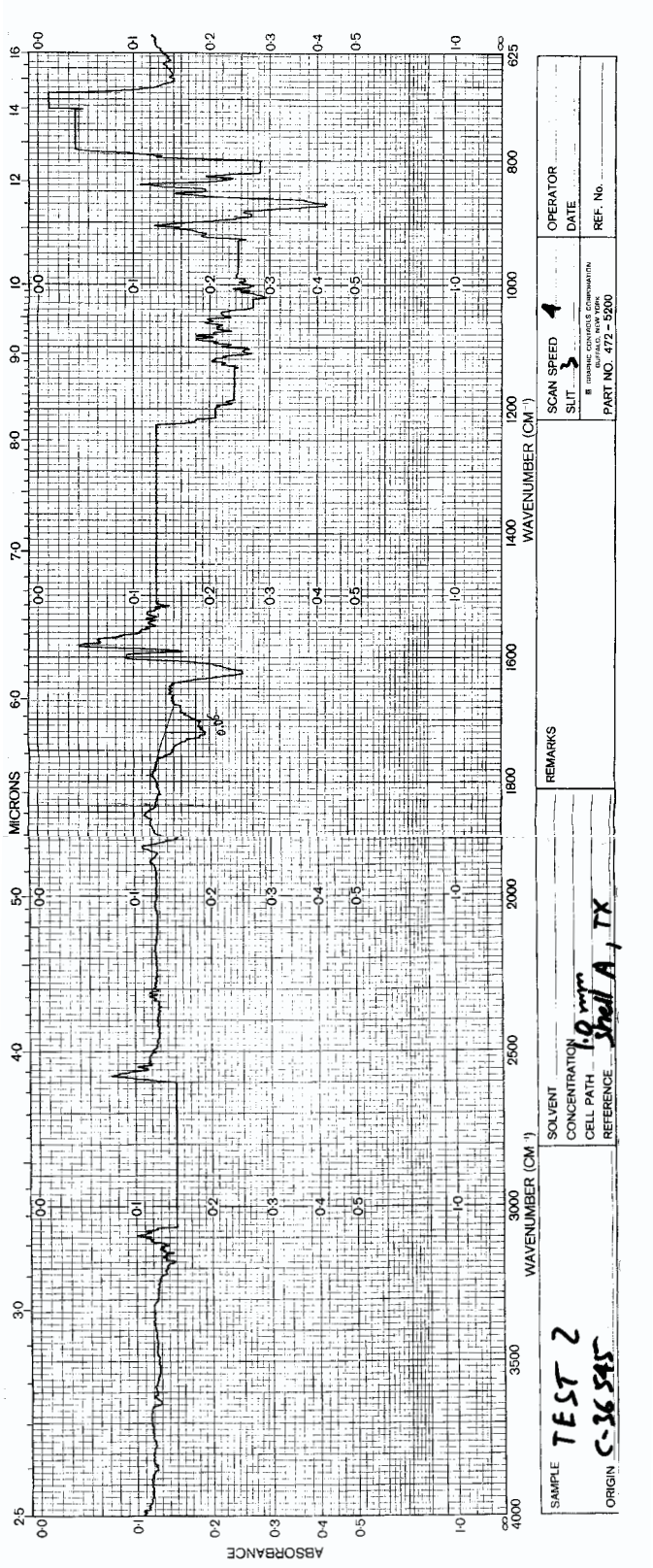

Figure 3.16: Infrared scan for the tested Ramapo oil with 1-mm cell path and new oil as reference beam. Little to none of oxidation inhibitor was detected at 3660 cm^{-1}. Carbonyl compounds detection region at 1700-1730 cm^{-1} shows more absorbance than that of TU oil in Figure 3.17.

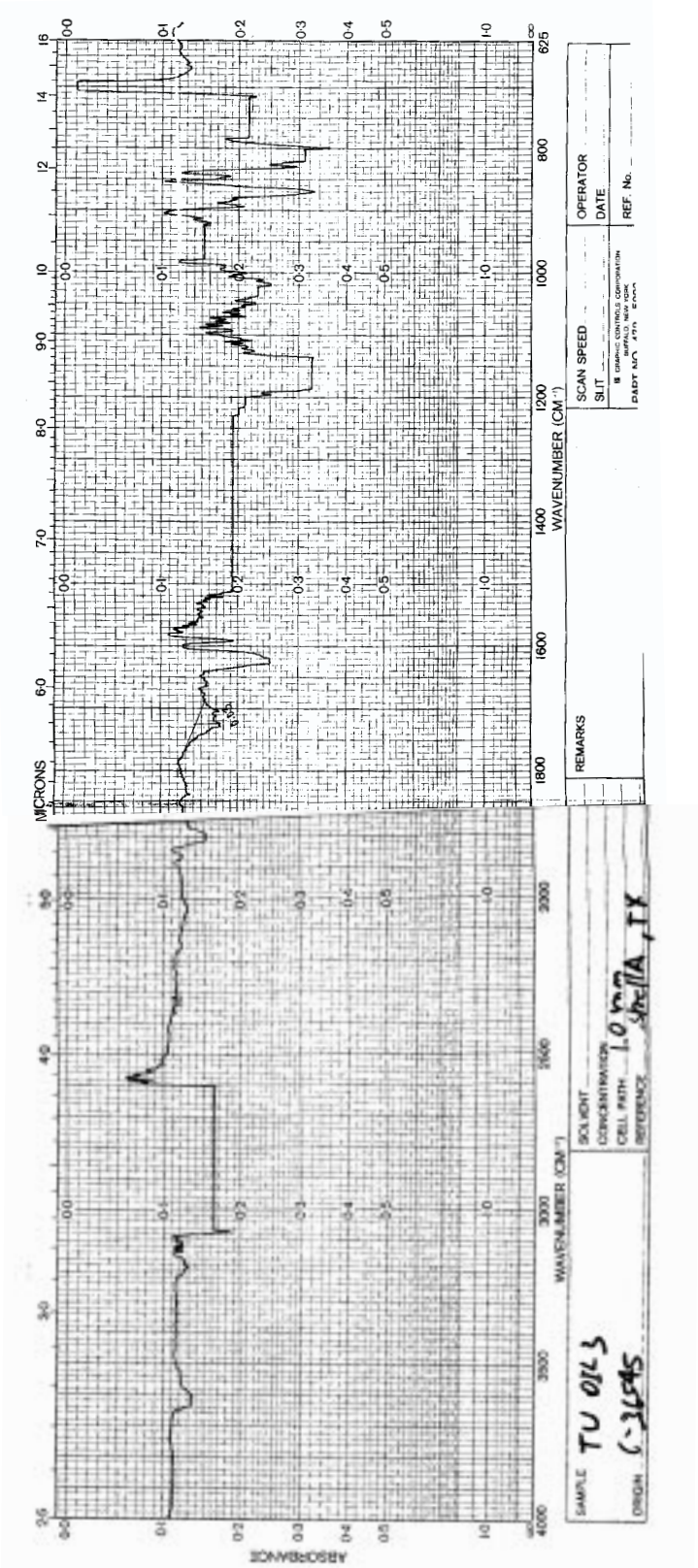

Figure 3.17: Infrared scan for the tested TU oil with 1-mm cell path and new oil as reference beam. Little to none of oxidation inhibitor was detected at 3660 cm^{-1}. Carbonyl compounds detection region at 1700-1730 cm^{-1} shows less absorbance than that of Ramapo oil in Figure 3.16.

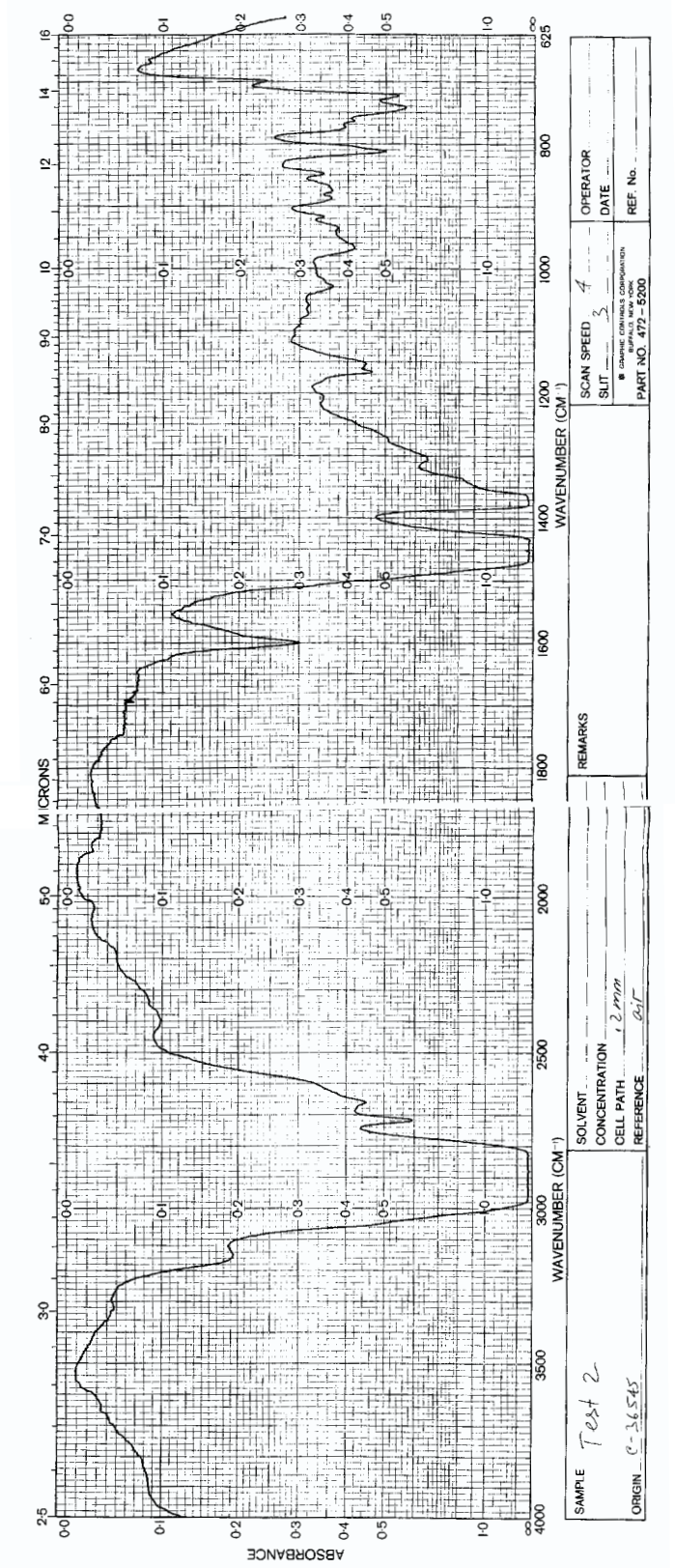

Figure 3.18: Infrared scan for the tested Ramapo oil with 0.2 mm-cell path and air as reference beam. The absorbance difference in signature band around 700-1200 cm^{-1} shows that the Ramapo and Texas Utility oils are different products.

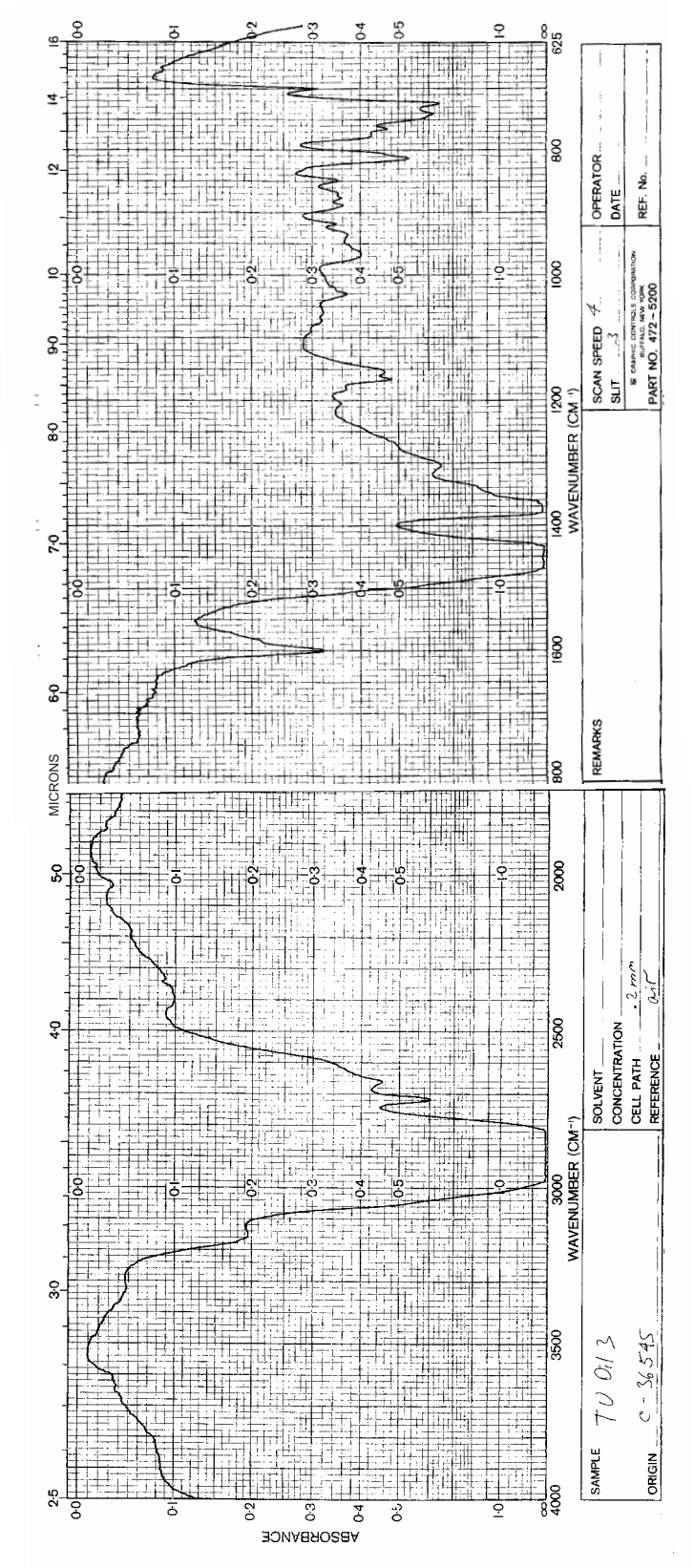

Figure 3.19: Infrared scan for the tested TU oil with 0.2 mm-cell path and air as reference beam. The absorbance difference in signature band around 700-1200 cm^{-1} shows that the Ramapo and Texas Utility oils are different products.

Oil Type	Fresh Shell [65]	Lab-Aged Shell	Texas Utility	Ramapo
Solubility (ppm), 35°C	102	104	108	142
Conductivity (pS/m)	0.7 (35°C)	7.2 (70°C)	9.5(35°C)	10.1(35°C)

Table 3.10: Comparison of measured water solubility at 35°C and conductivity in differently conditioned oils.

3.6.4 Measurement Results

The oil is contained in a 1000 mL kettle. It is well mixed by a magnetic stirrer and the temperature is controlled by an Omega temperature probe and controller. The moisture is bubbled into the kettle by flowing a constant air flow through a flask of deionized water.

The measured oil solubilities and conductivities are listed in Table 3.10 and the curves are shown in Figure 3.20. The conductivities of the oils are measured by a gapped tuning capacitor immersed in the oils.

3.6.5 Discussion

The results obtained with fresh oil, lab-aged oil, and the Texas Utility oil are very close, whereas the result for Ramapo oil is very different from the rest. Lab tests show the Ramapo oil is not very aged, however, an erratic power factor is measured. There might be contaminants or moist particles in the Ramapo oil that cause the observed moisture sensor response. Indeed Golovan' et al [73] also observed that the increase of polar impurities in the oil "leads to a significant increase in oil hygroscopicity and a breakdown of the linear relationship between the water uptake capacity and the relative humidity of the air". This observation also serves as a caution for using the moisture sensor in contaminated oil. Because of the nonlinear behavior of the sensor output, the predicted value of solubility of Ramapo oil is only a rough estimation. The proposed method is effective only when the sensor response is linear. Another possibility is that the contaminants in the oil could affect the chemical reaction process of the Karl Fischer titration and cause a false reading.

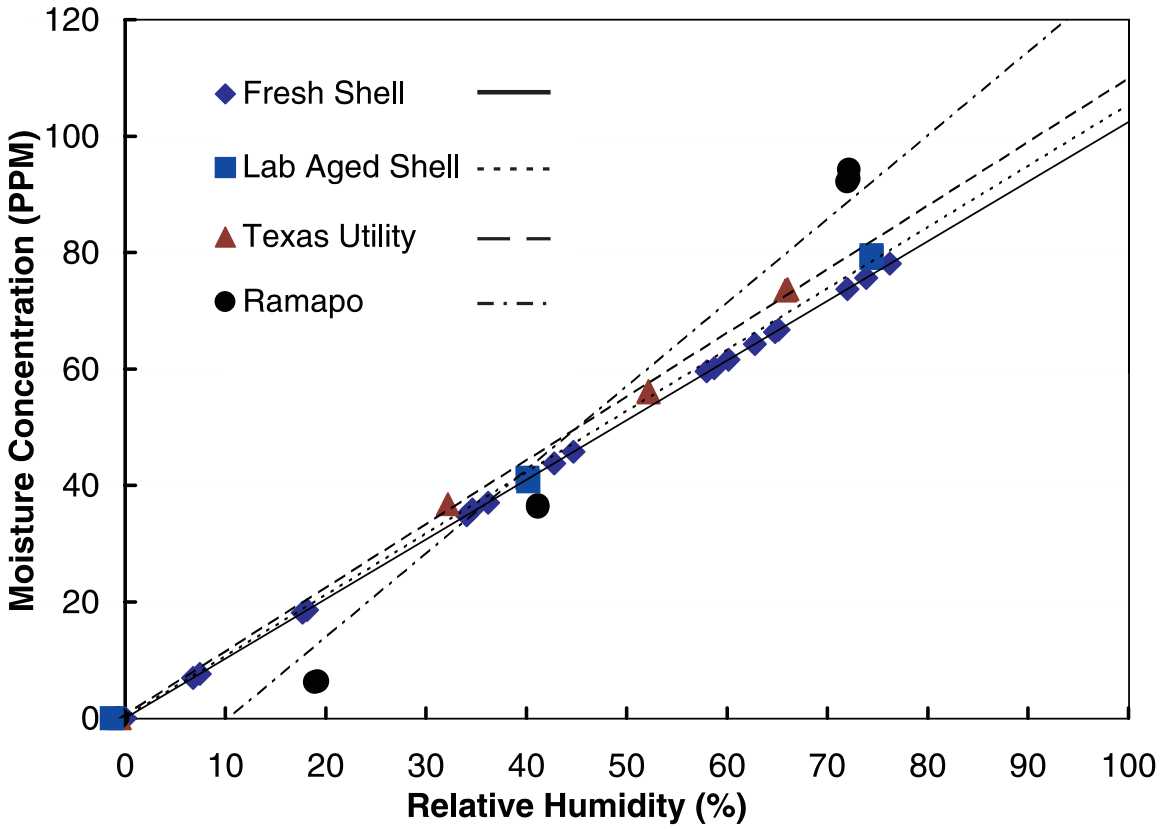

Figure 3.20: Measurements of moisture concentration versus the relative humidity for differently conditioned oils at 35°C.

Griffin *et al.* at Doble Engineering Company [24] extensively studied moisture solubility in mineral oils. From their measurements of ten in service aged oils and two oils with accelerated oxidation in the laboratory, they concluded that: "oils which are in serviceable condition show little change in their water solubility characteristics. Only when the oil is severely aged or contaminated would the solubility be expected to increase significantly." Our results agree with Doble's conclusion.

3.7 Summary

Several sets of classic moisture equilibrium curves are studied and a comparison is given for each method. Caution should be taken when using such curves because they differ by measurement techniques, data sources, and generating methods. An experimental

case study shows that Oommen's curves match the experimental data best. A new set of moisture equilibrium curves was constructed using Oommen's method for moisture in oil up to the saturation moisture content.

When the system is not in equilibrium, these equilibrium curves cannot be used to find the moisture in paper. The three-wavelength interdigital dielectrometry sensor described in the following chapters is able to measure the spatial profile of the moisture distribution in the pressboard. This provides an alternative method when the transient system is not in equilibrium.

Water solubility is one of the important parameters of transformer insulation. A measurement technique exploiting the linearity between the relative humidity of the oil and the moisture content of the oil to indirectly measure the solubility is proposed. It avoids the difficulty of achieving full saturation of the test sample and associated errors. However, it can give the correct solubility only when the sensor response maintains linearity. Results of differently aged oils show that normal operation under service temperature is less likely to significantly change the water solubility. This agrees with Griffin's results [24].

Chapter 4

Universal Curves

4.1 Introduction

The complex dielectric permittivity of pressboard, $\varepsilon^* = \varepsilon' - j\varepsilon''$, is a function of its temperature, moisture content, and frequency. The real part of the permittivity gives the dielectric constant, while the imaginary part characterizes the power dissipation in the material. The moisture effects have been qualitatively discussed in Chapter 1. Similarly the temperature has strong effects on the dielectric properties. In general, both permittivity and conductivity increase with temperature. The resistivity of the solid insulation can change up to three orders of magnitude between 0°C and 80°C [74].

In transformer pressboard of medium and low humidity, it has been shown that the dielectric spectrum does not vary in shape with temperature and moisture content, but there is a logarithmic shift in amplitude and frequency. Research conducted by Y. Sheiretov at MIT [3, 75], Jonscher et al at Chelsea Dielectrics Group in the UK [76], and Nettelblad et al at ABB [77] suggest the existence of such a universal curve. Thus it is possible to create a universal curve, with appropriate temperature correction factors, containing information about the moisture contents from transformer pressboard dielectrometry measurements.

Extensive measurements of dielectric properties of transformer pressboard as a function of moisture and temperature were conducted in the interest of quantifying effects

that will allow the prediction of moisture content of insulation by measuring its dielectric spectrum, thus allowing an on-line non-destructive method. From oil-free pressboard measurements, it can be observed that a universal curve does exist. Preliminary tests for oil-impregnated pressboard show the same trend.

Such measurements were taken by MIT undergraduate students Madhu Sarda and Noemi Altamirano [78] under the author's supervision as part of their MIT Undergraduate Research Opportunity Program and Advanced Undergraduate Projects.

Similar tests have been done by Nettelblad [77] for oil-free cellulose, but no quantitative relationship is given. Nettelblad's results are shown in Figure 4.1 which exhibit a very similar shape to our measured results discussed in Section 4.2.

4.2 Measurements for Oil-Free Pressboard

Before the insulation is shipped to the transformer manufacturer, the oil-free pressboard needs to be dried and impregnated. The drying process may take a considerable amount of time for large objects, and accurately monitoring that process can assure the thoroughness of the drying as well as save time and money. Therefore measurements with oil-free pressboard has its important practical application.

4.2.1 Measurement Technique

The pressboard is placed in a lossy parallel-plate capacitor structure whose complex impedance is measured. The values of the complex permittivity of the material, averaged across the thickness, were obtained from the complex admittance Y according to (4.1).

$$\varepsilon^* = Y \cdot d/j\omega A = (G + j\omega C) \cdot d/j\omega A = \varepsilon' - j\varepsilon'', \tag{4.1}$$

where d is the electrode gap, A is the electrode area, G is the AC conductance between electrodes, and C is the capacitance between electrodes. Once a quantitative mapping is established for dielectric properties as a function of moisture and temperature, the

Moisture Level(%)	0, 0.6, 1.1, 1.9, 2.0, 2.3, 2.6, 3.2, 5.7
Temperature (°C)	30 (35), 40, 50, 60, 70

Table 4.1: Moisture and temperature levels for measurements performed for oil-free pressboard.

interdigital dielectrometry sensors can be used to continuously monitor the moisture distribution in the transformer insulation.

Hi-Val transformer pressboard manufactured by EHV-Weidmann Inc. is used for all experiments. The 1.7 mm thick pressboard was placed between the parallel-plate sensor, shown in Figure 4.2. The sensing plate was made out of a piece of printed-circuit board to ensure the sensing electrode and the guard ring in the same plane. The test cell was then placed in the test vessel shown in Figure 4.3 whose temperature and moisture levels can be monitored and controlled. When the ambient temperature was high, the test chamber temperature could not be brought down to 30°C and was kept at 35°C instead.

Temperature and relative humidity were monitored in the vessel by an Omega temperature controller and a Harley relative humidity sensor. The relative humidity inside the vessel was varied in order to achieve different moisture contents of the pressboard. The moisture content in the pressboard is estimated using Jeffries' curves [50] in Figure 3.4 by measuring the relative humidity in the test vessel. Oil-free measurements were taken at the moisture and temperature levels shown in Table 4.1.

4.2.2 Measurement Results

Dielectrometry data was collected for the five temperatures at the nine moisture levels in Table 4.1 for forty five data sets in all. Data of different moisture levels at the same temperature were also compared. Both ε' and ε'' increase as moisture and temperature are increased. All results are plotted in 3-D in Figure 4.4 and Figure 4.5. It is observed that a general shape is common to all temperatures and moisture levels.

Figure 4.6 shows the dielectric spectrum for different temperatures at 2.0% moisture

content. Both ε' and ε'' increase as temperature increases, however, the shape remains the same.

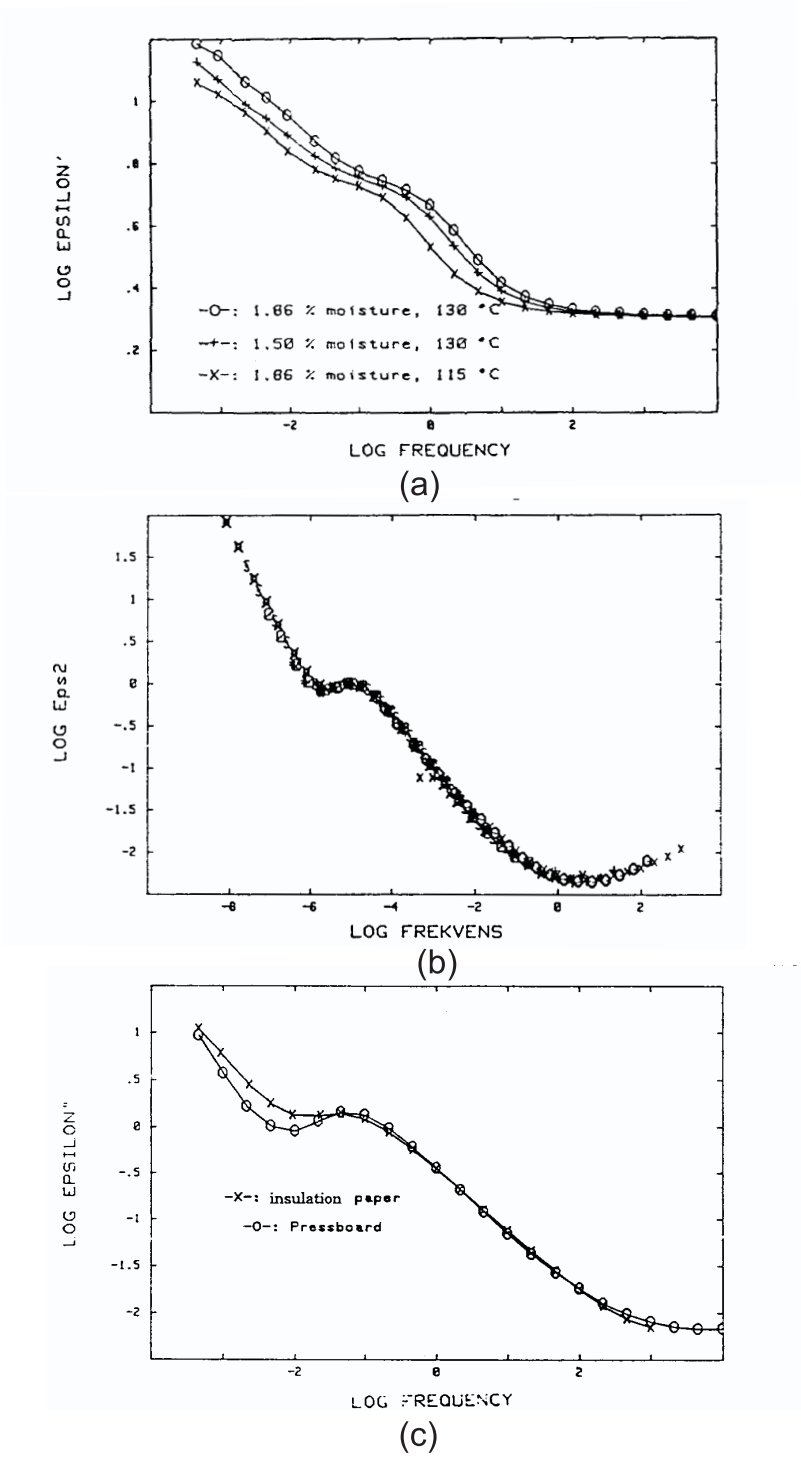

Figure 4.1: Nettelblad's results for (a) ε' for humid paper at high temperatures as a function of frequency. (b) Master curve of ε'' for humid paper (c) ε'' of dry pressboard and insulation paper at 130° C [77].

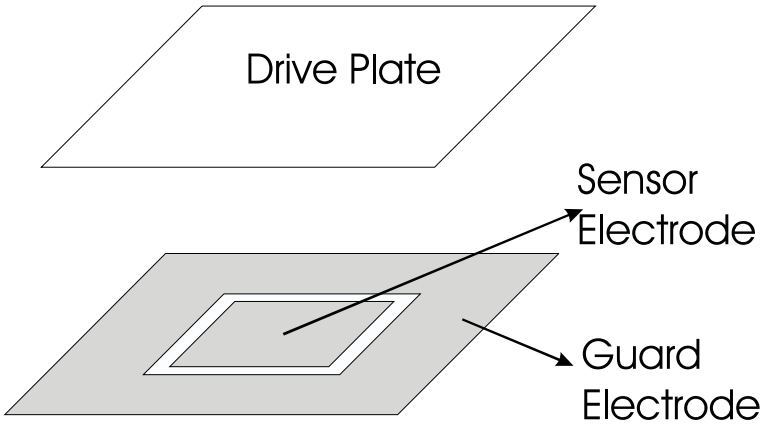

Figure 4.2: Parallel-plate sensor used for dielectrometry measurements of pressboard as a function of moisture and temperature.

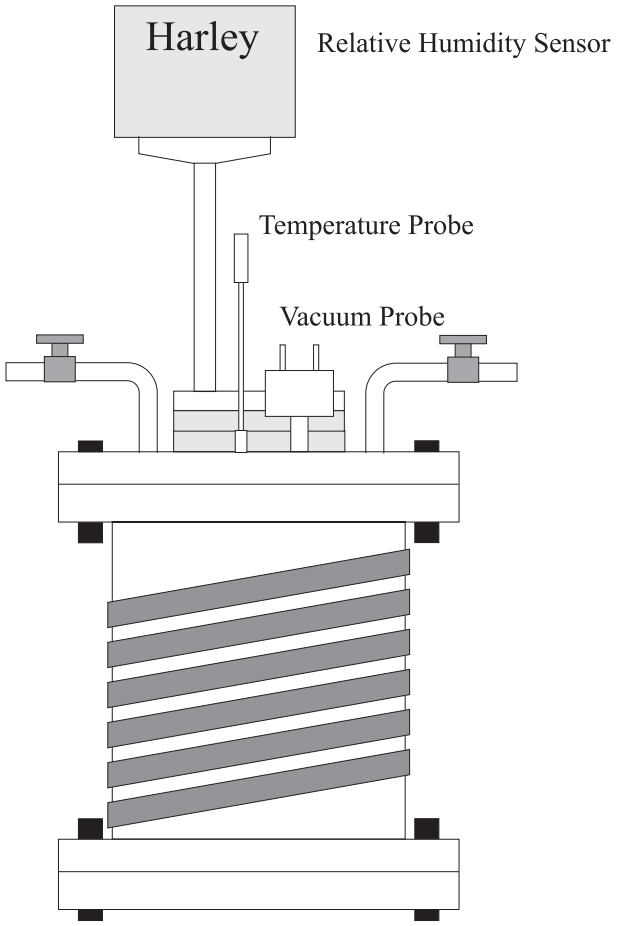

Figure 4.3: Test vessel used for oil-free pressboard measurements.

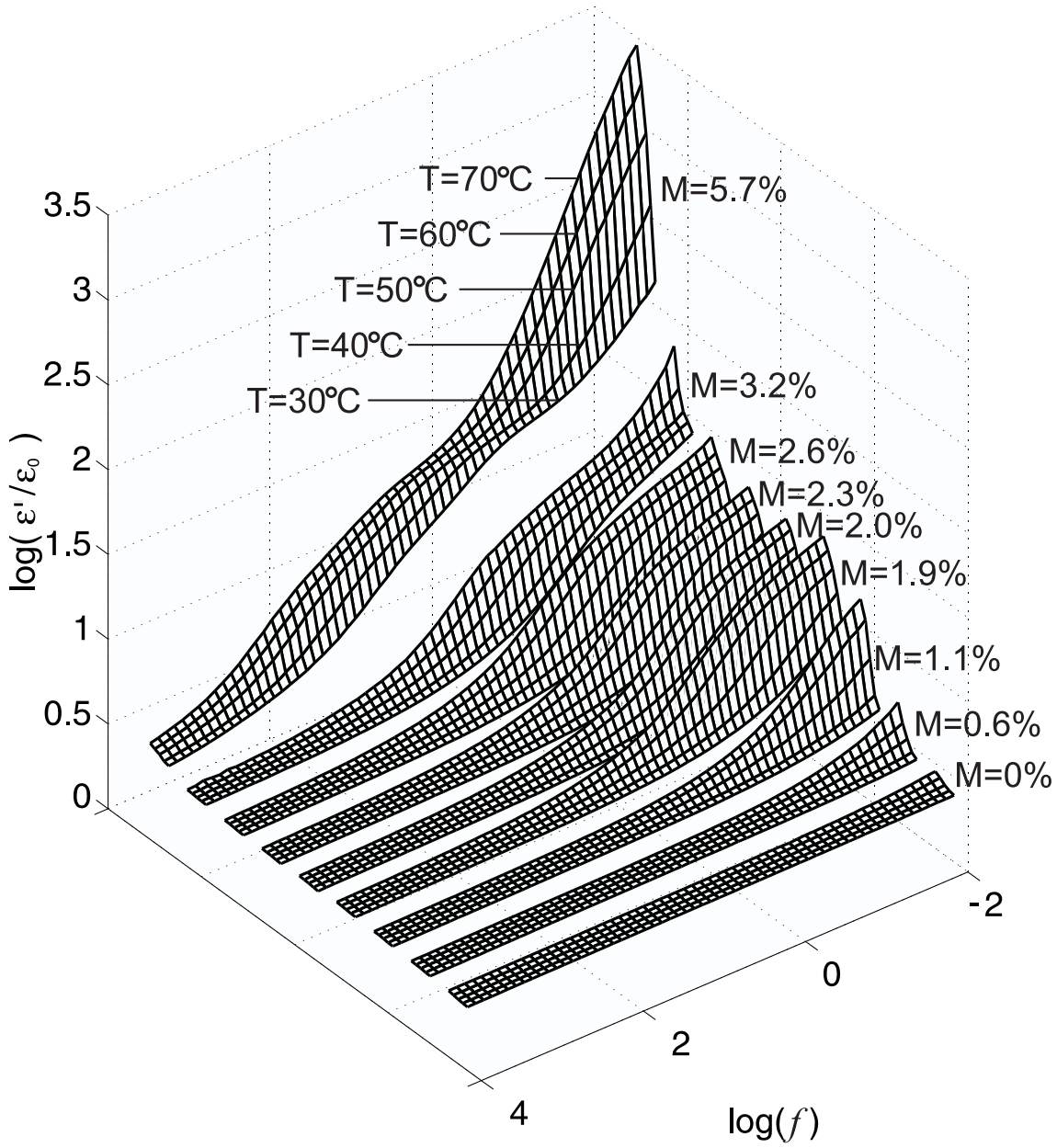

Figure 4.4: A full spectrum of ε' obtained for nine moisture levels and five temperatures.

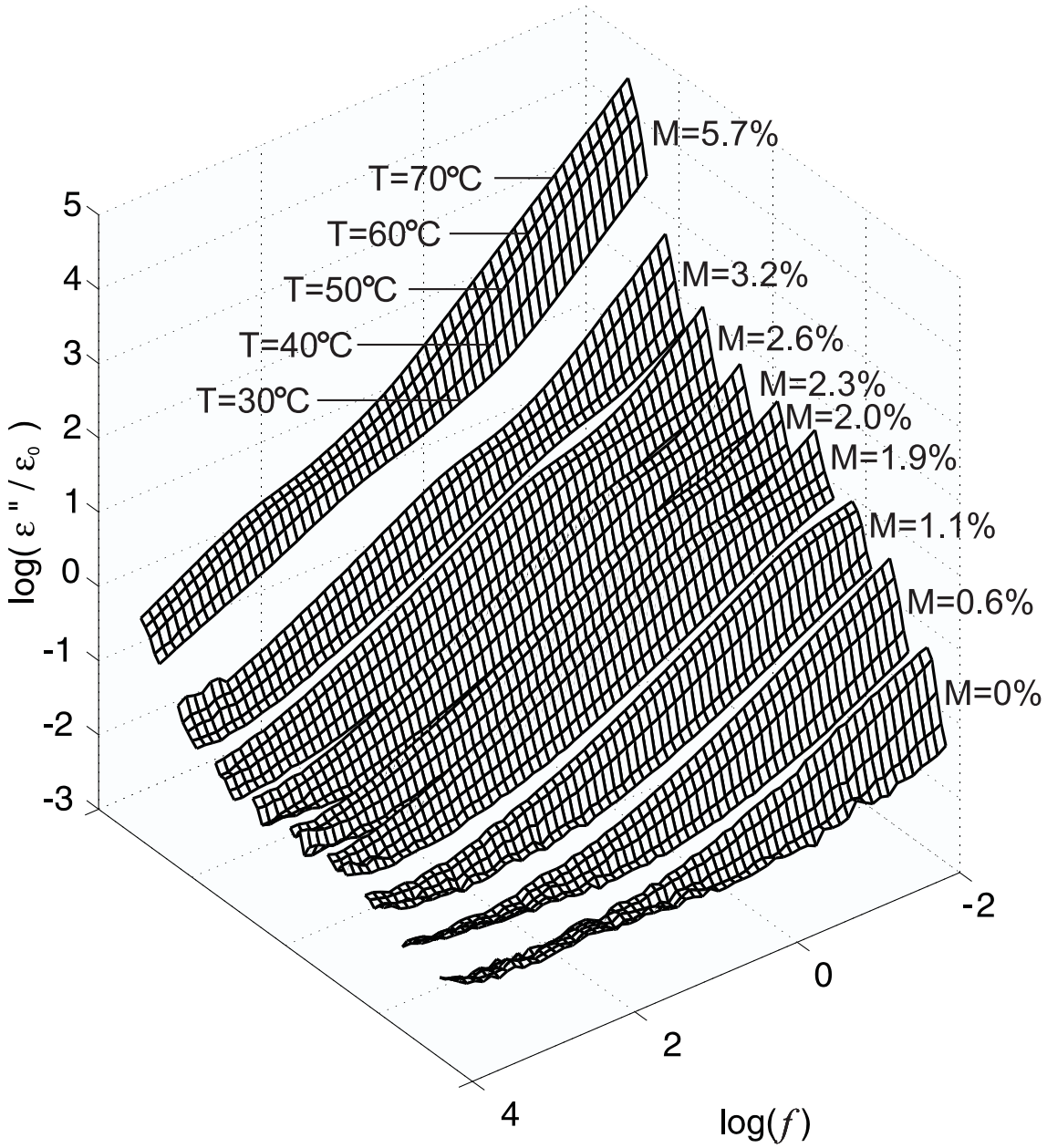

Figure 4.5: A full spectrum of ε'' obtained for nine moisture levels and five temperatures.

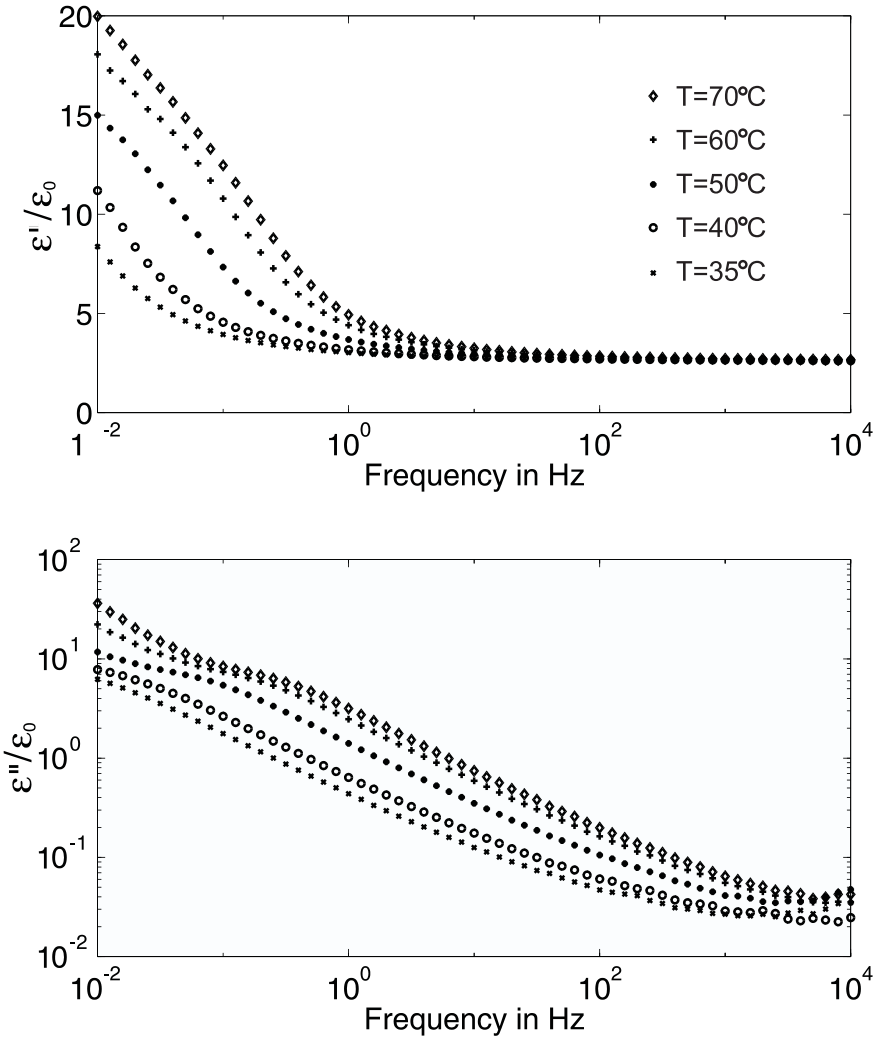

Figure 4.6: Dielectric spectrum of oil-free pressboard at 2.0% moisture content for five temperatures.

Discrete logarithmic frequency shifting with an increment of 0.1 in $\log_{10}(f)$ of all forty-five measured oil-free pressboard data sets to minimize least square differences confirm the existence of a universal curve in Figure 4.7.

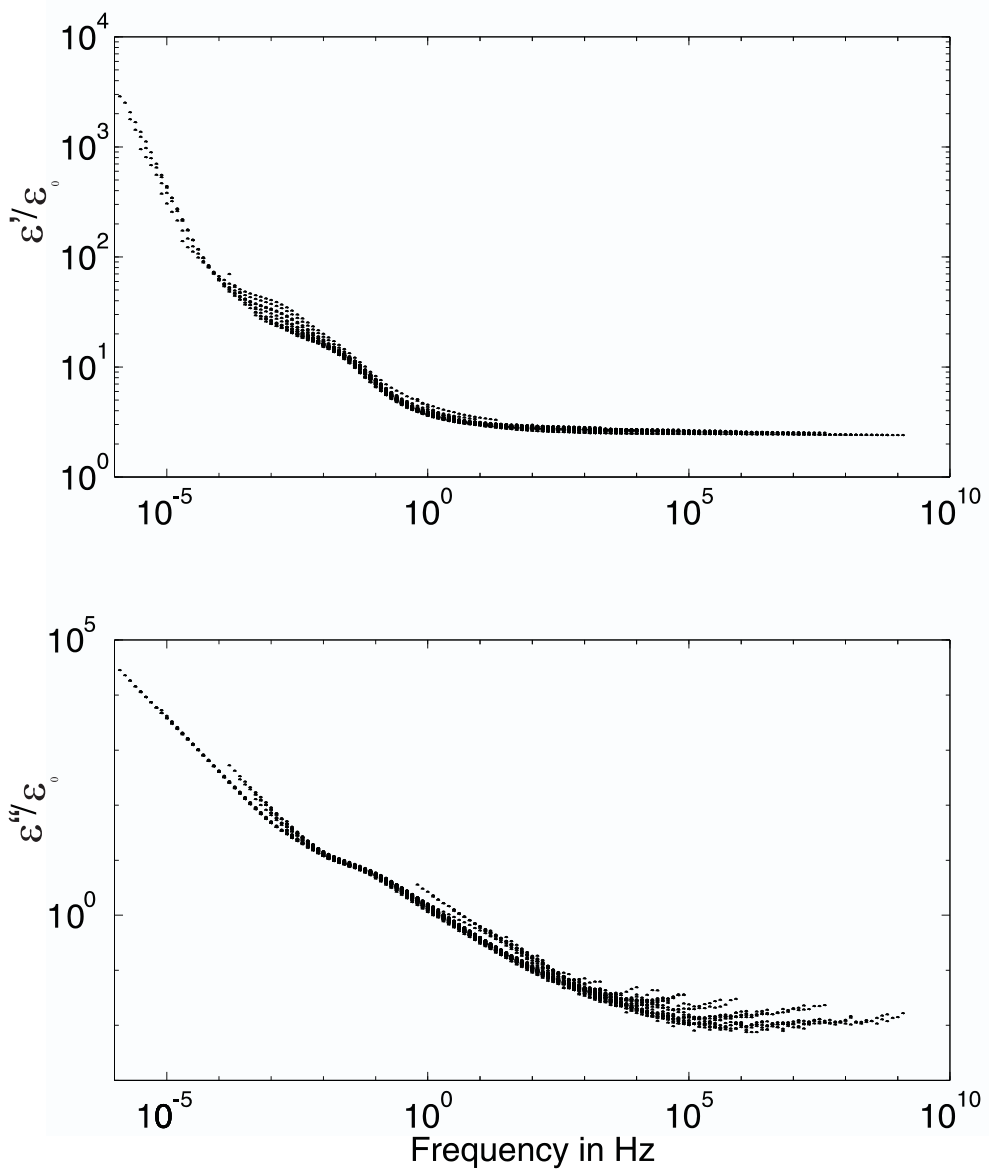

Figure 4.7: Discrete frequency shifting of all forty five measured oil-free pressboard data sets to minimize least square differences suggests the existence of a universal curve.

4.3 Effective Dielectric Constant of Pressboard

In order to compare our measured value of pressboard dielectric constant with its nominal value, a study is given for the effective dielectric constant of the porous cellulosic pressboard structure. Transformerboard is produced from new high-grade cellulose raw materials. The theoretical maximum density of a body of cellulose fibers is about 1.4×10^3 kg/m^3 [79]. The capacity to be impregnated with insulating oil requires a pore volume and corresponding capillary spaces of the order of 10 to 20%. The relative dielectric constant for the fiber is $\varepsilon_F = 5.1$ and the capillary spaces will be filled either by air or oil with known relative dielectric constant of $\varepsilon_{air} = 1$ and $\varepsilon_{oil} = 2.2$. The goal is to find the effective dielectric constant ε_P for the porous pressboard. We use subscript F to designate fibers and P to designate pressboard.

4.3.1 Wiener Limits

Early work of Wiener provided the limiting values for effective dielectric constant values for heterogeneous mixtures as a function of the mixture geometry [80]. The parallel configuration shown in Figure 4.8, provides the upper limit on dielectric constant of pressboard filled with material X, ε_{PX},

$$\varepsilon_{PX} = (1-n)\varepsilon_F + n\varepsilon_X, \tag{4.2}$$

where ε_X is the dielectric constant of the filler, either air or oil, and n is the volume fraction of the filler and pressboard

$$n = \frac{V_X}{V_P} = \frac{V_{oil}}{V_P} = \frac{V_{air}}{V_P}, \tag{4.3}$$

with $0 < n < 1$, V being the volume, and $V_P = V_F + V_X$. For the same type of pressboard, n is the same regardless if it is filled with air or oil. The geometric parameters for each capacitor are also given in Figure 4.8 as a fraction of the equivalent capacitor's area A and thickness d.

The series configuration in Figure 4.9 provides the lower limit for ε_{PX},

$$\varepsilon_{PX} = \frac{\varepsilon_F\varepsilon_X}{n\varepsilon_F + (1-n)\varepsilon_X}. \tag{4.4}$$

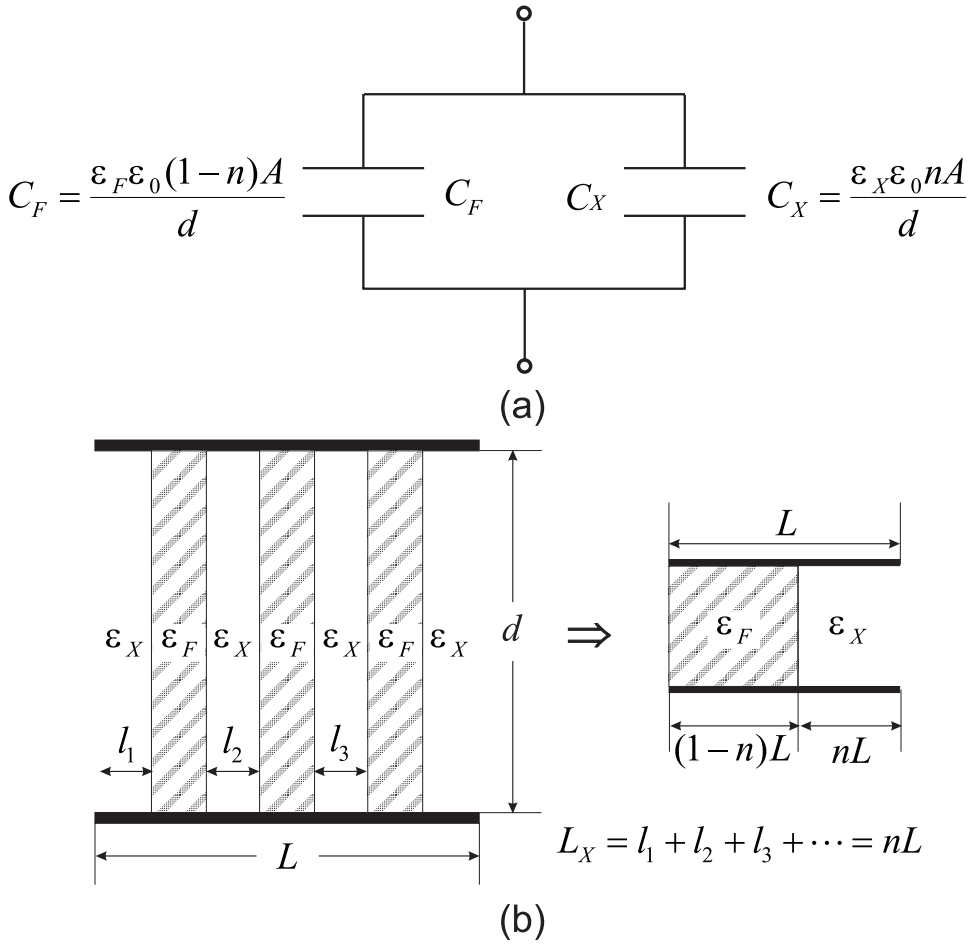

Figure 4.8: The (a) equivalent circuit elements and (b) equivalent structure for the parallel limiting model for pressboard composed of fiber with relative dielectric constant ε_F and filling material (air or oil) with relative dielectric constant ε_X.

The two limits are equal when $\varepsilon_F = \varepsilon_X$, with $\varepsilon_{PX} = \varepsilon_F = \varepsilon_X$.

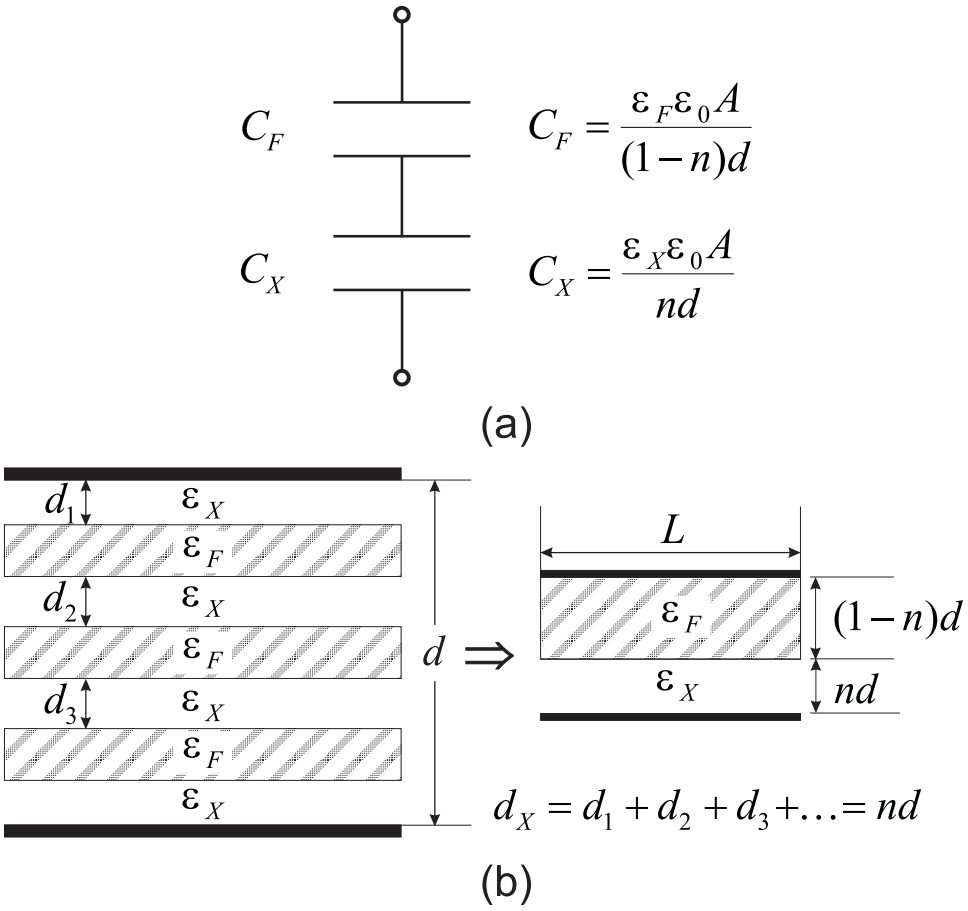

Figure 4.9: The (a) equivalent circuit elements and (b) equivalent structure for the series limiting model for pressboard composed of fiber with relative dielectric constant ε_F and filling material (air or oil) with relative dielectric constant ε_X.

4.3.2 Mixed Model

Moser [79] pointed out that a more realistic method of determining the dielectric constant of the oil-impregnated transformerboard insulation is based on a schematic structure of the fiber matrix in which cube-like volume elements of oil are embedded in the solid fiber material, which also has a cube-like structure, as shown in Figure 4.10. The V_B in Figure 4.10 is equivalent to V_P discussed here.

The edge ratio "K" of the cube elements (relative edge length) depends on the volume ratio V_{oil}/V_P:

$$K = \sqrt[3]{V_{oil}/V_P} \tag{4.5}$$

For a sufficiently fine subdivision, the embedded cube elements with the relative edge length "K" represent the oil-filled pores randomly distributed in the fiber matrix [79]. The structure can be represented by the circuit shown in Figure 4.11.

For oil-free pressboard, neglecting the weight of the air between the fibers, the weight of the pressboard is equal to the weight of the fibers present in the pressboard,

$$V_P \rho_{Pair} = V_F \rho_F, \tag{4.6}$$

where V_P is the pressboard volume, ρ_{Pair} is the air-filled pressboard density, V_F is the fiber volume, and ρ_F is the fiber density. The volume of pressboard is the same for oil-impregnated and oil-free pressboard, therefore, the volume of oil in impregnated pressboard is:

$$V_{oil} = V_P - V_F. \tag{4.7}$$

Equation (4.6) gives:

$$V_F = V_P \frac{\rho_{Pair}}{\rho_F}. \tag{4.8}$$

where ρ_F=1.43 g/cm^3. Substituting (4.8) into (4.7) gives

$$V_{oil} = V_P(1 - \frac{\rho_{Pair}}{\rho_F}), \tag{4.9}$$

and

$$K^3 = n = \frac{V_{oil}}{V_P} = \frac{V_{air}}{V_P} = 1 - \frac{\rho_{Pair}}{\rho_F}. \tag{4.10}$$

ρ_{Pair} (g/cm^3)		0.8	0.9	1.0	1.1	1.2	1.3	1.4	1.43
$n = 1 - \rho_{Pair}/\rho_F$		0.44	0.37	0.30	0.23	0.16	0.09	0.02	0.00
$K = n^{1/3}$		0.76	0.72	0.67	0.61	0.54	0.45	0.28	0.00
ε_{Poil}(4.2)	parallel	3.82	4.03	4.23	4.43	4.63	4.84	5.04	5.10
(4.12)	mixed	3.62	3.82	4.03	4.24	4.47	4.72	5.00	5.10
(4.4)	series	3.23	3.43	3.65	3.91	4.21	4.55	4.96	5.10
ε_{Pair} (4.2)	parallel	3.29	3.58	3.87	4.15	4.44	4.73	5.01	5.10
(4.12)	mixed	2.86	3.14	3.42	3.73	4.06	4.43	4.89	5.10
(4.4)	series	1.82	2.02	2.28	2.62	3.07	3.72	4.70	5.10

Table 4.2: The calculated dielectric constant of oil-impregnated and oil-free pressboard as a function of oil-free pressboard density for three different models given in (4.2), (4.4), and (4.12).

The dielectric constant of the mixed insulation modeled in Figure 4.11 is

$$\varepsilon_{Poil} = \varepsilon_F[1 - K^2(1 - \frac{1}{1 + K(\frac{\varepsilon_F}{\varepsilon_{oil}} - 1)})]. \tag{4.11}$$

Generalizing (4.11) for any filler material with relative dielectric constant ε_X yields

$$\varepsilon_{PX} = \varepsilon_F[1 - K^2(1 - \frac{1}{1 + K(\frac{\varepsilon_F}{\varepsilon_X} - 1)})]. \tag{4.12}$$

4.3.3 Estimated Dielectric Constant with Different Models

The dielectric constant of oil-free pressboard can be calculated in a similar way [81]. The dielectric constant of oil-impregnated and oil-free pressboard as a function of oil-free pressboard density are shown in Figure 4.12 and Figure 4.13 for the three different models given in Figure 4.8, Figure 4.9, and Figure 4.11. The computed data are tabulated in Table 4.2.

All the analysis is for dry air and pressboard, i.e. there are no moisture effects. The manufacturer reported value of the relative dielectric constant for the oil-impregnated case for Hi-Val pressboard that is used in the experiments of this chapter is 3.8 which corresponds to an oil-free pressboard density of 0.9 g/cm^3. Equation (4.12) gives the dielectric constant as $\varepsilon_{Pair} = 3.1$ for oil-free pressboard.

ρ_{Pair} (g/cm^3)	0.8	0.9	1	1.1	1.2	1.3	1.4
$\frac{dK}{d\rho_{Pair}}$	-0.40	-0.45	-0.52	-0.62	-0.79	-1.15	-3.06
Oil							
$\frac{d\varepsilon_{Poil}}{dK}$	-2.18	-1.95	-1.71	-1.44	-1.13	-0.76	-0.27
$\frac{d\varepsilon_{Poil}}{d\rho_{Pair}}$	0.88	0.88	0.89	0.89	0.89	0.88	0.82
Air							
$\frac{d\varepsilon_{Pair}}{dK}$	-4.99	-4.61	-4.18	-3.68	-3.09	-2.32	-1.06
$\frac{d\varepsilon_{Pair}}{d\rho_{Pair}}$	2.01	2.08	2.17	2.28	2.44	2.68	3.24

Table 4.3: Calculated sensitivity of the dielectric constant to the density of the pressboard using the mixed model of (4.12) for oil and air filler materials.

During the experiment, depending how much pressure is applied between the test structure, the pressboard can be compressed thereby increasing the pressboard density. The sensitivity of the dielectric constant of the pressboard to the pressboard density is

$$\delta\varepsilon_{PX} = \frac{d\varepsilon_{PX}}{d\rho_{Pair}}\delta\rho_{Pair} = \frac{d\varepsilon_{PX}}{dK}\frac{dK}{d\rho_{Pair}}\delta\rho_{Pair}, \tag{4.13}$$

where

$$\frac{d\varepsilon_{PX}}{dK} = -\varepsilon_F K\left[2 - 2(1 + K(\frac{\varepsilon_F}{\varepsilon_X} - 1))^{-1} - K\frac{\varepsilon_F}{\varepsilon_X}(1 + K(\frac{\varepsilon_F}{\varepsilon_X} - 1))^{-2}\right], \tag{4.14}$$

$$\frac{dK}{d\rho_{Pair}} = -\frac{1}{3\rho_F}(1 - \frac{\rho_{Pair}}{\rho_F})^{-2/3}. \tag{4.15}$$

The calculated slope of $\delta\varepsilon_{PX}$ versus $\delta\rho_{Pair}$ is listed in Table 4.3. The dielectric constant of oil-free pressboard is more sensitive to the change of density of the pressboard. Roughly a 10% change in density, which is equivalent in 10% change in volume, can cause more than a 20% change in the dielectric constant.

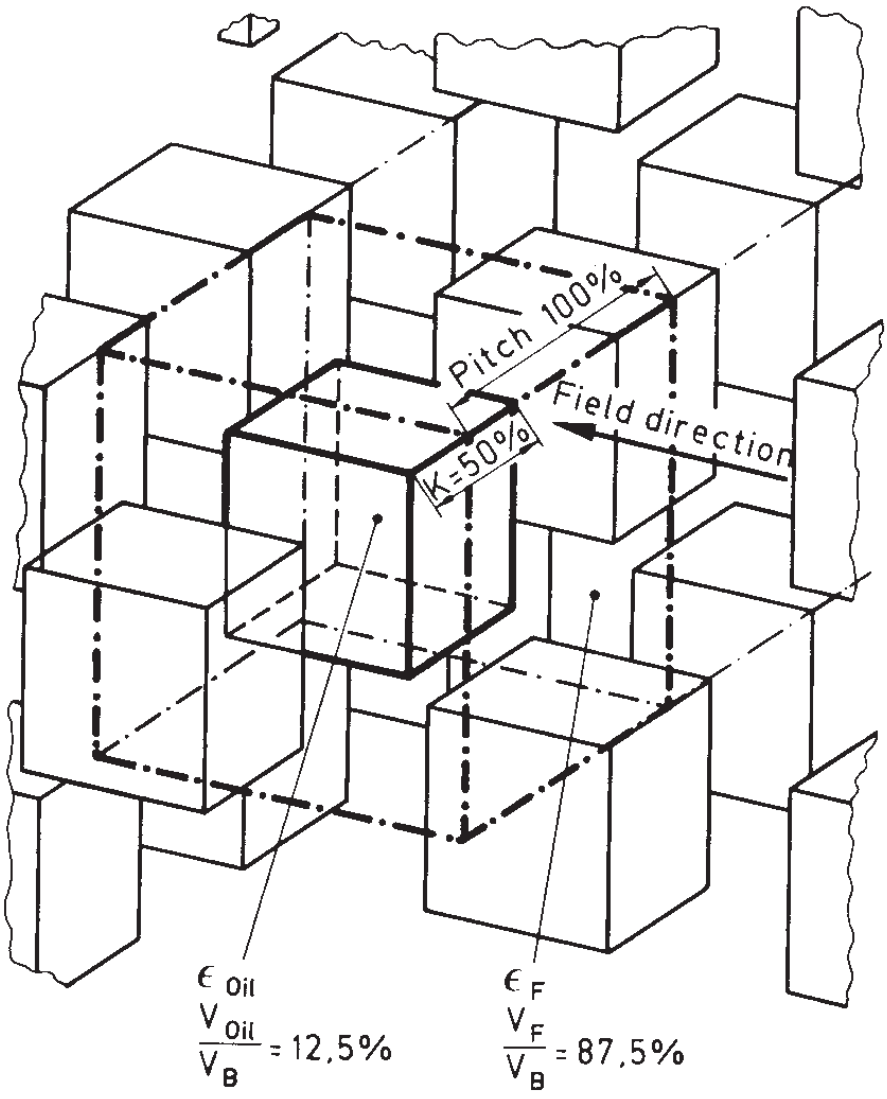

Figure 4.10: Diagram of oil (ε_{oil}) embedded in solid fiber (ε_F) in idealized cube form; example with edge ratio K=50% [79].

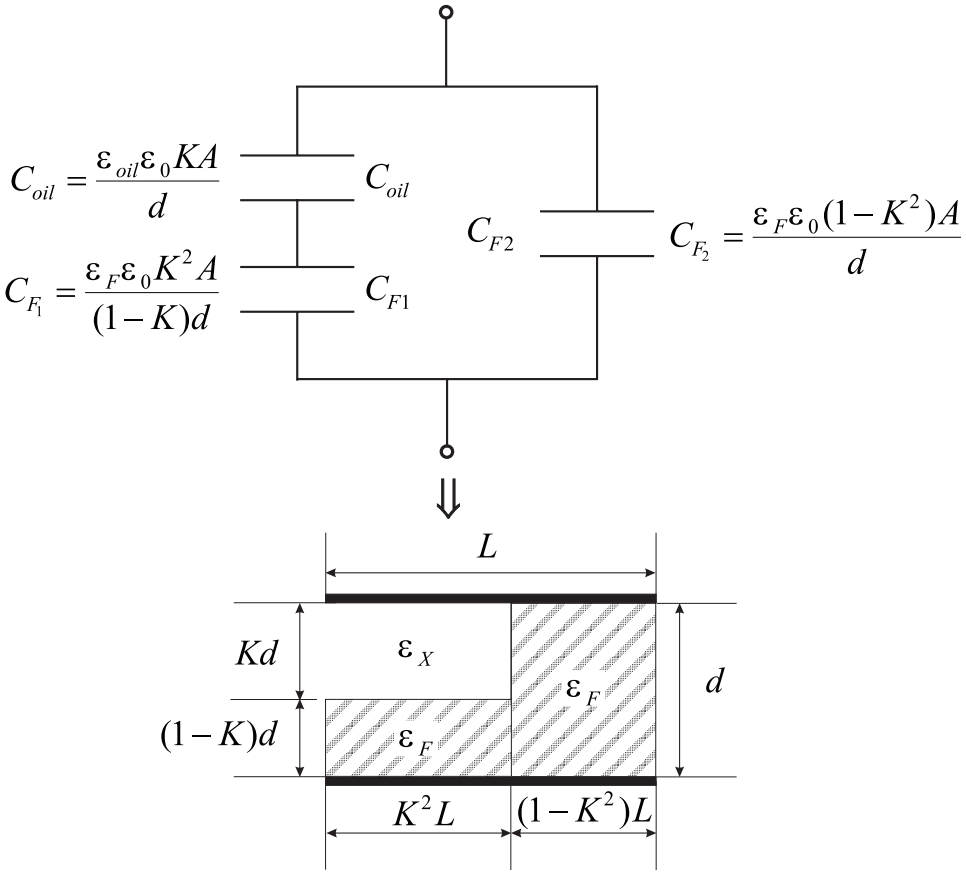

Figure 4.11: Equivalent circuit for the partial capacitances of an oil-impregnated fiber matrix.

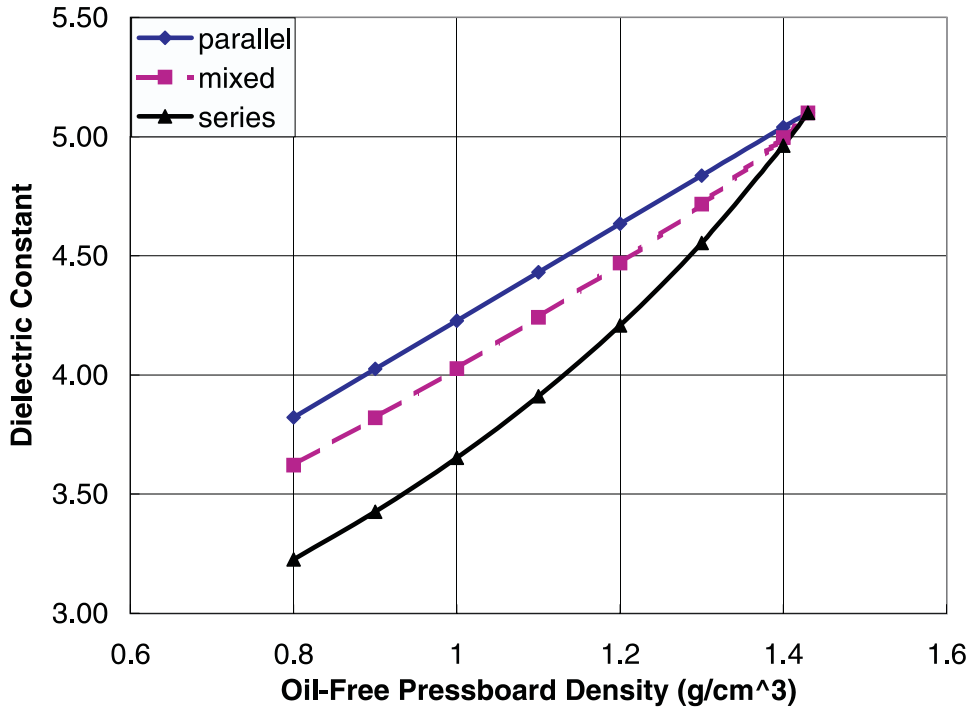

Figure 4.12: The calculated relative dielectric constant of oil-impregnated pressboard as a function of oil-free pressboard density for the three different models given in Figure 4.8, Figure 4.9, and Figure 4.11.

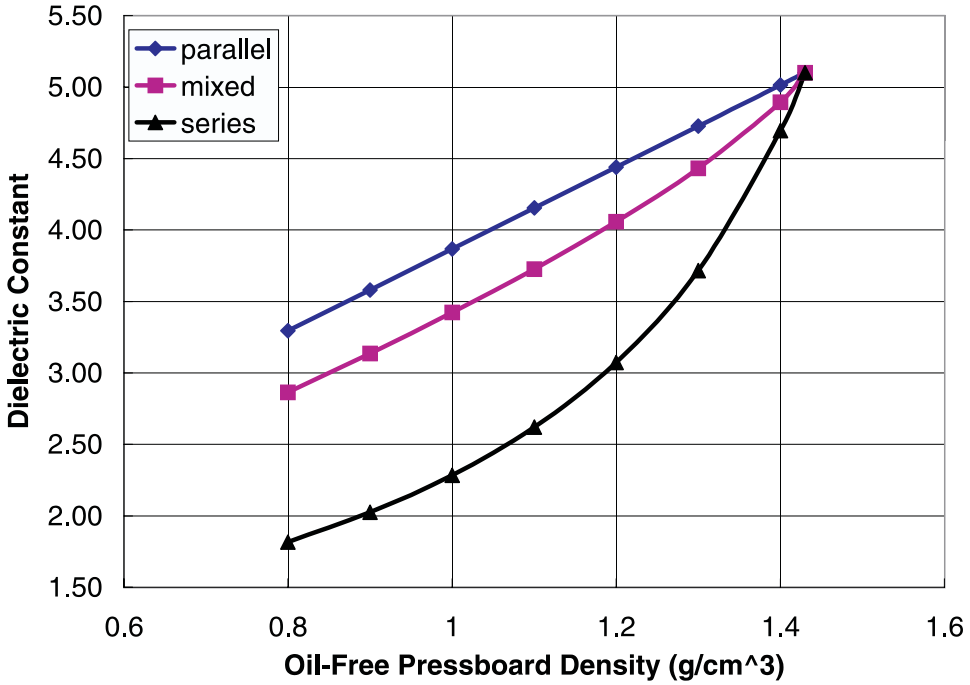

Figure 4.13: The relative dielectric constant of oil-free pressboard as a function of oil-free pressboard density with three different models given in Figure 4.8, Figure 4.9, and Figure 4.11.

4.4 Error Analysis

Whenever measurements are made, errors are made–the single exception being when the measurement is a discrete count [82]. Two concepts that are important to the ensuing treatment of errors are precision and accuracy. Precision is descriptive of the degree of care and refinement employed in making a measurement. Accuracy is descriptive of the correctness of the result of the measurement. The following major factors affect the parallel-plate sensor measurement accuracy presented in this chapter:

1. The Omega series CN 310 solid-state temperature controller with T type thermal probe has an accuracy of $\pm 2.0^{\circ}$C [83].

2. Humidity measurement: the Harley Moisture meter has an accuracy of $\pm 3.5\%$ [68].

3. The air gap between the pressboard and the sensor electrodes: due to the rough texture of the pressboard, there is air space between the pressboard and sensor electrode. It cannot be easily modeled as a flat air layer because the pressboard is touching the sensor electrode at some places. At low frequency, the conduction current is dominant, and a pure air layer model will exclude the conduction current effect. The existence of such an air gap will decrease the measured relative permittivity of the pressboard.

4. Geometric parameters: the effective sensing area and the spacing between two electrodes. The sensor has area of $(2547 \pm 6) \times 10^{-6}$ m^2. The spacing between two electrodes depends on the sample thickness. The variation is about δd=0.01 mm.

5. Gain and phase: the directly recorded data from the controller box.

The controller has a resolution of 0.01 dB for the gain measurement and 0.01 degree for the phase measurement. However, as we point out in the beginning of this section, this does not guarantee an accuracy of 0.01 dB or 0.01 degrees. To estimate the deviation of the gain and phase measurement, we use the sensor measurement in air as a reference system. Measurements were taken using the parallel-plate sensor of Figure 4.2 with gap 1.58 mm in air for 64 frequencies from 0.005 Hz to 10^4 Hz. The average

	Gain (dB)	Phase (degree)	ε_{air}
Measured	-27.96±0.01	0.01±0.06	1.000±0.002
Theoretical	-27.96	0.00	1.00

Table 4.4: The average values of measured gain and phase in air over 64 frequencies and the estimated relative dielectric constant of air.

measured gain and phase are tabulated in Table 4.4. Therefore there is ±0.01 dB of deviation of the gain measurement and 0.01 degrees of offset and ±0.06 degrees of deviation of the phase measurement. These numbers can be used as a representative standard deviation in other measurements.

The last two error effects due to geometry and Gain/Phase on measured complex permittivity can be directly calculated. Using a short-circuit interface box (see Chapter 6 for more details), the measured output voltage V_O of the interface box is

$$V_O = \frac{j\omega C^*}{j\omega C_F} V_D = 10^{G/20} e^{j\varphi\pi/180}, \tag{4.16}$$

where C^* is the complex capacitance of the test sample, C_F is the known external circuit feedback capacitor, V_D is the applied driving voltage, G is the measured gain in dB, and φ is the measured phase in degrees. Then C^* is

$$C^* = 10^{G/20} e^{j\varphi\pi/180} C_F / V_D, \tag{4.17}$$

which is related to the complex permittivity as

$$\varepsilon^* = \varepsilon' - j\varepsilon'' = C^* d/A. \tag{4.18}$$

Therefore,

$$\varepsilon' = \frac{10^{G/20} C_F d}{V_D A} \cos(\varphi\pi/180), \tag{4.19}$$

and

$$\varepsilon'' = -\frac{10^{G/20} C_F d}{V_D A} \sin(\varphi\pi/180). \tag{4.20}$$

The error propagation from observable variables to the estimated variables can be written as

$$\delta\varepsilon = \frac{\partial\varepsilon}{\partial d}\delta d + \frac{\partial\varepsilon}{\partial A}\delta A + \frac{\partial\varepsilon}{\partial G}\delta G + \frac{\partial\varepsilon}{\partial P}\delta\varphi, \tag{4.21}$$

where ε could be ε' or ε''. The partial derivative in (4.21) for ε' are obtained from (4.19) as

$$\frac{\partial \varepsilon'}{\partial d} = \frac{10^{G/20} C_F \cos(\varphi\pi/180)}{V_D A} = \varepsilon'/d, \tag{4.22}$$

$$\frac{\partial \varepsilon'}{\partial A} = -\frac{10^{G/20} C_F d \cos(\varphi\pi/180)}{V_D A^2} = -\varepsilon'/A, \tag{4.23}$$

$$\frac{\partial \varepsilon'}{\partial G} = \frac{10^{G/20} C_F d \cos(\varphi\pi/180)}{V_D A} \cdot \frac{\ln(10)}{20} = \varepsilon' \frac{\ln(10)}{20}, \tag{4.24}$$

$$\frac{\partial \varepsilon'}{\partial \varphi} = -\frac{10^{G/20} C_F d}{V_D A} \frac{\pi}{180} \sin(\varphi\pi/180) = -\varepsilon' \frac{\pi}{180} \tan(\varphi\pi/180). \tag{4.25}$$

Similarly, the partial derivative in (4.21) for ε'' are obtained from (4.20) as

$$\frac{\partial \varepsilon''}{\partial d} = \varepsilon''/d, \tag{4.26}$$

$$\frac{\partial \varepsilon''}{\partial A} = -\varepsilon''/A, \tag{4.27}$$

$$\frac{\partial \varepsilon''}{\partial G} = \varepsilon'' \frac{\ln 10}{20}, \tag{4.28}$$

$$\frac{\partial \varepsilon''}{\partial \varphi} = \varepsilon'' \frac{\pi}{180} \cot(\varphi\pi/180). \tag{4.29}$$

Equations (4.22) - (4.29) can be concisely written as

$$\begin{bmatrix} \delta\varepsilon' \\ \delta\varepsilon'' \end{bmatrix} = \begin{bmatrix} \varepsilon'/d & -\varepsilon'/A & \varepsilon' \frac{\ln 10}{20} & -\varepsilon' \frac{\pi}{180} \tan(\varphi\pi/180) \\ \varepsilon''/d & -\varepsilon''/A & \varepsilon'' \frac{\ln 10}{20} & \varepsilon'' \frac{\pi}{180} \cot(\varphi\pi/180) \end{bmatrix} \begin{bmatrix} \delta d \\ \delta A \\ \delta G \\ \delta\varphi \end{bmatrix}, \tag{4.30}$$

with φ ranging from 0 to -90 degrees.

The calculated error bars with δd=0.01 mm for the test in Figure 4.6 at 70°C and 2.0% moisture content are shown in Figure 4.14 and the percentage error in the complex permittivity is shown in Figure 4.15. Even though the absolute value of the error in the estimation is small at high frequency, because the value of the complex permittivity is also small at that range, the percentage error actually is about the same for ε' and very large for ε''. Overall the errors caused by the geometric parameters and the gain and phase measurements are small and within 10% for this test.

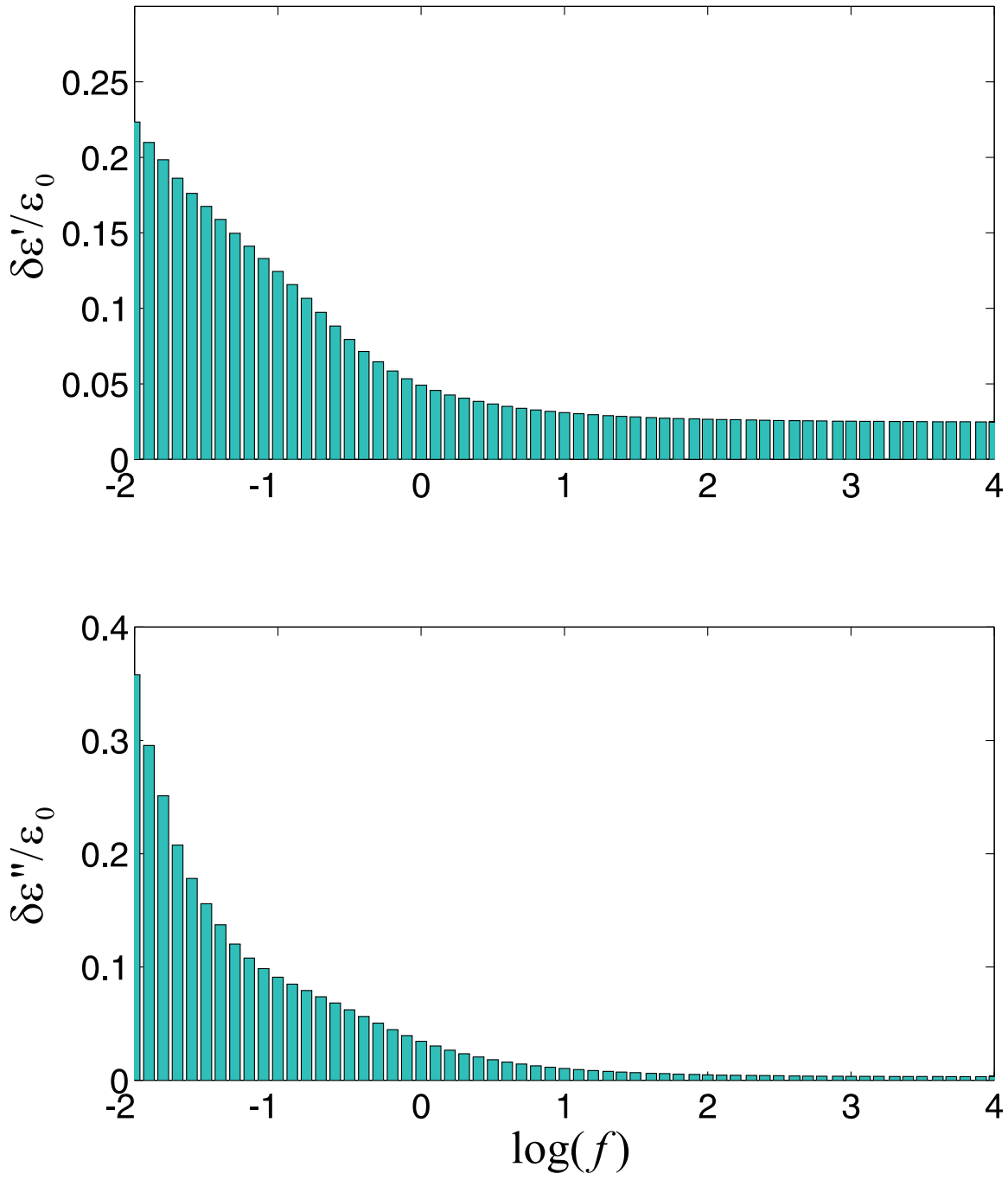

Figure 4.14: The estimated error bars for the complex dielectric permittivity in Figure 4.6 measured for oil-free pressboard at 70°C and 2.0% moisture content.

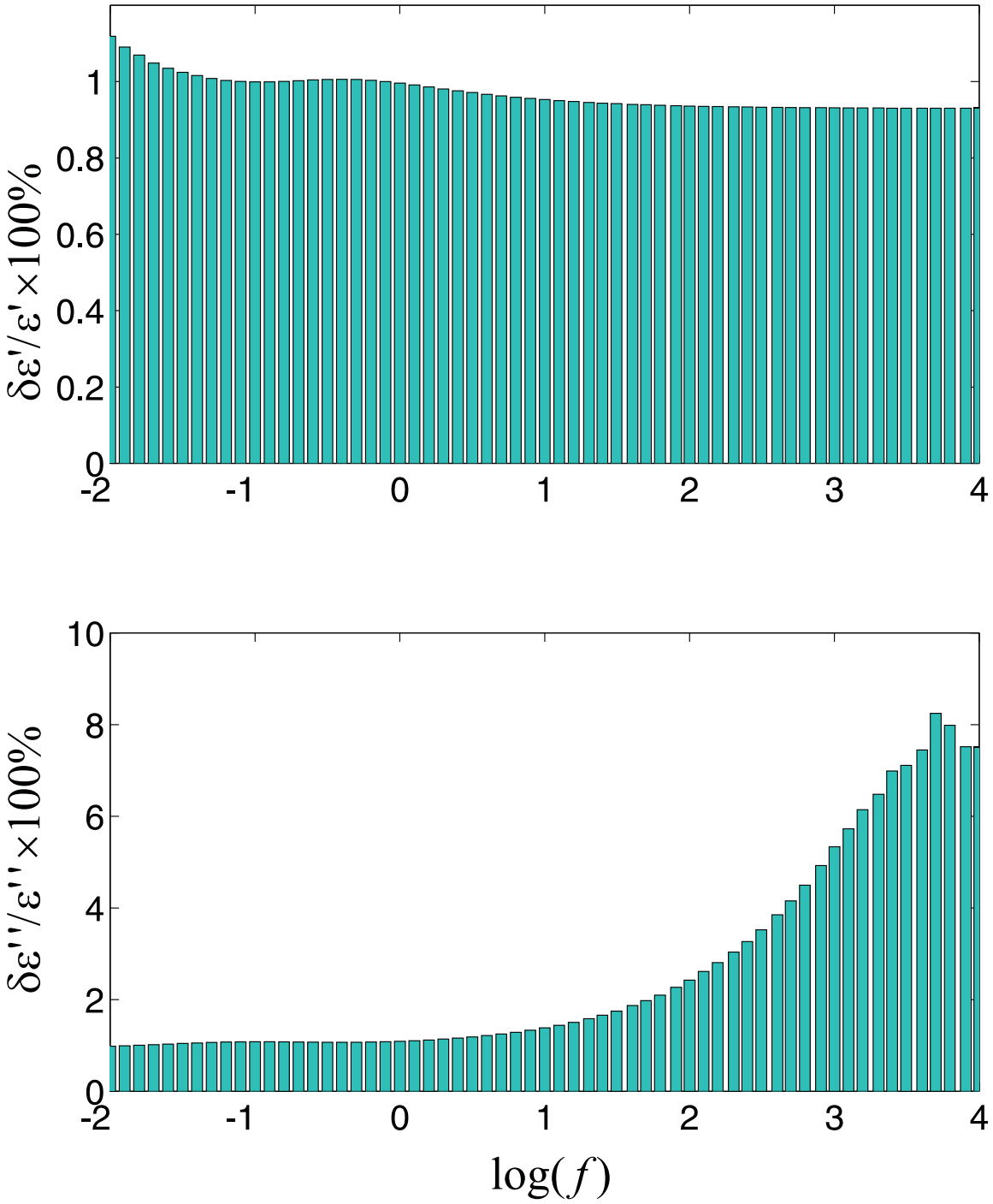

Figure 4.15: The estimated error percentage for the complex dielectric permittivity in Figure 4.6 measured for oil-free pressboard at 70° C and 2.0% moisture content.

4.5 Universal Curve Model and Fitting

The most important task of establishing such a universal curve was to find the proper model. A polynomial fit is easiest and can fit the data fairly well at the measured frequency. However it blows up at high frequency, and has no physical meaning. A time invariant RC circuit model does not fit the dispersive nature of the pressboard. Even simple dielectric models such as the low frequency dispersion model in [84] would not account for the double inflection points in the measurements.

The complex dielectric permittivity has the following relationship with the complex susceptibility

$$\varepsilon^*(\omega) = \varepsilon_0(1 + \chi^*(\omega)) = \varepsilon_0(1 + \chi'(\omega) - j\chi''(\omega)) \equiv \varepsilon'(\omega) - j\varepsilon''(\omega). \tag{4.31}$$

The inverse Fourier transform of the complex susceptibility is called the dielectric response function $f(t)$

$$f(t) = \frac{1}{2\pi}\int_{-\infty}^{+\infty} \chi^*(\omega)e^{j\omega t}d\omega. \tag{4.32}$$

Helgeson has summarized some of the most commonly observed dielectric response functions that have an analytical Fourier transform or can be numerically transformed in [7]. Helgeson generalized that depending on the type of polarization process, f(t) can be for a wide range of times modeled with any of the following expressions shown in Figure 4.16. Most of these functions have analytical Fourier transforms and their shapes are shown in Figure 4.17.

• Curie-von Schweidler

The Curie-von Schweidler model is widely observed in practice, which shows that the time dependence of the relaxation current after the sudden removal of a polarizing field follows the power law [76, 85, 86]

$$\mathrm{f}(t) = At^{-n}, 0 < n < 1. \tag{4.33}$$

Its Fourier transform is

$$\chi^*(j\omega) = \frac{A\Gamma(1-n)}{(j\omega)^{1-n}}, \tag{4.34}$$

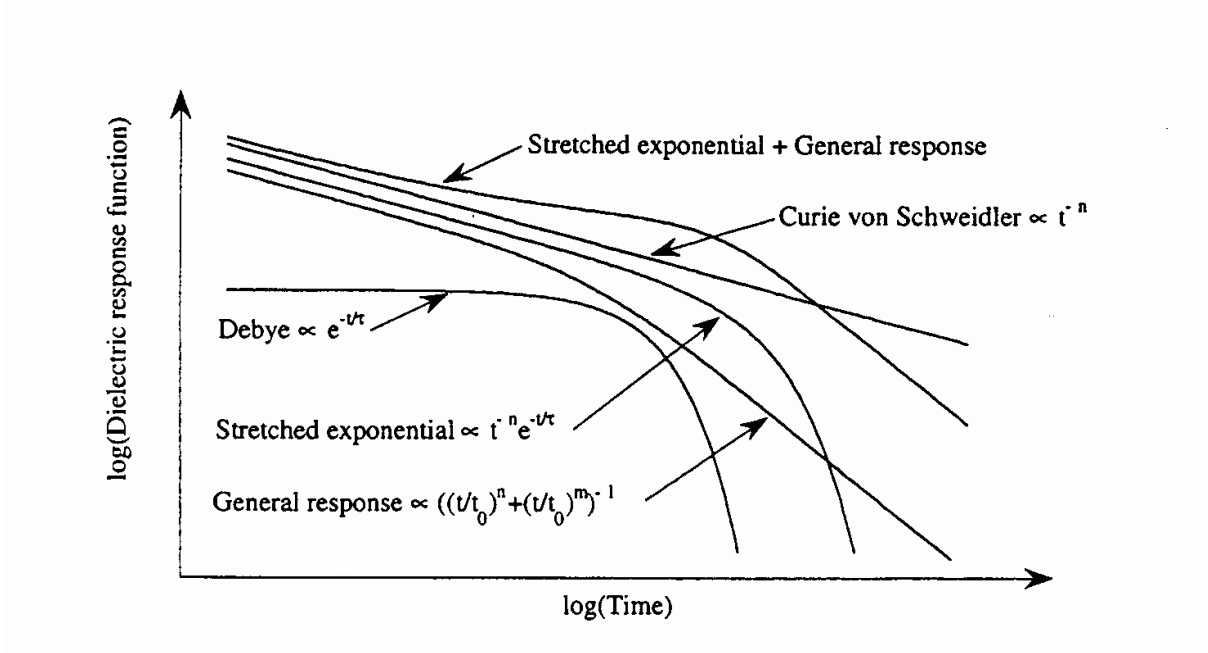

Figure 4.16: Different types of dielectric response functions f(t) for dielectric materials in the time domain [7].

where $\Gamma(1-n)$ is the gamma function defined by the integral

$$\Gamma(n) = \int_0^\infty t^{n-1} e^{-t} dt. \tag{4.35}$$

- General Response

The general response model is the time domain model of a frequency domain loss peak (dipolar material) [76]:

$$\mathrm{f}(t) = \frac{A}{(\frac{t}{t_0})^n + (\frac{t}{t_0})^m}. \tag{4.36}$$

In a log-log plot the general response model will have a slope n for $t < t_0$ and a slope $m \geq 1$ for $t > t_0$ where $m > n > 0$. This model diverges at zero time and is therefore not valid for arbitrary short times.

In general it is not possible to solve analytically the Fourier transform of the general response model. However, for times $t \ll t_0$ and times $t \gg t_0$ the general response model can be approximated with the Curie-von Schweidler model and the transform is

approximated:

$$\chi^*(j\omega) \approx \begin{cases} \frac{At_0^n\Gamma(1-n)}{(j\omega)^{1-n}}, t < t_0 \\ \frac{At_0^m\Gamma(1-m)}{(j\omega)^{1-m}}, t > t_0 \end{cases} \tag{4.37}$$

• Stretched Exponential:

The stretched exponential model is a modification of the Curie-von Schweidler model [84]:

$$\mathrm{f}(t) = At^{-n}e^{-mt}. \tag{4.38}$$

Its Fourier transform is

$$\chi^*(j\omega) = \frac{A\Gamma(1-n)}{(m+j\omega)^{1-n}} \tag{4.39}$$

• Stretched Exponential +General Response

$$\mathrm{f}(t) = A_1t^{-n_1}e^{-m_1t} + \frac{A_2}{(\frac{t}{t_0})^{n_2} + (\frac{t}{t_0})^{m_2}}. \tag{4.40}$$

This model is the time domain model for a charge carrier system. In a log-log plot, this model will have three different slopes n_1, n_2, and m_2. Similarly, $m_2 > 1 > n_2$. Its Fourier transform is also a summation of the transform of the stretched exponential and general response.

• Debye

$$\mathrm{f}(t) = \frac{\chi_0}{\tau}e^{-\frac{t}{\tau}} \tag{4.41}$$

The classic Debye expression represents a physical process that is valid for dielectric liquids but is hardly seen in solid dielectric materials. It was derived under the assumption that the dipoles are not interacting, which is true only for polar liquids but not for solid dielectric materials. Its Fourier transform is

$$\chi^*(\omega) = \frac{\chi_0}{1+j\tau\omega}. \tag{4.42}$$

Neither of the above individual models in Figure 4.17 will give the shape of our experimental curves.

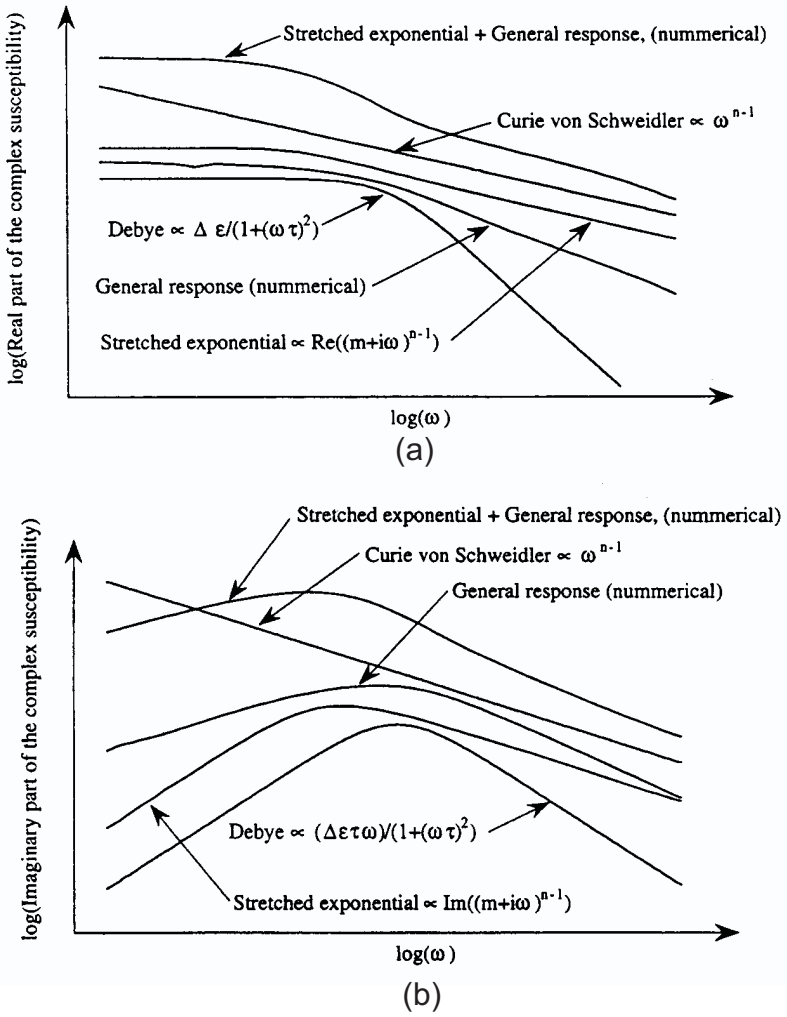

Figure 4.17: The real and imaginary parts of the complex susceptibility for different models of a dielectric material in the frequency domain [7].

ε_d	$\omega_d(rad/s)$	n_d	ε_b	ε_q	$\omega_q(rad/s)$	n_q	p	$\sigma_p(pS/m)$	ε_p
1.27	0.455	0.045	30.7	2.96	4.17	0.996	0.656	3.48×10^4	1.16×10^4

Table 4.5: The parameters of the universal curve model by a least squares fit of the experimental data to the model in Figure 4.19 described by (4.43) and (4.44).

A model developed by Hill et al. [87] for biological cell tissues was used and is shown in Figure 4.19 to have similar double inflection features to the measurements of Figure 4.7. Their original data are shown in Figure 4.18.

Hill et al.'s model consists of low frequency diffusion described by relative permittivities ε_{diff} and ε_b capacitors in parallel, low frequency dispersion for the single series capacitor described by relative permittivities ε_{qdc}, and a lossy bulk dielectric described by the RC parallel structure with constant conductivity σ_p and relative permittivity ε_p. The model parameters are further described by the following set of equations:

$$\varepsilon_{diff} = \varepsilon_d (j\omega/\omega_d)^{n_d - 1}, \tag{4.43}$$

$$\varepsilon_{qdc} = \varepsilon_q \left((j\omega/\omega_q)^{n_q - 1} + (j\omega/\omega_q)^{-p} \right), \tag{4.44}$$

where n_d, n_q, and p have values between zero and one. Other model parameters: ε_b, ε_p, and σ_p are frequency independent.

The logarithmic shifting is mathematically represented by

$$k = E_a \cdot (1/T - 1/T_0)/\kappa + k_1(M - M_0) + k_2(M - M_0)^2 + k_3(M - M_0)^3, \tag{4.45}$$

where E_a is the thermal activation energy, κ is Boltzmann's constant, T is the temperature in Kelvin, T_0 is the reference temperature and chosen to be 323 °K (50 °C), M is the moisture concentration in percent, and M_0 is the reference moisture concentration and in this case is 2.0%.

Using a constrained minimization routine of Matlab [88], *constr*, the parameters of the model in Figure 4.19 are listed in Table 4.5 and the shifting parameters are listed in Table 4.6 by fitting the experimental data shown in Figure 4.4 and Figure 4.5.

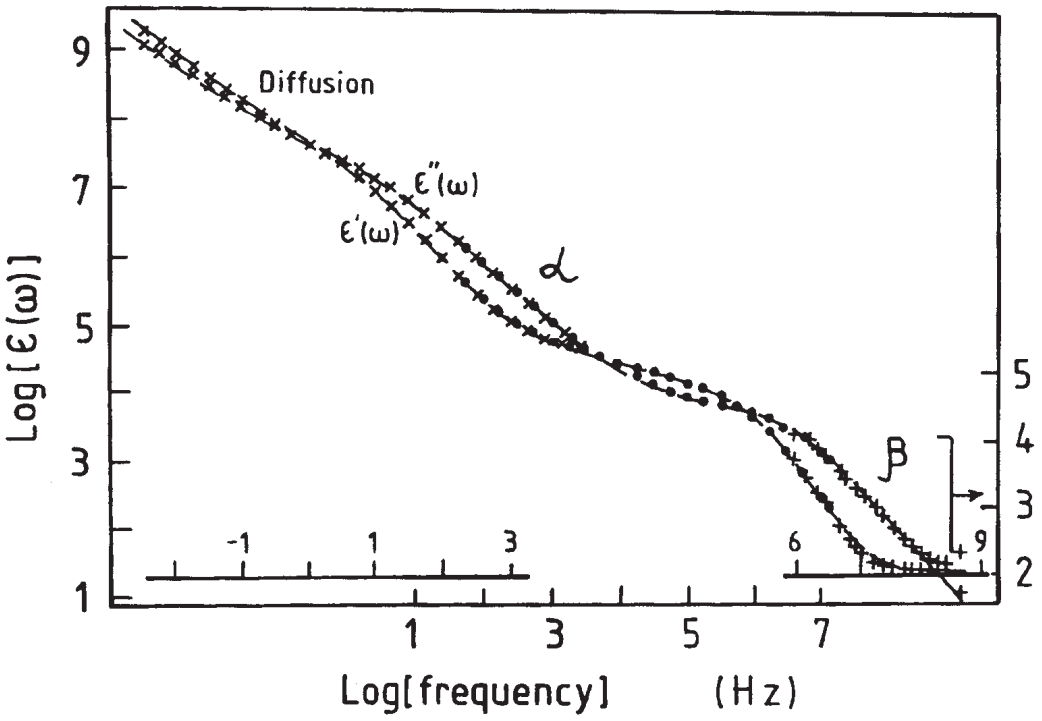

Figure 4.18: The measured frequency dependence of the real, $\varepsilon'(\omega)$, and the imaginary, $\varepsilon''(\omega)$, parts of the complex dielectric permittivity of samples of leaves from the Jade (Crassula Portulacaceae) plant. The curves through the data points have been obtained using the model circuit shown in Figure 4.19. The three data sets at low, mid, and high frequencies are indicated by cross, circular, and plus symbols, respectively. The individual sets of data are shown with their scales and have been reconstructed to give the single characteristic [87].

$E_a/\kappa(^\circ\mathrm{K})$	k_1	k_2	k_3
3.79×10^3	-1.23	0.218	-0.0348

Table 4.6: The parameters of the logarithmic shifting for the experimental data to fit to the universal curve in Figure 4.19.

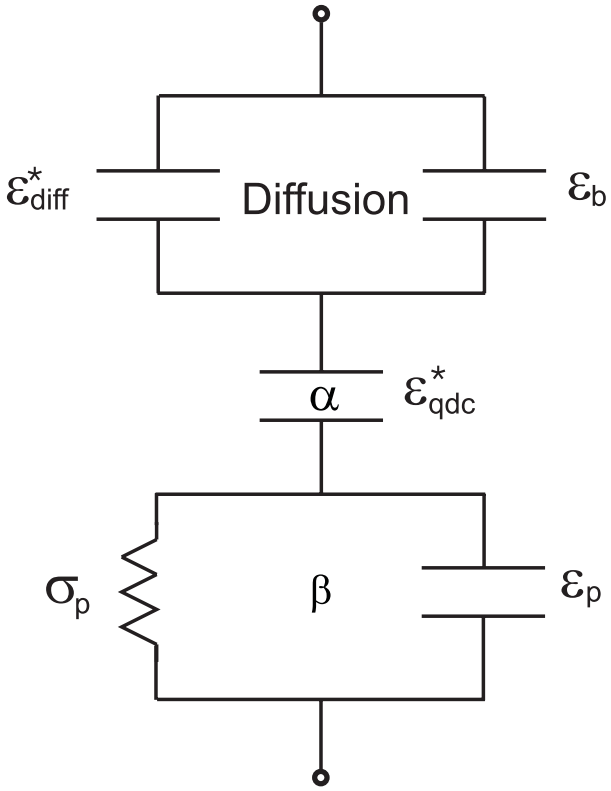

Figure 4.19: Equivalent circuit model for determining the Universal Curve described by (4.43) and (4.44).

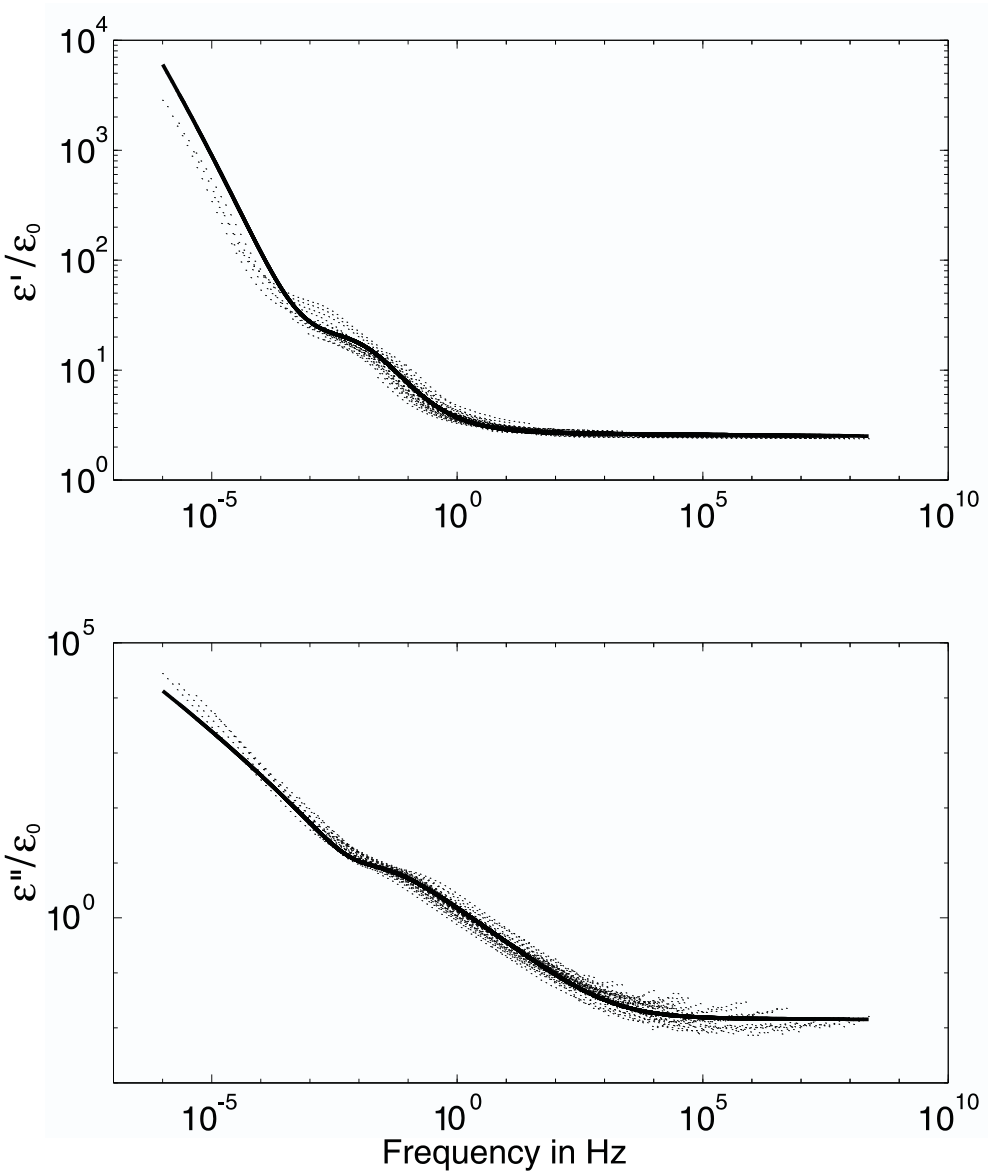

Figure 4.20: Universal curve for oil-free pressboard. The solid line is the curve calculated from the model. The dotted lines are the data points of Figure 4.4 and Figure 4.5 shifted in frequency according to the parameters in Table 4.6 with (4.45).

Moisture Content(%)	0, 1.12, 1.16, 1.34, 1.48, 1.82, 7.81
Temperature (°C)	30, 40, 50, 60, 70

Table 4.7: Moisture content and temperature levels at which oil-impregnated measurements were conducted.

4.6 Measurements for Oil-Impregnated Pressboard

The system used for oil-impregnated pressboard consists of an oil reservoir and a testing chamber. Oil was stored and conditioned in the oil reservoir. This oil was then transported to the testing chamber where the pressboard samples were impregnated and processed. The same parallel-plate sensor, used in the oil-free measurements, was used for oil-impregnated pressboard measurements. The parallel-plate sensor was placed inside the testing chamber for measurements. The moisture levels and temperatures at which measurements were conducted are shown in Table 4.7.

As can be observed, the range of moisture levels for this case is limited. This is due to the fact that diffusion of moisture from the oil to the pressboard takes much longer than that in the oil-free pressboard case. Thus the control of the moisture level is more difficult and it takes much longer for high levels of moisture to diffuse into the pressboard.

4.6.1 Measurement Technique

Hi-Val 1.7 mm thick transformer pressboard impregnated with Shell Diala AX oil was used for the oil-impregnated pressboard measurements. The oil had to be conditioned in the oil reservoir at 70°C. Achieving a broad range of moisture levels for this case was a challenge since high relative humidity oil is hard to achieve at high temperature.

Once the oil was conditioned it was then circulated into the test chamber where pressboard samples were placed to absorb the moisture introduced into the oil. A mesh wire net was placed inside the test chamber to ensure that both sides of the pressboard would remain exposed to the oil. The pressboard samples were conditioned

by filling the test chamber with oil from the reservoir. Oil was then circulated within the test chamber to allow for a uniform mixture of the oil to occur. Samples were left to condition in the testing chamber for at least 48 hours.

After conditioning a sample, the parallel-plate sensor was assembled with the sample placed between the plates. An even amount of force was applied on each corner by nylon bolts in order to minimize air gaps between the sensor and the pressboard. The assembled sensor was then placed in the test chamber.

Oil-impregnated measurements were conducted at 30, 40, 50, 60, and 70°C for each moisture level. The first measurement was taken at 70°C and the temperature was decreased by 10°C after each set of measurements. Due to the large thermal mass of oil, it took longer for the temperature to decrease and stabilize compared to the oil-free case, but since the diffusion time for the oil-impregnated pressboard is also much longer than that of the oil-free pressboard, it was still reasonable to assume that within the time frame of temperature change, the moisture is constant in the pressboard sample throughout the measurements for each moisture level.

For the oil-impregnated case moisture measurements of oil were also performed. Before each set of measurements the oil's moisture content was measured using the Mitsubishi Moisture Meter. The same measurement was conducted after the last measurement at 30°C. There were some discrepancies in these measurements due to the equipment and solution used.

Like the oil-free case there were other parameters of the system that were monitored, including relative humidity and temperature of both the test chamber and oil reservoir. Oil conductivity was also monitored because the aging of oil causes it to become more conductive. This provided a way to determine when it was necessary to change the oil in the system.

4.6.2 Measurement Results

The data collected for oil-impregnated measurements show similar trends to those exhibited in the oil-free case further confirming that a universal curve does exist. However,

a broader range of moisture levels is desired in order to accurately find the universal curve. Figure 4.21 shows values of dielectric properties at 1.82% moisture content for five temperatures. Figure 4.22 shows the measured dielectric properties at 70°C for moisture levels: 0%, 1.3%, 1.5%, and 2.9%. More data for different moisture levels are needed to establish a reliable relationship.

4.7 Summary

Comprehensive experiments relating the dielectric properties of the oil-free pressboard to the temperature and moisture effects have been performed. The results agree with the literature reported results. A dielectric model for biological tissue is adopted here for the cellulose-structured pressboard. The universal curve is found by fitting the data to the model. Preliminary measurements with the oil-impregnated pressboard show similar trends.

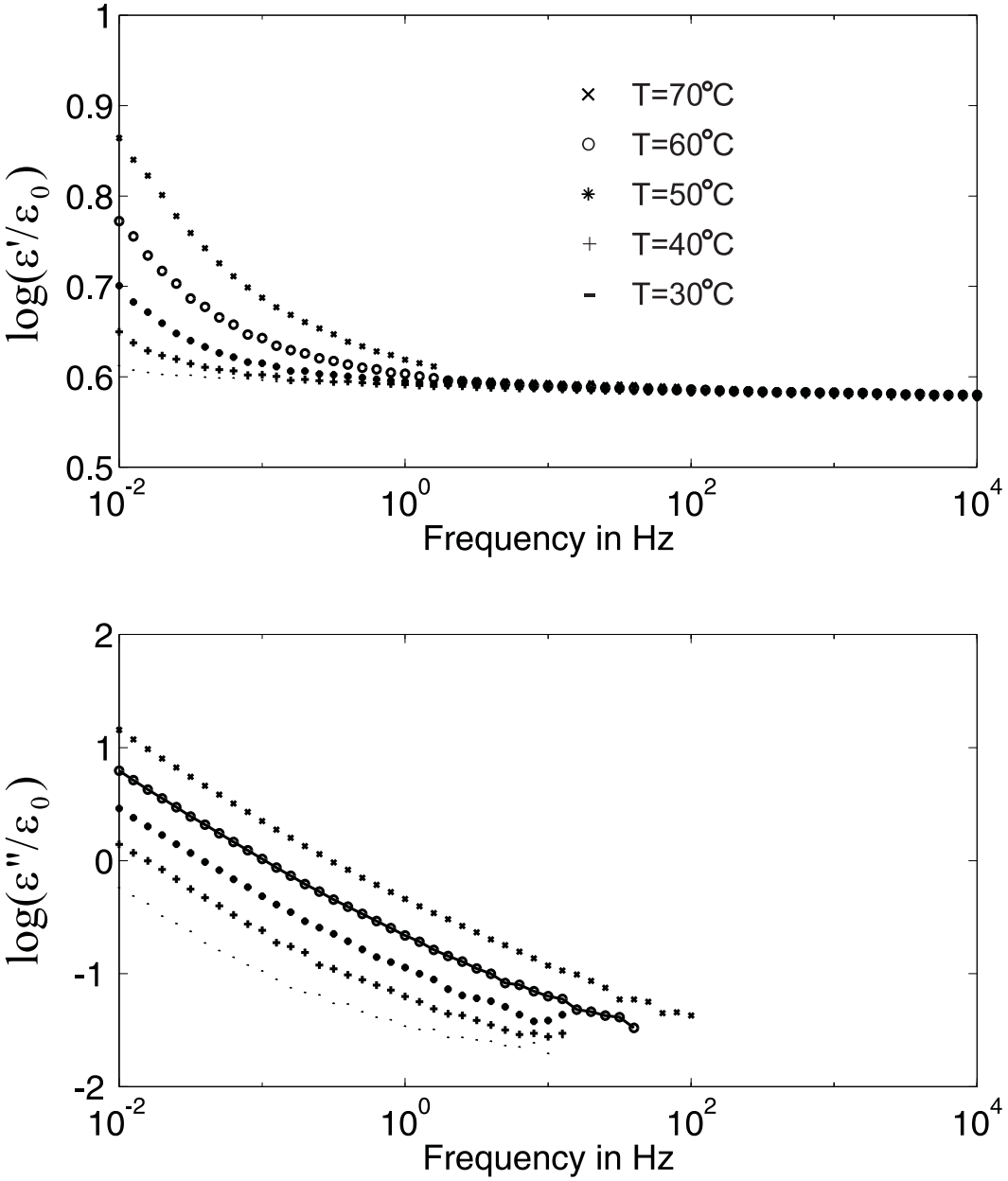

Figure 4.21: Dielectric properties of oil-impregnated pressboard at moisture content 1.5% at five temperatures.

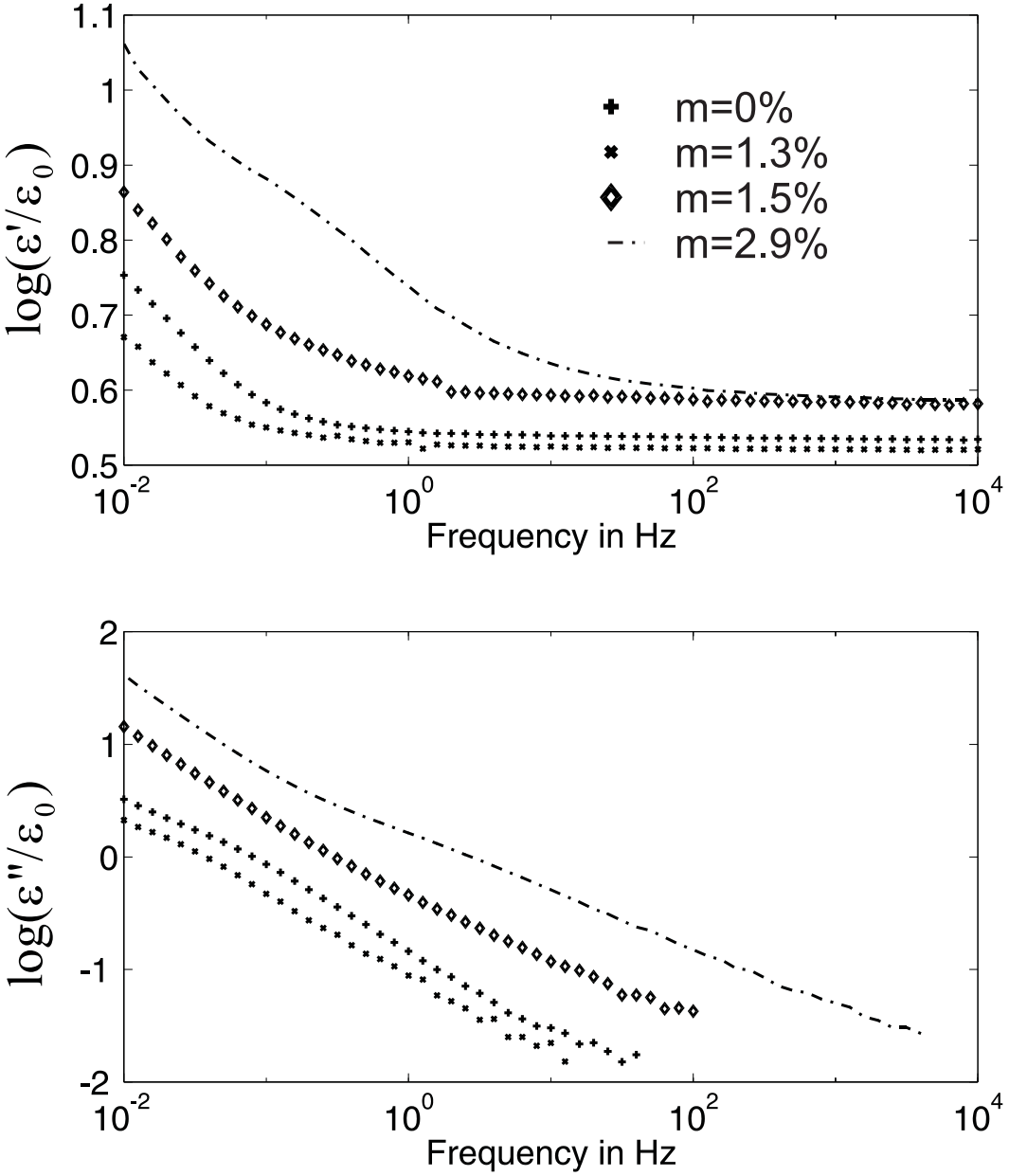

Figure 4.22: Dielectric properties of oil-impregnated pressboard at 70° C for four moisture levels.

Chapter 5

Early Design Sensor Measurements

5.1 Measurement Setup

A typical measurement setup for interdigital dielectrometry measurements is shown in Figure 5.1. The sensor is connected to a microprocessor-controlled controller box through an electronic interface circuit. The controller box controls various operating parameters, generates a sinusoidal drive voltage, measures an output voltage from the interface circuitry, and records data. The interface box's main function is to buffer the signal and raise its input impedance. A computer serves as a data acquisition system as well as interface between operator and the controller. The commands sent from the computer to the controller can either be manually typed or programmed and run automatically.

5.2 Multi-wavelength Sensor

The earlier design of the three-wavelength sensor by Dr. Philip von Guggenberg [2] is shown in Figure 5.2 and Figure 5.3 is a detailed drawing of the sensor head. The flexible sensor consists of three sets of electrodes deposited on a common flexible polyimide substrate (Kapton) with wavelengths of 1, 2.5, and 5 mm. The sensing electrodes are shielded in the $x-y$ plane by guard electrodes driven by the buffer stage of the interface

circuit, and the guard electrodes are shielded by ground electrodes [2, 3]. A thin (5 μm) layer of parylene covers the sensor on both sides to prevent moisture absorption by hydrophilic Kapton. The moisture in the volume of Kapton significantly deteriorates its insulating properties. A single wavelength sensor is also shown in Figure 5.4.

For each wavelength, one set of electrodes is driven with a variable frequency AC voltage and a high impedance measurement is made of the induced voltage on the alternate set of sensing interdigitated electrodes loaded by a known load capacitance. The gain magnitude G and phase ϕ of this floating voltage depend on the permittivity ε and electrical conductivity σ of the medium adjacent to the sensor. As described in Chapter 2, with three different penetration depths it is possible to calculate spatial profiles of permittivity and conductivity from the measured gain and phase of the floating voltage as a function of frequency for each sensor wavelength.

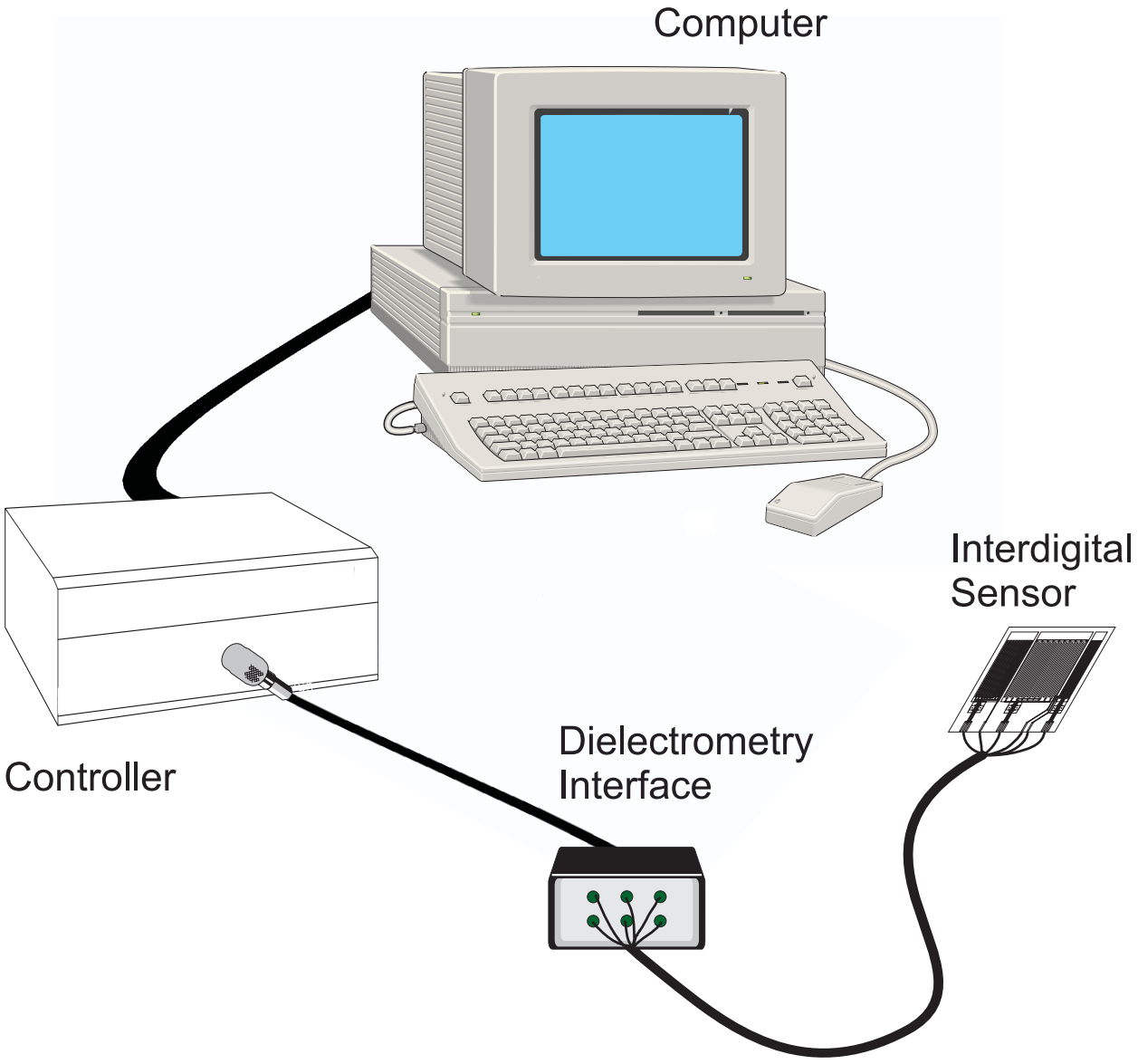

Figure 5.1: General measurement setup using an interdigital sensor.

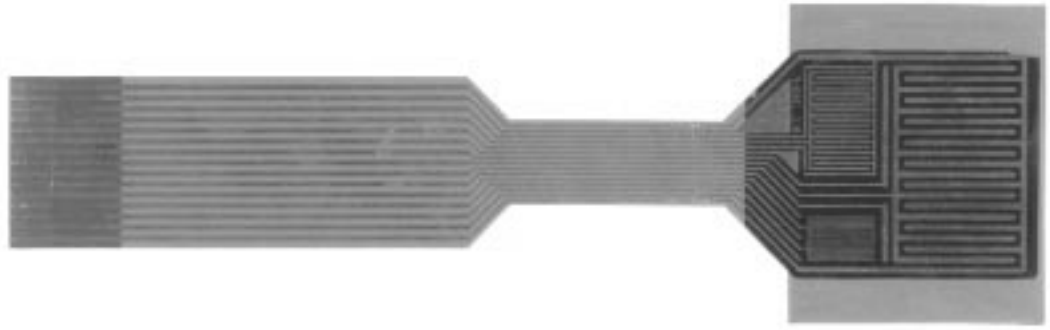

Figure 5.2: Earlier design of the Kapton three-wavelength interdigital sensor.

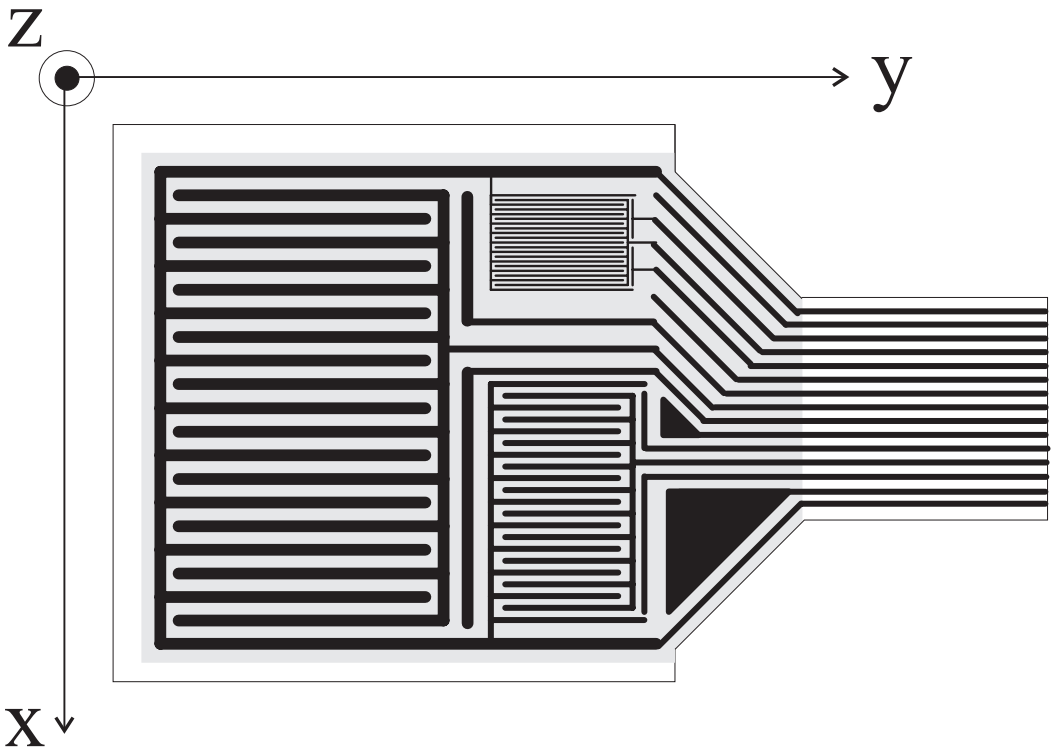

Figure 5.3: Detailed drawing of the Kapton three-wavelength interdigital sensor head (illustration by D. E. Schlicker [89]).

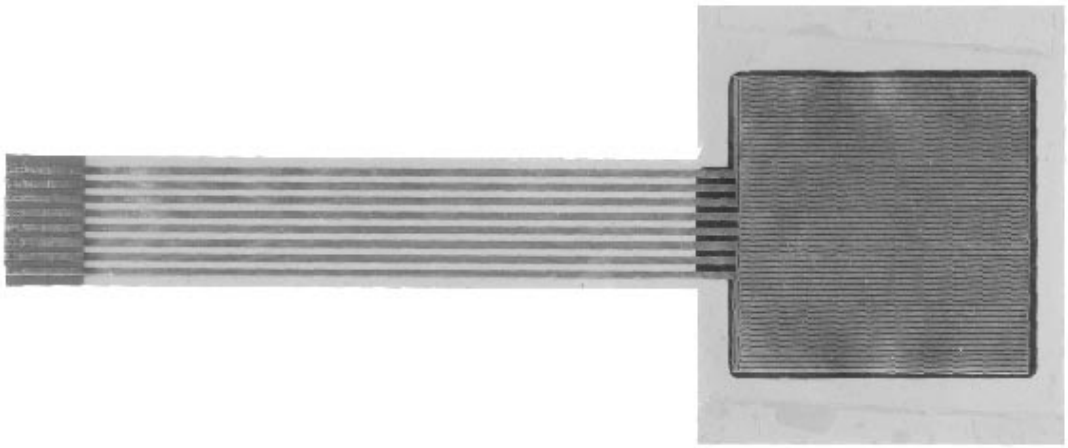

Figure 5.4: The Kapton 1 mm single-wavelength interdigital sensor.

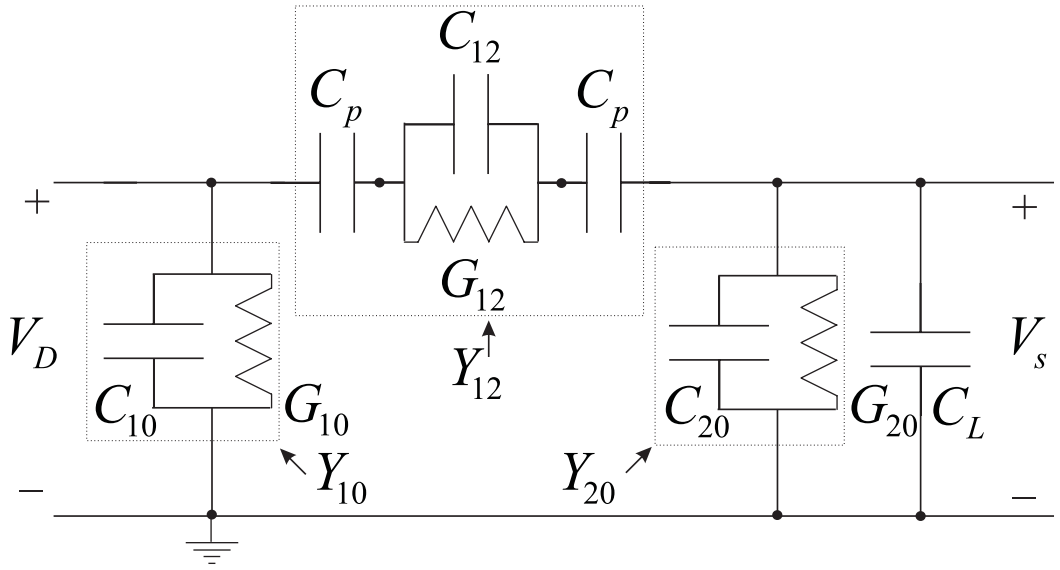

Figure 5.5: The equivalent circuit of the floating-voltage measurement of an interdigital sensor with a parylene coating resulting in capacitances C_P and with known load capacitor C_L.

5.3 Lumped Circuit Model

When the lumped parameter representation of the sensor structure is used, the test response is equivalent to voltage gain G and phase ϕ of the RC circuit shown in Figure 5.5. The complex voltage measured at the sensing electrodes V_S can be expressed in terms of the driven voltage V_D and radian frequency ω as:

$$\frac{V_S}{V_D} = Ge^{j\phi} = \frac{Y_{12}}{Y_{12} + Y_{20} + j\omega C_L} \tag{5.1}$$

where Y_{12} is the transadmittance between driven and sensing electrodes which primarily reflects the dielectric properties of the test materials, Y_{20} is the admittance between the sensing electrode and ground, and C_L is the known load capacitance of the electronic interface. Admittance Y_{20} is primarily due to substrate properties but has a small contribution from the test material due to fringing fields. Moreover,

$$Y_{12} = \frac{j\omega C_p(G_{12} + j\omega C_{12})}{2G_{12} + j\omega(2C_{12} + C_p)}, \tag{5.2}$$

$$Y_{20} = G_{20} + j\omega C_{20}, \tag{5.3}$$

so the complex gain is expressed in terms of equivalent circuit elements as:

$$Ge^{j\phi} = \frac{G_{12} + j\omega C_{12}}{G_{12} + j\omega C_{12} + (G_{20} + j\omega(C_{20} + C_L))\,(2G_{12} + j\omega(2C_{12} + C_p))\,/(j\omega C_p)}. \quad (5.4)$$

In most cases, G_{20} is very small because the substrate is highly insulating and thus purely capacitive and only a negligible conduction current flows through the testing material and terminates at the ground electrode. We thus neglect G_{20} for simplicity of illustration of the sensor response here. The inversion computer algorithm can account for finite G_{20} if necessary. Setting $G_{20} = 0$, (5.4) reduces to

$$Ge^{j\phi} = \frac{G_{12} + j\omega C_{12}}{G_{12}(1 + 2a) + j\omega(C_{12}(1 + 2a) + aC_p)}, \quad (5.5)$$

where $a = (C_{20} + C_L)/C_p$ and is almost a constant approximately independent of test material properties except for fringing field effects. When the test material is highly insulating or the frequency ω is high, the circuit is essentially a capacitive voltage divider and (5.5) simplifies to

$$Ge^{j\phi} = \frac{C_{12}}{C_{12}(1 + 2a) + aC_p}, \quad (5.6)$$

which means a constant gain and zero phase over all frequency. In fact that is the way we test if a sensor is clean by measuring its response in air. A typical measurement in air is shown in Figure 5.6. A contaminated sensor would have significant phase at low frequency.

In general, at high frequency, $\omega C_{12} >> G_{12}$, the capacitive properties of the medium dominates and the response looks like that of air, i.e. gain is a constant and phase is zero; at low enough frequency, $G_{12} >> \omega C_{12}$, the medium behaves like a short circuit between the parylene coatings and again the gain is a constant and phase is zero. In between the gain increases and the phase goes through a valley and back to zero at low frequency. A simulation of typical response that goes through the transition is shown in Figure 5.7. When the medium is more insulating the characteristic curve shifts to the left; when the medium is more conducting, the curve shifts to the right.

The dielectric spectrum of Shell Diala A oil is measured using the interdigital sensor and the sensor response is converted to the dielectric properties shown in Figure

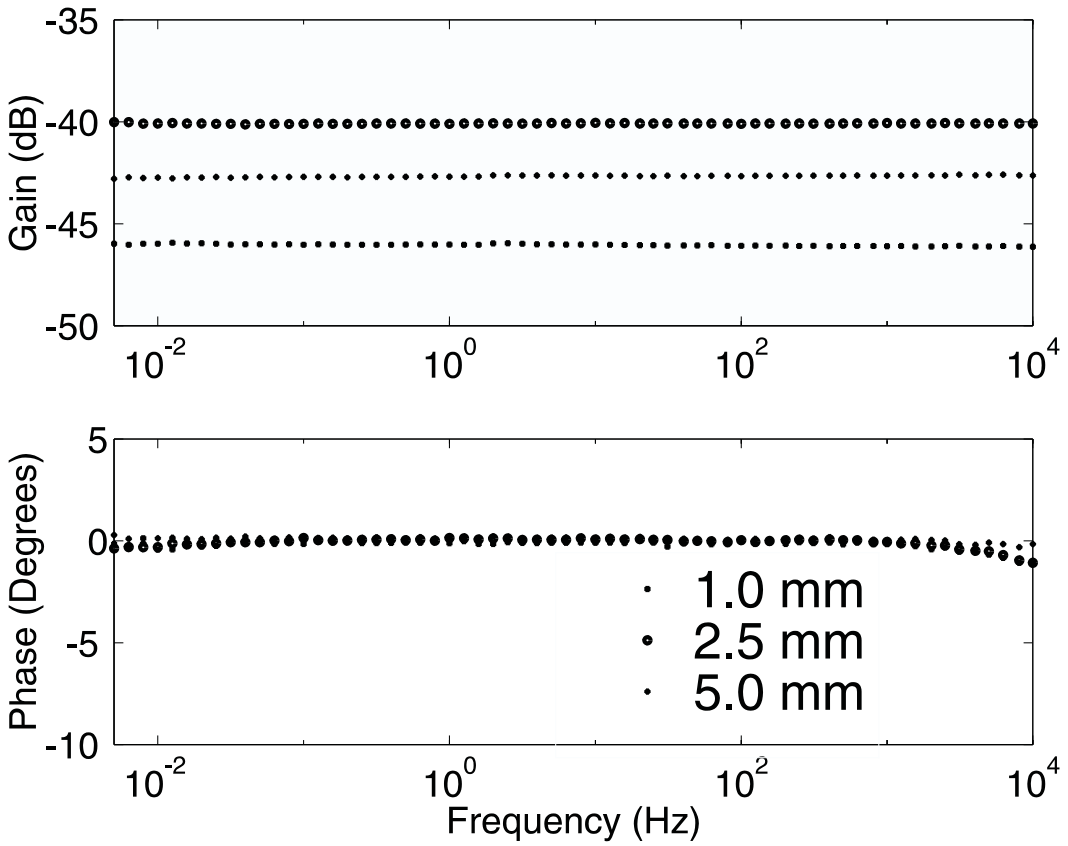

Figure 5.6: Gain and phase measurement in air showing flat gain curves with near zero phase using a clean Kapton three-wavelength interdigital sensor like that in Figure 5.2.

5.8 using the continuum model algorithm developed by previous students [2, 90, 91]. The literature reported relative dielectric constant of oil is 2.2, consistent with the estimated value. Oil is a non-dispersive material, i.e. the conductivity does not change with frequency. Since

$$\log(\varepsilon''/\varepsilon_0) = \log(\frac{\sigma}{\omega\varepsilon_0}) = \log(\sigma/\varepsilon_0) - \log(\omega), \tag{5.7}$$

for frequency independent conductivity, the curve of $\log(\varepsilon''/\varepsilon_0)$ versus $\log(\omega)$ is a straight line with a slope of -1. The curve fitted to the data by linear regression has good agreement with this.

As was shown in Chapter 2, a continuum model of an interdigital sensor provides a closed-form solution for a set of idealized interdigitated electrodes (an infinite array of infinitely long microstrip conductors of zero thickness). An algorithm first written by

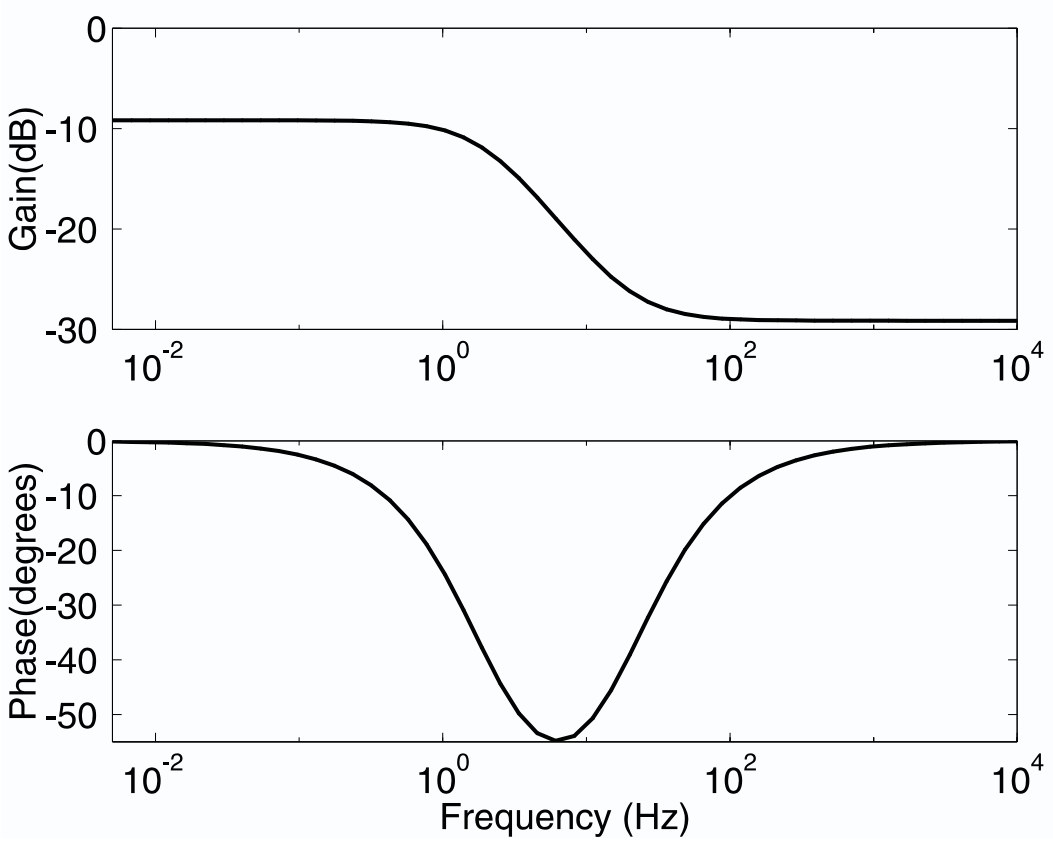

Figure 5.7: Simulated response for the sensor circuitry with $C_p = 110pF$, $C_L = 3pF$, $C_{12} = 4pF$, $G_{12} = 500pS$, and $C_{20} = 100pF$.

Zaretsky [1] and modified by von Guggenberg [2] and Sheiretov [3] has implemented the continuum model. Lesieutre of MIT has written a code based on the continuum model that takes into account the finite thickness of the sensor electrodes [92,93]. A 2D finite-element model using computer software such as Ansoft Maxwell allows assumption of finite thickness of the electrodes as in Figure 5.9, allowing for numerical calculation of electric and magnetic fields and associated physical properties.

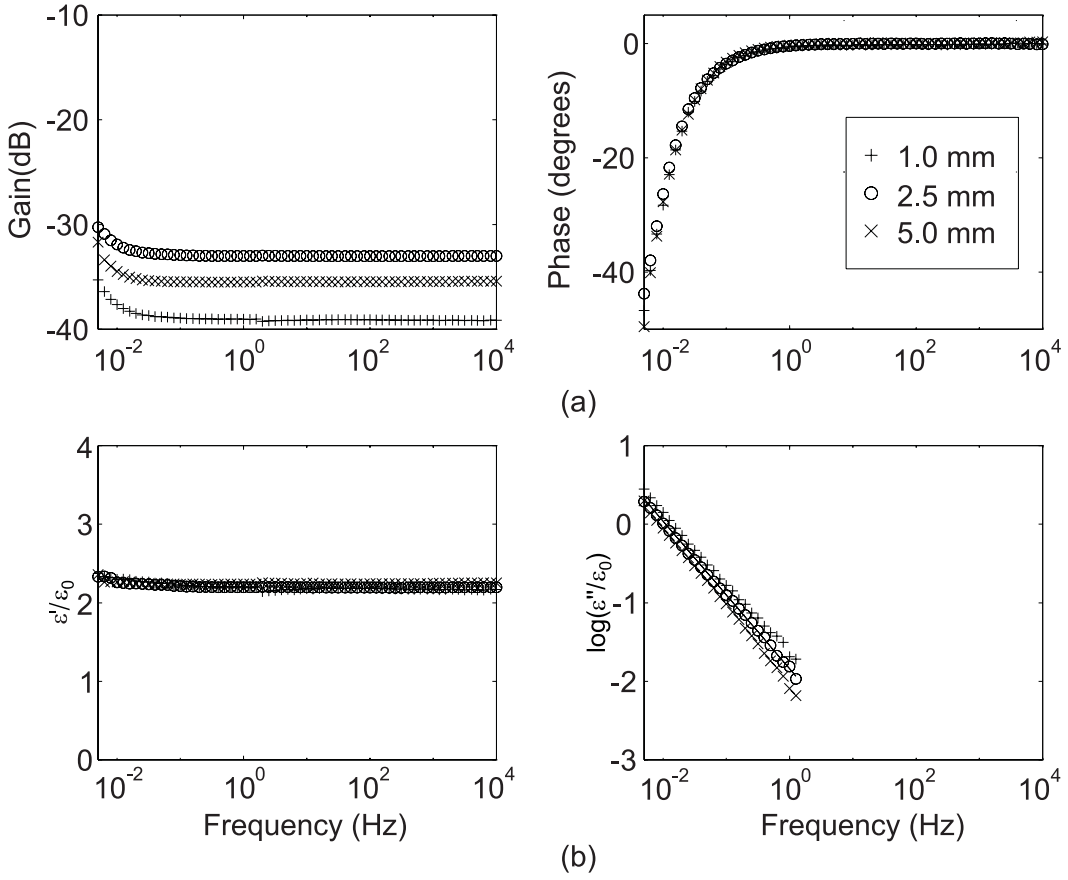

Figure 5.8: (a) Measured sensor response in Shell Diala A oil at room temperature. (b) Estimated dielectric properties of Shell Diala A oil from measurements of (a) using a continuum model algorithm.

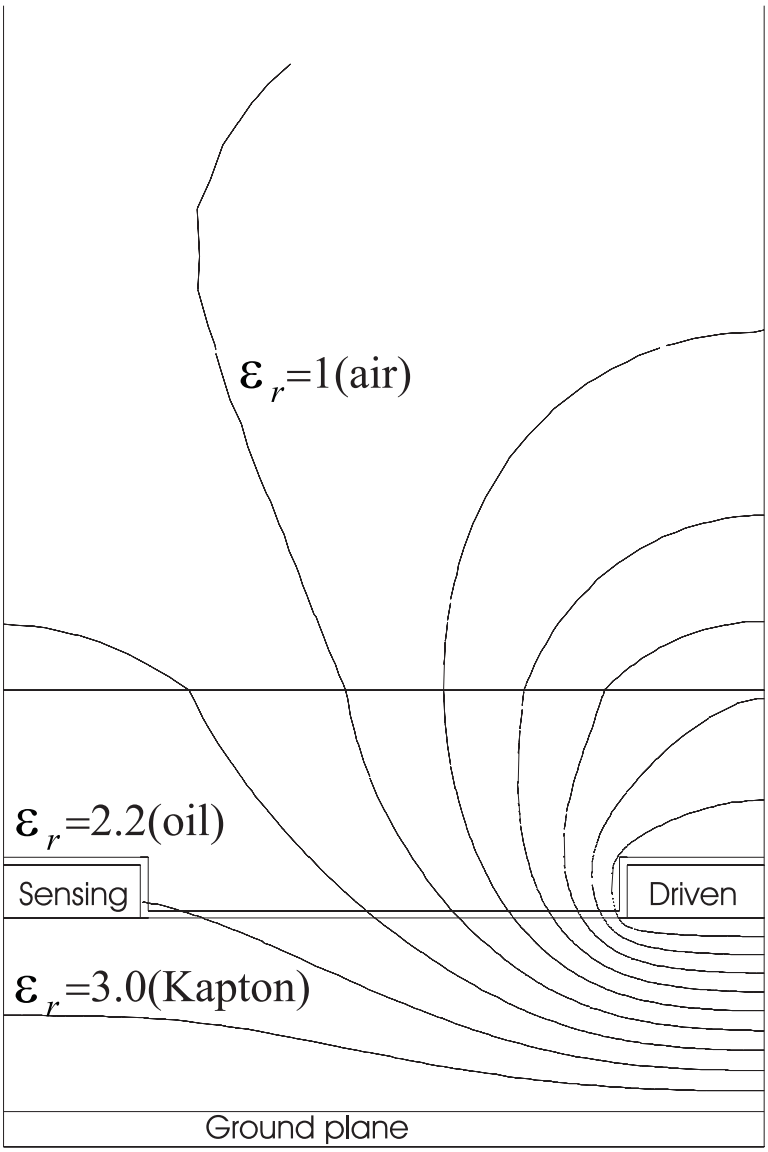

Figure 5.9: Equipotential lines in the half-cell geometry of an 1 mm interdigital sensor with lossless dielectrics using the finite element computer software Ansoft Maxwell. Relative permittivity of parylene coating is ε_r=3.05. The driven electrode (right) is at 1 V peak potential, the sensing electrode (left) is at 0.2 V potential, and the ground plane is at 0 V [94]. The interelectrode spacing a is 0.32λ.

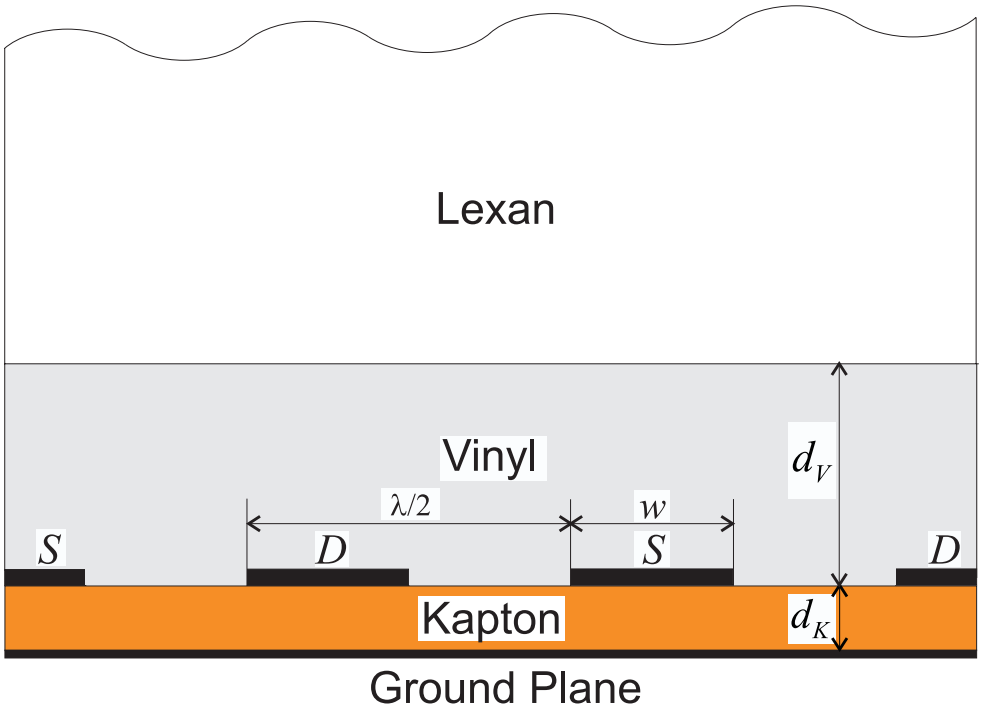

Figure 5.10: The cross-section of the interdigital sensor with two layers of materials above it. The relative permittivities of the polycarbonate Lexan sheet and the vinyl film have been estimated to be 2.6 and 3.8 respectively.

5.4 Experimental Verification of the Penetration Depth

The goal of the series of experiments presented in this section which were conducted jointly with Alexander Mamishev is to actually test the dependence of the sensor response on the thickness of the material above the sensor. Figure 5.10 depicts the cross-section of the experimental setup. Two materials with known properties form a two-layer medium. When the thickness of the lower material is reduced, the interlayer boundary moves down, and the influence of the upper material increases. The upper material is thick enough to be considered infinitely thick.

Two commercially available insulating polymers, monolithic pieces of 1/2 inch thick

Lexan (GE polycarbonate brand name) and 0.19 mm thick thin-filmed samples of vinyl, are used. The thin film enables us to control the thickness of the test sample by changing the number of sheets of vinyl. In order to press the whole structure together and provide a good contact between the materials, a heavy slab of lead was positioned on top of the test cell. In general, a highly conductive metal would strongly affect the distribution of the electric field in the studied region, unless it is sufficiently far from the strong field region. It can be seen from (2.1) that the electric field excited by the sensor dies away exponentially with the vertical coordinate with the penetration depth of $\lambda/2\pi$. Let us denote the distance at which the electric field potential reduces by one order of magnitude as an effective penetration depth of our sensor. The total thickness of Lexan was 17 mm, which is about 10 times the effective penetration depth of 1.8 mm for the 5 mm longest wavelength.

The schematic view of the experimental setup in Figure 5.10 shows one and a half periods of the interdigitated electrodes. The label D refers to the driven electrode and S refers to the sensing electrode. A one volt peak sinusoidal voltage was applied to the driven electrode. The voltage magnitude and phase of the sensing electrode was measured and recorded. As the distance d_v becomes smaller the influence of dielectric properties of the Lexan becomes stronger which is illustrated below.

The dielectric permittivity of the materials had been predetermined using a parallel-plate capacitor of known geometrical dimensions with

$$\varepsilon_a = \frac{\pi C}{L + W + W\ln(\frac{\pi L}{d}) + L\ln(\frac{\pi W}{d}) + \frac{\pi LW}{d}} \tag{5.8}$$

where L and W are the length and width of the parallel-plate capacitor, d is the distance between the plates, and C is its capacitance. Equation (5.8) takes into account the fringing fields of a parallel-plate capacitor and is derived using a Schwarz-Christoffel transformation.

Using (5.8) with guarded parallel plate measurements, the relative dielectric permittivities of the polycarbonate Lexan sheet and the vinyl film have been estimated to be 2.6 and 3.8 respectively. The conductivity of Lexan is on the order of 10^{-15} S/m and

in our frequency range its effect is negligible. The conductivity of vinyl is on the order of 10^{-9} S/m, and the vinyl appears to be a dispersive material. Only a qualitative discussion of conductivity effects is given in this section.

As discussed above, according to the idealized model, the effective penetration depth of an interdigital sensor is about one-fifth of the sensor's spatial wavelength λ. In our case, microscope measurements show that the metallization ratio is close to 0.5 for 5 mm and 2.5 mm wavelengths, and is about 0.36 for the 1 mm wavelength as described in Section 5.7. The results of a high frequency scan at 1 kHz are shown in Figure 5.11 for all three wavelengths. A good correspondence with theory can be observed. The 1 mm wavelength measurements do not respond to the changes of the vinyl thickness because in almost all cases the thickness exceeds one-third of 1 mm. The response of the 2.5 mm structure flattens off at about 0.7 mm, and for 5 mm at about 1.2 mm. It should be noted, however, that since distinction must be made between levels of attenuation which differ only by 1 or 2 dB, the sensitivity to the error in such measurements is relatively high. Of course, if the difference between the values of the dielectric permittivity of the two materials was larger, the effect of the movement of the interlayer boundary would have been more observable.

As seen from Figure 5.11, given the geometrical dimensions of this setup, the measurements with the 5 mm wavelength are the most descriptive in terms of sensitivity of the sensor to the position of the interlayer boundary. The results of the frequency scans for setups with varying thickness are shown in Figure 5.12 and Figure 5.13.

At high frequencies, the gain is approximately equal to the ratio of the capacitances in (5.6). Since the dielectric permittivity of vinyl is higher than that of Lexan, the equivalent capacitance measured by the sensor becomes smaller as the distance d_v decreases. Thus, the gain shifts towards the flat gain of the non-conductive Lexan-insulated interdigital capacitor. As the frequency is lowered, the slightly conductive vinyl makes the test cell behave like a first order system with one pole and one zero in the transfer function. It has a minimum in the phase-frequency curve whose position is determined by the location of the pole and zero (see Figure 5.13). It should be noted

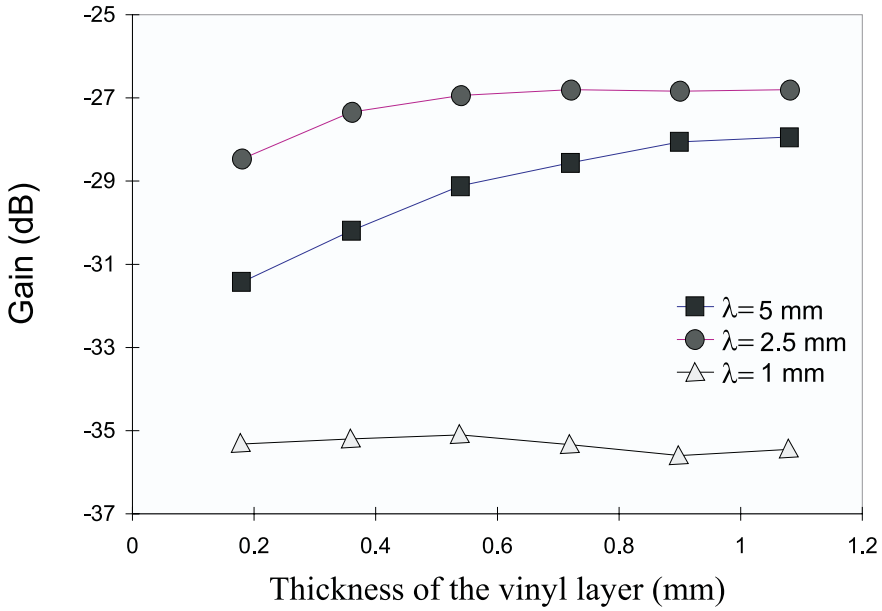

Figure 5.11: High frequency ($f = 1$ kHz) experimental estimation of the effective penetration depth of a three-wavelength sensor by varying the thickness of the vinyl layer adjacent to the sensor of Figure 5.10 [9].

that depending on the ratio of interelectrode capacitances and conductances, and the load capacitance, the phase minimum may shift either to the left or to the right, since the conductivity of Lexan is lower, and the dielectric permittivity is lower than that of vinyl.

The data shown in Figure 5.11 have a very small negative phase-shift but is not considered, primarily because it does not affect the overall estimation of the effective penetration depth. In the plots shown in Figure 5.14, the gain, measured at the frequency of 10 kHz (the right-most data points in Figure 5.12, curve 1), is compared with the gain calculated with a finite-element electric and magnetic field calculation package Ansoft Maxwell (curve 2). The irregularity of the shape of the experimental curve 1 is mostly due to the A/D conversion limitations at 10 kHz. The highest frequency of the sweep had been used to reduce effects of the vinyl conductivity on the output data.

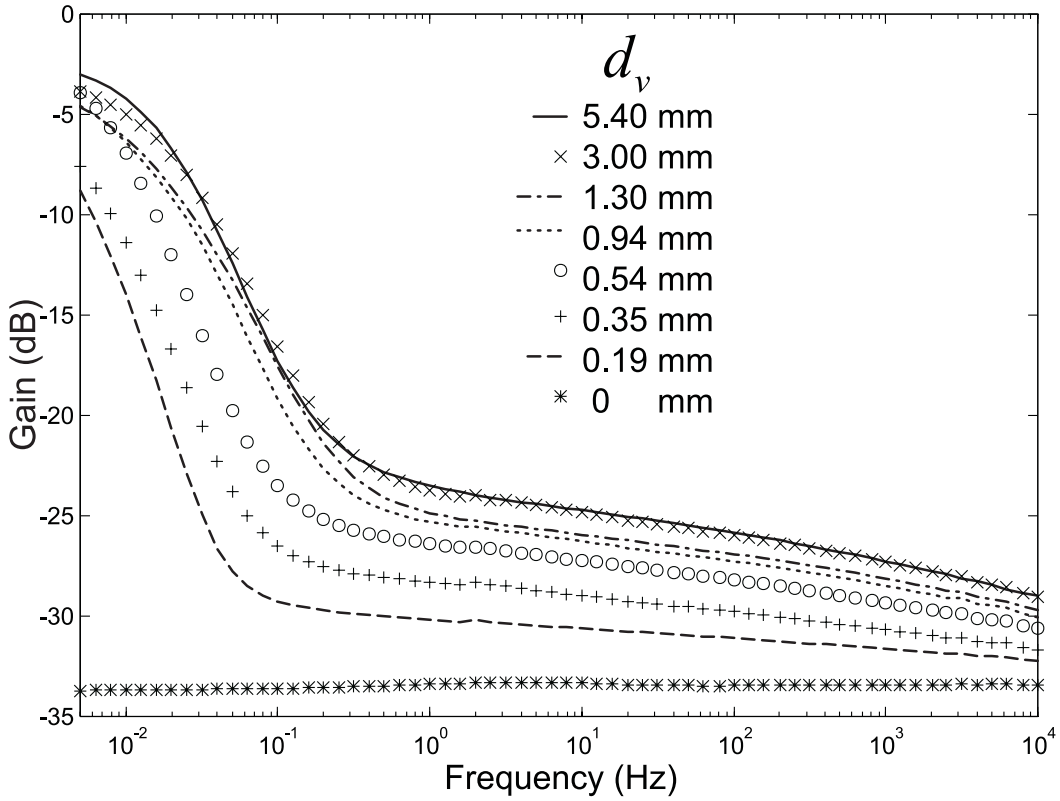

Figure 5.12: Measured response of the 5 mm wavelength sensor's gain to the movement of the interlayer boundary, d_v, in Figure 5.10.

5.5 Moisture Dynamics Experiments

5.5.1 Oil-Free Pressboard

Tests were performed using 3-mm thick oil-free Hi-Val pressboard at room temperature under vacuum so that the moisture diffused out of the pressboard. Before vacuum, a full frequency scan was taken under equilibrium at 13% relative humidity. Then the chamber was vacuumed down to 2 torr at room temperature and kept at this level for all measurements shown in Figure 5.15. As the moisture leaves the pressboard, it becomes more insulating and the frequency spectrum shifts to the left.

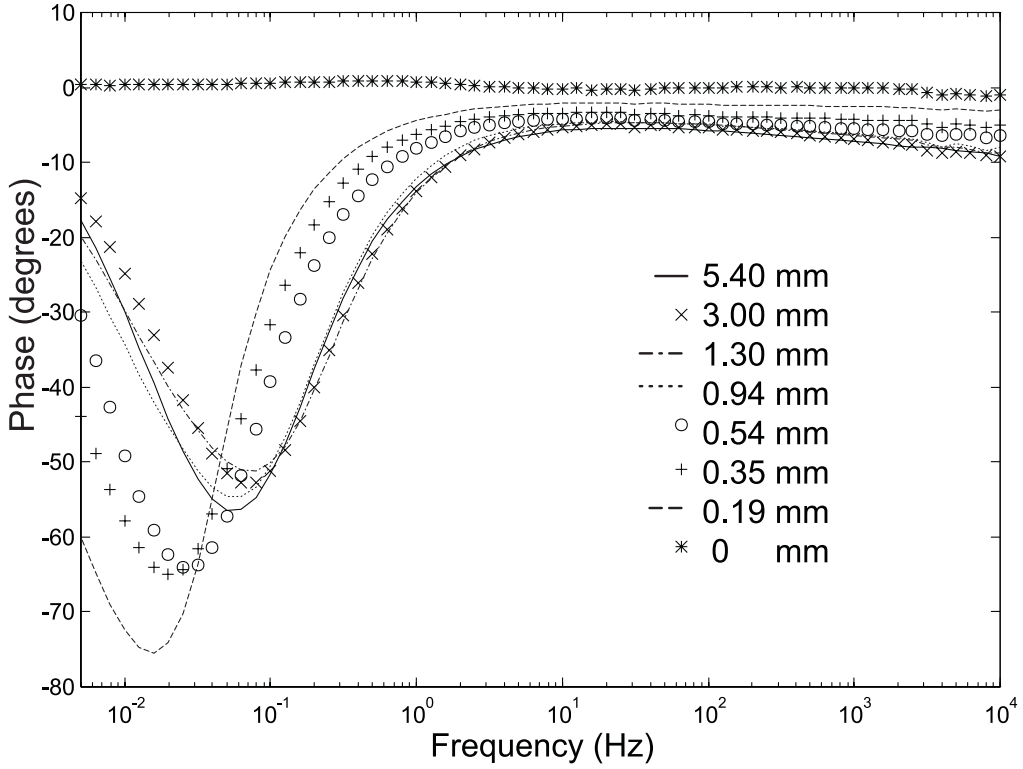

Figure 5.13: Response of the 5 mm wavelength sensor's phase to the movement of the interlayer boundary, d_v, in Figure 5.10.

5.5.2 Oil-Impregnated Pressboard

To simulate the commercial impregnation procedure for transformers, two pieces of oil-free Hi-Val pressboard (2 mm thick) were dried under vacuum for 24 hours and were impregnated with Shell Diala A oil at 70°C. A full frequency scan (0.005 to 10,000 Hz) was measured under equilibrium in ambient air at 70°C. Using the parameter estimation program for homogeneous materials with the continuum model that relates measured gain and phase to complex permittivity, we obtain the dielectric spectra in Figure 5.16. The three wavelengths approximately give the same complex permittivity values indicating that the moisture distribution is essentially uniform throughout the pressboard. The relative permittivity at high frequency is about 3.8 which is consistent with manufacturer's specifications [81]. The difference of ε' at low frequency may be

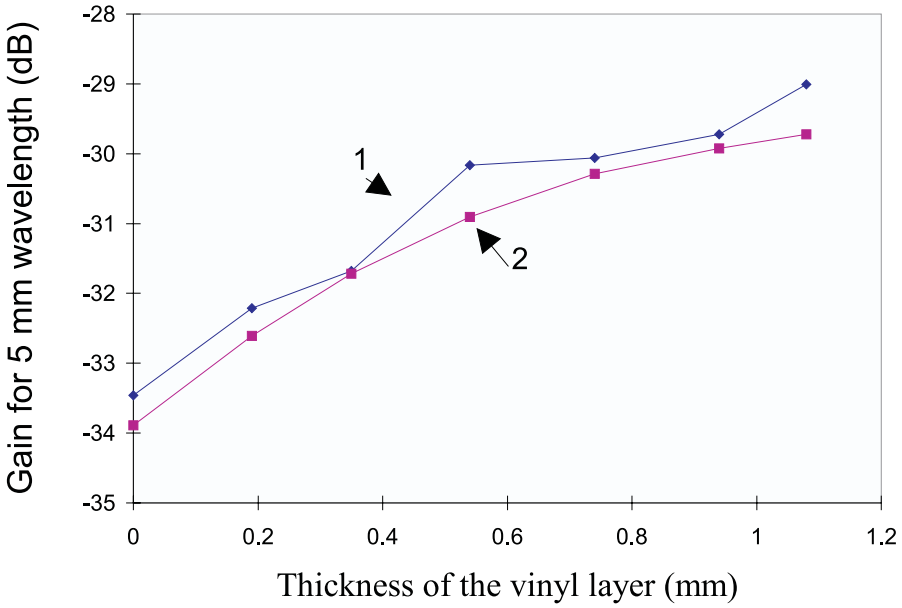

Figure 5.14: Comparison of the measured (1) and theoretical ($\varepsilon_r = 2.6$ for Lexan and $\varepsilon_r = 3.8$ for vinyl) (2) response of the interdigital sensor ($\lambda = 5$ mm) at 10 kHz.

due to the presence of the electrical double layer. By linear regression, the slope of the ε'' curve is -0.7, indicating that it is dispersive , i.e., the conductivity changes with frequency. This verifies the non-ohmic property discussed in [11]. As discussed earlier in section 5.3, a constant conductivity would have a slope of $\log(\varepsilon'')$ versus $\log(f)$ of -1.

More quantitative analysis of the diffusion process is given in the next two chapters.

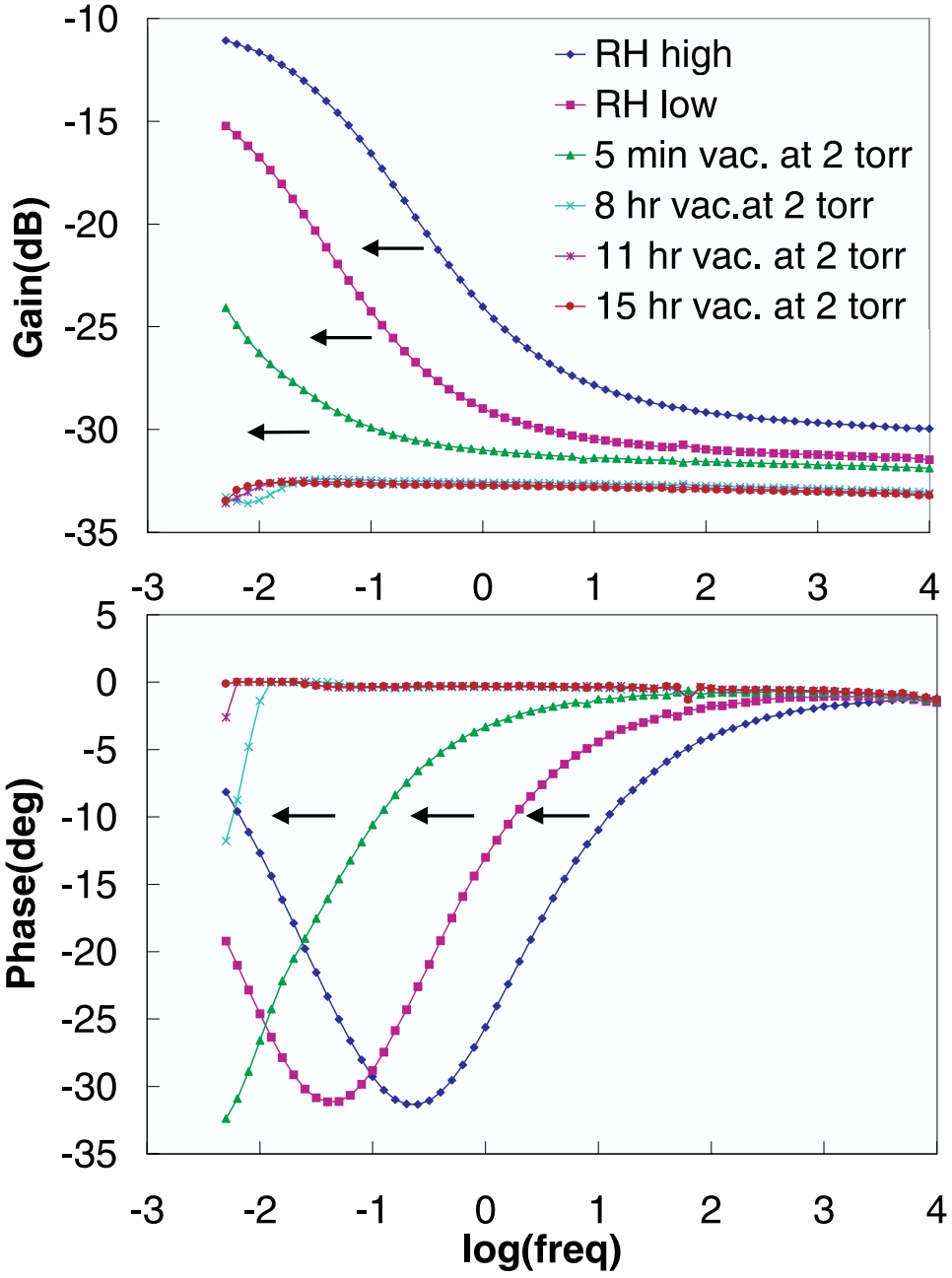

Figure 5.15: The measured response of the 5.0 mm wavelength when the moisture leaves the pressboard due to vacuum. As the moisture is reduced, the pressboard is more insulating and the curves shift to the left.

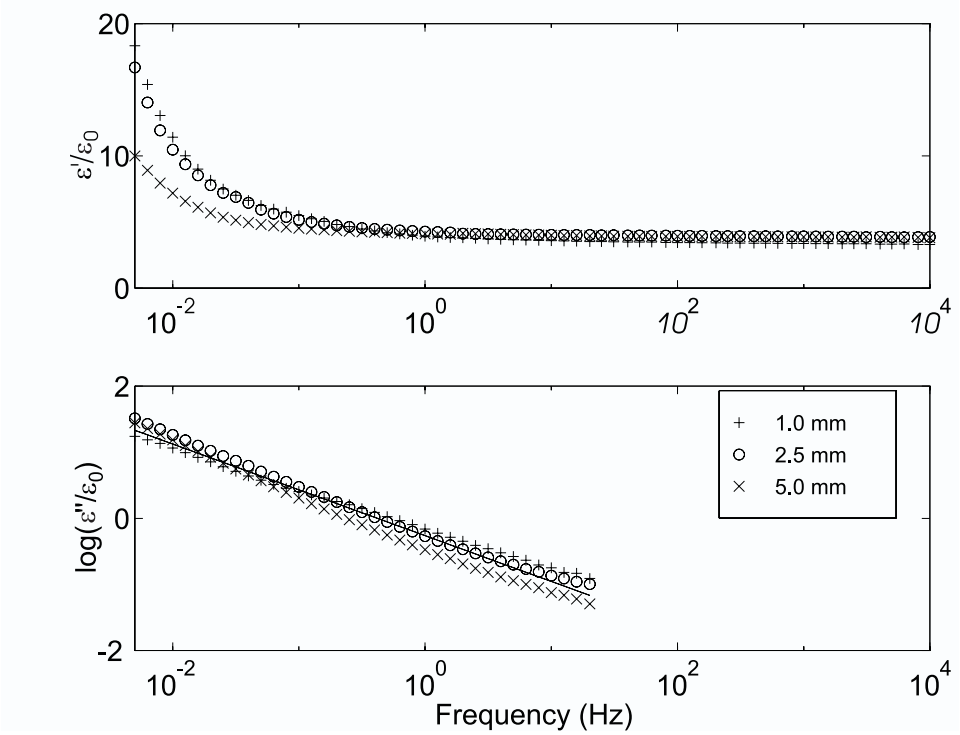

Figure 5.16: Dielectric spectra for 2 mm thick oil-impregnated EHV-Weidmann Hi-Val pressboard at ambient air in equilibrium at 70°C. The slope of $\log \varepsilon''$ *vs.* $\log f$ *is about -0.7 indicating a frequency dispersive conductivity.*

	Oil (pS/m) (1 Hz)	**Pressboard** (pS/m) (1 Hz)
Sample 1, before first injection	4.5	4.3
Sample 1, 17 hours after first 0.6 PPM ASA-3	124	8.9
Sample 2, before second injection	112	22.5
Sample 2, 13 hours after second 0.6 PPM ASA-3	230	23.1

Table 5.1: Comparison of the conductivity of pressboard and oil before and after injection of Anti-Static Additive ASA-3 at 70°C using parallel-plate sensor.

5.6 Antistatic Additive Measurements

Anti-static additives are used to increase the conductivity of insulating materials in order to reduce electrification due to liquid flow or high electrostatic charges on the surface. Shell Anti-Static Additive ASA-3 and 1 mm thick pressboard are used for this investigation.

We inject 0.6 PPM ASA-3 into the oil-pressboard system. It increases the measured conductivity of oil at 70 °C by about 30 times. However, the measurement for oil-impregnated pressboard using either the three-wavelength or single-wavelength sensors shows only a very small change in signal.

To further study this, we repeat the process but measure the pressboard complex permittivity using a parallel plate sensor. Sample 1 is enclosed within a parallel plate sensor and the complex permittivity is measured before and after ASA-3 injection to fresh oil. The additive diffuses through the pressboard edges. A long time is then allowed to ensure that the diffusion process is complete. Sample 2 is thoroughly immersed in the 0.6 PPM ASA-3 oil for three days and is then placed within the parallel plate sensor. Its conductivity is higher than Sample 1 in part due to absorption of moisture. Another 0.6 PPM ASA-3 is injected, and the conductivity of Sample 2 increases very little after 13 hours. The results are shown in Table 5.1. The change of conductivity of the oil-impregnated pressboard is far less than that of oil.

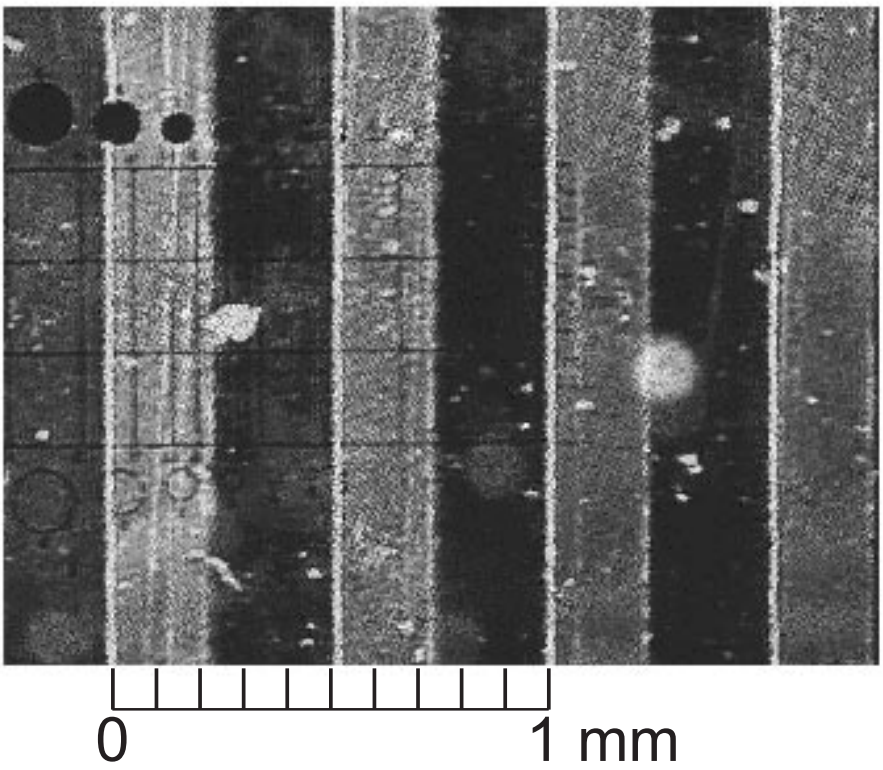

Figure 5.17: Microscope picture of the 1 mm wavelength electrodes of a three-wavelength Kapton sensor. The spacing between the drive and sense electrodes is about $a = 0.30\lambda$.

5.7 Non-idealness of the Sensor

Early simulations of the continuum model compared to measured sensor responses showed large discrepancies that cannot be explained by the finite thickness of the electrodes and measurement errors. It was discovered by this thesis work that this is mainly caused by the difference between the electrodes' spacing a in the theoretical model and in the real sensor. The sensor is designed to have a quarter of the wavelength spacing between drive and sensing electrodes, but microscope measurements reveal the non-idealness of the manufactured accuracy. Shown in Figure 5.17, the spacing between the two electrodes is about 0.30λ rather than the intended 0.25λ.

Measurement results for Sensor #16 to Sensor #20 are given in Table 5.2 to show

Wavelength	$\lambda = 1mm$	$\lambda = 2.5mm$	$\lambda = 5mm$
Sensor #16	0.3214	0.2750	0.2616
Sensor #17	0.3062	0.2723	0.2597
Sensor #18	0.3156	0.2748	0.2611
Sensor #19	0.3142	0.2735	0.2607
Sensor #20	0.3189	0.2760	0.2609
Average	0.3153	0.2743	0.2608
Standard Deviation	0.0058	0.0014	0.0007

Table 5.2: Measured interelectrode spacing ratio (a/λ) for five Kapton sensors. The designed value is a/λ=0.25.

the variations from sensor to sensor. Therefore it is important to measure each individual sensor or calibrate with known dielectrics, typically air, before estimating the material properties from sensor output. The most severe deviations from the designed 0.25λ spacing occur for the 1 mm wavelength.

5.8 Summary

The measurement technique using interdigital dielectrometry sensor and early design of the three-wavelength sensor are presented in this chapter. Representative measurements with the early design sensor for oil, oil-free pressboard, and oil-impregnated pressboard are discussed. The multi-wavelength interdigital sensor is capable of monitoring the moisture diffusion process in pressboard.

The ASA-3 additive does not easily diffuse into the pressboard, and thus the dielectric properties of oil-impregnated pressboard do not change significantly. Further study is needed to reach quantitative conclusions.

Chapter 6

Measurements of Pressboard Using Improved Sensor

6.1 New Sensor Design

The idealized model, which allows a closed form expression for the sensor's electric field, requires that the electrodes be an infinitely long and wide array of infinitely thin microstrips placed on the surface of the insulating substrate. The thickness of the electrodes (35 μm for the earlier design of Figure 5.2), the finite length (25 mm) and finite number of fingers (10 for each wavelength), the capacitance of the leads of the electrodes to ground and to each other, and the variations of metallization ratio (described as ratio of the area covered with copper to the total area of the sensor, designed to be 50%) are the most important contributors to the discrepancies between the theoretical model and real measurement data.

Experiments and analysis performed over the past few years led to development of an improved design of a three-wavelength sensor. The sensor shown in Figure 6.1 is free of some of the problems associated with the previous design. In particular, employment of a separate guard plane for each wavelength, minimization of cross-coupling between the leads and the sets of interdigital electrodes themselves, significant reduction of end effects and parasitic capacitances, and change of insulating substrate from hydrophilic

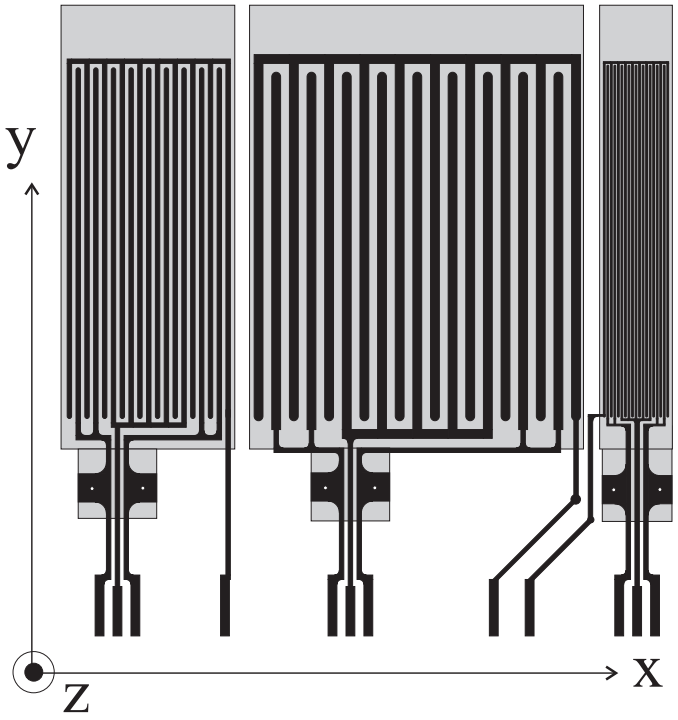

Figure 6.1: The improved design of the Teflon three-wavelength sensor [95].

Kapton to hydrophobic Teflon are the most important features of this improved design.

6.2 New Interface Box

As discussed in Chapter 5, the previous Kapton sensor design measures the induced voltage on the capacitively loaded sensing electrodes. We call this a floating voltage measurement. Similarly, the sensing electrodes can also be virtually grounded by external circuitry and the current that flows into the sensing electrodes can be measured. This is called a short-circuit measurement. A new interface box was designed and built for short-circuit measurements as shown in Figure 6.2. Graduate student Darrell E. Schlicker of the MIT High Voltage Research Lab is the principal designer of the box. It has the following new features:

- 10-volt driving signal to provide high signal-to-noise ratio;
- allows each wavelength to run individually to avoid cross-coupling;
- uses the short circuit measurement technique which increases the resolution, simplifies the equivalent circuitry, and is more robust to noise.

The equivalent circuitry for short-circuit measurements is shown in Figure 6.3 with sensing voltage virtually grounded so that $V_S = 0$. The measured complex gain for output voltage V_O and driving voltage V_D in terms of equivalent circuit elements is:

$$\hat{G} = \frac{V_O}{V_D} = -\frac{G_{12} + j\omega C_{12}}{j\omega C_F} \tag{6.1}$$

where V_O is the output voltage of the op-amp, V_D is the driving voltage applied at the sensor electrodes, G_{12} is the transconductance and C_{12} is the transcapacitance between the sensing and driving electrodes, and C_F is the known feedback capacitor in the interface circuitry. The voltage from the controller box is amplified to 10 volts through an op-amp, therefore V_D has 180 degrees of phase shift to the voltage output from the controller. This cancels the negative sign in (6.1). For purely capacitive materials, the measured gain should have zero phase.

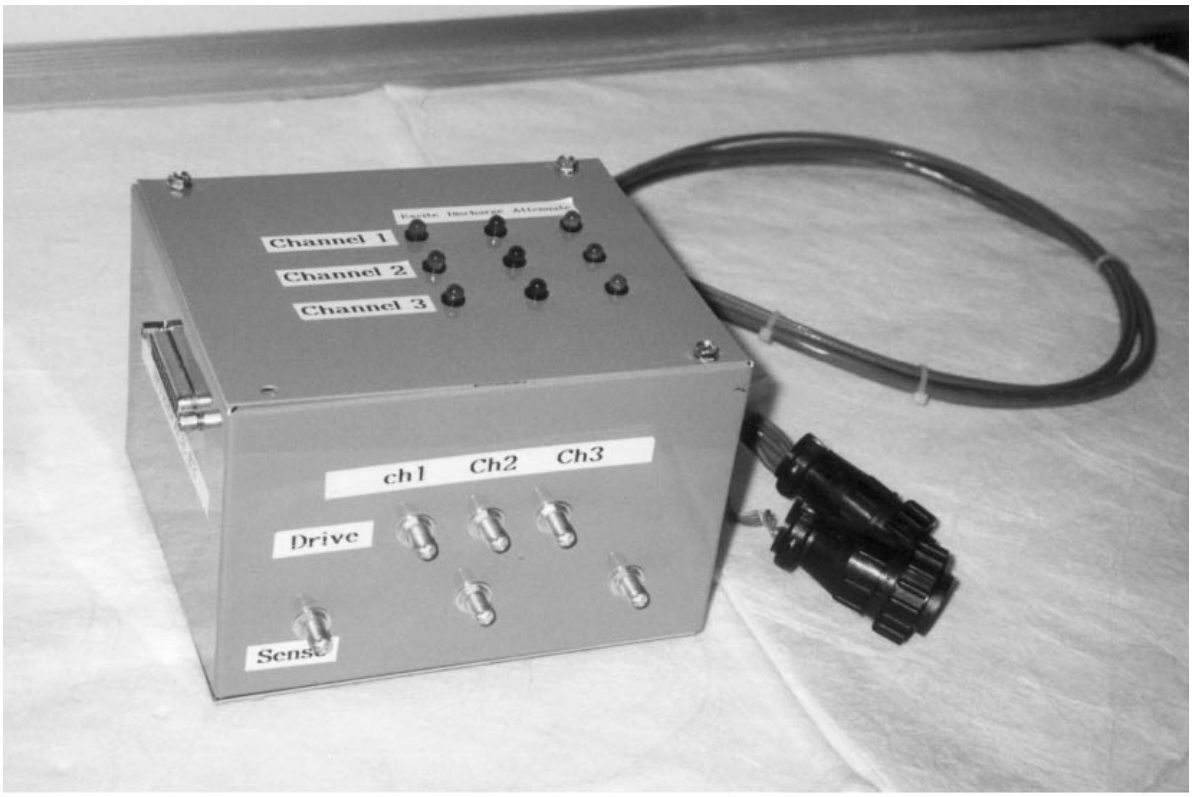

Figure 6.2: The new short-circuit interface box with the cable to the controller box connected at the back.

6.2.1 Feedback Capacitor

The feedback capacitors are chosen according to the external impedance. Since the controller box can only measure a maximum of 5 V in magnitude (about 14 dB), according to (6.1), to avoid saturation especially at low frequencies the capacitors should be large in order to lower the gain. However the capacitors should also be small enough such that at high frequency the measured voltage is above the noise level. Because of the conflicting constraints, the new interface box implemented a new feature: the capability of switching the feedback capacitors. When a higher capacitance is needed to lower the gain, an attenuation signal can be sent from the controller to the interface box to close the relay, connecting another capacitor in parallel to the original feedback capacitor. The effective feedback capacitance is tested by connecting an external known capacitor. One such test is shown in Figure 6.4 with test capacitors

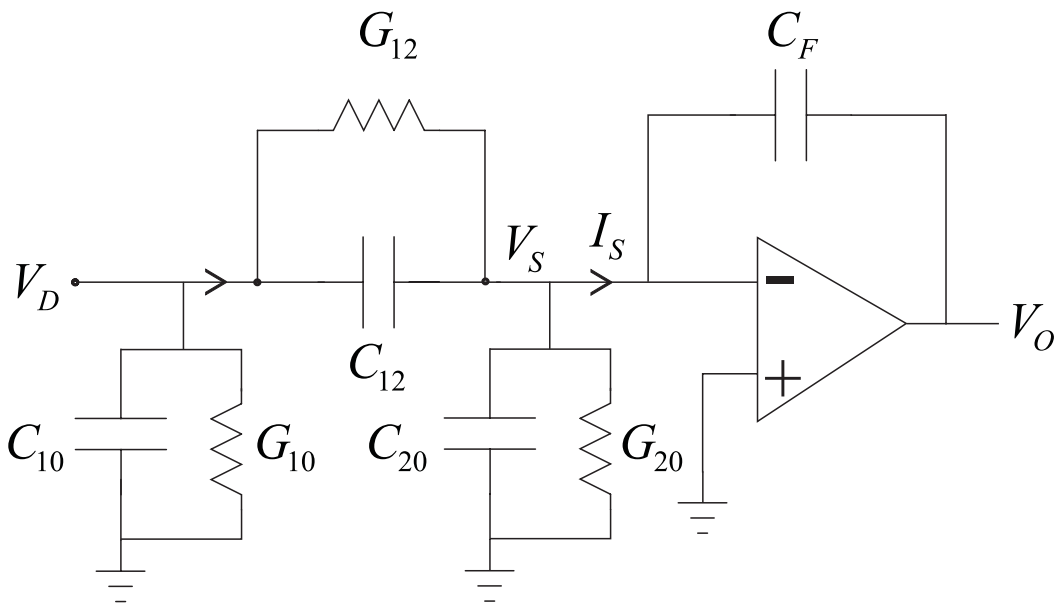

Figure 6.3: Equivalent circuit for short-circuit measurement.

of 80.6 pF, 56.1 pF, and 47.0 pF respectively for the three channels corresponding to 1.0 mm, 2.5 mm, and 5.0 mm wavelengths for the interdigital sensors. The gain is constant and the phase is close to zero. This also serves as a test of the proper functioning of the interface box. Had there been any contamination in the circuit board or leakage current through the op-amp, the gain would not be constant with frequency. The calculated effective feedback capacitances are 1317 pF, 809 pF, and 1370 pF for the three channels.

The new Teflon sensor measurement in air with the new interface box is shown in Figure 6.5 with feedback capacitances of 1317 PF, 809 pF, and 1370 pF respectively for the 1.0 mm, 2.5 mm, and 5.0 mm wavelengths. A comparison of measured data and theoretically predicted data using two different algorithms is shown in Table 6.1. Both theoretical sets of data are obtained for ideal structures with 0.5 metalization ratio whereas the actual sensor metalization ratio might vary. Lesieutre's program takes into account the finite thickness of the electrodes (14 μm) and is therefore close to the measured response. Sheiretov's program assumes zero electrode thickness. The capacitance and relative permittivity for a 1 mm wavelength sensor in air estimated

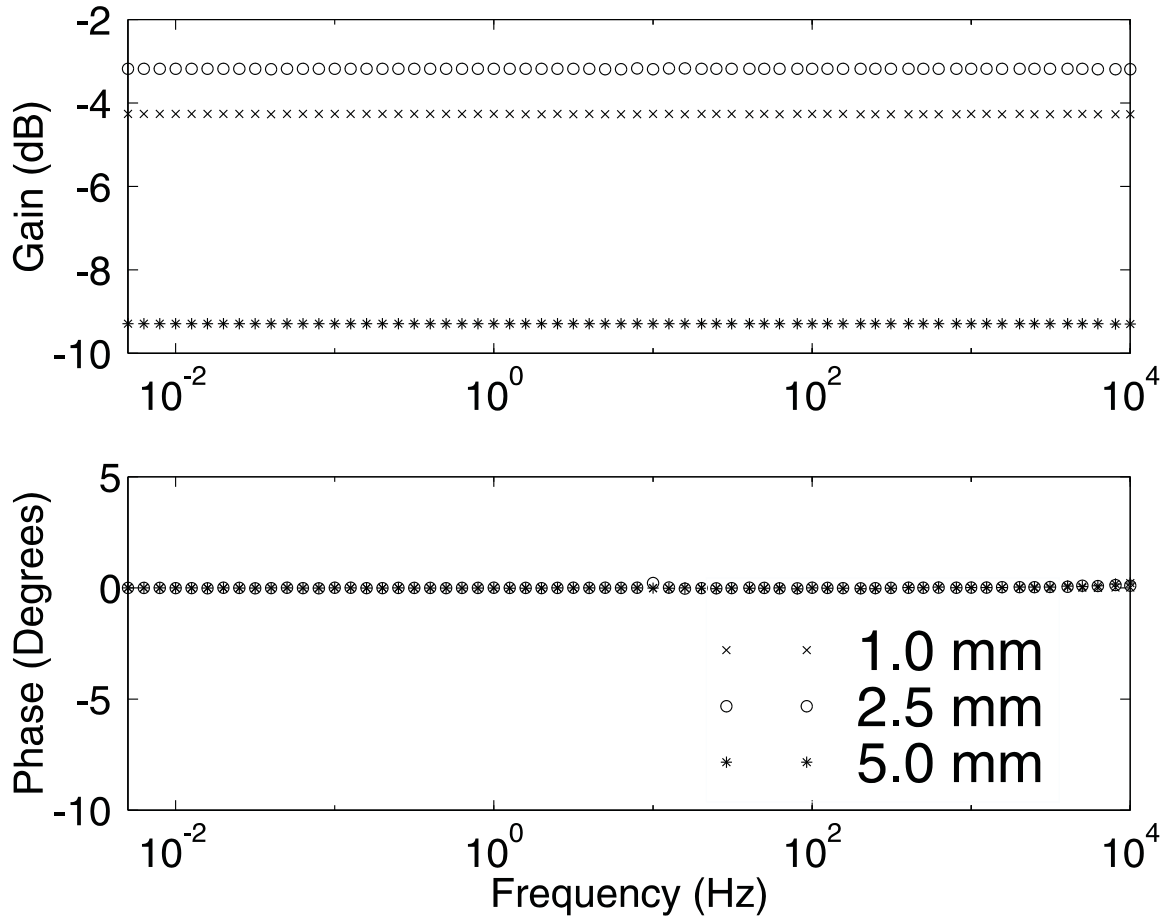

Figure 6.4: Feedback capacitance tests for the new interface box with test capacitance of 80.6 pF, 56.1 pF, and 47.0 pF respectively for the three channels corresponding to 1.0 mm, 2.5 mm, and 5.0 mm wavelengths for the interdigital sensor. The effective feedback capacitances are: 1317 pF, 809 pF, and 1370 pF.

using Lesieutre's program [93] for 0.6 dB variation in the gain measurement are listed in Table 6.2. Error bars due to the deviation are given in the parentheses.

	Experiment	**Lesieutre**	**Sheiretov**
1.0 mm (dB)	-30.89	-31.34	-32.05
2.5 mm (dB)	-33.8	-33.74	-34.49
5.0 mm (dB)	-42.9	-42.58	-43.19

Table 6.1: The measured gain of the Teflon sensor in air and theoretically predicted gain using different programs. Sheiretov's program takes the sensor electrodes to have zero height whereas Lesieutre's program allows finite height electrodes, here taken to be 14 μm.

Gain (dB)	C_{12} (pF)	$\varepsilon/\varepsilon_0$
-31.34	3.57	1
-30.77 (+0.6 dB)	3.81 (+6.7%)	1.1 (+10%)
-31.94 (-0.6 dB)	3.33 (-6.7%)	0.9 (-10%)

Table 6.2: The capacitance and relative permittivity for the 1 mm wavelength sensor in air estimated using Lesieutre's program for 0.6 dB variation on the gain measurement. Error bars due to the deviation are given in parentheses.

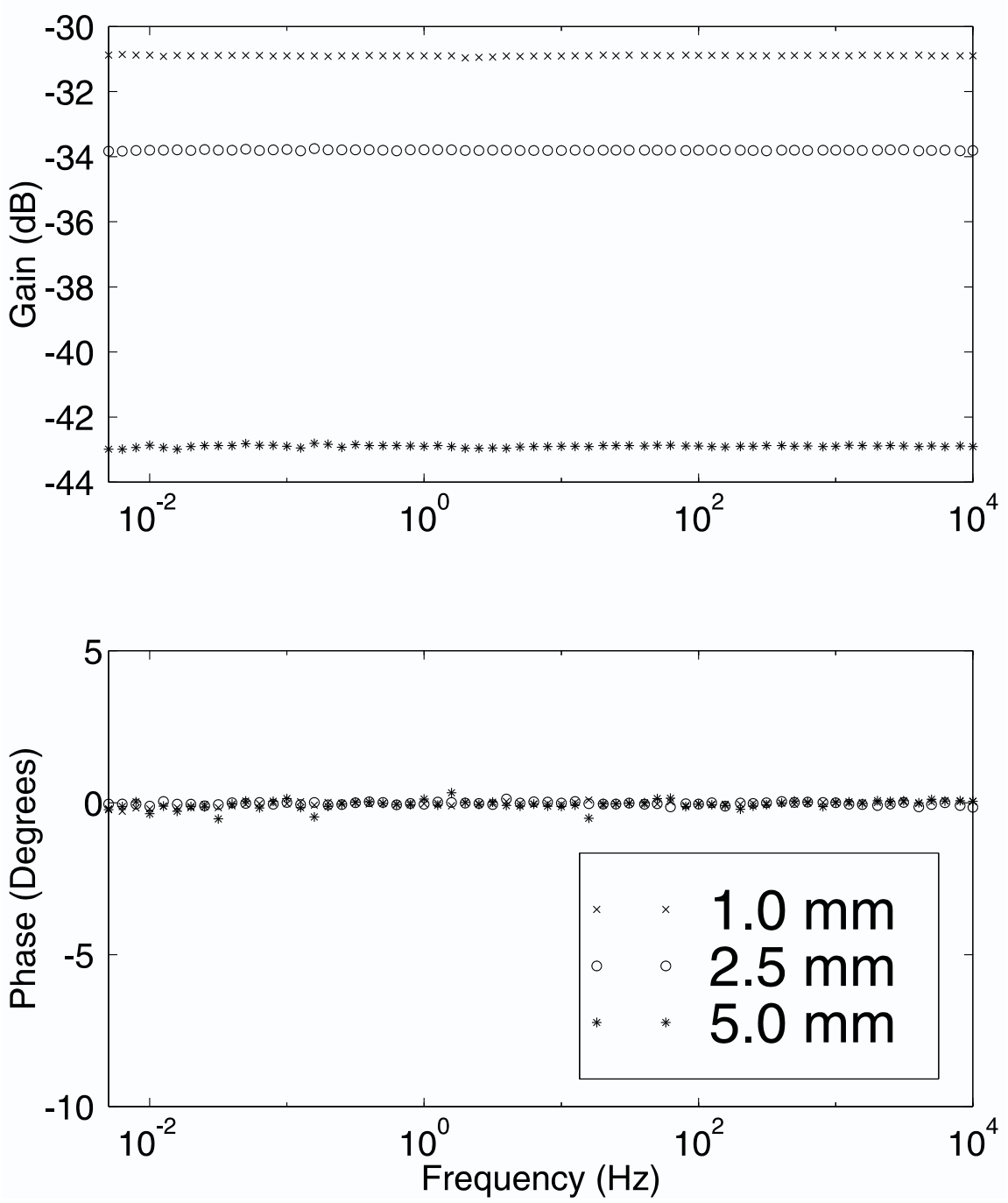

Figure 6.5: The new Teflon sensor measurement in air with new interface box with feedback capacitance of 1317 pF, 809 pF, and 1370 pF respectively for the 1.0 mm, 2.5 mm, and 5.0 mm wavelengths.

6.2.2 Cross-coupling

To illustrate the cross-coupling effects, we compare measurements taken with the three wavelengths driven both simultaneously and individually for oil-free pressboard. The results shown in Figure 6.6 clearly indicate interference from adjacent wavelength signals when all three wavelengths are simultaneously driven. The difference is more significant at low frequencies when conduction dominates. The gain in Figure 6.6 exceeds 0 due to the amplified 10-volt driving voltage, i.e. the measured V_O is greater than the controller box output of one volt.

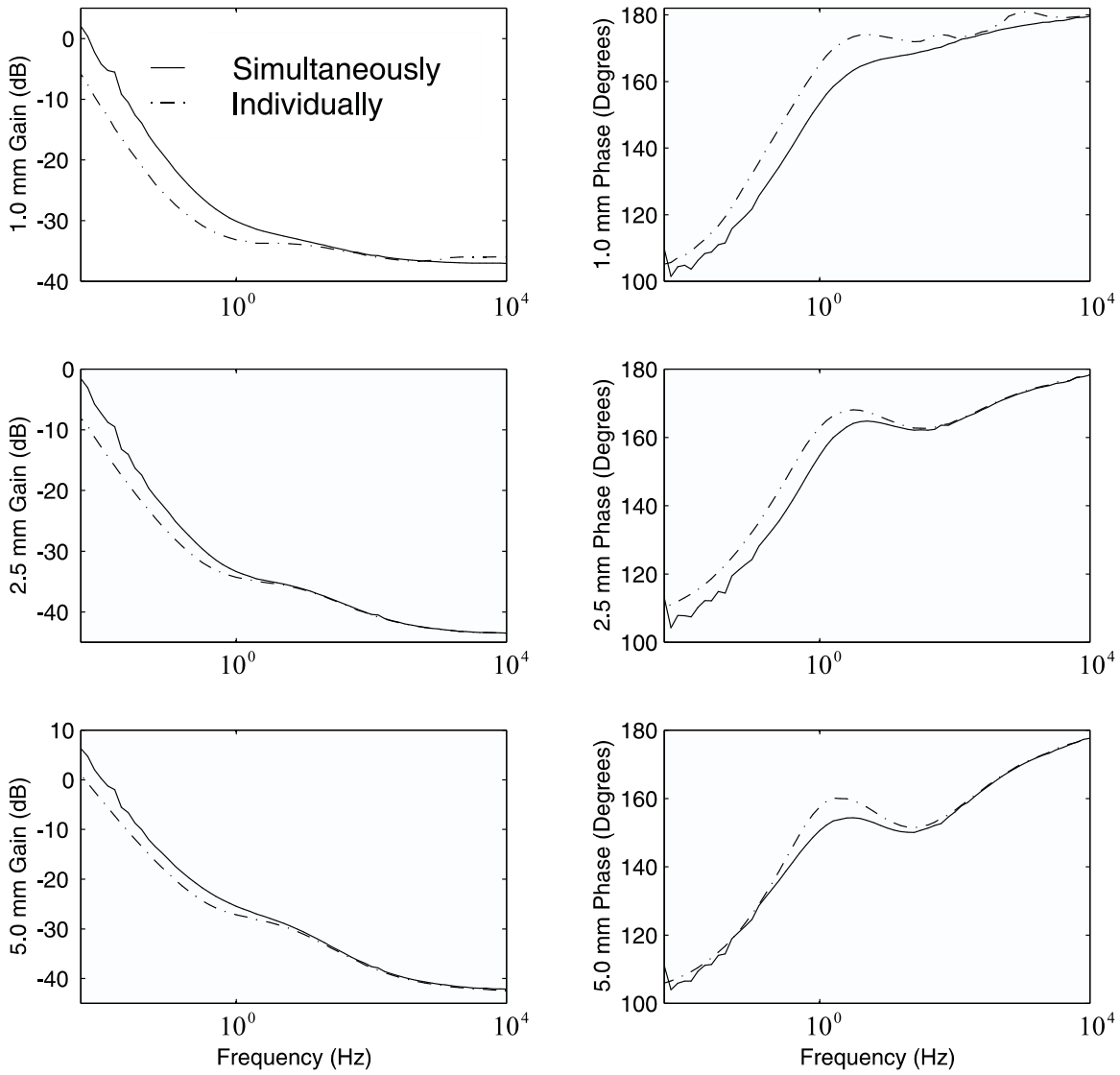

Figure 6.6: The effects of cross-coupling in oil-free pressboard measurements are demonstrated by comparing measurements with all wavelengths simultaneously excited (solid line) or each wavelength individually excited (dash-dotted line) over the frequency range of 0.005-10 kHz.

6.3 Experimental Setup

The experimental system shown in Figure 6.7 was designed and constructed for moisture diffusion measurements using interdigital dielectrometry sensors. It is built inside a stainless steel hood for better shielding, support, and protection. The testing chamber is made of a Varian 8" O.D. stainless steel vacuum nipple. The reservoir is made of a Pyrex 250 mm I.D. dessicator. Both have a volume of about 6500 ml. The larger volume of oil provides better thermal stability and volume measurement accuracy. There are two side-viewing ports for monitoring oil level, moisture bubbling, and sensor structure inside the chamber. Since the top often needs to be taken apart, we want to disconnect as few parts on the top as possible. Thus, the temperature probe and two flow outlets are transferred to the bottom flange, and the vacuum port is combined with the Harley moisture meter and is connected to the top by the Swagelok quick connector. A picture of the real system is shown in Figure 6.8.

The comprehensive plumbing system allows a variety of circulation, transport, and processing of the oil in the reservoir and testing chamber. The temperature, vacuum, and relative humidity of the chamber are well monitored and controlled. A conductivity cell is incorporated to measure the complex permittivity of the oil. This provides more information relating to dielectrometry measurements of pressboard using the interdigital sensor.

The three-wavelength sensor testing structure in Figure 6.9 is inside the chamber and includes two back-to-back interdigital dielectrometry sensors to allow simultaneous measurement of two samples. The porous Teflon and aluminum plates squeeze the whole structure, and at the same time allow maximum mass-transfer between the test samples and the surrounding environment.

The SMA hermetic seal feed-through from Pasternack Enterprises keeps the experiment chamber vacuum and pressure tight while getting the electrical signal to the interface box.

A new fixture for holding the connecting wires from the sensor shown in Figure

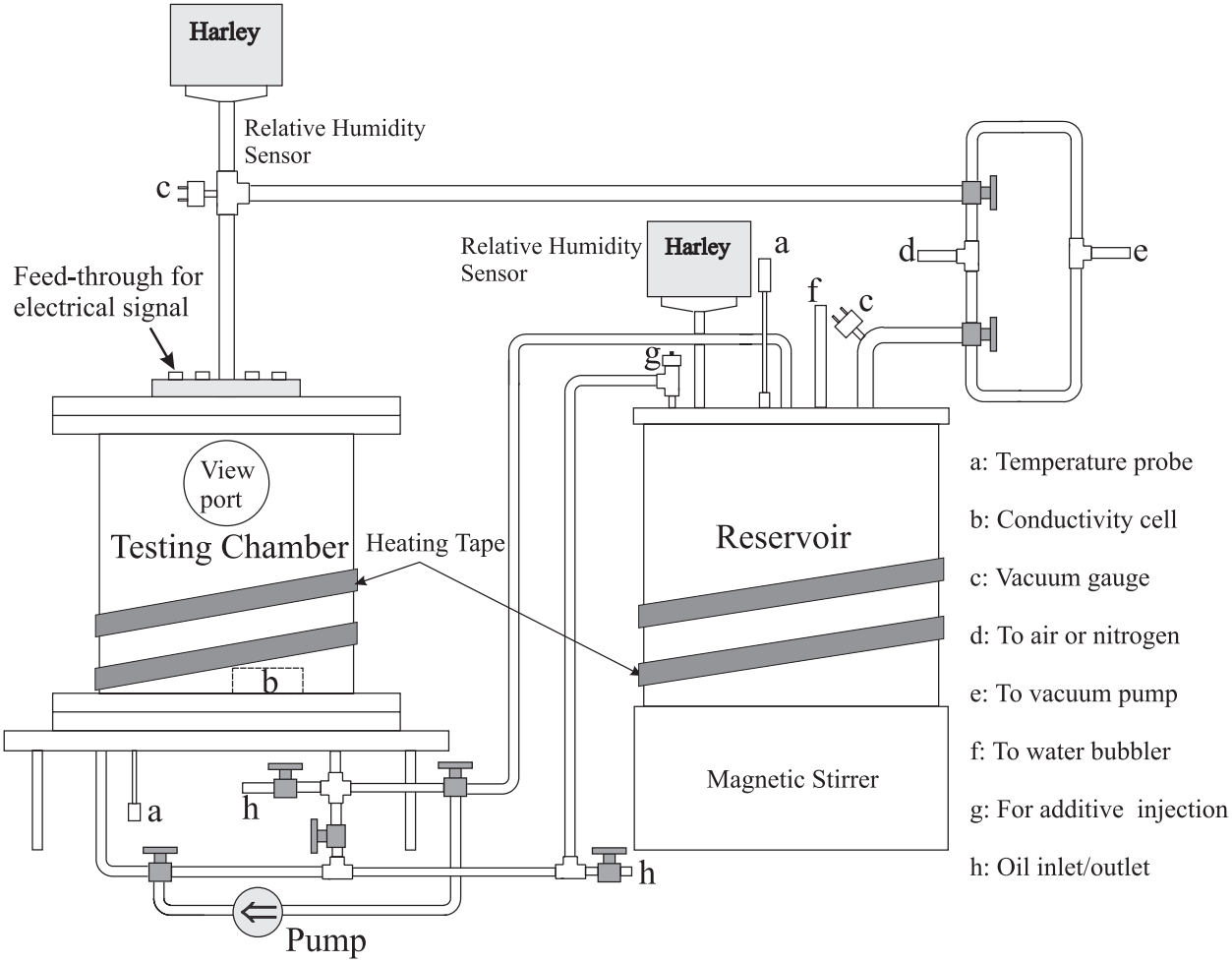

Figure 6.7: Schematic of the bench-top apparatus for moisture and additive diffusion experiments using dielectrometry measurements.

6.10 is designed to allow use of rigid coaxial cables which provide better mechanical stability and signal quality.

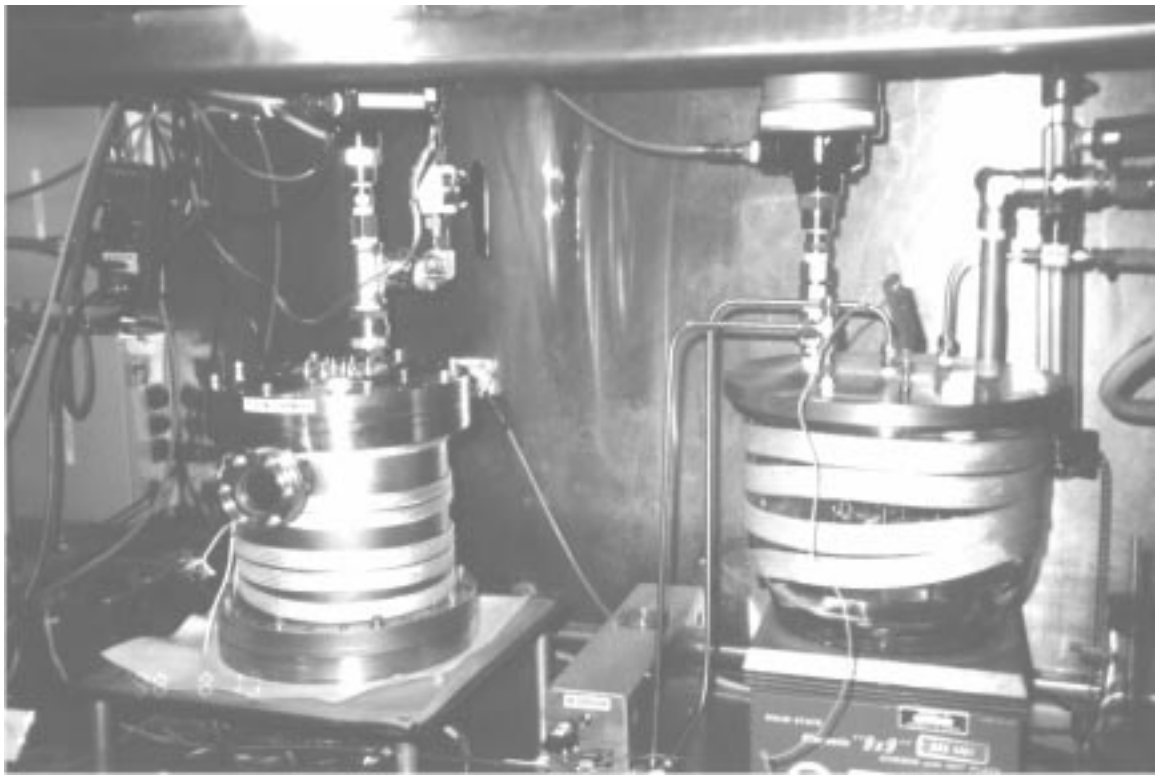

Figure 6.8: The bench-top apparatus for moisture and additive diffusion experiments using dielectrometry measurements.

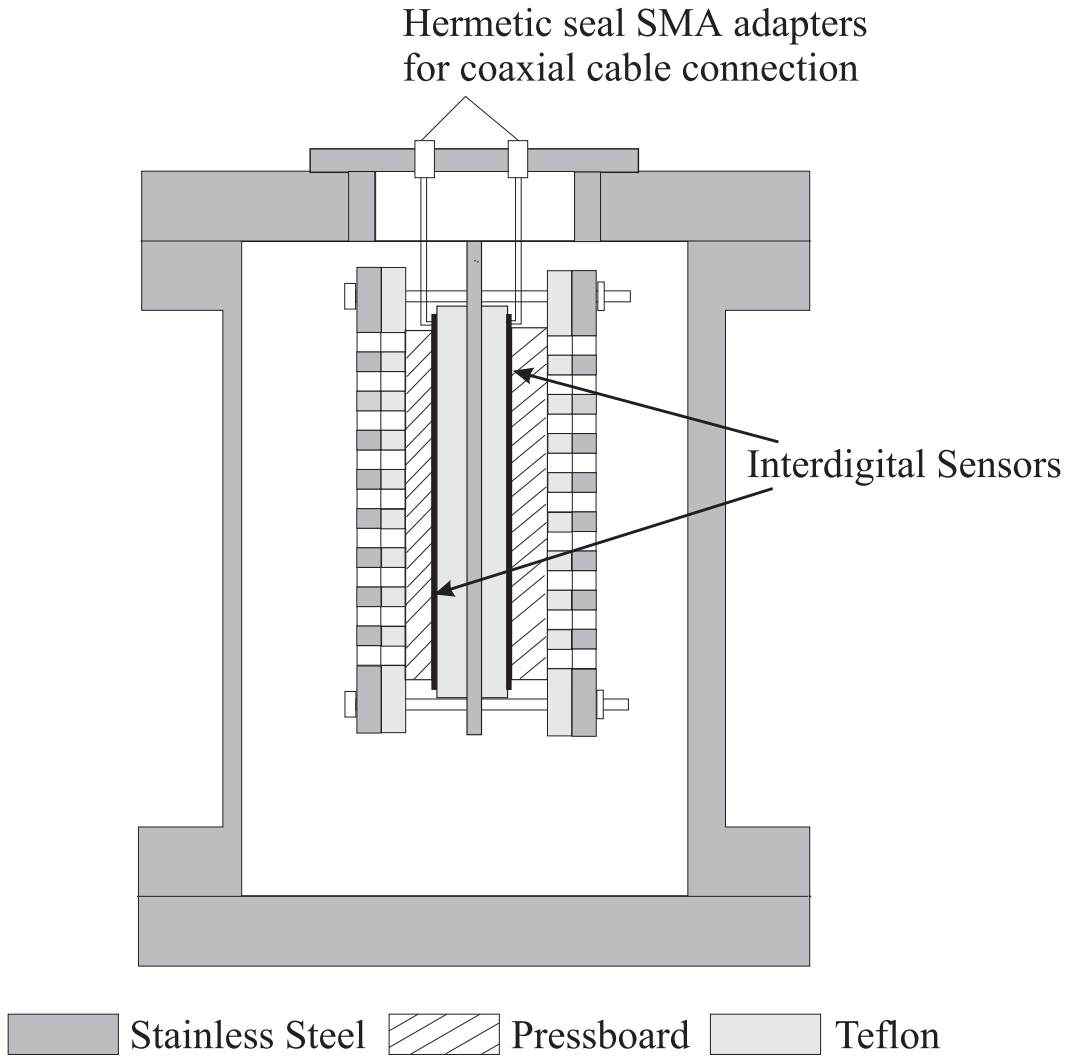

Figure 6.9: Test structure simultaneously using a pair of three-wavelength sensors in laboratory bench-top measurements.

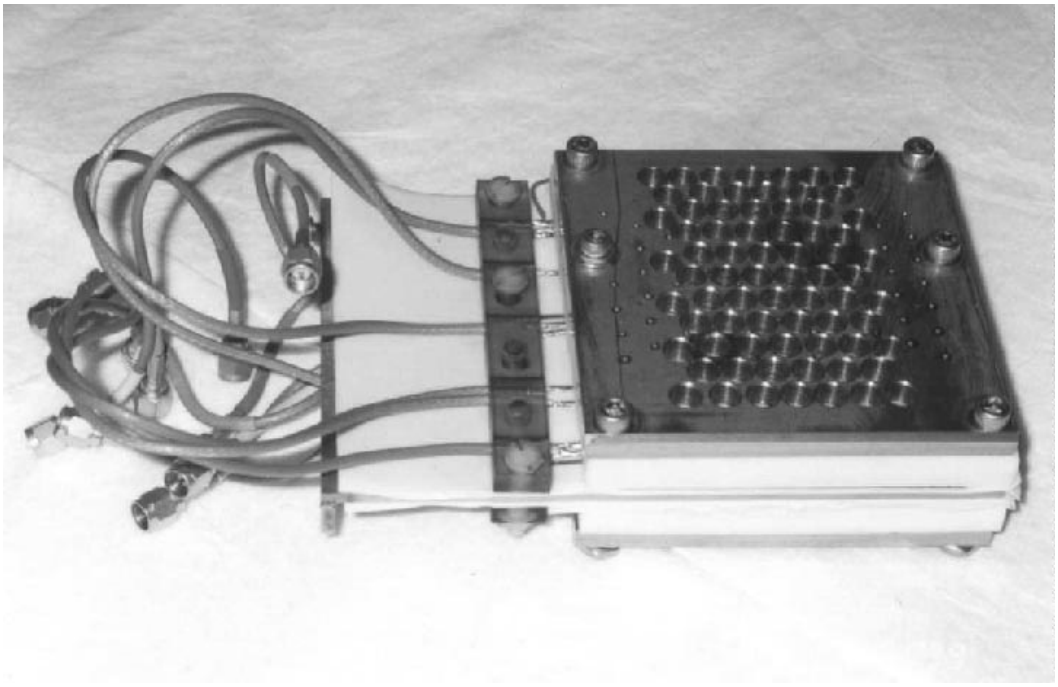

Figure 6.10: New fixture for holding the connecting wires from the sensor.

6.4 Experiment Description

Many tests have been performed for both oil-free and oil-impregnated pressboard under various temperature and moisture conditions. Only representative data using the new sensor, new interface circuitry and new experimental system are presented here.

As shown in Figure 6.9 for the test structure, the interdigital sensor is attached to one side of the pressboard, whereas the other side of the pressboard is exposed to ambient conditions through a perforated steel plate. The four side edges of the pressboard sample are sealed with silicon glue to only allow one dimensional diffusion transverse to the pressboard surface. The test sandwich structure is placed in a vacuum-tight chamber whose temperature and moisture can be monitored and controlled as shown in Figure 6.7.

The tests were performed at five temperatures: 30, 40, 50, 60, and 70°C. Hi-Val pressboard, manufactured by EHV-Weidmann Industries, Inc., was used in all experiments. The samples were either 1.0 mm or 1.5 mm thick. At each constant temperature, the oil-free pressboard was first vacuum-dried for over 24 hours. This gives a uniform zero initial moisture distribution. The moisture diffusion process starts by bubbling in a constant flow of moist air.

The signals from the sensing electrode were recorded at three frequencies: 0.1 Hz, 1 Hz, and 10 Hz. A complete dielectric spectroscopy sweep from 0.005 Hz to 10 kHz is also performed at the beginning and end of each experiment when the pressboard sample is in thermal and moisture equilibrium.

6.5 Effects of Pressboard Thickness

According to the diffusion equation with constant diffusion coefficient D

$$\frac{\partial C}{\partial t} = D\frac{\partial^2 C}{\partial x^2}, \tag{6.2}$$

the diffusion time constant for moisture diffusing from one side of the pressboard is

$$\tau = \frac{4d^2}{\pi^2 D}, \tag{6.3}$$

where d is the thickness of pressboard. It is proportional to the square of the thickness of the pressboard. The diffusion time constant of 1.5 mm thick pressboard should be 2.25 times that of 1.0 mm thick pressboard.

Experiments are carried out for moisture diffusion in 1.0 mm and 1.5 mm Hi-Val oil-free pressboard by bubbling moist air. Direct measurement results of the gain and phase are shown in Figure 6.11 for the 1.0 mm thick sample. The relative humidity of the ambient air for both tests are shown in Figure 6.12. It takes about 21 hours for the 1.0 mm piece to reach equilibrium, therefore it should take about 47 hours for the 1.5 mm piece to reach the same equilibrium.

The calculated transcapacitance and transconductance at f=10 Hz shown in Figure 6.13 confirm the theoretical prediction of the diffusion time constant: it takes about 50 hours for the 1.5 mm sample to reach equilibrium. The second hump in the 1.5 mm test is due to the periodic change of the relative humidity of the ambient air caused by the 24 hour periodic temperature change. The spatial resolution of the three-wavelength sensor is demonstrated by the delay in different wavelengths, i.e. the 5.0 mm wavelength responds to the increase of the moisture first and the 1.0 mm detects moisture last. Each signal follows approximately the same pattern governed by the diffusion dynamics. After a small initial delay, the signal grows at a high rate, after which it flattens off, indicating the end of the diffusion process. The 5.0 mm wavelength signal flattens off first because this wavelength reflects an average value of moisture of the entire pressboard thickness whereas the 1.0 mm measurement flattens off last because within its small penetration depth the diffusion process remains noticable for a longer period of time.

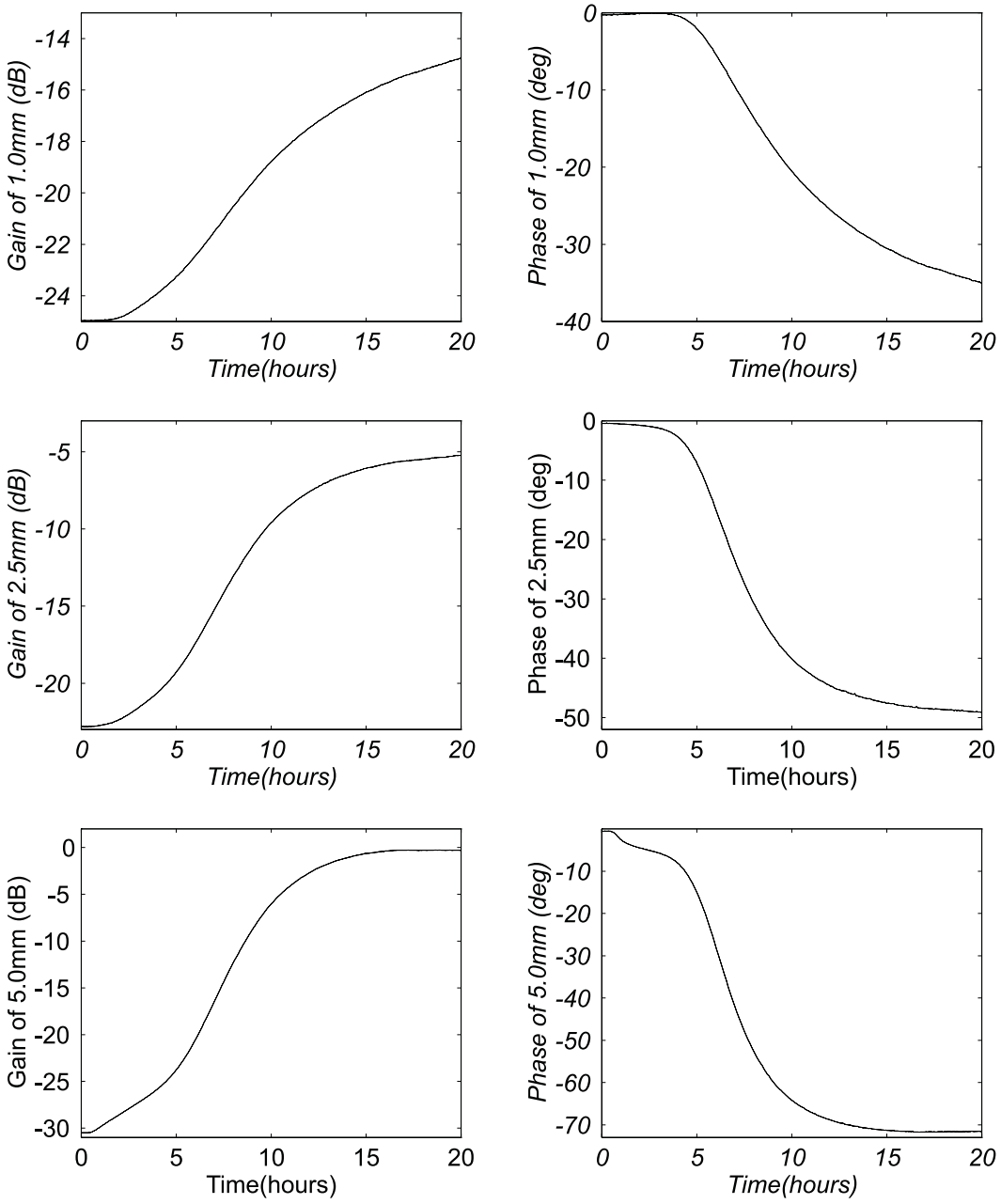

Figure 6.11: The measured Gain and Phase change of the three-wavelength sensor at 10 Hz for 1.0 mm thick oil-free pressboard under wetting process at 30° C.

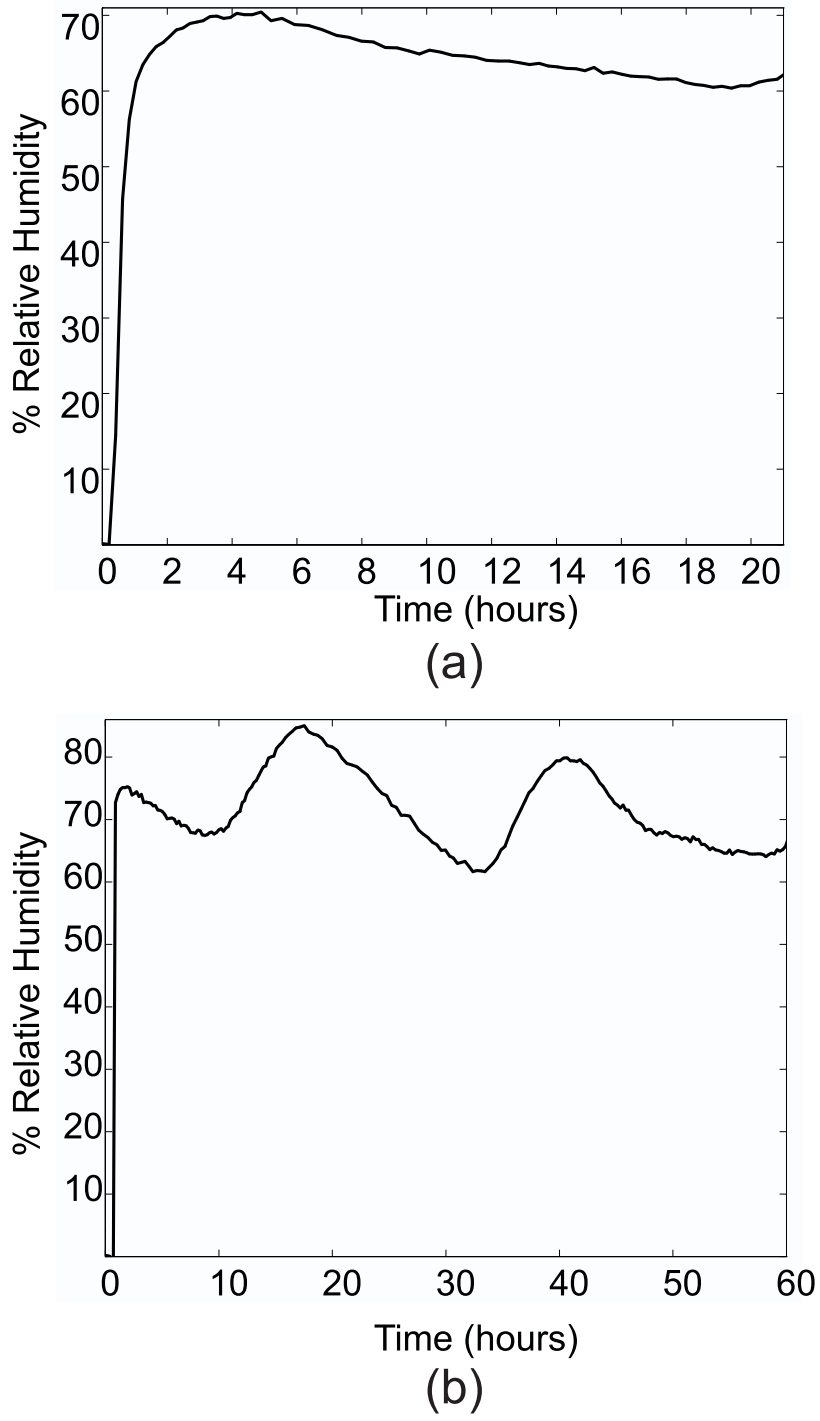

Figure 6.12: The relative humidity of the test chamber during the moisture diffusion process. (a) 1.0 mm pressboard at 30°C (b) 1.5 mm pressboard at 30°C. The periodic change of the relative humidity for (b) is due to the 24-hour ambient temperature change.

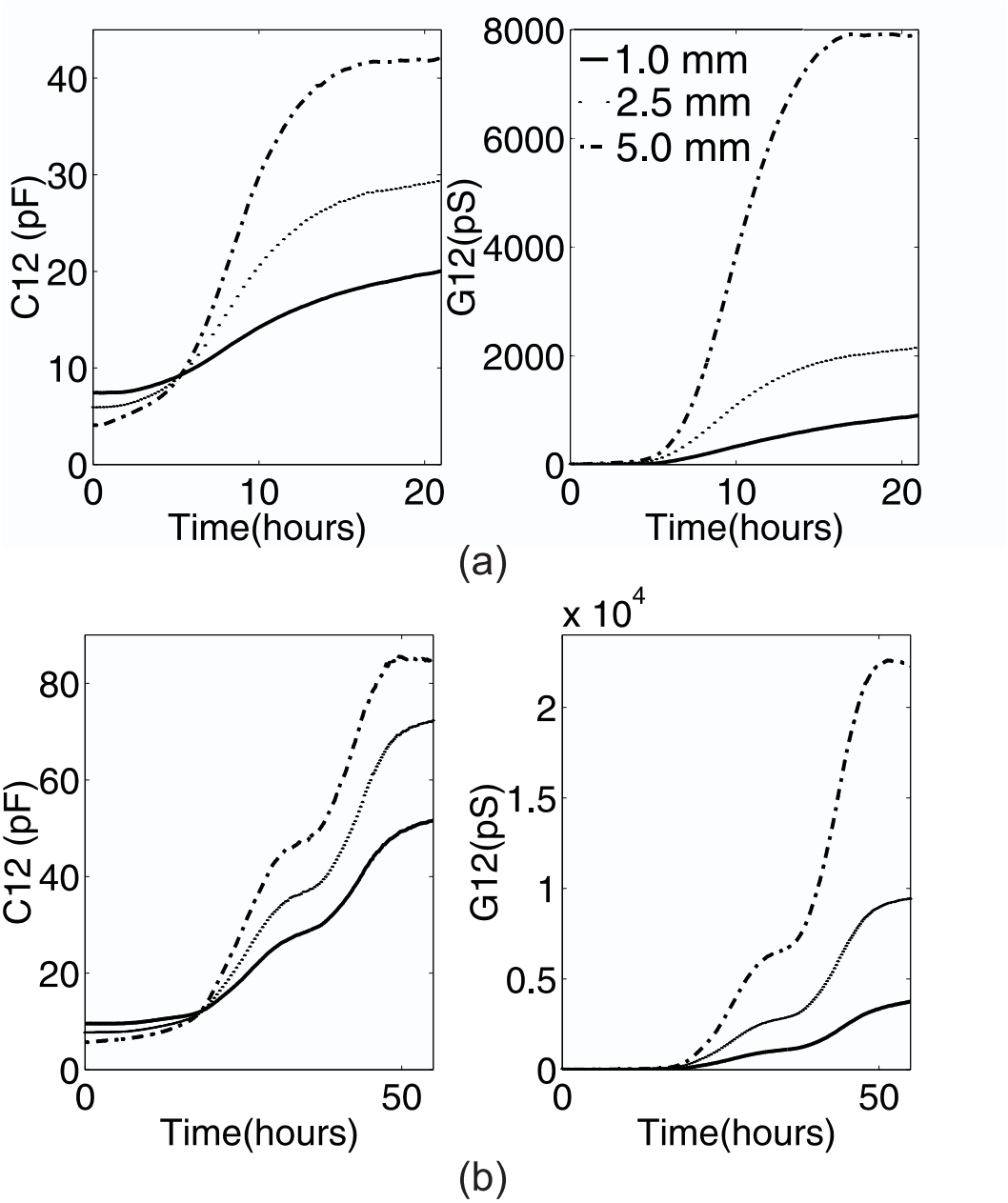

Figure 6.13: The transcapacitance and transconductance of the three-wavelength sensor oil-free pressboard under wetting process at f=10 Hz and 30° C. (a) 1.0 mm pressboard; (b) 1.5 mm pressboard.

6.6 Temperature Effects

As described in Chapter 3, earlier empirical work has employed a diffusion coefficient that is a function of temperature and moisture concentration:

$$D(C,T) = D_0 e^{kC+E_a(1/T_0-1/T)}, \tag{6.4}$$

where D_0, $k = 0.5$, E_a, and T_0 are constants, C is the moisture concentration in weight percent per unit weight dry cellulose, and T is the absolute Kelvin temperature. With an increase in T, the diffusion coefficient increases.

Moisture diffusion into the 1.5 mm thick Hi-Val oil-free pressboard is measured at different temperatures. An increase in the temperature causes the diffusion process to become faster as indicated in Figure 6.14 by the faster increase of the transconductance.

The relative humidity of ambient air of each test is shown in Figure 6.15. With the increase of temperature, the ambient relative humidity decreases. This is because the moist air bubbled into the test chamber has approximately the same water vapor pressure for all temperatures whereas the saturation water vapor pressure increases with temperature.

Quantitative analysis of the temperature dependence of the moisture diffusion coefficient is given in Chapter 7.

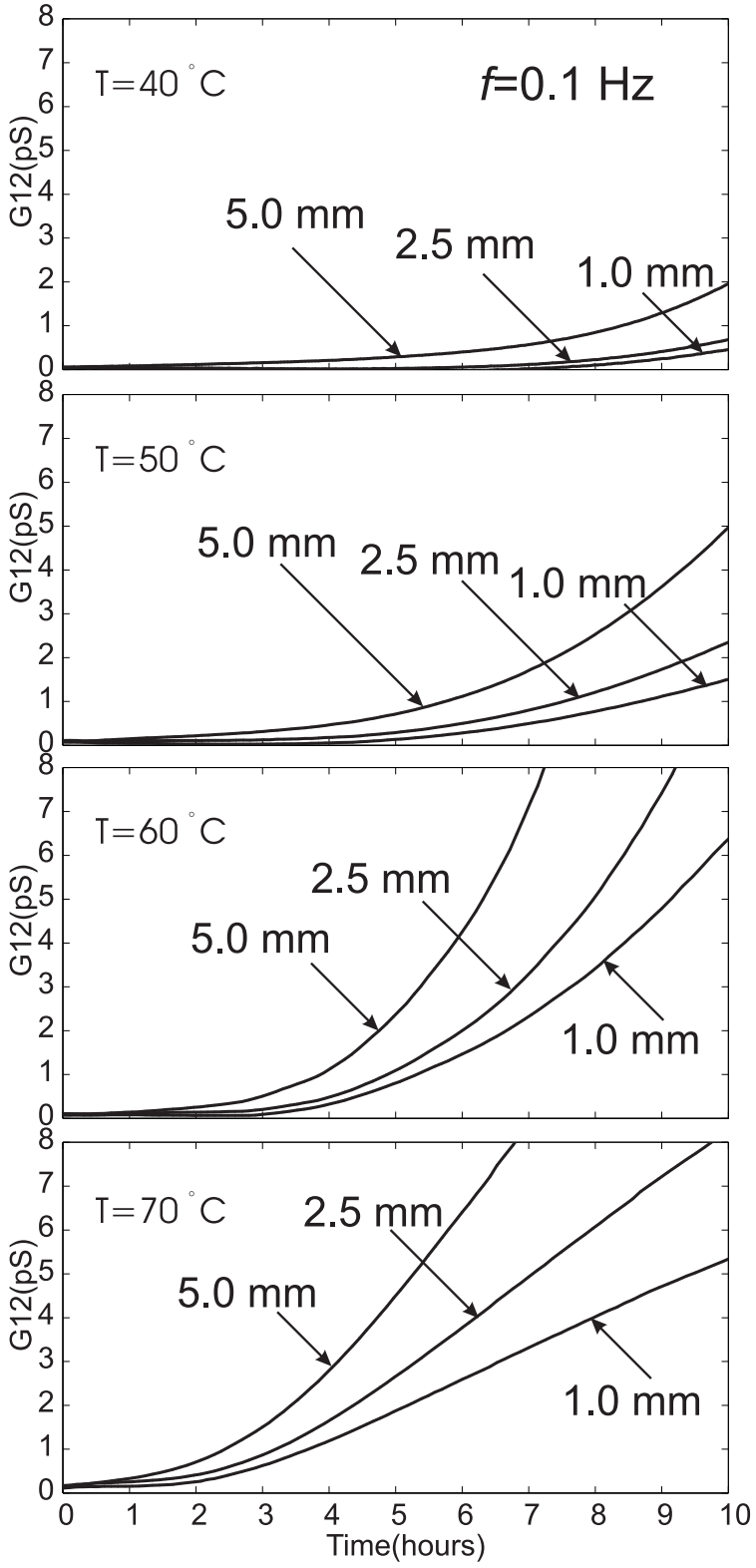

Figure 6.14: The measured transconductance of the Teflon three-wavelength sensor measurements for 1.5 mm oil-free pressboard under wetting process at $f = 0.1Hz$ for various temperatures.

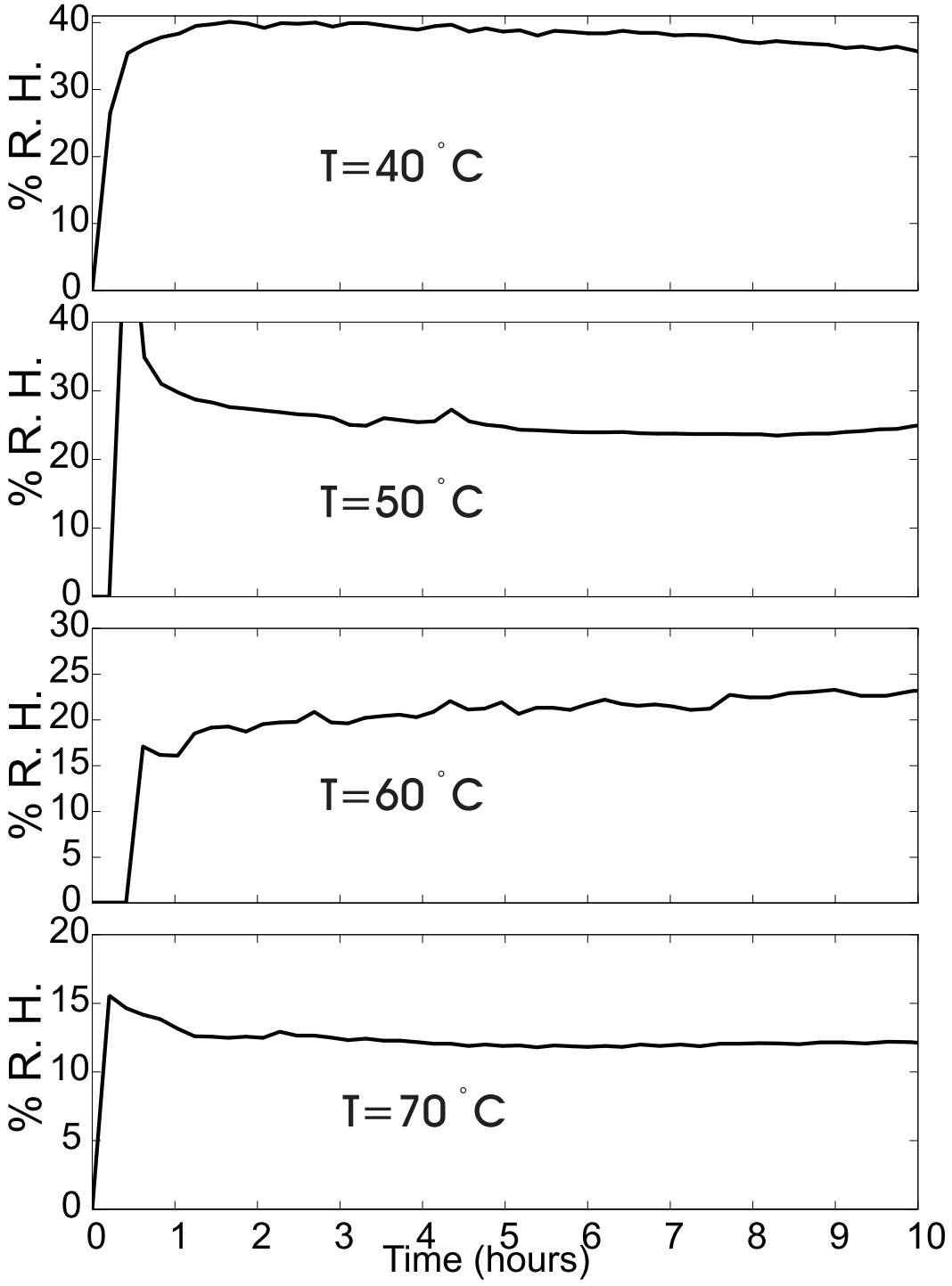

Figure 6.15: The air relative humidity of the test chamber at various temperatures.

6.7 Negative Conductance

From the measured gain and phase, the transcapacitance C_{12} and transconductance G_{12} are calculated from the lumped element circuit in Figure 6.3. For some data, the transconductance turns out to be negative. Intuitively, a negative transconductance may seem nonphysical, but if we analyze the equivalent circuit, there are many possible distributed element circuit combinations that make the transconductance negative.

Figure 6.16 shows one such distributed element model of the measured materials. The equivalent conductance G_{12} in terms of distributed elements is

$$G_{12} = \frac{2G_1(G_1^2 + \omega^2 C_1(C_1 + C_2)) + G_2(G_1^2 - \omega^2 C_1^2)}{(2G_1 + G_2)^2 + \omega^2(2C_1 + C_2)^2}. \tag{6.5}$$

When the last term in the numerator in (6.5) is negative and is greater in magnitude than the sum of all the positive terms, G_{12} could be negative.

Another model is shown in Figure 6.17 for which the corresponding G_{12} is

$$G_{12} = \frac{G_1\left[G_1^2(3G_1^2 - \omega^2 C_2^2 + 6\omega^2 C_1^2 + 8\omega^2 C_1 C_2) + \omega^4 C_1^2\,(3C_2^2 + 3C_1^2 + 8C_1 C_2)\right]}{\left(3G_1^2 - \omega^2(C_2^2 + 3C_1^2 + 4C_1 C_2)\right)^2 + 4\omega^2 G_1^2(3C_1 + 2C_2)^2}. \tag{6.6}$$

Again, when the magnitude of the negative term in the numerator is greater than the sum of all the positive terms, G_{12} is negative.

6.8 Summary

An improved bench-top apparatus was designed and built to implement various moisture measurements using an interdigital dielectrometry sensor. Diffusion processes in oil-free pressboard are monitored at five different temperatures using the interdigital dielectrometry sensor technology. Improved short-circuit measurement techniques and hardware design provide better quality signals and results. Sensor measurements agree well with theoretical analysis for effects of pressboard thickness and temperature. The ability of the interdigital sensor to be able to measure the moisture distribution is demonstrated through the bench-top experimental results.

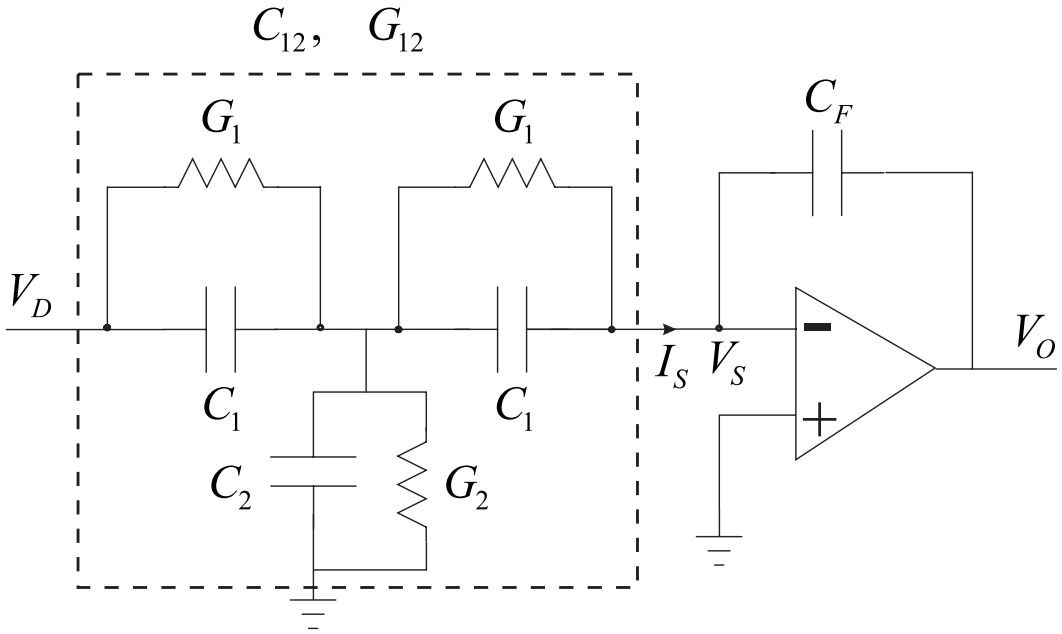

Figure 6.16: The distributed element circuit model for possible negative transconductance.

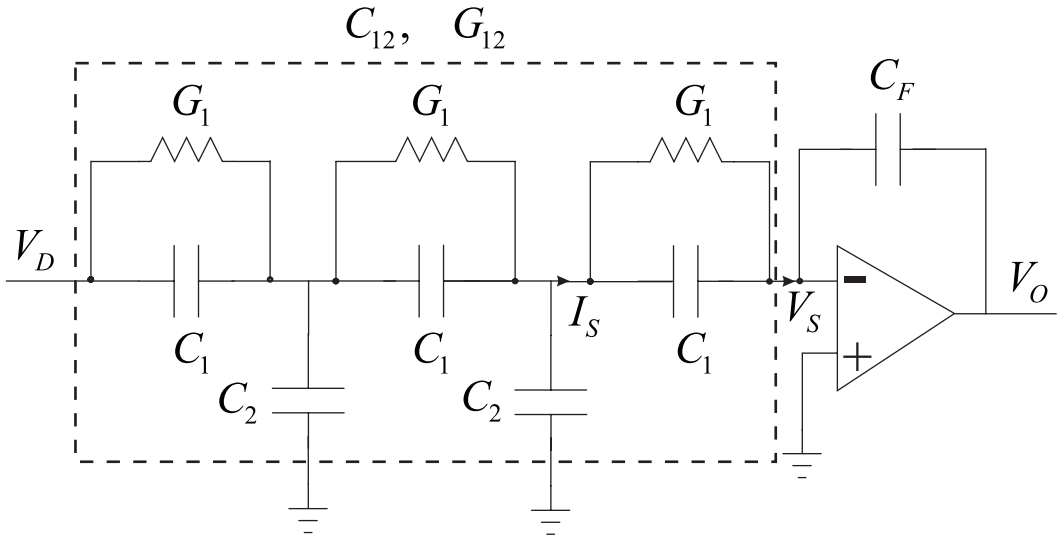

Figure 6.17: Another distributed element circuit model for possible negative transconductance.

Chapter 7

Diffusion Analysis

7.1 Introduction

As shown in Chapter 6, the interdigital sensor can be used to measure the diffusion of moisture in pressboard. Similar tests using interdigital sensors have been done by other investigators to measure moisture diffusion into thin epoxy films [96].

Tests performed for oil-free Hi-Val pressboard at five temperatures: 30, 40, 50, 60, and 70°C are used to analyze the moisture profile and determine the diffusion coefficient.

7.2 Boundary Conditions

The measurement setup and structure are as shown in Figure 6.7 and Figure 6.9. The moist airflow keeps the relative humidity of the testing chamber at a nearly constant level, which gives a constant moisture boundary condition at the pressboard-air interface. The other side of the pressboard is against the sensor, which imposes a zero flux boundary condition.

The air relative humidity is monitored by the Harley relative humidity sensor and the value is converted to the moisture in pressboard boundary using air-pressboard equilibrium curves drawn by Oommen [23] from Jeffries' data [50] shown in Figure 3.4.

At each temperature each curve is fitted with a 6th-order polynomial to be conveniently used for converting continuous relative humidity values to moisture concentration in paper:

$$y = a_6x^6 + a_5x^5 + a_4x^4 + a_3x^3 + a_2x^2 + a_1x + a_0, \tag{7.1}$$

where x is the air relative humidity in percent and y is the moisture in paper in percent by weight. The coefficients in (7.1) are listed in Appendix C. For temperatures between each 10 degrees, a linear interpolation is used.

7.3 Moisture Spatial Profile

In this section, the outputs of the three wavelength sensor at 70°C are used to find the moisture spatial profiles and then the diffusion process is simulated using a constant moisture diffusion coefficient model until the simulation reasonably matches the experimental profile [17]. The algorithm was developed by Mamishev and described in detail in [97].

7.3.1 Distribution of Dielectric Properties

Even though the change of the pressboard properties through its thickness is gradual in the discussed experiment, the pressboard in the model is represented as a three-layer medium with each layer thickness corresponding to the effective penetration depth of 0.3λ for each wavelength λ of the sensor. This is illustrated in Figure 7.1. In other words, the number of wavelengths limits the spatial resolution of the sensor, and only three regions can be distinctively identified with the three-wavelength sensor of Figure 6.1. Described later in this section, the knowledge of the temporal dynamics of the process helps to improve this representation when plotting moisture profiles.

Figure 7.3 shows the values of measured transcapacitance for each of the three electrode pairs. Each signal follows approximately the same pattern dictated by the diffusion dynamics. After a small initial delay, the signal grows at a high rate, after which it flattens off, indicating the end of the diffusion process experiment.

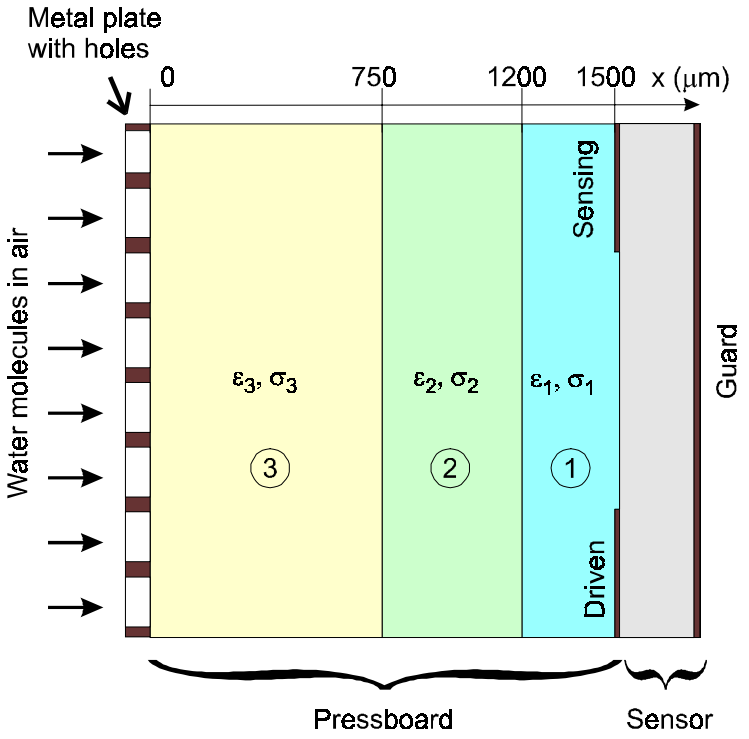

Figure 7.1: A schematic representation of the experimental arrangement. The 1.5 mm thick oil-free pressboard is modeled as a three-layer medium with distinct properties for each layer related to the quantity of moisture in each layer.

The relative amplitude of change of transconductance is normally larger than that of the transcapacitance due to the high electric conductivity growth with the increase of the moisture concentration. Nevertheless, as demonstrated below, the transcapacitance provides sufficient sensitivity for the moisture profile measurements.

7.3.2 Moisture Profiles

The ambient relative humidity is shown in Figure 7.2 and for most of the time is near a constant of 12-13%. The transcapacitance signals at 10 Hz in Figure 7.3 were used to generate the curves of moisture concentration in the pressboard layers, assuming a linear relationship between the capacitance values and the moisture levels at each moment of time. That is, the zero level of moisture concentration corresponds to the lowest capacitance value in Figure 7.3 for each wavelength. The highest capacitance

value for each wavelength corresponds to the moisture level of 1.8% in the pressboard which is 12% R.H. in ambient air. In both cases, at the initial time point and the final time point, the moisture profile is believed to be flat and in equilibrium at 0% and 1.8%, respectively. The intermediate values of the moisture concentration are taken to be linearly proportional to the measured transcapacitance.

Figure 7.4 shows the change in the average values of moisture concentration in the three regions that correspond to the penetration depths of the three wavelengths of the sensor. The average value corresponds to the cumulative amount of moisture in all regions within reach of a given penetration depth. The small difference between the moisture concentration measured by the 2.5 mm and the 1.0 mm wavelengths is related to a relatively small signal delay difference in the detection time analysis. Since the right side blocked boundary condition eliminates the moisture escape, the gradient-driven diffusion process results in a nearly flat moisture concentration profile across regions 1 and 2 of the pressboard indicated in Figure 7.1.

Figure 7.5 shows calculated moisture profiles from dielectrometry measurements for 14 distinct moments of time in 2 hour intervals. The moisture spatial profiles were calculated from the measurement data using multi-variable parameter estimation algorithms for the three-wavelength sensor combined with the moisture measurement data of the ambient environment together with moisture equilibrium curves of Figure 3.4.

The experiment is terminated after about 30 hours, when the signals essentially stop changing. At this point, the moisture profile is expected to be almost uniform and at the maximum value of 1.8%. The profile at 28 hours has these characteristics.

Now, it is possible to evaluate the moisture diffusion coefficient from the moisture dynamics presented in Figure 7.5. By simulating the diffusion process using a standard finite difference technique, one can match the measured profiles. The estimated value of the diffusion coefficient at 70°C is $D = 2.3 \times 10^{-11}$ m^2/s. Figure 7.6 shows theoretical moisture profiles generated using the estimated value of diffusion coefficient that are in reasonable agreement with the measured profiles in Figure 7.5.

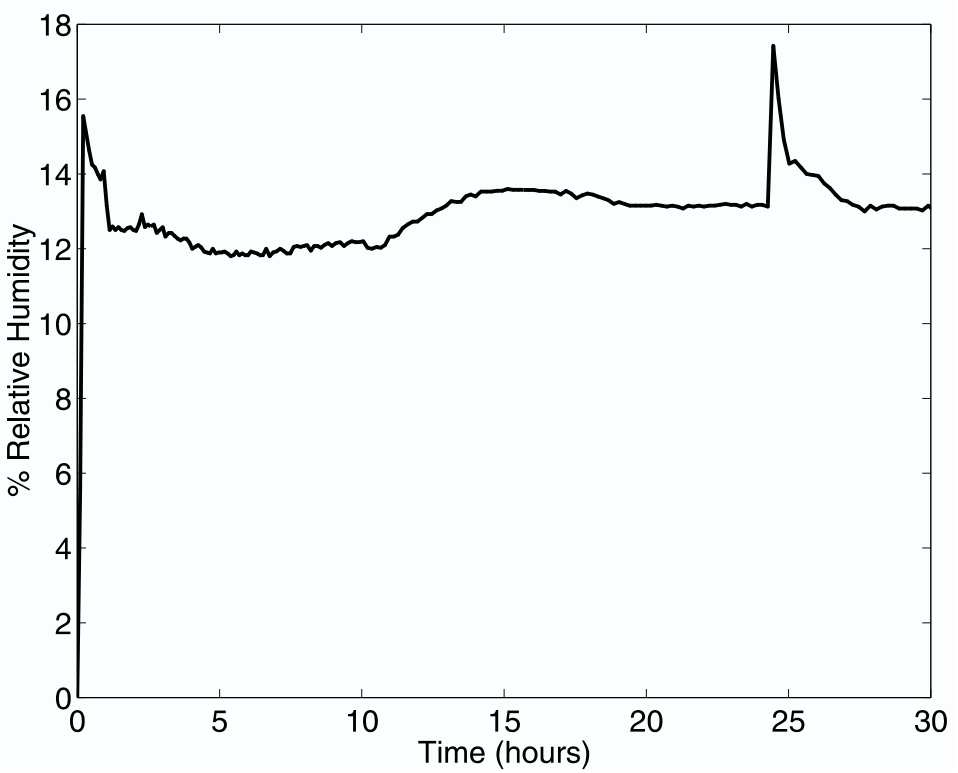

Figure 7.2: Measured relative humidity of the ambient at 70°C.

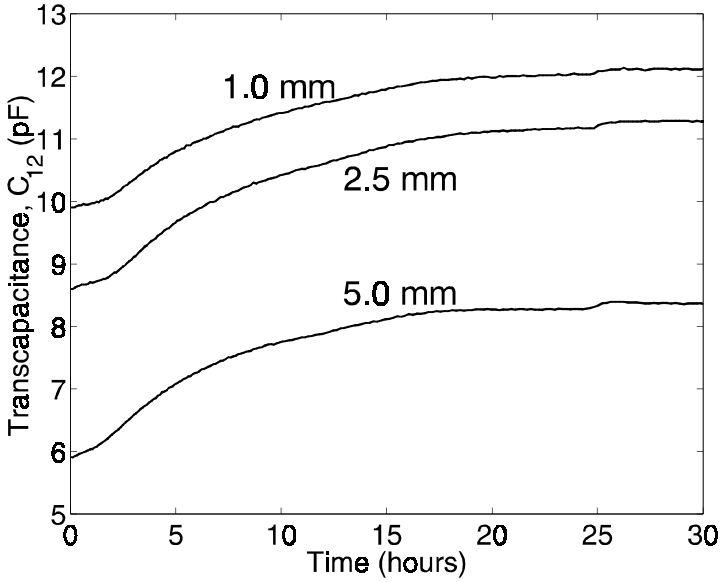

Figure 7.3: Measured capacitance at 10 Hz between each electrode pair throughout the moisture diffusion experiment in 1.5 mm thick oil-free pressboard for each sensor wavelength at 70°C.

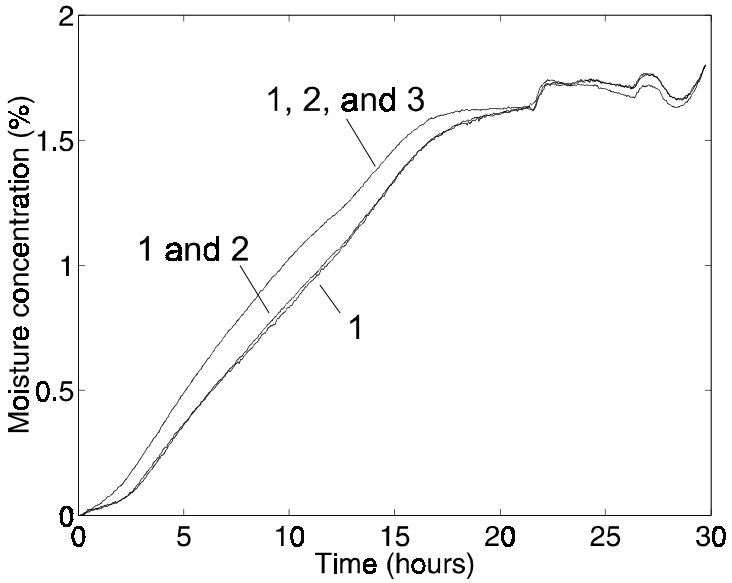

Figure 7.4: Average moisture level measured by each wavelength: region 1 (1 mm), regions 1 and 2 (2.5 mm), and regions 1, 2, and 3 (5 mm).

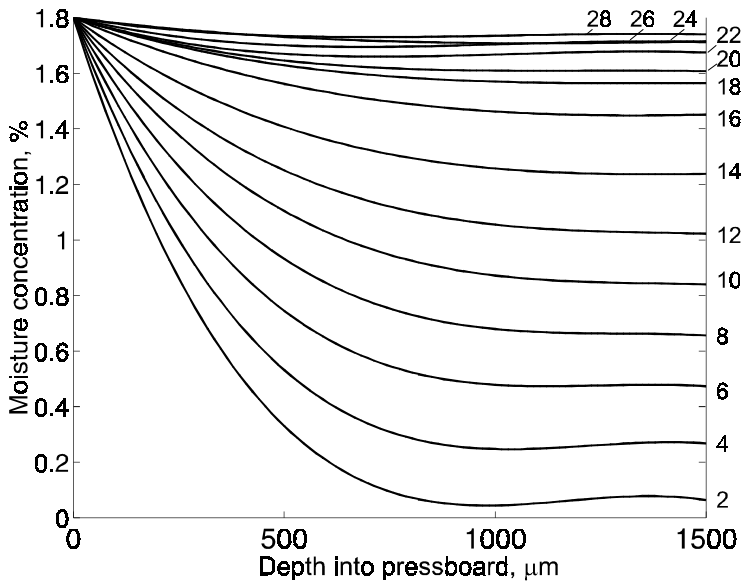

Figure 7.5: Calculated spatial profiles of moisture concentration across the thickness of the oil-free pressboard from dielectrometry measurements. Numbers next to the curves correspond to the time in hours at which the profile was measured.

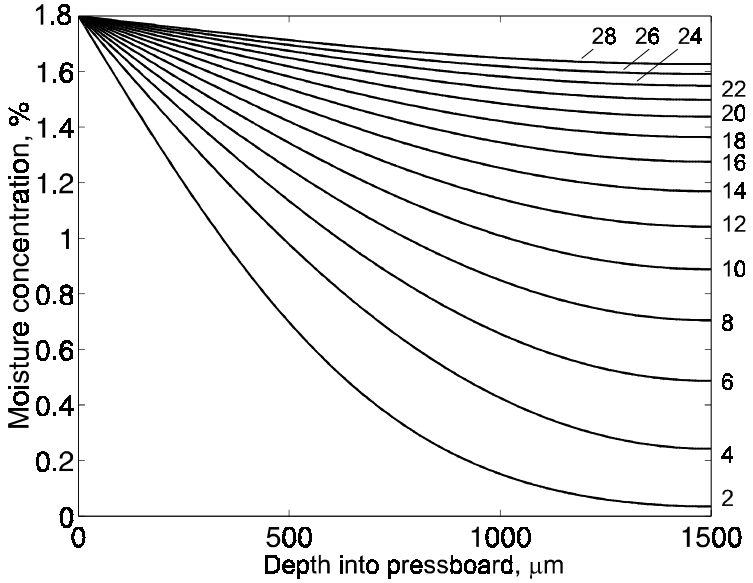

Figure 7.6: Theoretical spatial profiles of moisture concentration across the thickness of oil-free pressboard using a constant diffusion coefficient of $D = 2.3 \times 10^{-11}$ m/s^2. *Numbers next to the curves correspond to the time in hours after the moisture was stepped on to 1.8% at* $x = 0$.

7.4 Calculation of Diffusion Coefficient as a Function of Temperature and Moisture Concentration

In this section, a linear relation between the transcapacitance and the moisture concentration is also assumed, and the output of the shortest wavelength of 1 mm at different temperatures is used to find the diffusion coefficient as a function of concentration and temperature. The shortest wavelength provides the most accurate values of moisture concentration because the moisture distribution near the zero flux boundary is essentially constant within its relatively small penetration depth.

This section analyzes the signals from the sensing electrodes taken at 1 Hz sinusoidal frequency. The 1.0 mm wavelength sensor measures the transadmittance of the region close to the sensor-pressboard interface. The moisture concentration at the sensor-pressboard interface at any time during the diffusion process is measured using a linear relationship between the transcapacitance and the moisture concentration.

7.4.1 Solving the Non-linear Diffusion Equation

Our goal is to find the diffusion coefficient D and the moisture spatial profiles during the entire diffusion process. The diffusion of moisture is defined mathematically in one dimension by Fick's law of diffusion:

$$\frac{\partial C}{\partial t} = \frac{\partial}{\partial x}(D\frac{\partial C}{\partial x}). \tag{7.2}$$

When D is a constant, the closed form solution for zero initial distribution and constant boundary condition C_1 at $x = l$ and zero flux at $x = 0$ is

$$C = C_1 \left\{ 1 - \frac{4}{\pi} \sum_{n=0}^{\infty} \frac{(-1)^n}{2n+1} \; e^{-t/\tau_n} \cos \frac{(2n+1)\pi x}{2d} \right\}, \tag{7.3}$$

where

$$\tau_n = \frac{4l^2}{D(2n+1)^2\pi^2}. \tag{7.4}$$

When the diffusion coefficient is concentration-dependent, (7.2) becomes non-linear and no general analytical solution for finite sample thickness is available. Numerical methods are then employed to solve the diffusion equation.

The empirical temperature and moisture concentration dependence model of (7.5) is used here to find the corresponding parameters, D_0, k, and E_a, for Hi-Val pressboard from our experiments:

$$D(C,T) = D_0 e^{kC + E_a(1/T_0 - 1/T)}. \tag{7.5}$$

Let

$$dz = D(C,T)dC, \tag{7.6}$$

so that (7.2) becomes

$$\frac{\partial C}{\partial t} = \frac{\partial^2 z}{\partial x^2}. \tag{7.7}$$

Equation (7.7) is discretized for numerical calculation

$$\frac{C_j^{n+1} - C_j^n}{\Delta t} = \frac{z_{j+1}^{n+1} - 2z_j^{n+1} + z_{j-1}^{n+1}}{(\Delta x)^2}, \tag{7.8}$$

where superscript n corresponds to time steps and subscript j corresponds to space steps. This backward time scheme is chosen for stability of the algorithm [98].

Then, z can be derived in terms of C from

$$dz = D(C,T)dC = D_0 e^{kC + E_a(1/T_0 - 1/T)}dC, \tag{7.9}$$

as

$$z = \frac{D_0}{k} e^{kC + E_a(1/T_0 - 1/T)}. \tag{7.10}$$

Linearize each term on the right-hand side of (7.10)

$$z_j^{n+1} \equiv z(C_j^{n+1}) = z(C_j^n) + (C_j^{n+1} - C_j^n)\left.\frac{\partial z}{\partial C}\right|_{j,n} = z(C_j^n) + (C_j^{n+1} - C_j^n)D(C_j^n). \tag{7.11}$$

Standard numerical procedures are then carried out to solve (7.8).

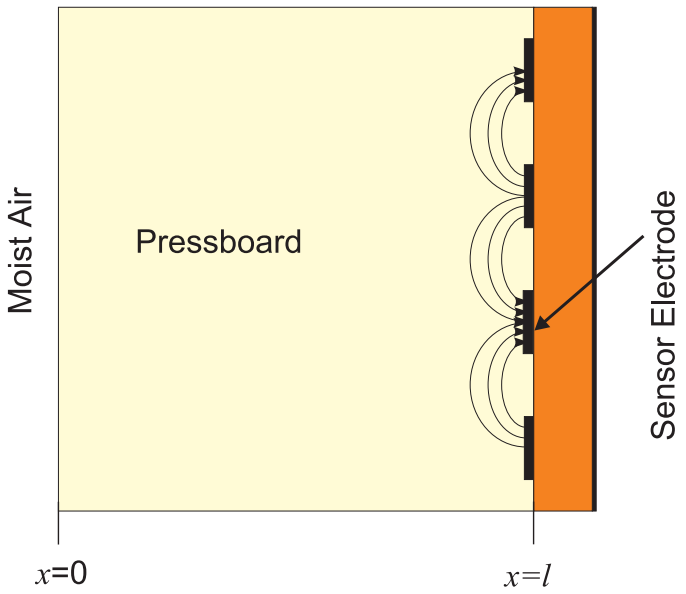

Figure 7.7: 1 mm wavelength sensor detects changes near the pressboard-sensor surface at $x = l$ while the moisture diffuses from the ambient at $x = 0$.

D_0	k	E_a
0.67×10^{-12} m^2/s	0.45	7646°K

Table 7.1: Diffusion coefficient parameters obtained from measurements using a least squares fit for oil-free pressboard.

To find the parameters for the diffusion coefficient, the measured moisture concentration of the 1 mm wavelength sensor is taken at five different temperatures and the Matlab built-in function for least squares fit, *leastsq*, in the optimization toolbox is used to find the parameters that minimize the sum of the error squares of the moisture concentration.

The results are shown in Table 7.1.

7.4.2 Discussion

For $T = 70$°C, the diffusion coefficient at the start when $C = 0\%$ is $D = 1.9 \times 10^{-11}$ m^2/s, and at the end when $C = 1.8\%$ is $D = 4.3 \times 10^{-11}$ m^2/s. The average is about 3.1×10^{-11} m^2/s. This is close to the value that is estimated in Section 5.3 for a constant diffusion coefficient model, 2.3×10^{-11} m^2/s . In this section, the diffusion

coefficient is found by minimizing the sum of the error squares between the measured moisture concentration and the theoretical values for various temperatures, whereas the approach in Section 5.3 uses a constant diffusion coefficient to do a forward simulation until the calculated profile closely matches most of the measured profile.

The spatial profiles of the diffusion process at 60°C with the diffusion coefficient as a function of concentration, and as a constant $D = 2.4 \times 10^{-11}$ m^2/s (an average of D at $C = 0\%$ and $C = 3.0\%$) are shown in Figure 7.8. The curves are plotted from 2 hours to 30 hours at 2-hour intervals. At first, since the moisture concentration is low, the diffusion coefficient in most regions is smaller than the average value, so the curves for constant diffusion coefficient increase faster than the concentration dependent curves. When the moisture in the pressboard increases, the diffusion speed also increases, thus the concentration dependent curves exceed the constant diffusion curves. The experimental curves in Figure 7.5 also show the trend of reaching the final moisture distribution very fast near the end. The constant diffusion coefficient simulation in Figure 7.6 would not be able to fit into this phenomena.

The diffusion coefficient for oil-free pressboard calculated here is much smaller than that reported by Foss in [62]. This could be due to three reasons. First, the materials are different. Foss' data are for A50P281A Kraft paper made from 100% sulphate fiber with a thickness of 0.01 inch. The reported value in [99] by Quarshie is close to our results given in Table 7.2. Quarshie used 50 layers of Manilla paper, each 0.045 mm thick.

Second, our sample is tightly compressed. Pressure has been shown to slow down the diffusion process [99]. For the EHV-Weidmann T-IV pressboard that Quarshie tested, the diffusion coefficient of unclamped pressboard is about 1.3 times that of clamped pressboard.

Third, due to the porous squeezing structure at the pressboard-air interface, the pressboard is not completely exposed to the ambient at that interface. This might slow down the diffusion, but the effect should be small because according to the manufacturer, the diffusion in the direction parallel to the interface is much faster than that to

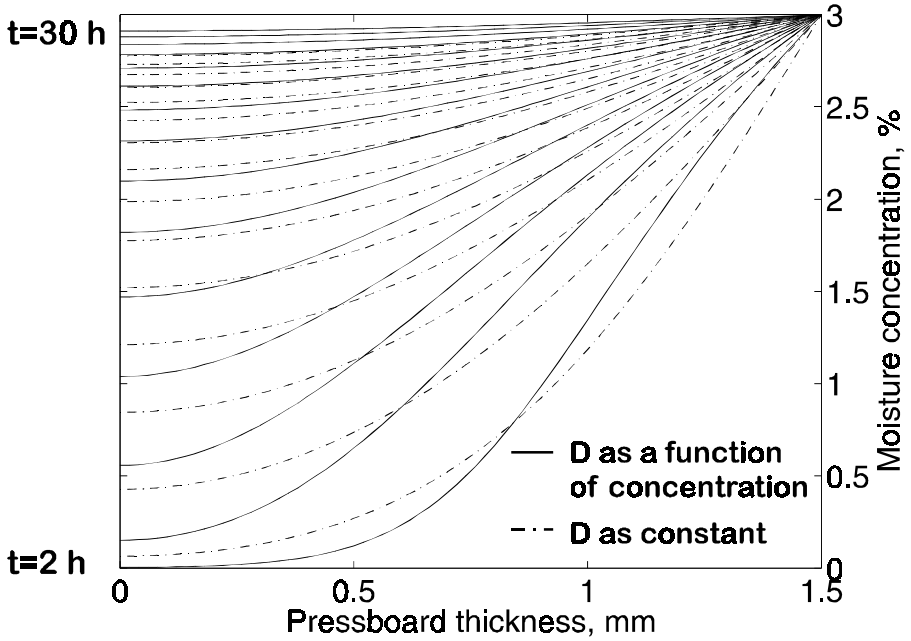

Figure 7.8: Calculated moisture profile in the pressboard at 60° C for moisture diffusion coefficient as a function of concentration using estimated parameters and as a constant $D = 2.4 \times 10^{-11}$ m^2/s, an average of D at $C = 0\%$ and $C = 3.0\%$, the measured boundary condition at 60° C.

Source	Du	Foss [62]	Quarshie [99]
Material	Pressboard	Kraft paper	Manilla paper
$C = 2.1\%$	2.5×10^{-11}	1.3×10^{-9}	1.3×10^{-11}
$C = 3.0\%$	3.8×10^{-11}	2.1×10^{-9}	4.8×10^{-11}

Table 7.2: A comparison of measured diffusion coefficient (m^2/s) and literature reported values at 60° C.

the direction perpendicular to the interface which we are studying.

Forth, analysis in Section 7.6 further examines the discrepancy in literature results. Possible numerical errors are identified in Foss' study. The second and third causes are studied with experiments in the Couette Facility in Chapter 8.

7.5 Forward Simulation of the Sensor Response with Established Mapping

Using the established universal curve described in Section 4.5 relating moisture and temperature effects to the dielectric properties of the oil-free pressboard, we can simulate the diffusion process and corresponding dielectric change and sensor responses.

7.5.1 Simulation Procedures and Results

Using the program *diff.c* written by Prof. B. C. Lesieutre based on the continuum model, the forward process is simulated. The procedures can be briefly described as:

1. Given the temperature and moisture boundary conditions of experiments, numerically solve the diffusion equation using the diffusion coefficient estimated in Section 7.4; obtain moisture concentration distribution throughout the sample as shown in Figure 7.9.

2. Using the universal curve found in Chapter 4, obtain the conductivity and permittivity distribution for corresponding temperature and moisture concentration. The conductivity and permittivity profiles are shown in Figures 7.10 and 7.11.

3. With estimated dielectric properties and sensor geometry, use the continuum model to calculate the transcapacitance and transconductance shown in Figure 7.12. The measured transcapacitance and transconductance are shown in Figure 7.13 for comparison.

4. With known feedback capacitance and external circuitry, calculate the gain and phase as shown in Figure 7.14. The measured gain and phase are shown in Figure 7.15 for comparison.

7.5.2 Error Sources

The simulated results of Figure 7.12 and Figure 7.14 display trends very close to the measurements shown in Figure 7.13 and Figure 7.15, but the actual values differ, mainly

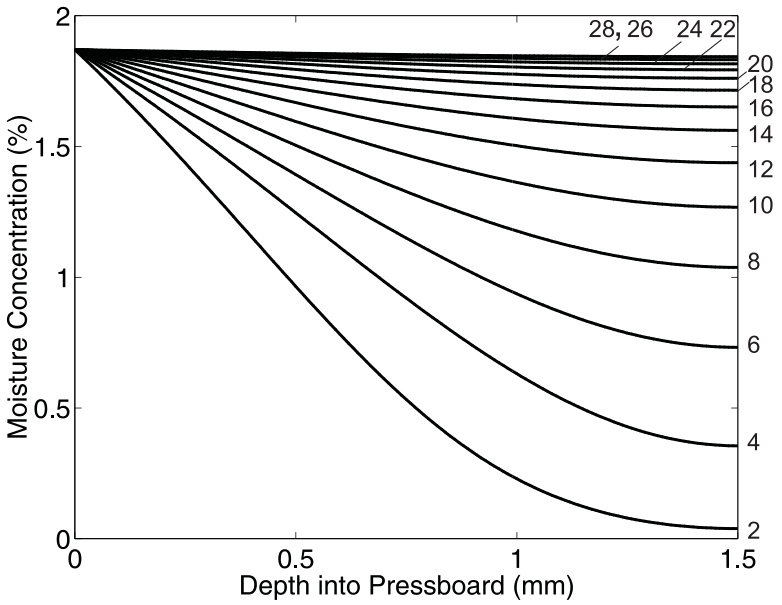

Figure 7.9: Calculated moisture profile in the pressboard at 70° C for moisture diffusion coefficient as a function of concentration using estimated parameters listed in Table 7.1.

the measured transcapacitance is larger than the simulated value. The difference is caused by the following reasons.

The main error source is introduced by the relative permittivity of the pressboard. As discussed in Chapter 4, for mapping from moisture and temperature to dielectric properties, the measured permittivity is very sensitive to the density of the pressboard, which is a function of compression. The bench-top experiment was more tightly compressed by stainless steel plates with stainless steel bolts while the moisture mapping experiments were performed with the parallel-plate sensor made of aluminum plate and printed circuit board (PCB) held together by nylon bolts. Therefore, the density of the pressboard used in bench-top measurements is higher than those used for finding the universal curve in Chapter 4 which corresponds to higher permittivity and higher transcapacitance.

The surface contact effects also contribute significantly to the permittivity values. Since the pressboard is porous, for oil-free pressboard there exists air space between the pressboard and electrodes. The measured equivalent permittivity will be smaller than

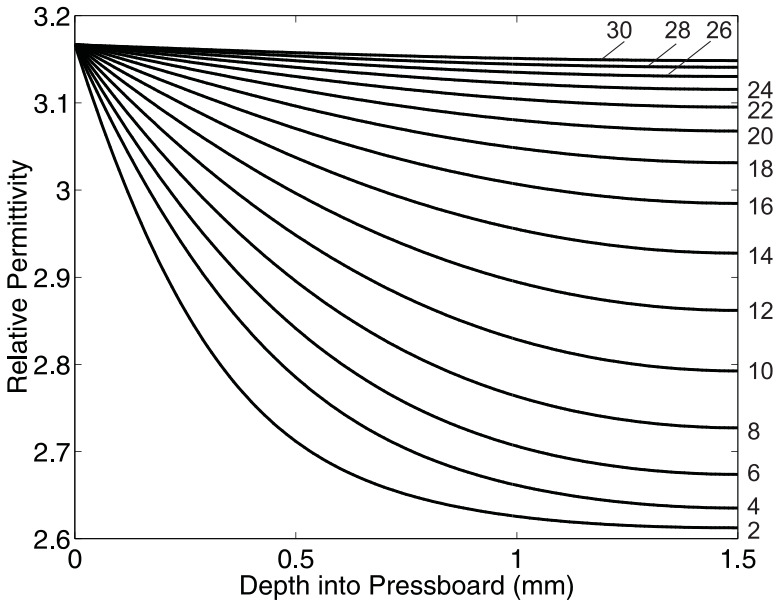

Figure 7.10: Calculated relative permittivity profile in the pressboard at 70°C and f=10 Hz for the moisture diffusion process of Figure 7.9 using the universal curve described by Tables 4.5 and 4.6.

that of the actual pressboard. The air space cannot be easily modeled as a pure air gap as the pressboard touches the electrodes. Since the bench-top structure is pressed more tightly, the air spacing is much smaller than that of the PCB sensor structure used in Chapter 4. Moreover, for the parallel-plate structure, the air space is present at both electrodes while for the interdigital sensor it only appears at one side.

The diffusion coefficient estimated can also introduce errors to the moisture profile and therefore to the dielectric property profile. The temperature in simulations is a constant while in real experiments there are deviations. Similarly, the experiment relative humidity is not perfectly constant as shown in Figure 7.2 while the theoretical simulation assumes a constant moisture boundary condition at the pressboard/air interface.

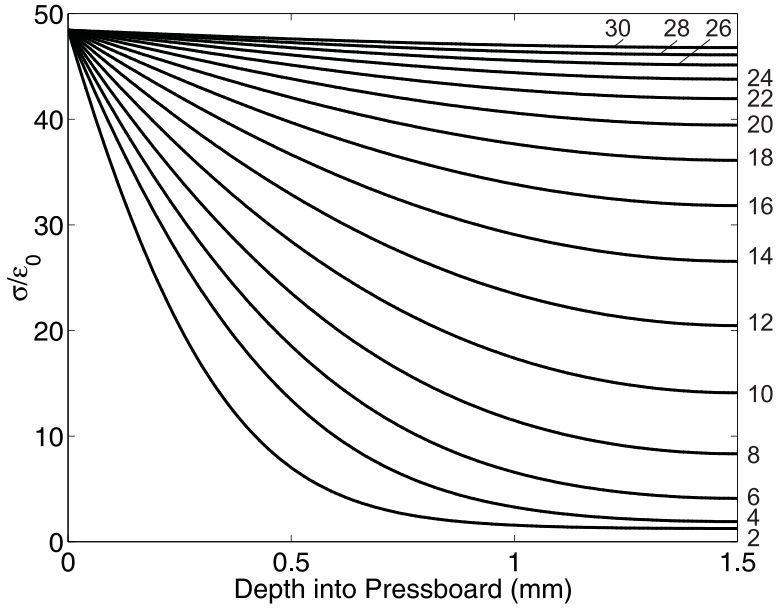

Figure 7.11: Calculated relative conductivity profile in the pressboard at 70°C and f=10 Hz for the moisture diffusion process of Figure 7.9 using the universal curve described by Tables 4.5 and 4.6.

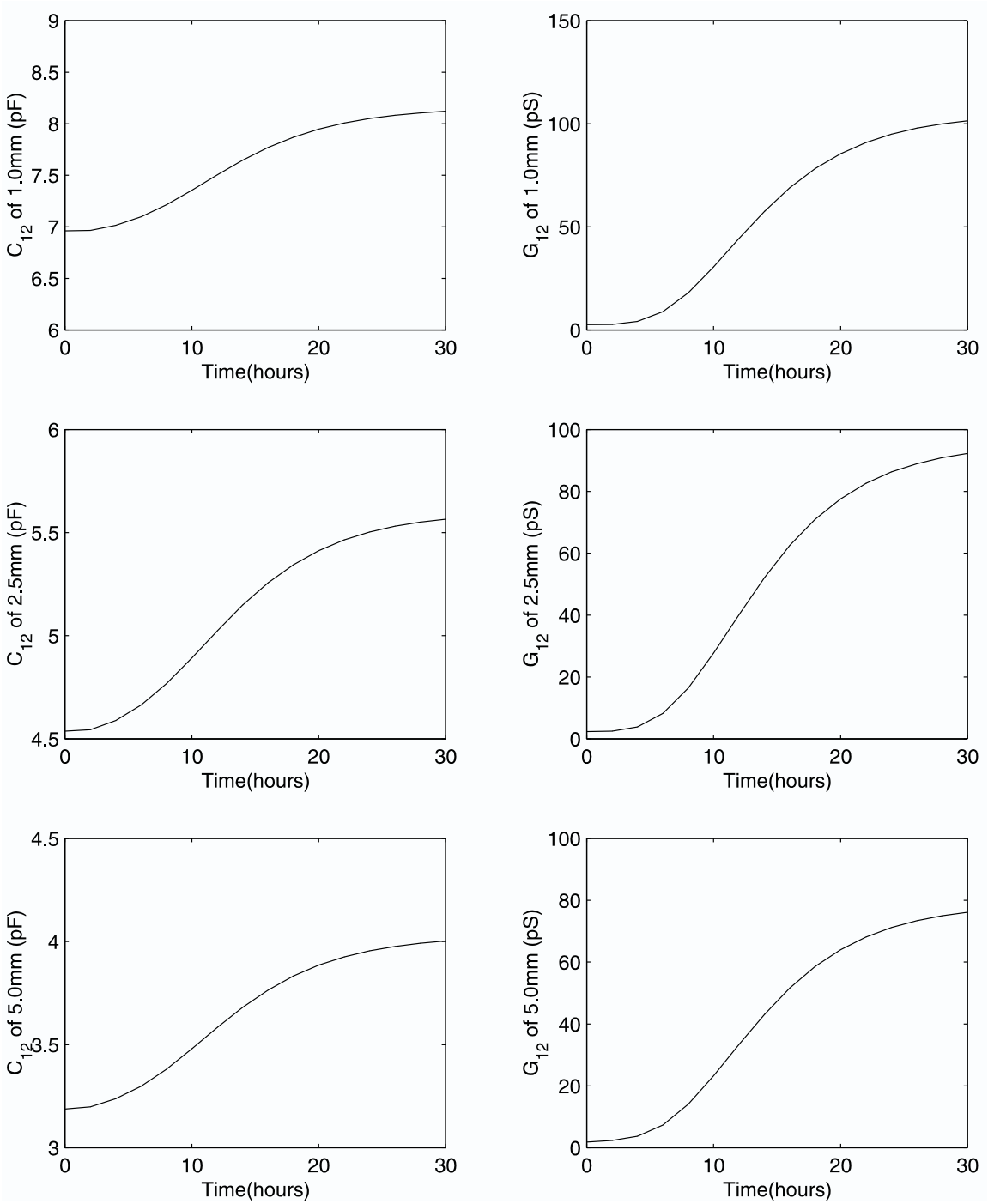

Figure 7.12: Calculated transcapacitance and transconductance at 70°C and f=10 Hz for the moisture diffusion process of Figure 7.9 using the universal curve described by Tables 4.5 and 4.6.

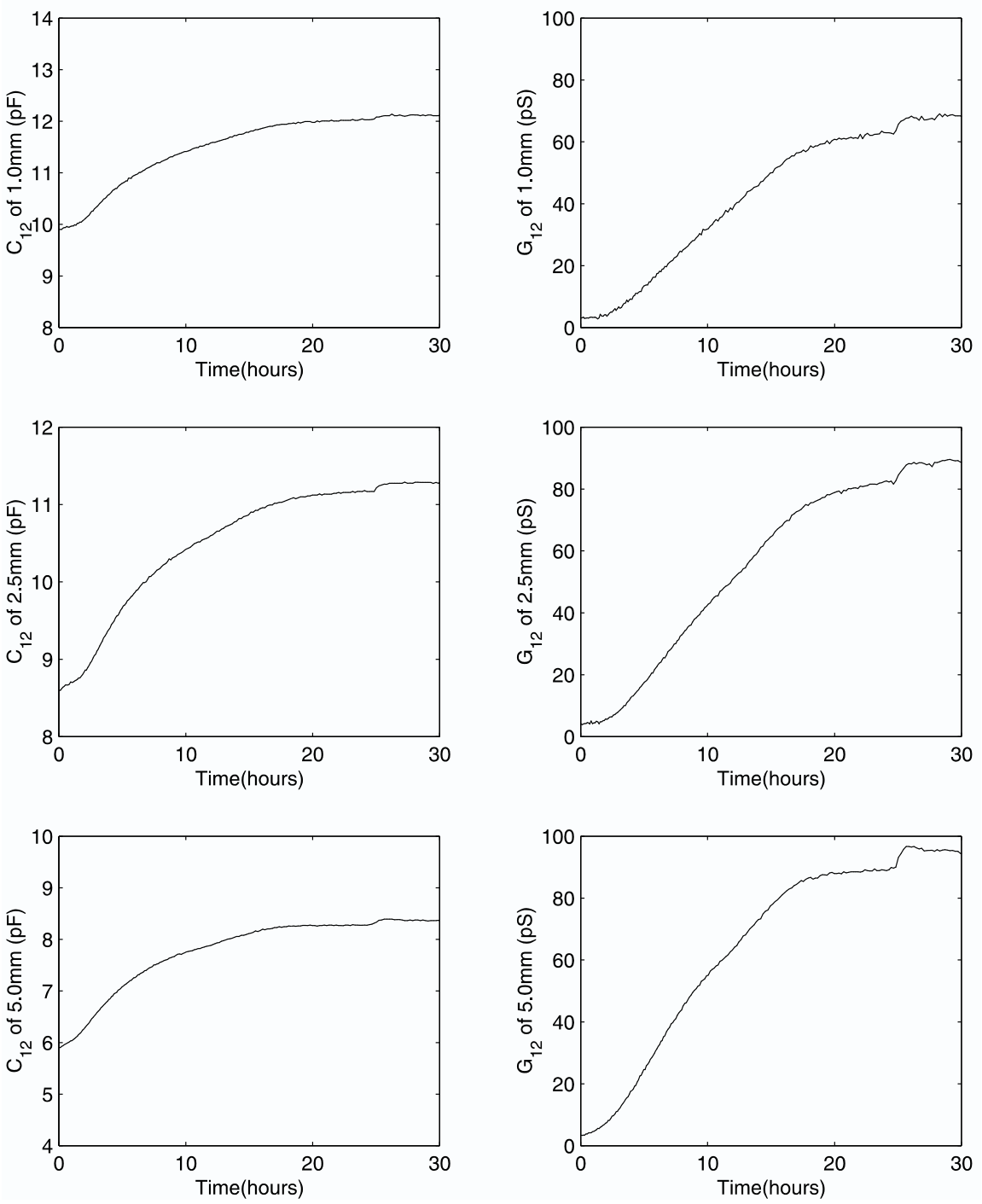

Figure 7.13: Measured transcapacitance and transconductance at 70° C and f=10 Hz for the moisture diffusion process with ambient relative humidity of Figure 7.2.

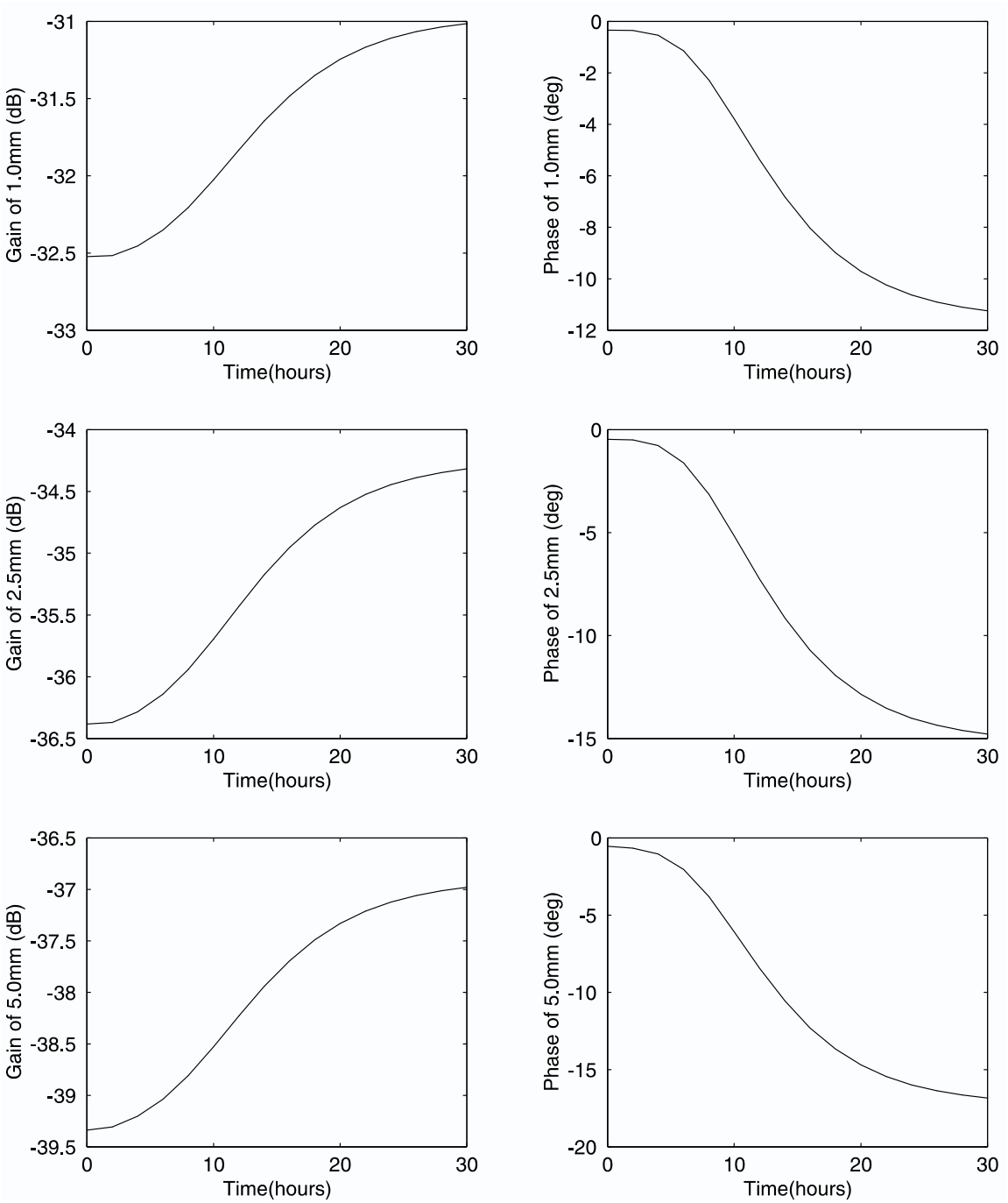

Figure 7.14: Calculated gain and phase at 70° C and f=10 Hz for the moisture diffusion process of Figure 7.9 using the universal curve described by Tables 4.5 and 4.6.

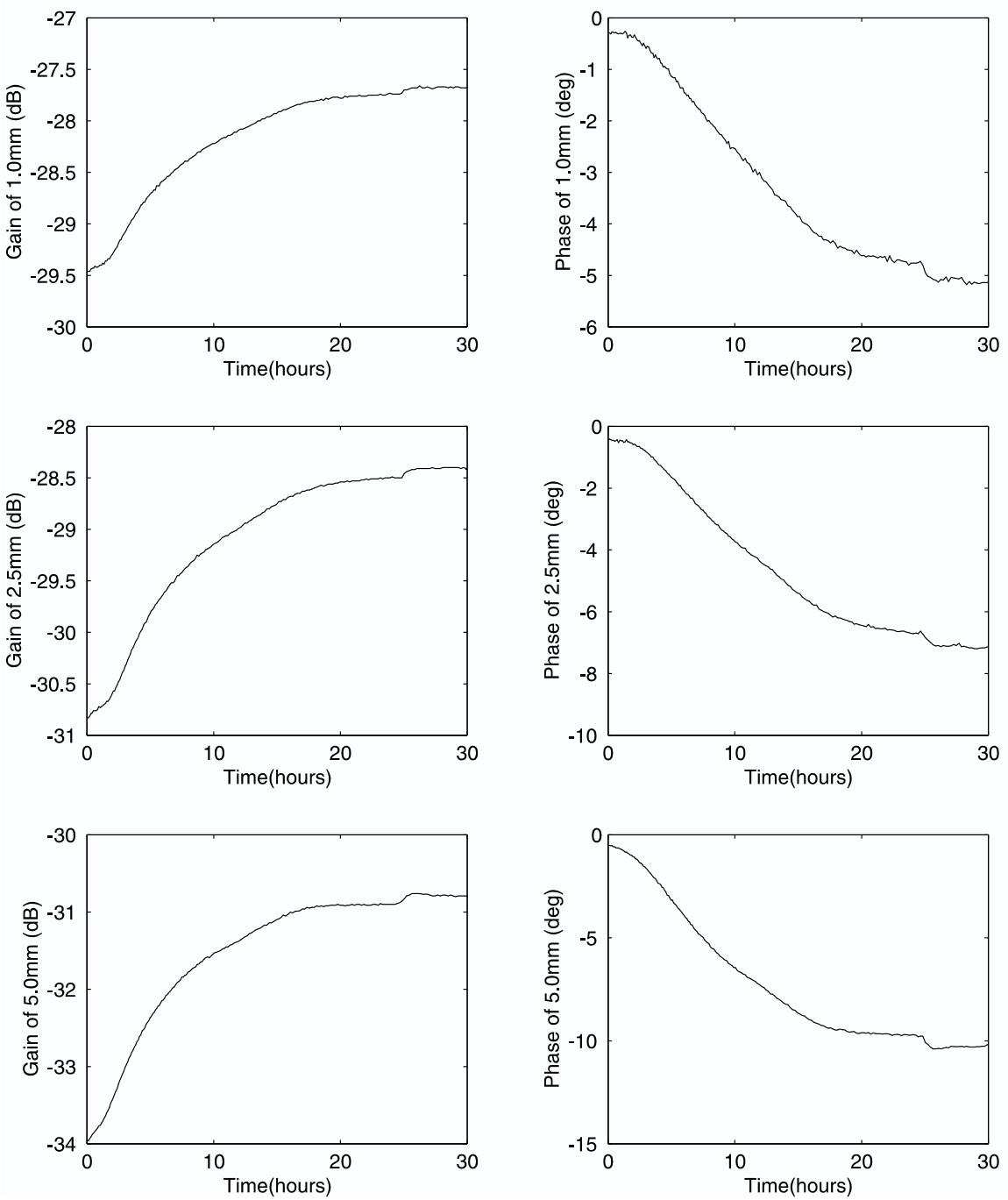

Figure 7.15: Measured gain and phase at 70°C and f=10 Hz for the moisture diffusion process with ambient relative humidity of Figure 7.2.

7.6 Summary and Analysis of Literature Study on the Diffusion Coefficient

To further understand the discrepancy of the diffusion coefficient between literature reported values and this thesis work, a careful examination is given to Foss' study. The diffusion coefficient of paper has been observed by several investigators to be concentration dependent [46, 100–102]. The diffusion coefficient increases with an increase in the moisture concentration. Physically this means that the already humidified paper permits the passage of moisture much more easily than dry paper. The phenomena is quite common for low-molecular weight substances such as moisture diffusion into high-polymeric solids such as paper [46].

Foss' formula for oil-free Kraft paper is based on two pieces of other researchers' experimental data. First, he fitted the moisture dependence based on Ewart's data for oil-soaked paper [46] as:

$$D(C) = D_1 e^{0.5C}. \tag{7.12}$$

If the moisture dependence of oil-free paper is different from oil-soaked, then this introduces error. In fact as Fullerton reported in [103] the concentration-dependence of the diffusion coefficient of oil-free A50P260A Kraft paper is

$$D(C) = D_1 e^{0.25C}. \tag{7.13}$$

Foss further fitted D_1 as a function of temperature using Ast's data for oil-free Kraft paper,

$$D_1(T) = D_0 e^{E_a(1/T_0 - 1/T)}. \tag{7.14}$$

It is not clear from the report how Foss implemented this step. If Foss assumed that Ast's diffusion coefficient is independent of moisture, it is not correct since Ast's experiments were performed at different moisture levels, therefore introducing further error. In fact, doing so will increase the temperature dependence by using the data that have both temperature and moisture dependence. This could partly explain why

Foss' diffusion coefficient is consistently higher than other literature values and that obtained in this thesis work.

Ast at General Electric performed tests of the moisture diffusion for A50P281A Kraft paper [63]. Ast's method is briefly stated here to explain how he obtained the diffusion coefficient from his measurements. The paper was exposed on one surface to essentially 0% R.H. maintained by drierite, while the other surface was exposed to an atmosphere of known relative humidity created by the vapor of salt solution. The amount of moisture that migrated through the pressboard from the moist side to the dry side was measured.

The steady state rate at which moisture diffuses through a plane surface of unit area at position x is proportional to the concentration gradient measured normal to the surface,

$$\frac{dQ}{dt} = -D(C,T)\frac{dC}{dx}, \tag{7.15}$$

where

Q = flow per unit area;

t = time;

C = concentration of the diffusing substance, in this case moisture;

x = distance in the direction of flow, measured normal to the surface;

D = diffusion coefficient.

When Q is measured in gm/cm^2, t in s, C in gm/cm^3, and x in cm, D has the dimensions cm^2/s.

Assuming a linear moisture diffusion profile and constant diffusion coefficient independent of moisture content, Ast estimated the moisture diffusion coefficient D as

$$D = -\left.\frac{dQ}{dt}\Big/\frac{dC}{dx}\right|_{x=l}, \tag{7.16}$$

where $x = l$ is the dry boundary and the moist boundary is at $x = 0$.

To determine the time-rate of moisture flow through the paper, the container containing the salt solution and the paper is periodically weighed to determine the loss in weight due to moisture diffusion from the salt solution through the paper to be

absorbed by the drierite. Determination of dC/dx, the moisture gradient in the paper, involved two major assumptions:

1) that the inner and outer surfaces of each paper pad were in moisture equilibrium with the respective ambients to which they were exposed, and

2) that the moisture content of the paper pad varied linearly with distance into the paper (i.e. C was a linear function of x and that dC/dx was therefore a constant).

The first assumption can be thought of as diffusion through an infinitely thin boundary layer. Therefore, the diffusion time approaches zero, and it is accurate to assume that the boundary is in moisture equilibrium with the ambient. This is also the assumption this thesis uses. The second assumption introduces error because the diffusion coefficient is a function of concentration, and thus the concentration profile is non-linear.

The original measured data and Ast's estimated diffusion coefficient are listed in Table 7.3. The paper thickness is l, T is the temperature, C_0 is the moisture content of the paper at the dry side, C_1 is the moisture content at the moist side, $\int \frac{dQ}{dt} da$ is the average rate of moisture transmission through the entire surface area, and dC/dx equals $(C_1 - C_0)/l$. Some of the last digits in the estimated diffusion coefficient are slightly different than Ast listed in Table II of his report due to Ast's round off errors. Table 7.3 results are computed in *Excel* where only the final result is rounded off. However, the value of dC/dx for Test No.1 is listed incorrectly in the original report as 1.18 rather than 1.16.

The general governing moisture diffusion equation is

$$\frac{\partial C}{\partial t} = \frac{\partial}{\partial x}(D\frac{\partial C}{\partial x}). \tag{7.17}$$

In steady state, $\frac{\partial C}{\partial t} = 0$, therefore

$$D\frac{dC}{dx} = A, \tag{7.18}$$

where A is a constant. Integration of (7.18) over dx gives

$$\int DdC = Ax + B, \tag{7.19}$$

No.	l (cm)	T (°C)	C_0 (gm/cm^3)	C_1 (gm/cm^3)	$\left\lvert\int \frac{dQ}{dt} da\right\rvert$ (gm/hr)	dC/dx (gm/cm^4)	D (cm^2/day)
1	0.0515	15.6	0	0.0595	0.0372	1.16	0.0309
2	0.0518	30	0	0.0552	0.093	1.07	0.0838
3	0.0518	51	0	0.0170	0.113	0.328	0.331
4	0.0518	51	0	0.0358	0.254	0.691	0.353
5	0.0518	82	0.00195	0.0312	2.2	0.565	3.74
6	0.126	15.6	0	0.0595	0.0252	0.472	0.0512
7	0.126	30	0	0.0552	0.0582	0.438	0.128
8	0.128	82	0.002	0.0312	1.09	0.228	4.59

Table 7.3: Ast's original measured data and estimated concentration independent diffusion coefficient for various levels of moisture concentration and temperature [63].

where B is a constant. When D is independent of C, D is constant for fixed temperature, therefore (7.19) becomes

$$C = \frac{A}{D}x + \frac{B}{D}, \tag{7.20}$$

i.e. C is a linear function of x. Ast's assumption is correct only when the diffusion coefficient is not a function of moisture concentration. However, earlier work [46, 100–102] and our experiments show that the diffusion coefficient is a function of moisture concentration. Therefore, errors will be introduced by Ast's assumption, especially when the concentration is high.

Assuming the empirical form of the moisture and temperature dependence in (7.5)

$$D(C,T) = D_0 e^{kC + E_a(1/T_0 - 1/T)}, \tag{7.21}$$

(7.19) becomes

$$\int D_0 e^{kC + E_a(1/T_0 - 1/T)} dC = Ax + B, \tag{7.22}$$

which integrates to

$$D_0 e^{kC + E_a(1/T_0 - 1/T)}/k = Ax + B, \tag{7.23}$$

with solution

$$C = \frac{1}{k}\left[\ln(k(Ax+B)/D_0) - E_a(1/T_0 - 1/T)\right]. \tag{7.24}$$

	D_0 (m^2/s)	k	E_a ($^\circ$K)
Ast Data	2.25E-11	0.1955	8834
Foss	2.62E-11	0.5	8140
Du	0.67E-12	0.45	7646

Table 7.4: Estimated coefficients for formula (7.5) from Ast's data and those of Foss and this thesis work.

Using the two boundary conditions at constant temperature T

$$\begin{cases} C = C_0\,, & x = 0 \\ C = C_1\,, & x = l \end{cases} \tag{7.25}$$

the two integration constants are

$$A = D_0 e^{E_a(1/T_0 - 1/T)}(e^{kC_1} - e^{kC_0})/(kl), \tag{7.26}$$

$$B = D_0 e^{kC_0 + E_a(1/T_0 - 1/T)}/k. \tag{7.27}$$

Therefore C at temperature T can be expressed as

$$C(x) = \frac{1}{k}\ln\left[\frac{(e^{kC_1} - e^{kC_0})}{l}x + e^{kC_0}\right], \tag{7.28}$$

and the rate of moisture diffusion is

$$\left|\frac{dQ}{dt}\right| = D\frac{dC}{dx} = A. \tag{7.29}$$

Knowing $\left|\frac{dQ}{dt}\right|$, C at either boundary, and T from the eight sets of measurements of Table 7.3, a least squares fit algorithm is used to find values of D_0, k, and E_a as listed in Table 7.4. The original data of Table 7.3 converted to SI units are also listed in Table 7.5.

The moisture profiles are shown in Figure 7.16 for a linear concentration distribution and for the distribution of (7.28) with diffusion coefficient as a function of concentration. This at least partly explains why using the concentration independent diffusion coefficient leading to the spatial linear concentration profile, Ast obtained non-physical values of diffusion coefficient that depended on the thickness of the sample.

No.	l (m)	T (K)	C_0 (%)	C_1 (%)	$\|dQ/dt\|$ (% m/s)
1	5.15E-04	288.6	0.000	9.15	6.36E-07
2	5.18E-04	303	0.000	8.49	1.59E-06
3	5.18E-04	324	0.000	2.62	1.93E-06
4	5.18E-04	324	0.000	5.51	4.34E-06
5	5.18E-04	355	0.300	4.80	3.76E-05
6	1.26E-03	288.6	0.000	9.15	4.31E-07
7	1.26E-03	303	0.000	8.49	9.95E-07
8	1.28E-03	355	0.308	4.80	1.86E-05

Table 7.5: Ast's original data converted to SI units.

Comparison of the diffusion coefficient $D(\times 10^{-10}$ m^2/s) for the tested conditions by different investigators is given in Table 7.6. Ast1 are those values obtained by Ast [63] using a linear concentration distribution. Ast2 is estimated from Ast's original data in this thesis using the empirical diffusion coefficient formula (7.5) with temperature and moisture dependence. Foss' formula consistently gives higher values than others possibily due to some numerical errors.

7.7 Summary

Real-time on-line measurement of the moisture diffusion process is achieved in this research project. For the first time, the time evolution of the moisture spatial profile in oil-free transformer pressboard has been estimated non-destructively. The moisture diffusion profiles have been obtained using the three-wavelength interdigital sensor with a fast algorithm suitable for on-line monitoring with real time display of results. The understanding of moisture-related processes in power transformers can be enhanced with this methodology.

There is no analytical solution of the time dependent moisture profiles for a moisture diffusion coefficient as a function of temperature and moisture concentration. Numerical methods of solving the non-linear diffusion equation are developed. The calculated results extend the existing small data base of diffusion studies. Literature results of

No.	Ast1	Ast2			Foss		
	D	$D(C_0)$	$D(C_1)$	$\bar{D}$	$D(C_0)$	$D(C_1)$	$\bar{D}$
1	0.358	0.0857	0.513	0.299	0.107	10.4	5.28
2	0.970	0.367	1.93	1.15	0.411	28.7	14.54
3	3.83	2.43	4.05	3.24	2.34	8.66	5.50
4	4.08	2.43	7.13	4.78	2.34	36.8	19.56
5	43.3	27.9	67.1	47.50	24.4	232	128.0
6	0.593	0.0857	0.51	0.299	0.107	10.4	5.28
7	1.48	0.37	1.93	1.15	0.411	28.7	14.54
8	53.1	27.9	67.137	47.5	24.5	232	128.06

Table 7.6: Comparison of the diffusion coefficient $D(\times 10^{-10}$ m^2/s) for the tested conditions by different investigators. Ast1 are those values obtained by Ast [63] using a linear concentration distribution. Ast2 is estimated from Ast's original data in this thesis using the empirical diffusion coefficient formula (7.5) with temperature and moisture dependence listed in Table 7.4. Foss' is estimated using (7.5) with temperature and moisture dependence listed in Table 7.4 given in [62]. $\bar{D} = (D(C_0) + D(C_1))/2$ is an average diffusion coefficient.

diffusion coefficient for cellulose insulation are compared and analyzed. The estimated diffusion coefficient is much smaller than the value reported by Foss, but is close to that of Quarshie at University of Nottingham. Numerical inconsistencies were found in Foss' study.

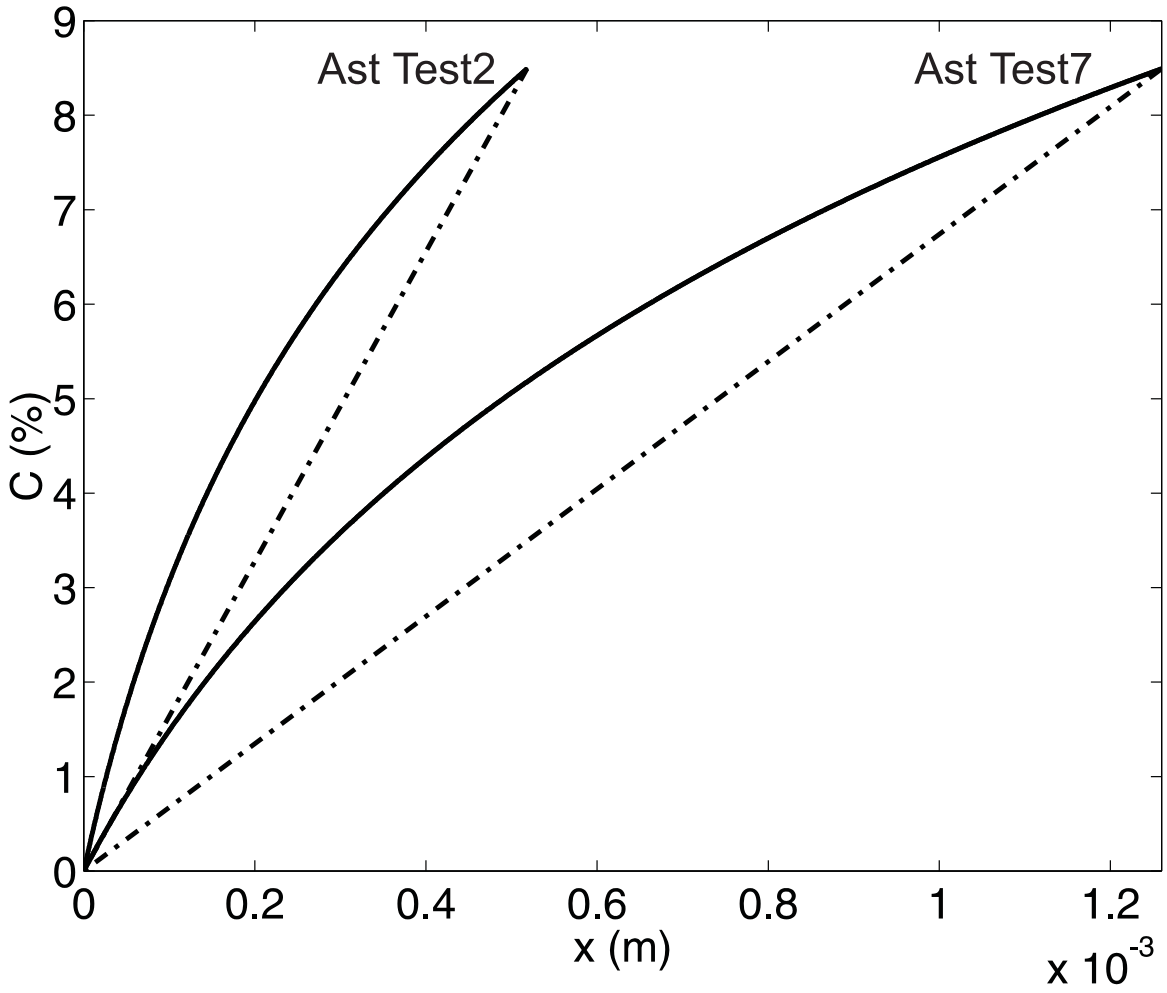

Figure 7.16: Comparison of the moisture profiles for a constant diffusion coefficient with linear concentration distribution (dash-dot lines) and diffusion coefficient as a function of concentration at 30°C with a nonlinear concentration distribution (solid lines). The top curves are for Ast's test 2 with sample thickness of 0.0518 cm and the lower curves are for Ast's test 7 with sample thickness of 0.126 cm as listed in Table 7.3.

Chapter 8

Couette Experiments

8.1 Couette Facility

Electrification and moisture diffusion processes can be isolated and studied in the laboratory with a compact apparatus called the Couette Facility (shown in Figure 8.1), originally developed as part of an Electric Power Research Institute project to study flow electrification [39, 89, 104, 105]. It is designed to create a controlled turbulent flow of oil between coaxial cylinders with inner cylinder rotating. The speed of rotation of the inner cylinder, pressure, temperature, the moisture content, and electric field in the annulus are computer-controlled. Thus, the environment inside a power transformer can be simulated in various operating regimes.

The Couette Facility includes a Varian vacuum chamber, Varian vacuum probe, GE vacuum pump, and various plumbing parts. The monitoring and controlling instruments are: Tettex Return Voltage Recovery Meter, Keithley Electrometer, Absolute Charge Sensor, Omega temperature probe and controller, Harley moisture sensor, conductivity cell, Current loop receiver for Harley moisture sensor, Cole Parmer Pump Controller, Ratiotrol Motor, Wavetek Arbitrary Waveform Generator Model 75, and Kenmore Dehumidier. Data acquisition and instrument control is accomplished using serial communications, GPIB protocol, digital I/O interfaces, A/D interfaces, and D/A interfaces. A schematic of the facility is shown in Figure 8.1 and a picture of the facility

is shown in Figure 8.2. The gap between inside cylinder and outside cylinder is one inch.

The possible dependence of the flow electrification hazard condition on moisture diffusion is illustrated in Figure 8.3. When the transformer is not in operation, the paper/oil system is in equilibrium at low temperature (20°C ambient) and operates at point A. When the transformer is energized, the temperature increases abruptly to 70°C. The thermal time constant of the cellulose insulation is much smaller than the mass transfer time constant associated with moisture diffusion. The ratio of the thermal diffusivity of oil-soaked cellulose to the mass diffusivity of oil-soaked cellulose under equilibrium 50% relative humidity and 80°C temperature conditions is of order of 10^4 [62]. The oil/paper interface reaches a new equilibrium essentially instantaneously while the moisture diffusion process from the pressboard takes a long time. The oil/paper interface instantaneously moves to the new low paper moisture equilibrium point B. A low concentration in moisture causes a highly insulating dry zone. After a long time, moisture deep in the pressboard diffuses to the interface and the whole system reaches equilibrium at point C, assuming a large amount of pressboard acting as a near infinite source of moisture.

During the transition period, the highly insulating interface between oil and paper allows static charge accumulation, which can rise to high enough values to cause partial discharges causing gas formation. This gas can rise to the high voltage region of a transformer and cause electrical breakdown that can result in catastrophic failures. By simulating the temperature transition, the three-wavelength sensor can measure the moisture diffusion profile and thus study the flow electrification phenomenon.

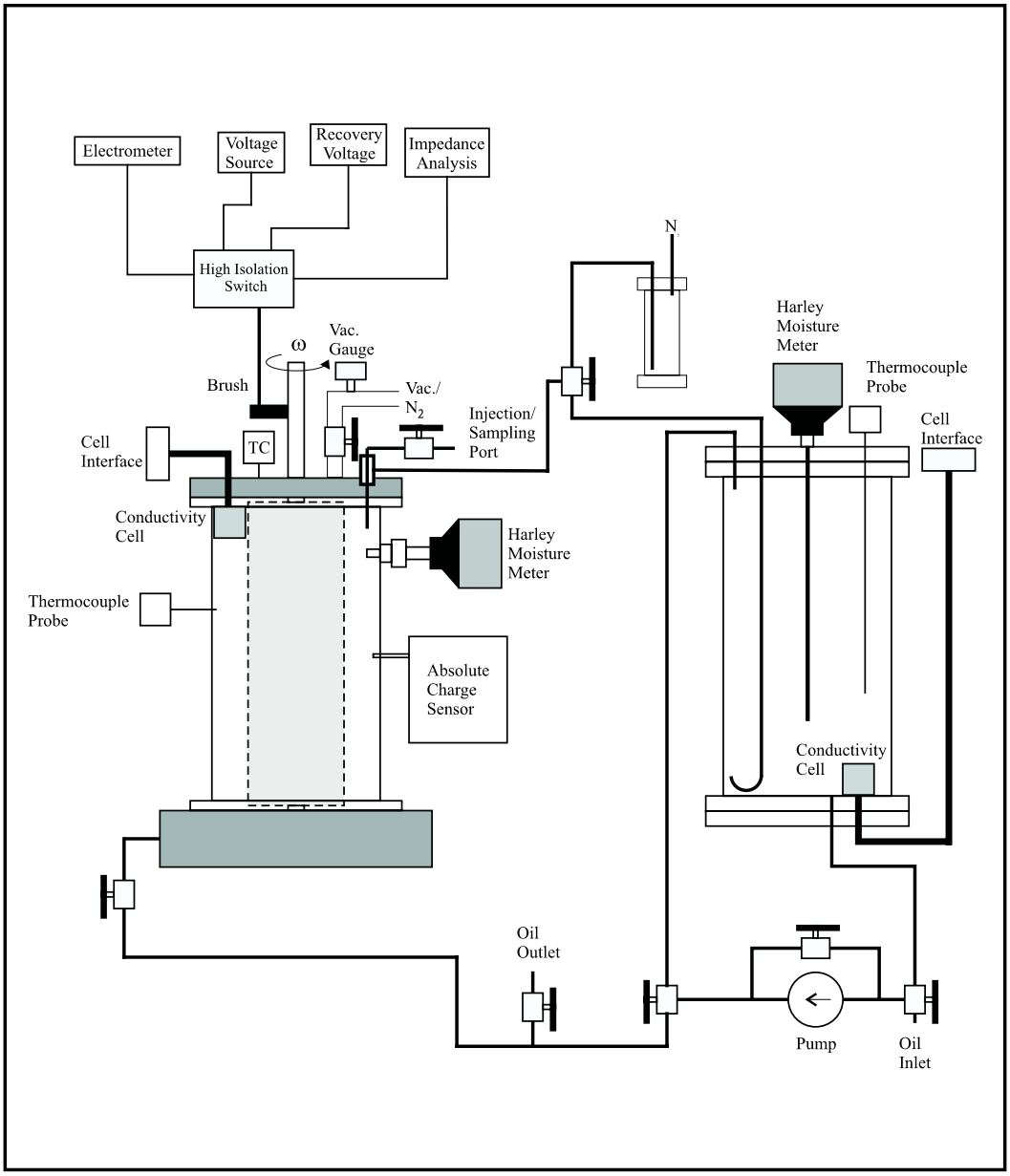

Figure 8.1: Couette Facility for monitoring moisture diffusion in oil and pressboard and to determine its effect on flow electrification [89].

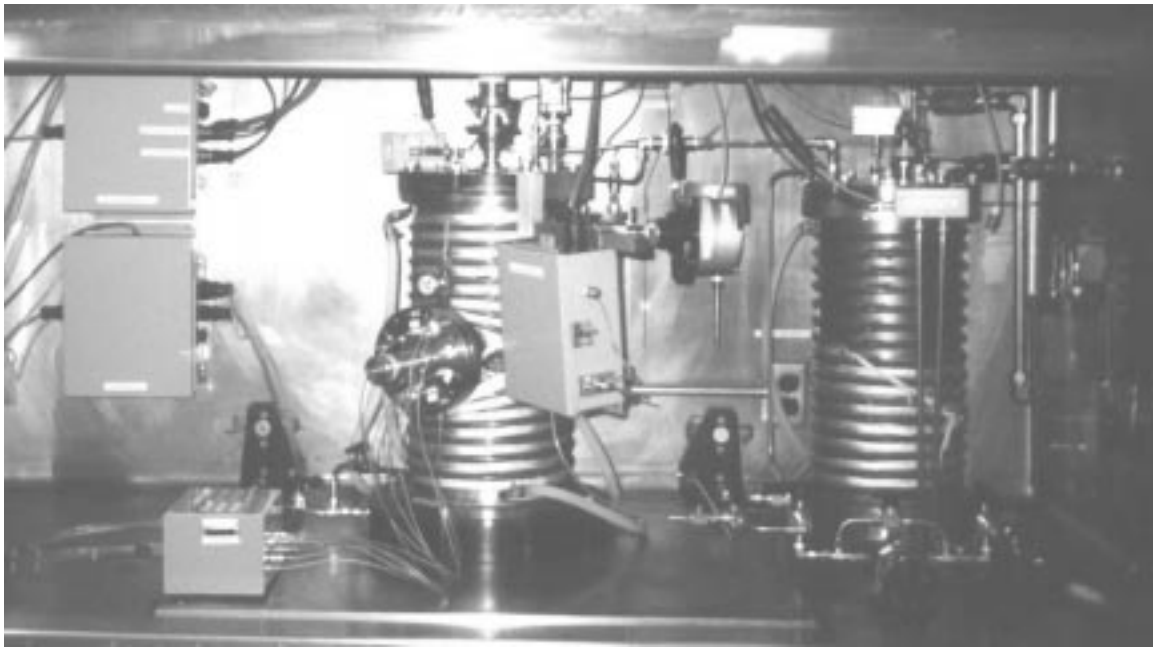

Figure 8.2: The Couette Facility inside the stainless steel hood.

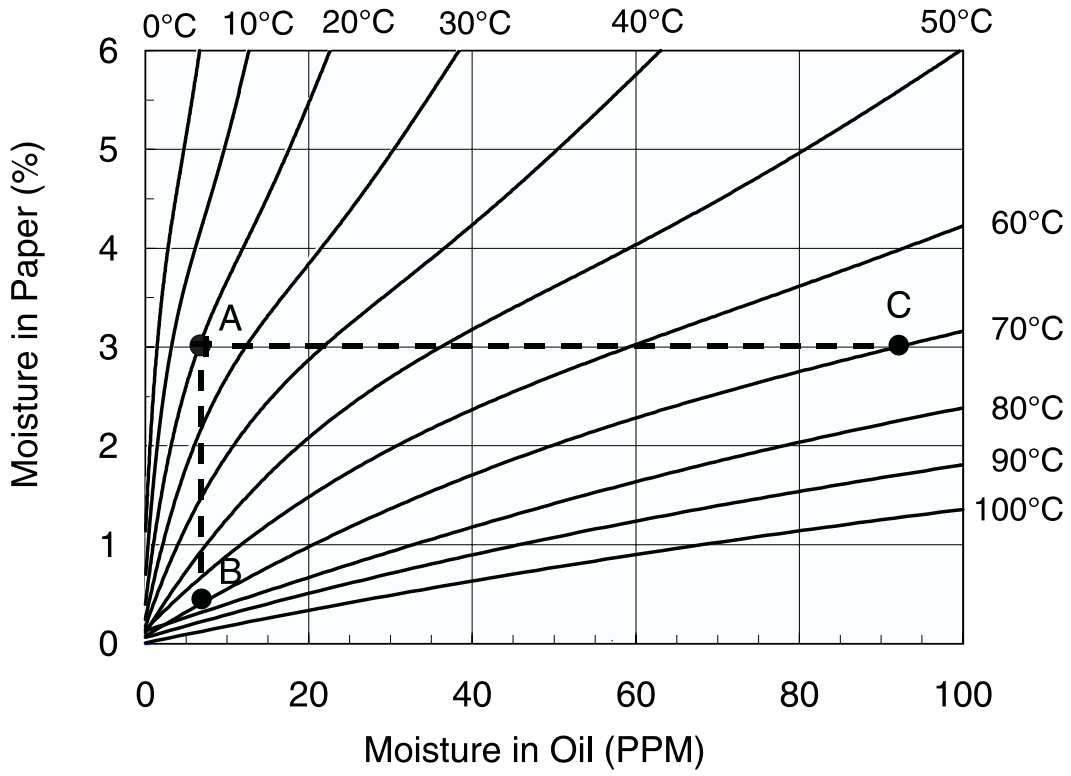

Figure 8.3: Flow electrification hazard condition analysis due to moisture diffusion as a step change in temperature from 20° C to 70° C moves the initial moisture equilibrium at A instantaneously to B, and then over many diffusion time constants the system reaches the new equilibrium point C at 70° C.

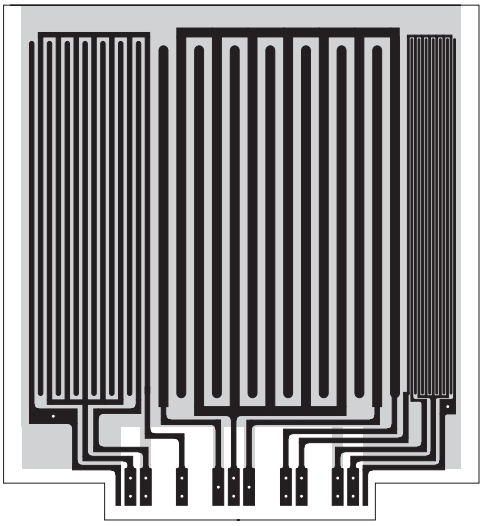

Figure 8.4: The modified design of the three-wavelength sensor to fit the Couette Facility.

8.2 Modified Sensor for the Couette Facility

The three-wavelength sensor is installed at the side port of the Couette Facility. The modified Couette sensor is shown in Figure 8.4. It is modified to fit into the side port of the Couette Facility. The total area is smaller than the regular Teflon sensor of Figure 6.1 due to the limited port size. This is accomplished by reducing the number of guard electrodes outside the sensing area. It is justified for the short-circuit mode as the guard electrodes are all firmly grounded and the outer cylinder of the Couette Facility is also grounded, therefore reducing the extra periods of guard electrodes will not significantly affect the field distribution. The signal cable comes into contact with the sensor leads perpendicularly from the back instead of the front for the bench-top apparatus. This has two advantages: first, the sensor leads would not be bent, thus avoiding a possible broken lead problem; second, having the wires coming from the back plane provides intimate contact for the sensor to the pressboard. In the bench-top experiments the pressboard is cut so as not to cover the lead-to-wire connecting section, whereas in the Couette Facility the pressboard covers the entire outer cylinder, therefore anything protruding from the sensor surface will affect the contact.

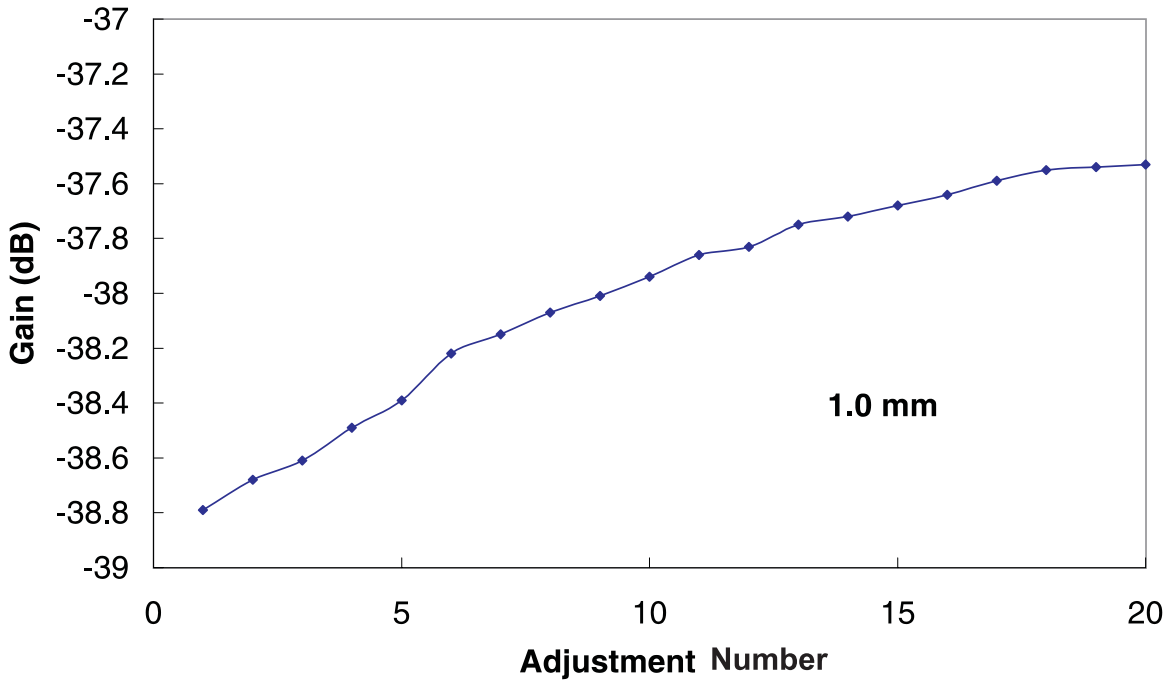

Figure 8.5: The 1 mm wavelength sensor response to the adjustment of the compression device at $f = 10^{3.796}$=6252 Hz. Each adjustment corresponds to an equal turning torque. As the sensor gets closer to the pressboard with increasing torque, the transcapacitance increases and so does the gain.

An adjustable compression device is used to keep the sensor in close contact with the pressboard. The measured gain at high frequency serves as an indication of the contact quality. Shown in Figure 8.5 is the 1 mm wavelength sensor response to the adjustment of the compression device at $f = 10^{3.796}$=6252 Hz. With increase of the adjustment number, the sensor gets pushed closer to the pressboard. The closer the sensor to the pressboard, the larger the transcapacitance, therefore the larger the gain. When the gain reaches a constant, the sensor is considered to have a good quality contact with the sample.

8.3 Moisture Diffusion Experiments

These experiments continue and extend earlier work by using the Couette Facility with the Absolute Charge Sensor (ACS) and terminal voltage/current measurements to monitor flow electrification phenomena. To measure moisture diffusion processes the inner surface of the outer cylinder is covered with pressboard, and the annulus is filled with air or transformer oil. The sensor is mounted in the side port of the Couette Facility, so that its surface is in intimate contact with the pressboard. Dielectrometry measurements are taken of moisture profiles in oil-free and oil-impregnated pressboard as a function of time, moisture and temperature. The ultimate goal of these experiments is to monitor and control the moisture dynamics inside the pressboard and to understand the effects of moisture on flow electrification.

The bench-top tests show that the diffusion coefficient measured for oil-free pressboard is much smaller than some reported values as discussed in Chapter 7. The Couette Facility results can confirm our original results of Chapter 7 in the bench-top apparatus.

The Couette measurements presented here include:

1. Tests of oil-free pressboard in the Couette Facility to measure the diffusion coefficient as a function of moisture and temperature and comparison with bench-top results;

2. Measurement of the drying process by circulating dry air flow;

3. Testing of dynamics for oil-impregnated pressboard with a step change in temperature.

Most of the measurements in this chapter and the next chapter were performed by visiting Prof. S. H. Kang under the author's supervision.

8.4 Measurement Results for Oil-Free Pressboard

Oil-free 1.15 mm thick EHV-Weidmann Hi-Val pressboard is installed adjacent to the inner wall of the outer cylinder of the Couette facility. The diameter of the pressboard cylinder is 7.92 inches with a length of 16.125 inches.

8.4.1 Wetting Process in Couette

Similar to the bench-top experiment, measurements are taken for moisture diffusion into pressboard at various temperature levels. The test results exhibit the same traits as the bench-top experiments. The experiment for 60°C is presented here as an example. The air relative humidity inside the Couette Facility during the wetting process is shown in Figure 8.6. It takes more time for the system to reach constant relative humidity than the bench-top apparatus due to the large volume of dry pressboard in the Couette Facility. The pressboard used in the Couette Charger has a total mass of more than 250 g, whereas each sample piece in the bench-top experiment has a mass of only 6 g. The calculated transcapacitance and transconductance at 60°C are shown in Figure 8.7.

The moisture profiles as a function of time t in hours constructed from the three-wavelength sensor and relative humidity sensor measurements using the method discussed in Section 7.3 is shown at the top of Figure 8.8. The theoretical moisture profiles using a diffusion coefficient that is a function of moisture concentration and temperature is shown at the bottom of Figure 8.8. The temperature dependence E_a and moisture dependence k used are the same as those listed in Table 7.1. The base diffusion coefficient D_0 is adjusted to be 3×10^{-12} m^2/s to match the experimental profile. This is 4.5 times that of the bench-top results. There are two major reasons for the diffusivity in the Couette experiment to be larger than that of the bench-top apparatus:

1. The pressboard in the bench-top apparatus is tightly compressed which slows the moisture diffusion. Quarshie [99] reported a 1.3 times of difference for longitudinal

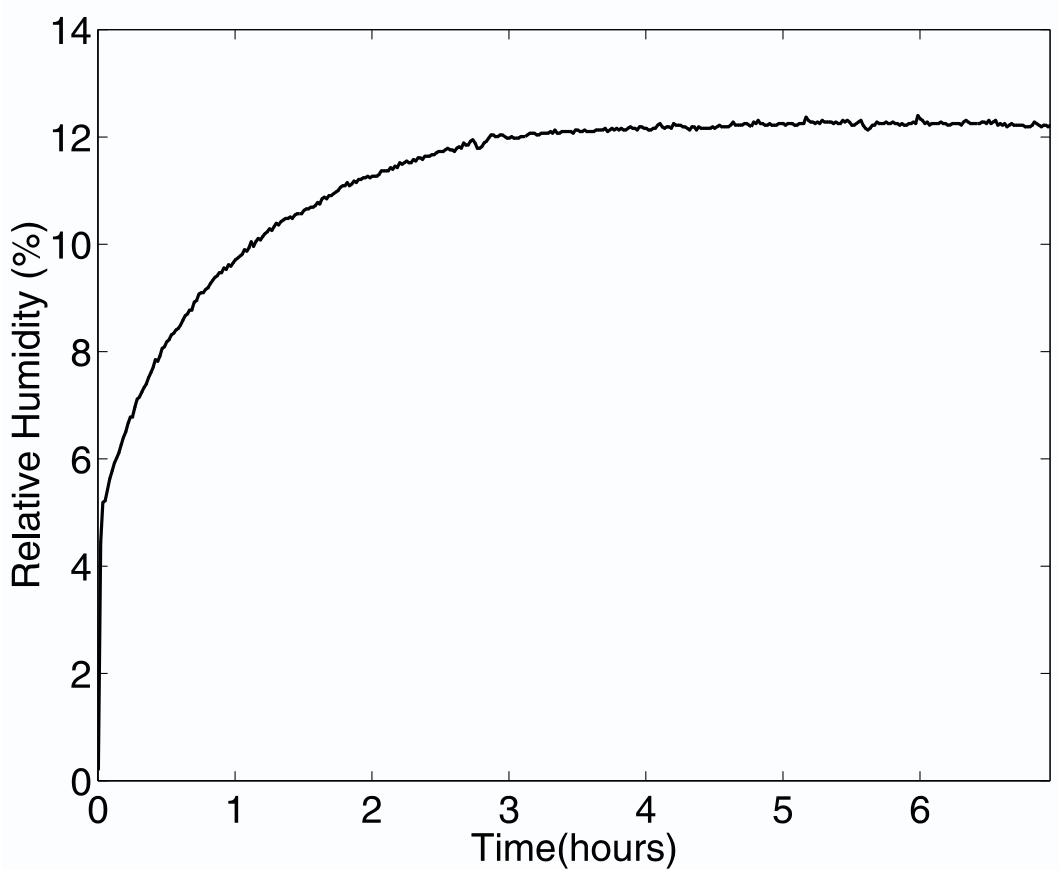

Figure 8.6: The air relative humidity of the Couette Charger during the wetting process at 60°C.

diffusion coefficient between non-clamped and clamped T-IV pressboard.

2. As shown in Figure 7.1, the test structure in the bench-top apparatus is held together by a porous plate on the front which prevents the pressboard from being completely exposed to the humid air. In the Couette Facility, the pressboard/air interface is left completely exposed.

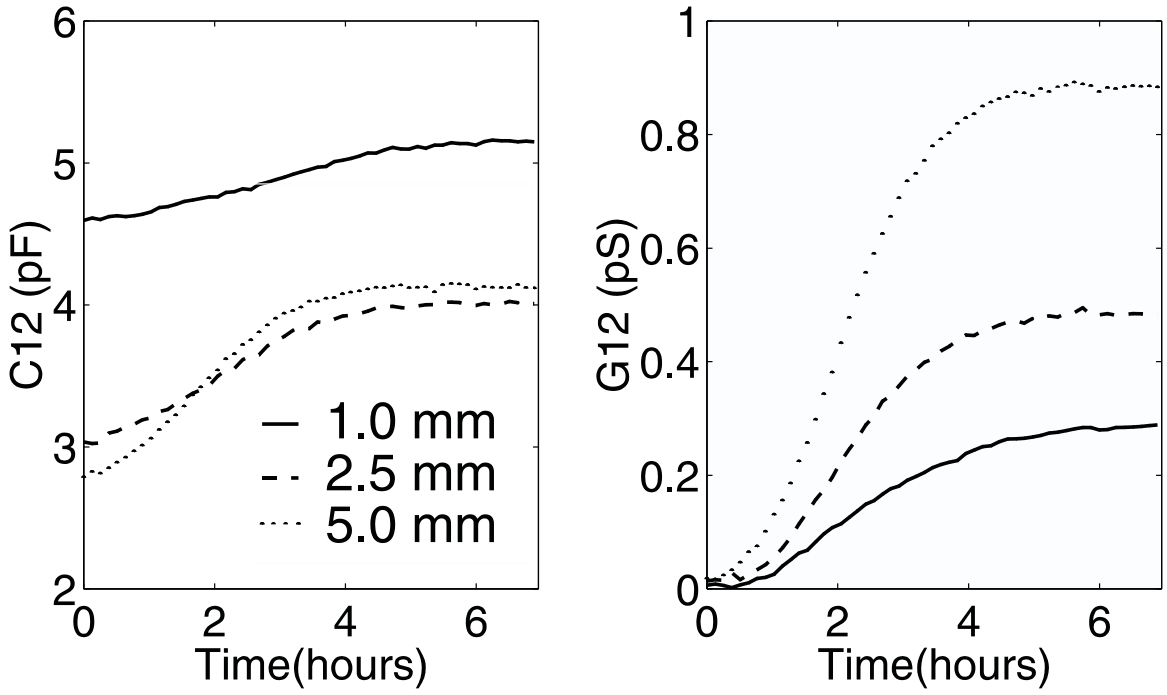

Figure 8.7: The calculated transcapacitance and transconductance at f=0.1 Hz for oil-free pressboard at 60°C.

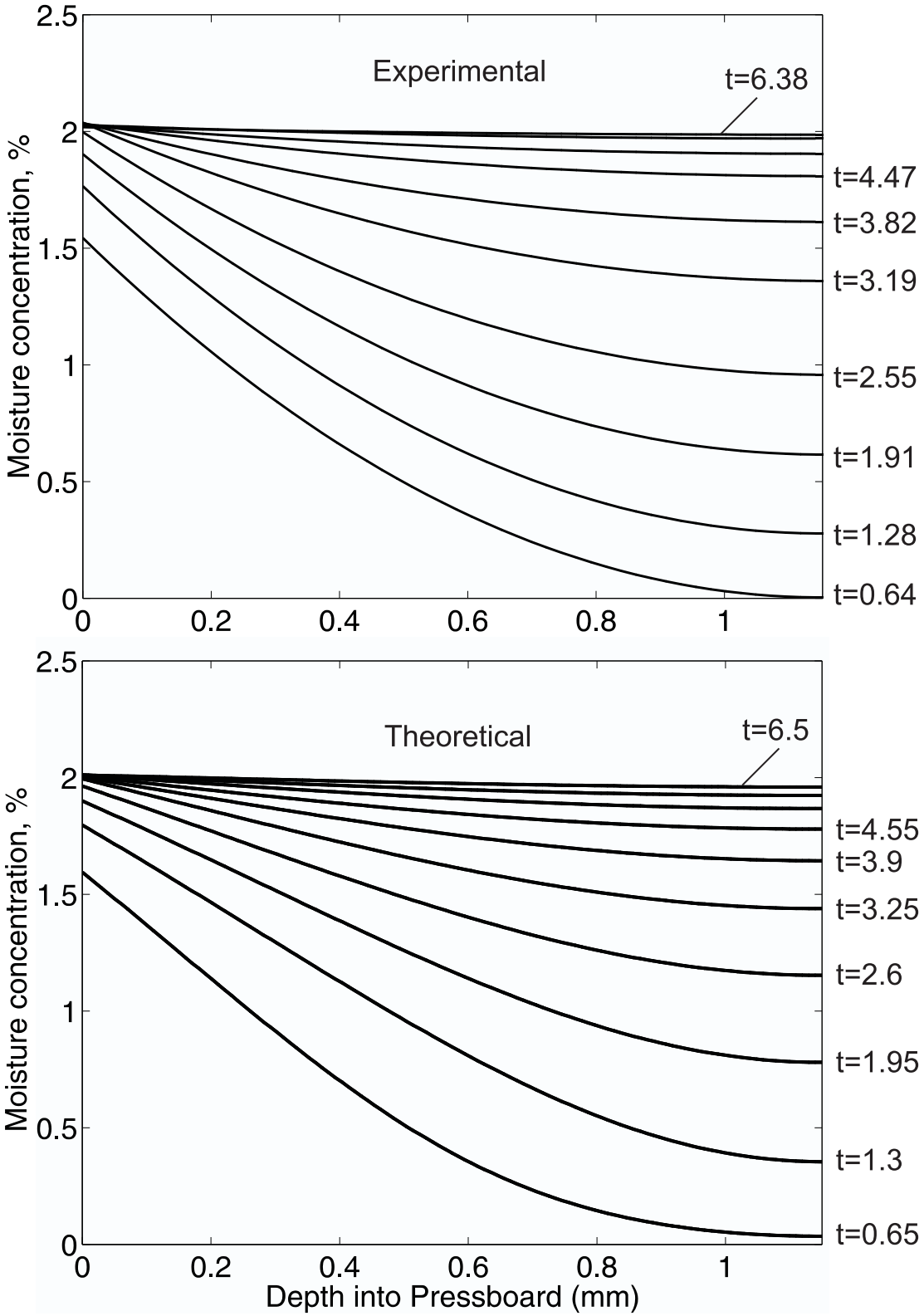

Figure 8.8: The moisture profile obtained from sensor measurements (top) and simulated (bottom) for the wetting process of oil-free pressboard at 60° C with time t in hours.

8.4.2 Drying Process in the Couette Facility

Most of the thesis experiments focus on the wetting processes of the pressboard. The reverse process, moisture leaving the pressboard, was implemented in the Couette Facility. The system was in equilibrium with ambient air at 17.8% relative humidity and 70°C prior to drying. The frequency sweep is shown in Figure 8.9. Air flow dried by drierite was then circulated into the Couette Charger. The Couette Charger relative humidity and temperature during the drying process are shown in Figure 8.10. The small step at about 1.6 hours is due to the change of saturated drierite.

The method for deriving moisture profiles from the sensor measurements discussed in Section 7.3 does not work well for the drying case. The linear assumption between the transcapacitance and the moisture content gives a non-monotonic moisture profile. Further study is needed for the drying process.

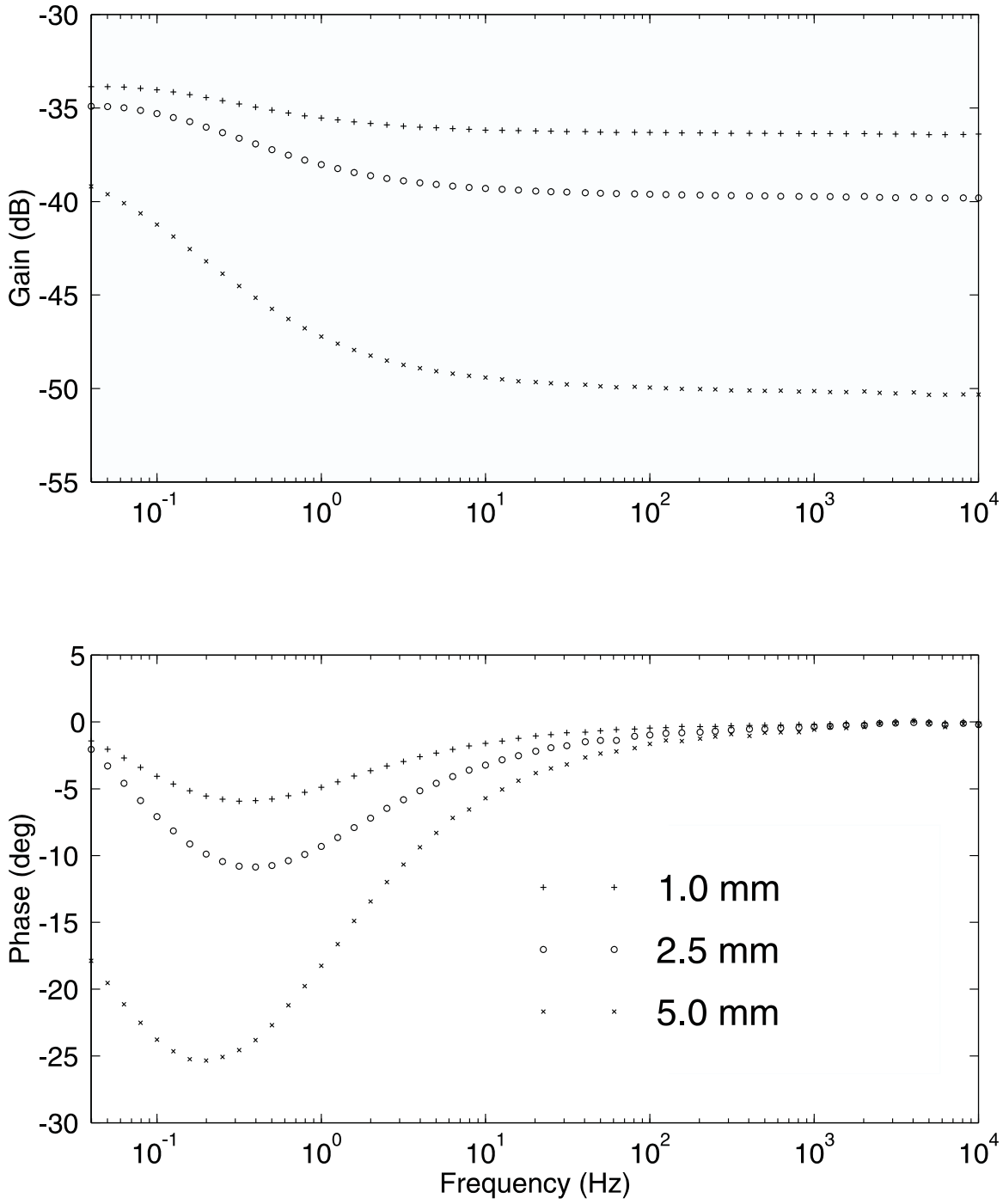

Figure 8.9: The frequency sweep of oil-free pressboard in equilibrium with ambient air at 17.8% relative humidity and 70°C prior to drying.

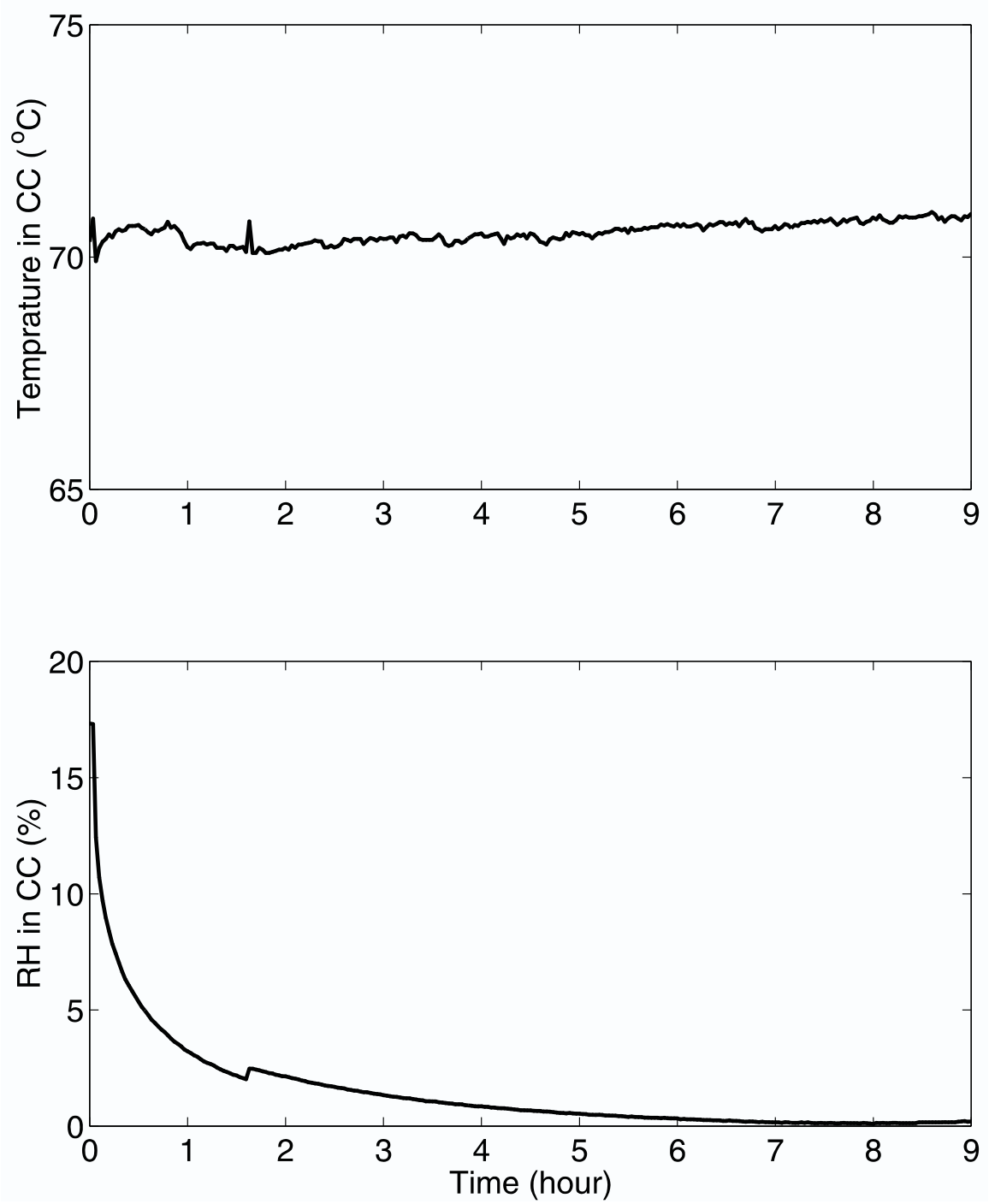

Figure 8.10: The air temperature and relative humidity of the Couette Charger during the drying process.

The measured gain and phase at $f = 0.1$ Hz of the three-wavelength sensor in the Couette Charger for oil-free pressboard during the drying process are shown in Figure 8.11. As the moisture left the pressboard, both transconductance and transcapacitance decreased. The sensor response can be visualized as the curves in Figure 8.9 shifting to the left of the frequency axis, i.e. the gain decreases to a constant and the phase goes to zero. Because the initial position at $f = 0.1$ Hz is at the left side of the phase valley in Figure 8.9, the phase change in Figure 8.11 actually moves through to the valley first and then comes back to zero.

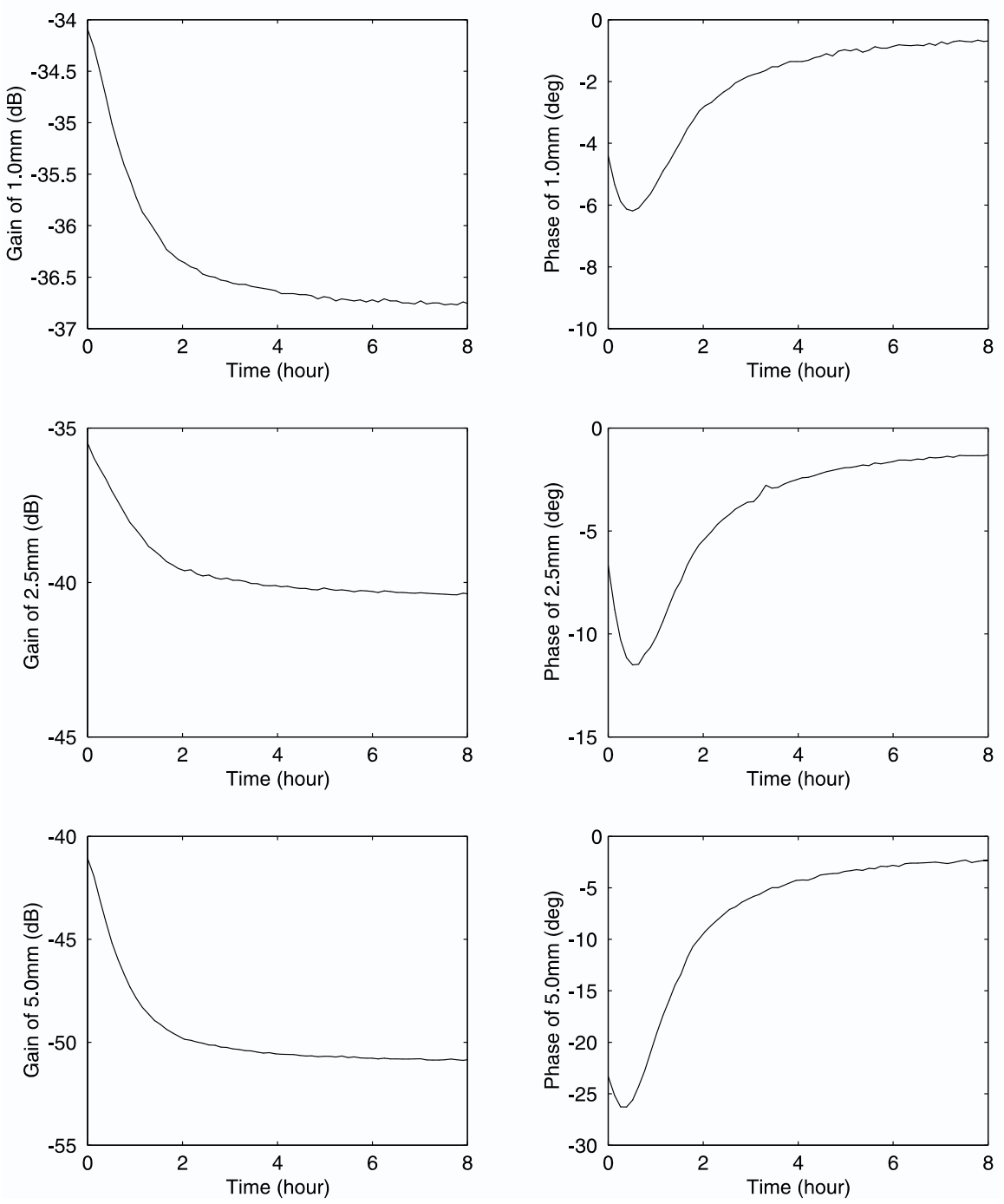

Figure 8.11: The measured gain and phase at $f = 0.1$ Hz of the three-wavelength sensor in the Couette Charger for oil-free pressboard during the drying process.

8.5 Measurement Results for Oil-Impregnated Pressboard

8.5.1 Measurements of Temperature Transient

The system was sealed and left undisturbed at 30°C for about 10 days. At time t=0, the temperature of the Couette was set to increase from 30°C to 70°C. The cooling system was turned off, thereby causing the ripple in the controlled temperature shown in Figure 8.12.

The system was sealed and stationary. The relative humidity sensor tip was very close to the pressboard-oil interface, therefore it closely measured the migration of moisture from the pressboard interface to oil. As discussed in Chapter 3, with the increase of temperature, the oil can hold more moisture than at low temperature, therefore the moisture in oil at the interface increases from about 15 ppm to about 58 ppm as shown in Figure 8.12. Because there was no mixing of the oil, and the diffusion time for oil-impregnated pressboard is much longer than for oil-free pressboard (refer to Table 3.2), the moisture redistribution predominantly occurred at the interface. Within the 30 hours of monitoring the temperature effects dominated. The interdigital sensor measurements in Figure 8.13 show no change for the first 30 hours except the beginning temperature transient period.

The transcapacitance and transconductance calculated from the measurements are shown in Figure 8.14. With the increase of temperature, both permittivity and conductivity increase, and therefore C_{12} and G_{12} should all be increased. The only exception is C_{12} for the 1 mm wavelength sensor. This has been repeatedly observed in the experiments. A possible cause is, due to different thermal expansion coefficients of the adjustable compression device and pressboard, the contact between the sensor and the pressboard might be changed due to the change of temperature. If the increase of C_{12} due to the increase of permittivity is smaller than the decrease of C_{12} due to the increase of gap, the overall effect will be a decrease of C_{12}. Since the 1 mm wavelength

is most sensitive to the gap, it is not surprising to see that the effect only appears for the 1 mm wavelength.

The temperature and the gain of the 5 mm wavelength are plotted on the same graph in Figure 8.15 for comparison. The precise overlap of the two "sinusoids" clearly demonstrates that the interdigital sensor instantaneously detects the dielectric property change due to the temperature change.

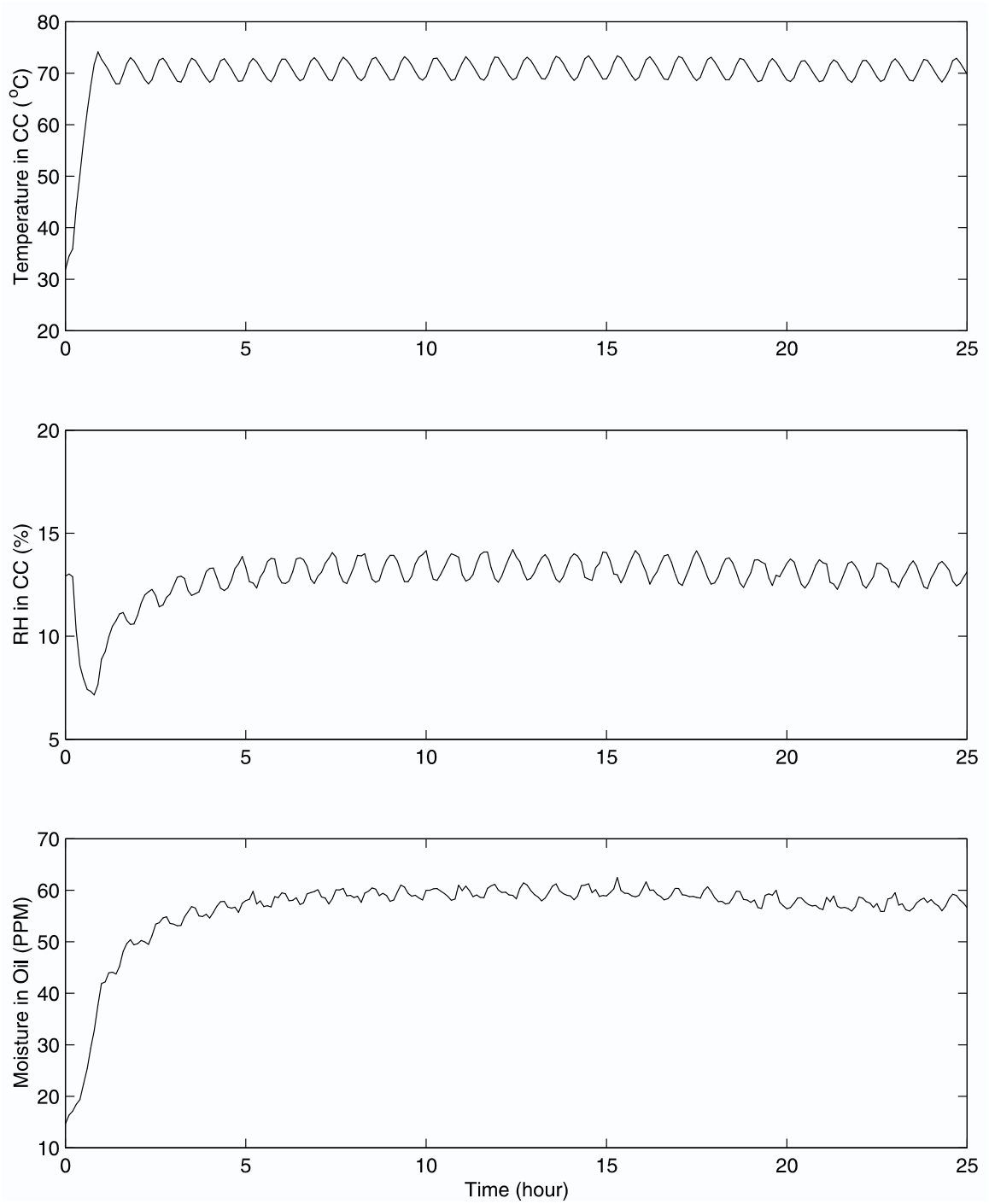

Figure 8.12: The oil temperature, relative humidity, and moisture concentration conditions in the Couette Charger when the temperature controller was set to 70° C. The cooling system was turned off, thereby causing the ripple in the controlled temperature.

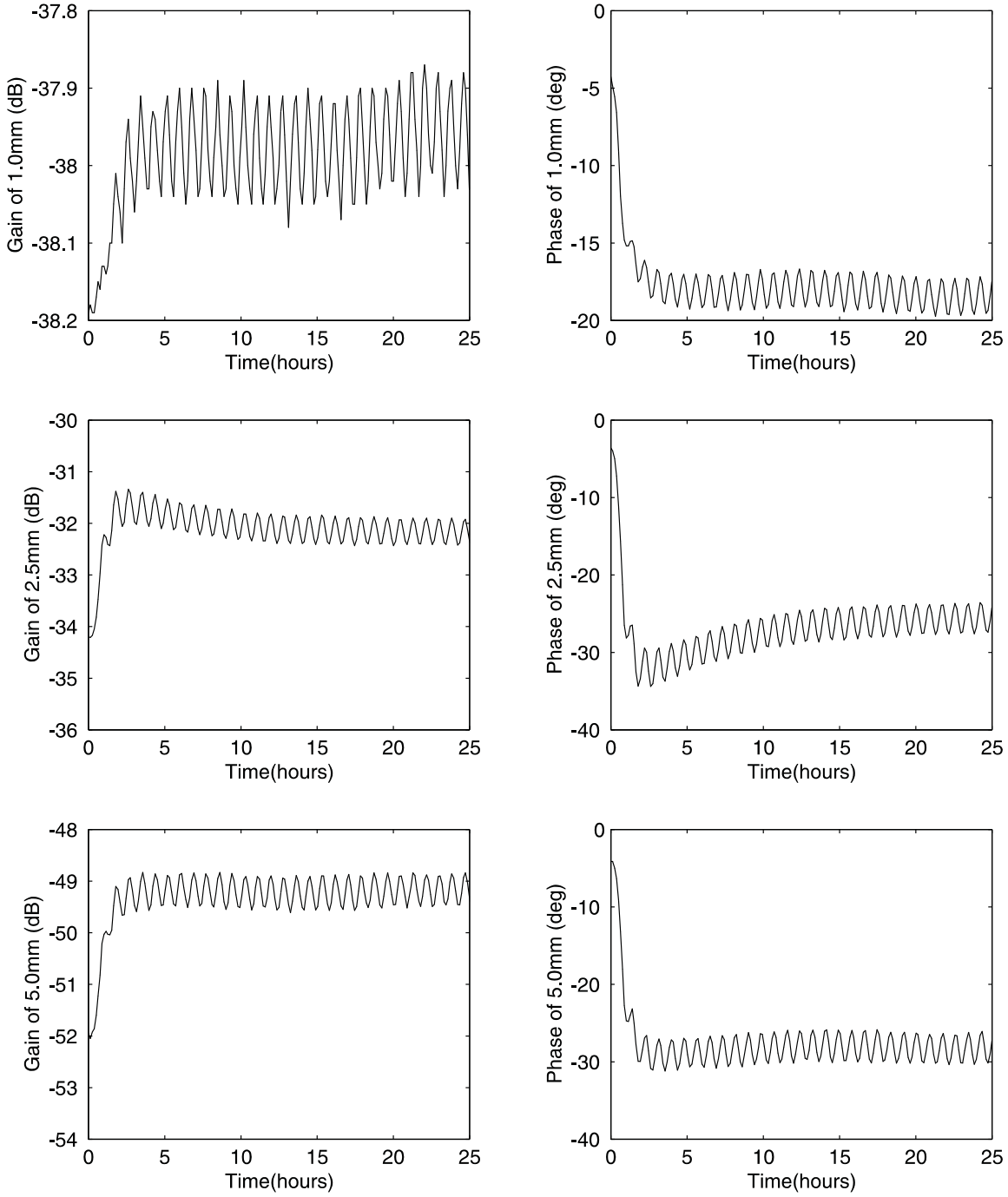

Figure 8.13: The measured gain and phase of the oil-impregnated pressboard at f=0.1 Hz when the temperature controller was set from 30°C to 70°C.

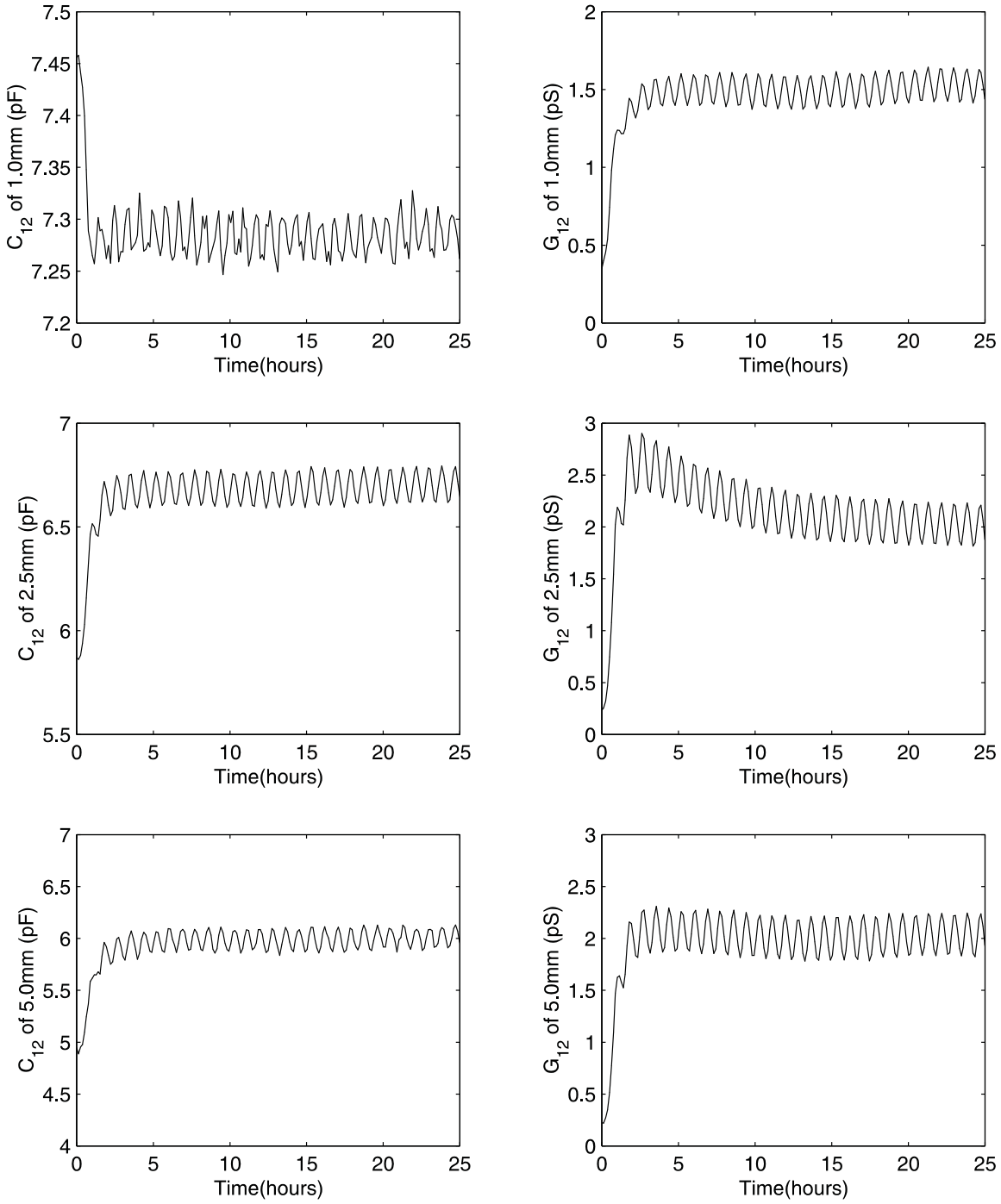

Figure 8.14: The transcapacitance and transconductance of the oil-impregnated pressboard from measurements at f=0.1 Hz when the temperature controller was set from 30°C to 70°C.

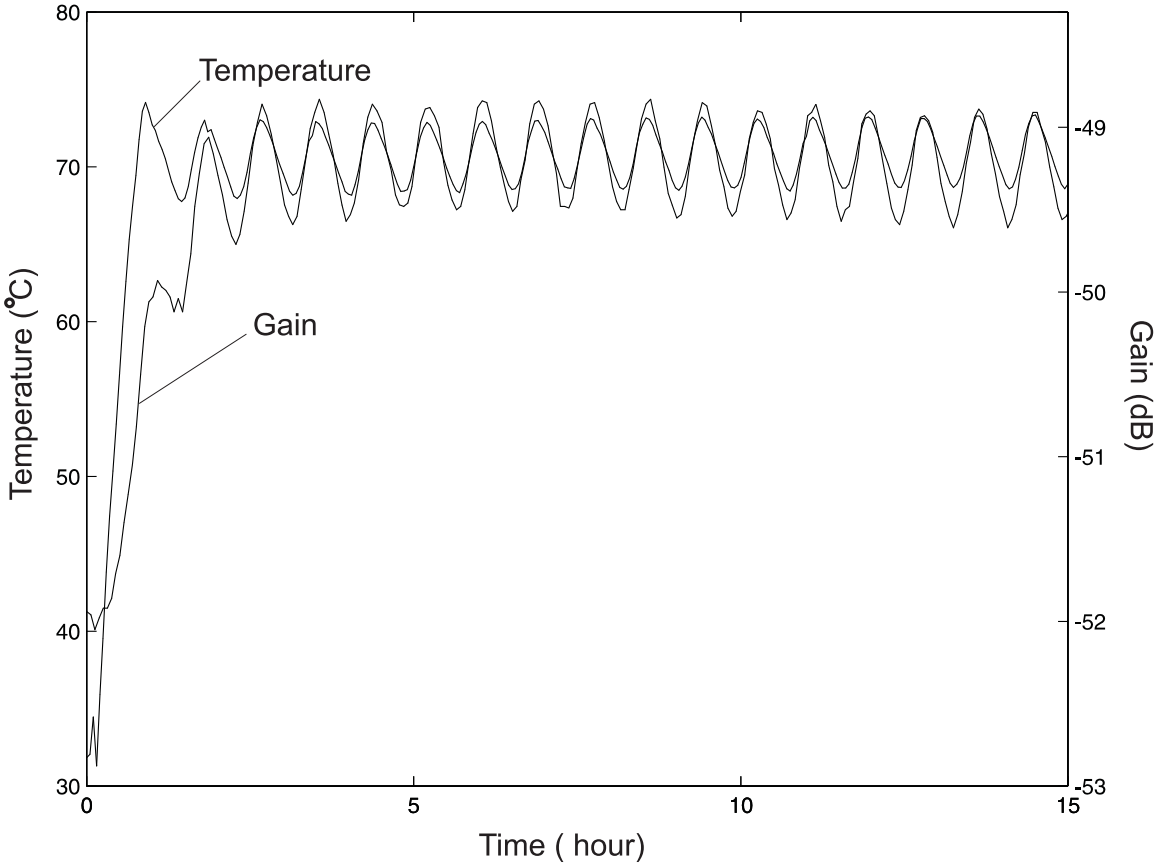

Figure 8.15: The temperature and gain of the 5 mm wavelength for oil-impregnated pressboard at f=0.1 Hz when the temperature controller was set from 30°C to 70°C. The overlap of the period of two "sinusoids" clearly demonstrates that the interdigital sensor instantaneously detects the dielectric property change due to the temperature change.

8.5.2 Simulation of Temperature Transient

This process is simulated using the same code *diff.c* by Prof. B. C. Lesieutre discussed in Chapter 7 to compare with experiment. The universal curve for oil-impregnated pressboard obtained by Y. K. Sheiretov [3] and later further fitted by D. E. Schlicker [89] and J. Castrillon [106] was used in this simulation. The data base was obtained for the low moisture range, therefore, the data did not exhibit the double inflection feature discussed in Chapter 4 for data with a wide moisture range, and the fitting curve is relatively simple:

$$\varepsilon^* = \varepsilon_\infty + \varepsilon_0 c(\frac{m}{f})^{-\gamma}, \tag{8.1}$$

$$c = 10^{-\gamma(f_T(T)+c_m)}(10^{c_1} - j10^{c_2}), \tag{8.2}$$

$$f_T(T) = 0.03375T - 1.7625, \tag{8.3}$$

where ε_∞=3 is the pressboard permittivity as f approaches infinity; m is the moisture concentration in percent defined as the weight of water divided by the total weight of the oil-impregnated sample; f is frequency in Hz; T is temperature in °C; γ=-0.7, c_1=-0.7798, c_2=-0.4724, and c_m=-0.684.

Since the standard way of defining the moisture content, denoted as m_f here, is the mass of water M_w divided by the mass of oil-free pressboard M_F, we need to convert m_f to the m used in (8.1), $m_i = M_w/(M_F + M_{oil})$. Assuming the volume ratio of oil to the pressboard is n, m_i is related to m_f with

$$m_i = m_f \frac{\rho_F}{\rho_F + \frac{n}{1-n}\rho_{oil}}, \tag{8.4}$$

where $\rho_F = 1.43 \times 10^3$ kg/m^3 is the density of fiber, and $\rho_{oil} = 0.885 \times 10^3$ kg/m^3 is the density of oil. For a typical value of $n = 0.3$, $m_i = 0.79 m_f$.

The real-time measured temperature and moisture boundary condition of Figure 8.12 were inputted to the program instead of constant temperature and a constant moisture boundary condition. The pressboard was tightly pressed against the inner wall of the outer cylinder, which was directly heated by the heating tape. The thermal

diffusivity is assumed to be infinite, i.e. the pressboard sample is uniform in temperature at any instant of time. The diffusion coefficient for oil-impregnated paper estimated by Guidi and Fullerton, discussed in Section 3.5.2, is used for the simulation. The simulated results and the measured results for the 5 mm wavelength are shown in Figure 8.16. The periodicity matches very well. The simulated amplitude of the "sinusoids" is larger than the measurements, indicating that the temperature effect of the constructed universal curve is larger than its actual value.

8.6 Summary

The interdigital sensor setup was combined in the transformer oil convective flow Couette Facility for studying temperature and moisture transients in pressboard. This facility minimizes the shortcomings of the bench-top apparatus and provides a better test model for transformer applications.

Measurements of moisture diffusion in oil-free pressboard and dynamics for oil-impregnated pressboard due to a temperature step change were performed. The diffusion coefficient for non-clamped oil-pressboard in the Couette Facility is about 4.5 times that of clamped sample in the bench-top apparatus. Forward simulation shows good agreements in trend with the experiments, but the actual values differ due to a few implementation error sources.

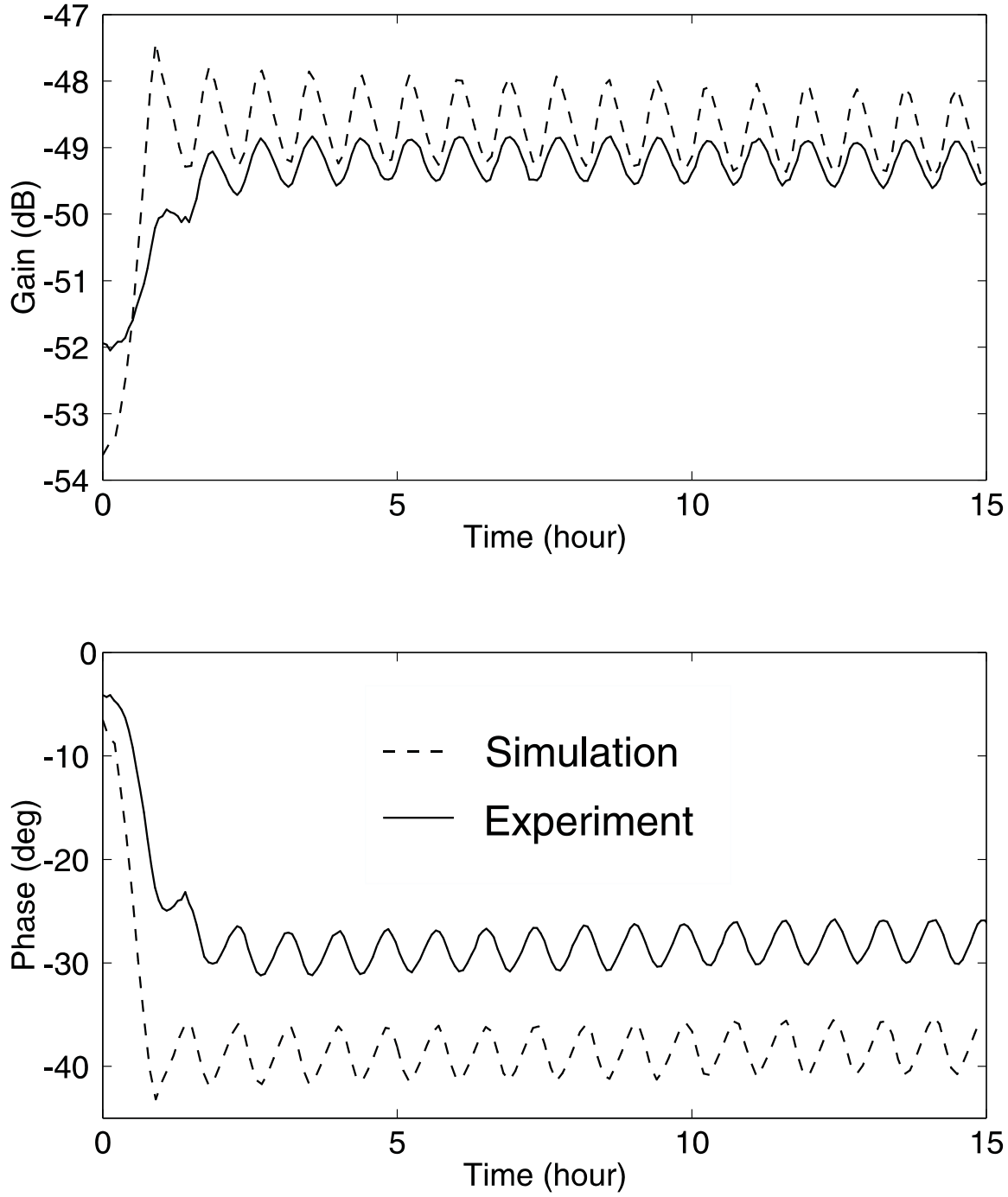

Figure 8.16: The simulated and measured gain and phase of the 5 mm wavelength for oil-impregnated pressboard at f=0.1 Hz when the temperature controller was set from 30°C to 70°C.

Chapter 9

Recovery Voltage Measurements

9.1 Introduction

So far all the dielectrometry measurements discussed have been conducted in the frequency domain. For linear systems, because the time-dependence of the current response to a step-function field and the frequency dependence of the dielectric susceptibility in response to a sinusoidal excitation are related by a Fourier transformation, measurements in one domain will give us information in the other domain.

Measurements of permittivity and dielectric loss as a function of frequency are an important technique for investigating dielectric materials. Measurement in the frequency domain can be carried out by applying a sinusoidal voltage with known frequency and amplitude across the test dielectric. From the amplitude and phase of the current through the material and the geometry of the object, the complex permittivity can be estimated. To obtain the spectrum of the complex permittivity this procedure is repeated at each frequency in the desired spectrum [107]. The typical frequency range that is of interest in high voltage insulation is from 0.001-10 kHz. The advantage of doing frequency measurement is the availability of precise commercial equipment, high precision due to the narrow band of frequency at any single measurement, and the availability of high frequency signals up to even the terahertz region.

The time-domain measurements have the advantage of requiring one single time

signal to determine a wide frequency range response. To detect aging or moisture content, it is necessary to analyze the low frequency part of the polarization spectrum (in the range of 0.0001 Hz to 50 Hz [108]). However it is very difficult to generate a 1 kV sinusoidal signal at 0.001 Hz [27]. The time-domain technique has its advantages over frequency-domain measurements for materials having very slow relaxations [28]. In fact different methodologies are suggested for different frequency bands [109]: infrared spectroscopy is suitable for the range of the shortest time constants; the middle range of the spectrum can be measured by the determination of dielectric loss at radio, audio or industrial frequencies while the DC methods are very suitable for investigating the range of longest time-constant.

Dielectric relaxation measurements have been widely applied to transformer insulation diagnostics. The time-domain measurement offers the advantage over frequency-domain measurement that a single time-domain waveform contains the same information as many separate frequency-domain measurements. Measurements of charging and discharging currents have been used for several decades. A particular time-domain method, recovery voltage measurement, has been extensively promoted in recent years for transformer diagnostics [86, 108–113].

The principle idea of a recovery voltage measurement is illustrated in Figure 9.2. It consists of three stages. The first stage is a charging stage in which a pulse voltage of width t_c is applied over a completely discharged test object (zero initial condition). During the charging period there will be polarization current through the test object. The second stage is the partial discharge of the system by short circuiting the test object for a period of time t_d and there will be depolarization current flowing through the circuit. Before the relaxation process finishes, the test object is open circuited and the recovery voltage is measured. The shape of recovery voltage response in most cases is a rise from zero volts at the time of open circuit to a peak value V_{max}, and then the voltage decays back to zero. The recovery voltage curve is characterized by its peak voltage V_{max}, initial slope of recovery voltage $\tan(\alpha)$, and time from the open circuit condition to maximum recovery voltage t_{crit}. By varying the charging time t_c

Figure 9.1: The Tettex Recovery Voltage Meter RVM 5461 [49].

and discharging time t_d, a signature of the system can be developed. The measured polarization spectrum is strongly influenced by the moisture content of the dielectrics and its aging condition. Therefore this method is used to do non-destructive testing of the insulation just as was proposed for using interdigital dielectrometry sensors.

The Tettex Recovery Voltage Meter RVM 5461 shown in Figure 9.1 is the only commercially available instrument for recovery voltage measurements. The Tettex RVM 5461 can output an excitation voltage range from 200 to 2000 VDC and charging time from 0.02 s to 10000 s in 1-2-5 steps. The default t_c/t_d ratio is 2:1. The testing temperature range is 5°C to 90°C.

9.2 Measurements with Parallel-Plate Electrodes

The recovery voltage investigation is first performed with parallel-plate electrodes with test dielectric materials between them. The electrodes have dimensions 97.23 ± 0.14 mm by 96.59 ± 0.09 mm.

The tests are taken for lab-aged oil and oil-soaked Hi-Val pressboard, and new

oil and oil-soaked Hi-Val pressboard. The pressboard used here is called oil "soaked" instead of "impregnated" because it is directly immersed into oil without going through the vacuum process involved in an impregnation process. The lab-aged pressboard has been in oil for 4 years at room temperature.

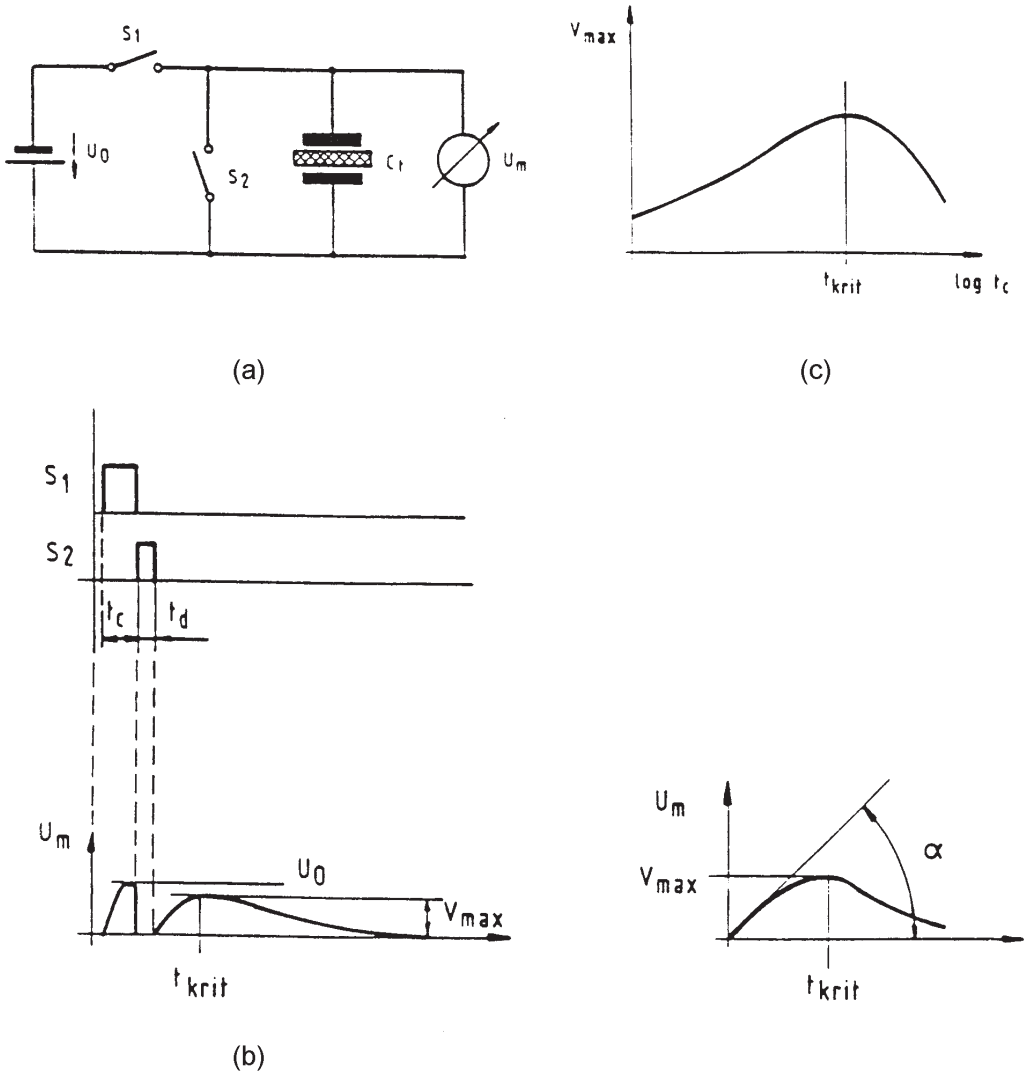

Figure 9.2: The Tettex Recovery Voltage Meter(RVM) measurement schematic [27]: (a) The principle circuit of voltage recovery measurement. (b) Time diagram of the RVM procedure. (c) Recovery voltage V_{max} as a function of charging time t_c.

9.2.1 Tests in the Frequency Domain

The test structure is first measured by general impedance measurement techniques to compare with the time domain measurements. The impedance of the structure is measured as a function of frequency by similar interface circuitry as used by the interdigital sensor.

The formulas for estimating dielectric properties from measured capacitance and conductance for parallel-plate electrodes with field confined between the two electrodes are:

$$\varepsilon = Cd/A, \tag{9.1}$$

$$\sigma = Gd/A, \tag{9.2}$$

where d is the electrode gap, A is the electrode area, G is the conductance between electrodes, and C is the capacitance between electrodes.

For tests with oil, we take into account the fringing fields by using the formula derived using a Schwarz-Christoffel transformation

$$\varepsilon = \frac{\pi C}{L + W + W\ln(\frac{\pi L}{d}) + L\ln(\frac{\pi W}{d}) + \frac{\pi LW}{d}}, \tag{9.3}$$

$$\sigma = G\varepsilon/C, \tag{9.4}$$

where L and W are the length and width of the parallel-plate capacitor. The difference with and without considering the fringing field for fresh Shell Diala AX oil at room temperature is shown in Figure 9.3. The average estimated relative permittivity for oil using the ideal parallel-plate formula (9.1) is 2.35 and considering fringing fields (9.3) is 2.27 . The difference is 3.5%.

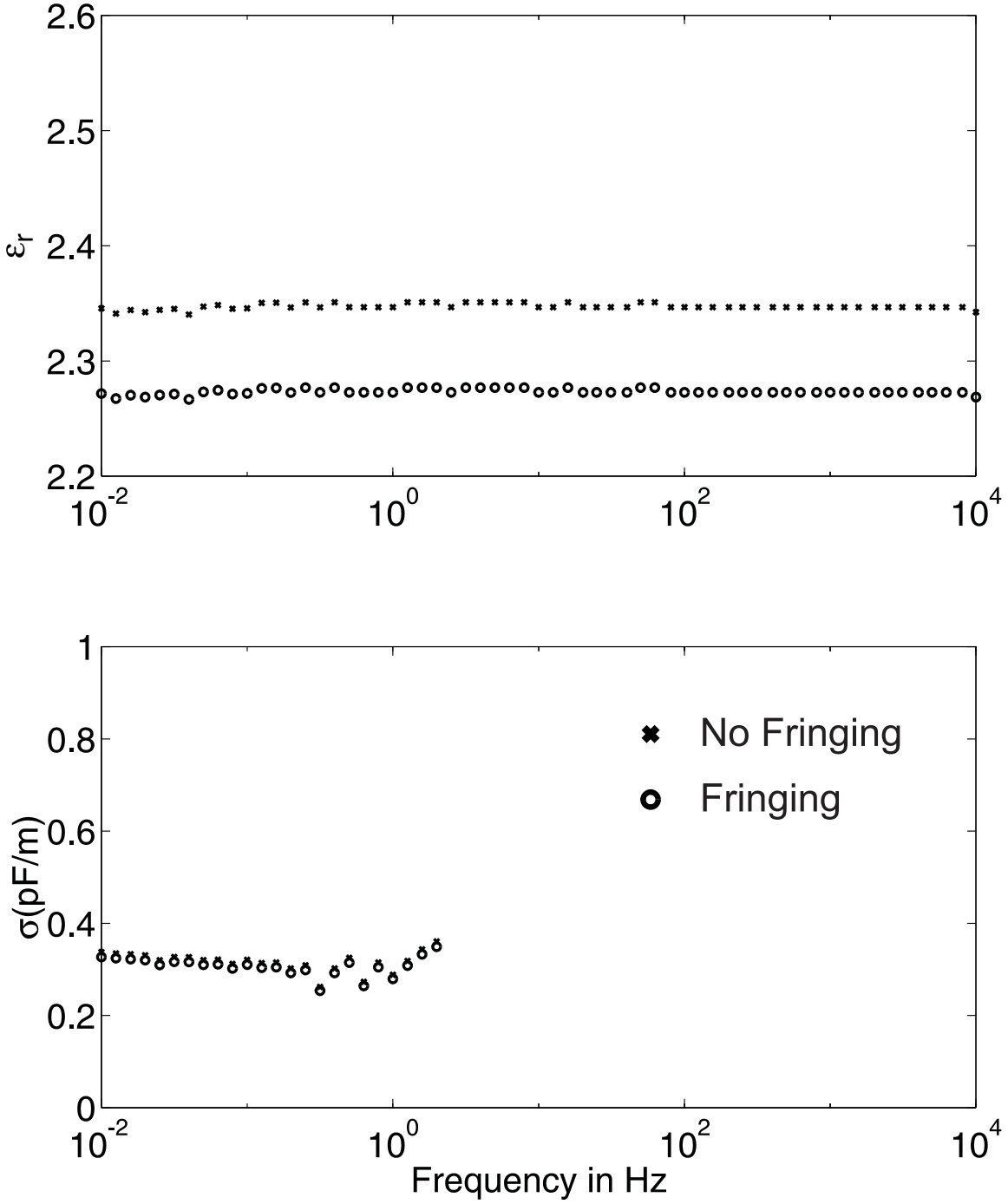

Figure 9.3: The dielectric spectrum of fresh Shell Diala A oil at room temperature calculated from parallel-plate electrode measurements using fringing field and non-fringing field formulas of (9.1)–(9.4).

For measurements with oil-impregnated pressboard samples only, because the lossy capacitor is surrounded by air, (9.3) is not applicable and we use the ideal formulas instead. This is justified by the relative large permittivity of the pressboard compared to that of air, and the field should be mostly confined within the electrodes. The length and width of the electrodes are much bigger than the spacing (each about 100 to 1) such that the fringing field effects should be rather small.

Figure 9.4 shows the measured results of new and aged oil and new and aged oil-soaked pressboard. The aged materials show significantly larger conductivity.

Next, the pressboard and oil are in series sandwiched in-between the electrodes shown in Figure 9.5. The pressboard is 1 mm thick and the oil layer is 0.7 mm thick separated by nylon washers. The effective permittivity and conductivity of the sandwich structure can be found in two ways: by directly measuring the new structure admittance and using (9.1) and (9.2); or using the known individual dielectric properties of oil and paper to calculate the equivalent admittance shown in Figure 9.6 as

$$Y_{eq} = \frac{Y_{oil} Y_{paper}}{Y_{oil} + Y_{paper}}. \tag{9.5}$$

and then use using (9.1) and (9.2) to find the effective dielectric properties for the test structure.

The calculated results are compared with measured results in Figure 9.7. Besides the measurement error, the electrical double layer between oil and pressboard might also contribute to the difference between measured and calculated values at low frequencies.

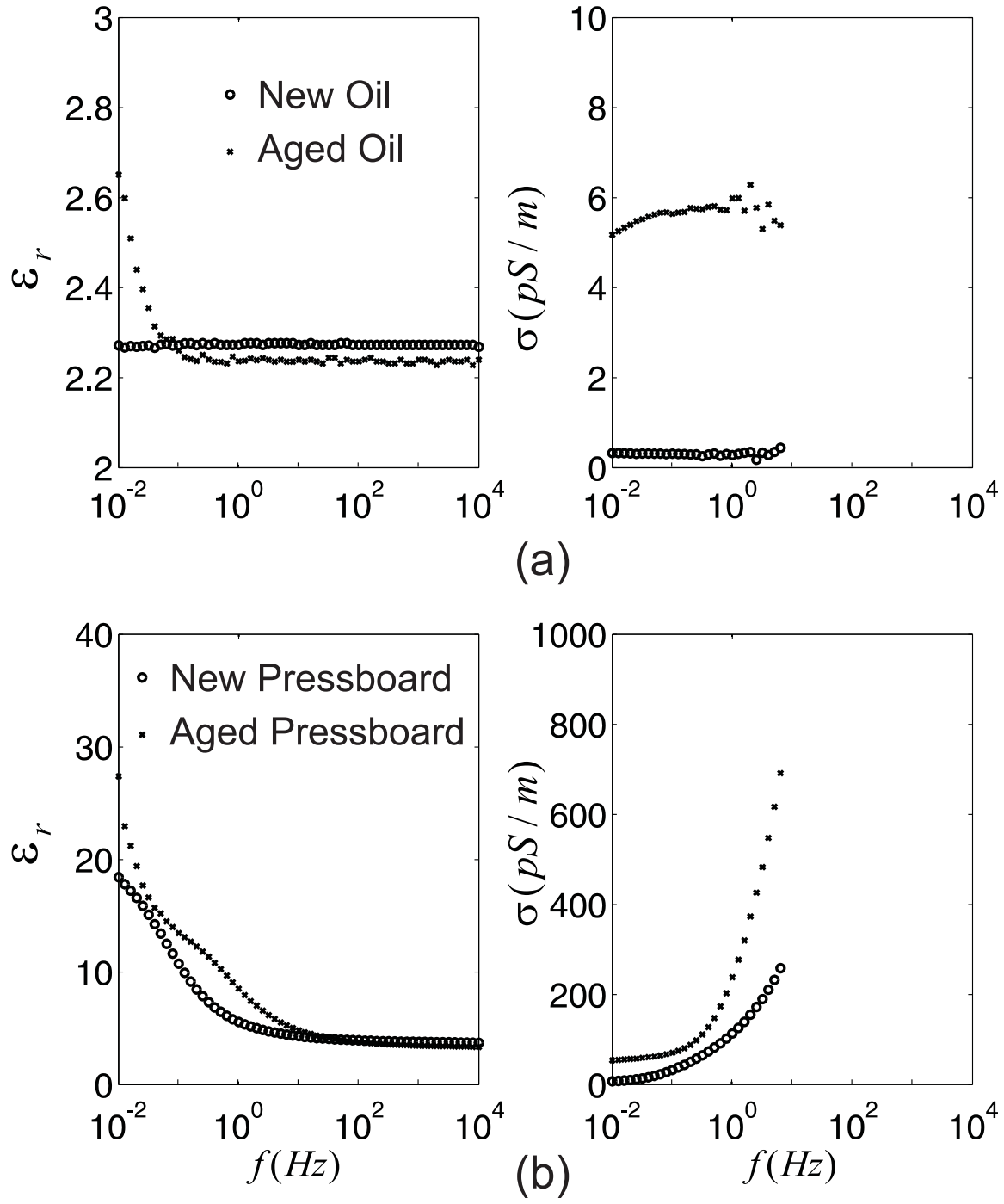

Figure 9.4: The dielectric spectrum measured by general impedance measurement techniques for new and aged oil and pressboard: (a) oil; (b) pressboard.

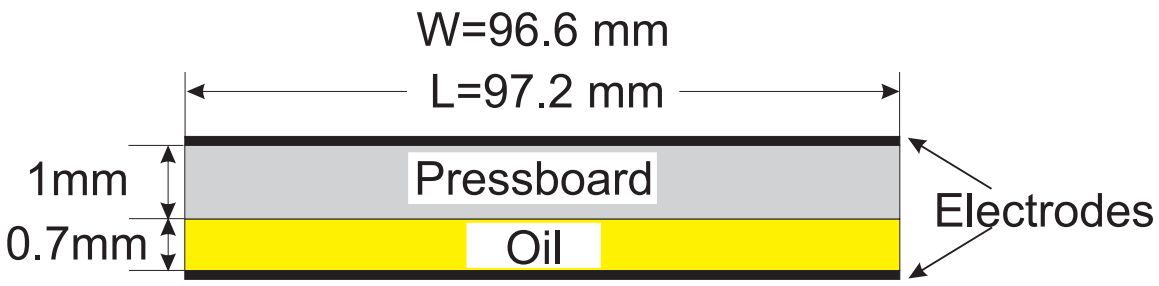

Figure 9.5: The test structure for the layered oil and pressboard.

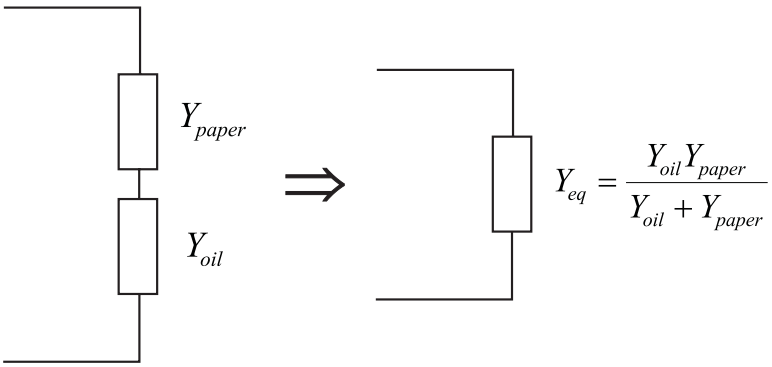

Figure 9.6: The equivalent circuit for the test structure of Figure 9.5 with pressboard and oil in series.

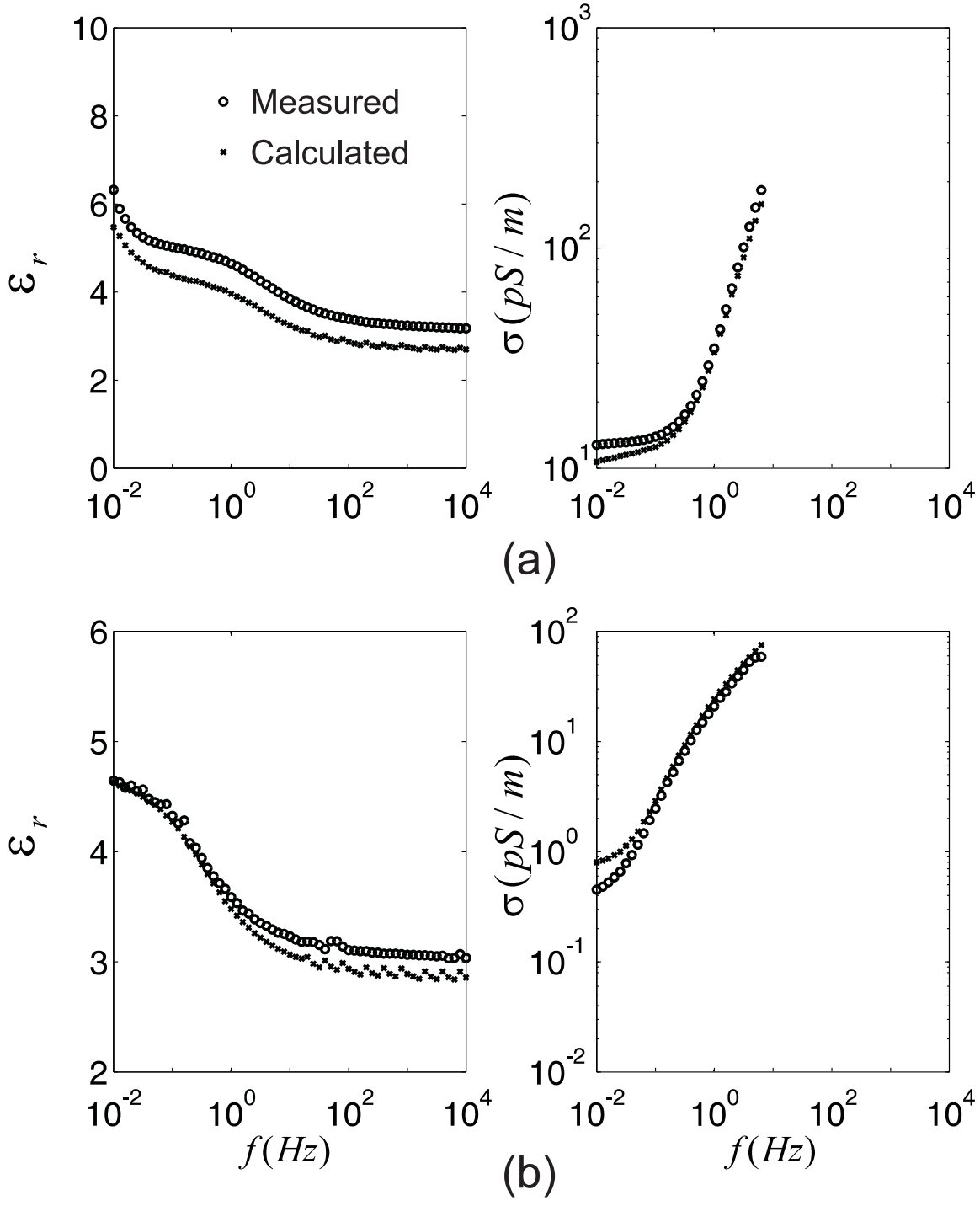

Figure 9.7: The calculated (from (9.5)) and measured effective dielectric spectrum by general admittance measurement techniques for a series layer of 1.0 mm thick oil-soaked pressboard and 0.7 mm thick oil: (a) Aged test sample; (b) New test sample.

9.2.2 Tests in Time Domain

The parallel-plate test structure is placed in a metal can which is guarded during the test. The metal can is placed inside a Teflon cover for insulating the applied high voltage. The RVM can perform two types of measurements. One is to measure the key parameters of the recovery voltage, the peak voltage V_{max}, the time from the open circuit condition to maximum recovery voltage t_{crit}, and initial slope of recovery voltage $\tan(\alpha)$, as a function of charging time t_c for a given charging voltage. The other method is to measure the shape of the recovery voltage as a function of open circuit time for a given charging time. For transformer insulation diagnostics, the first kind of measurement is most often used to get a signature of the insulation polarization spectrum. Polarization phenomena of different time constants can be observed by varying the charging time.

The peak recovery voltage measured as a function of charging time for new and aged oil-soaked pressboard is shown in Figure 9.8. Both are at room temperature. The applied charging voltage is 200 V, and $t_c/t_d = 2$. As clearly shown in the curves the aged pressboard has a peak closer to the time origin. In general, peaks to the left indicate more aged material than peaks to the right because the aging causes an increase of the conductivity and consequently the decrease of the dielectric relaxation time constant.

Figure 9.9 shows the recovery voltage as a function of open circuit time (the third stage) for a lab-aged pressboard-oil sandwich structure at various charging times at room temperature. The charging voltage is V_c=200 V and $t_c/t_d = 2$. With the increase of the charging time, the time at which the recovery voltage reaches maximum shifts to the right because the fast polarization components have decayed away during the longer discharge period.

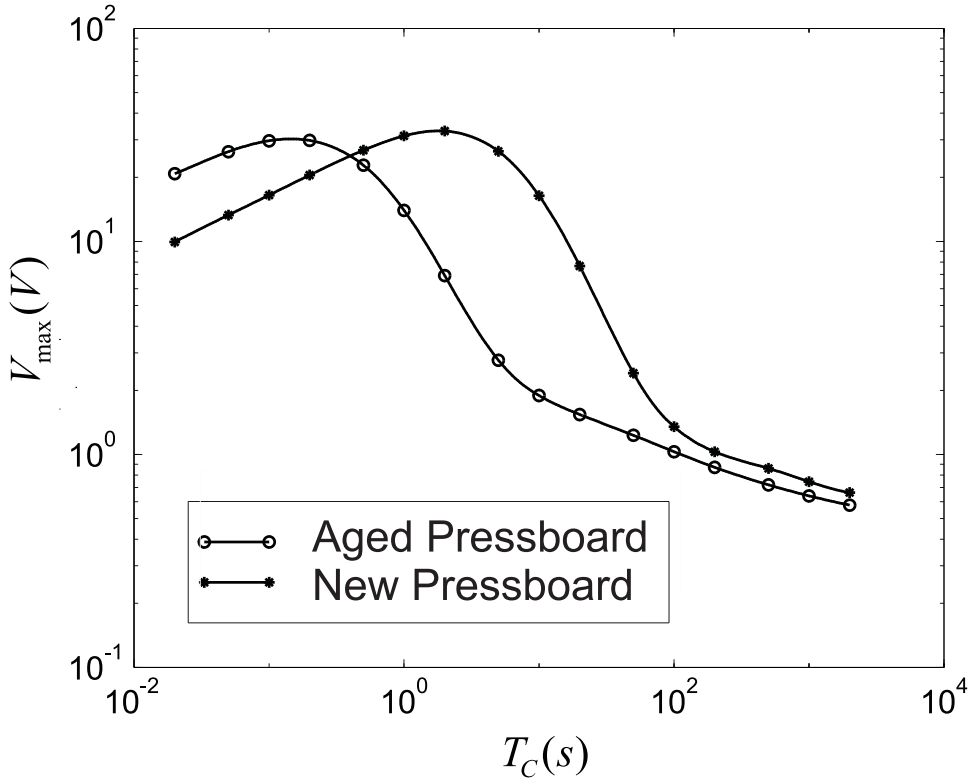

Figure 9.8: The measured maximum recovery voltage as a function of charging time t_c for lab-aged and new oil-soaked pressboard at room temperature with V_c=200 V, $t_c/t_d = 2$. Due to a smaller dielectric relaxation time constant, the aged pressboard has a peak closer to the time origin.

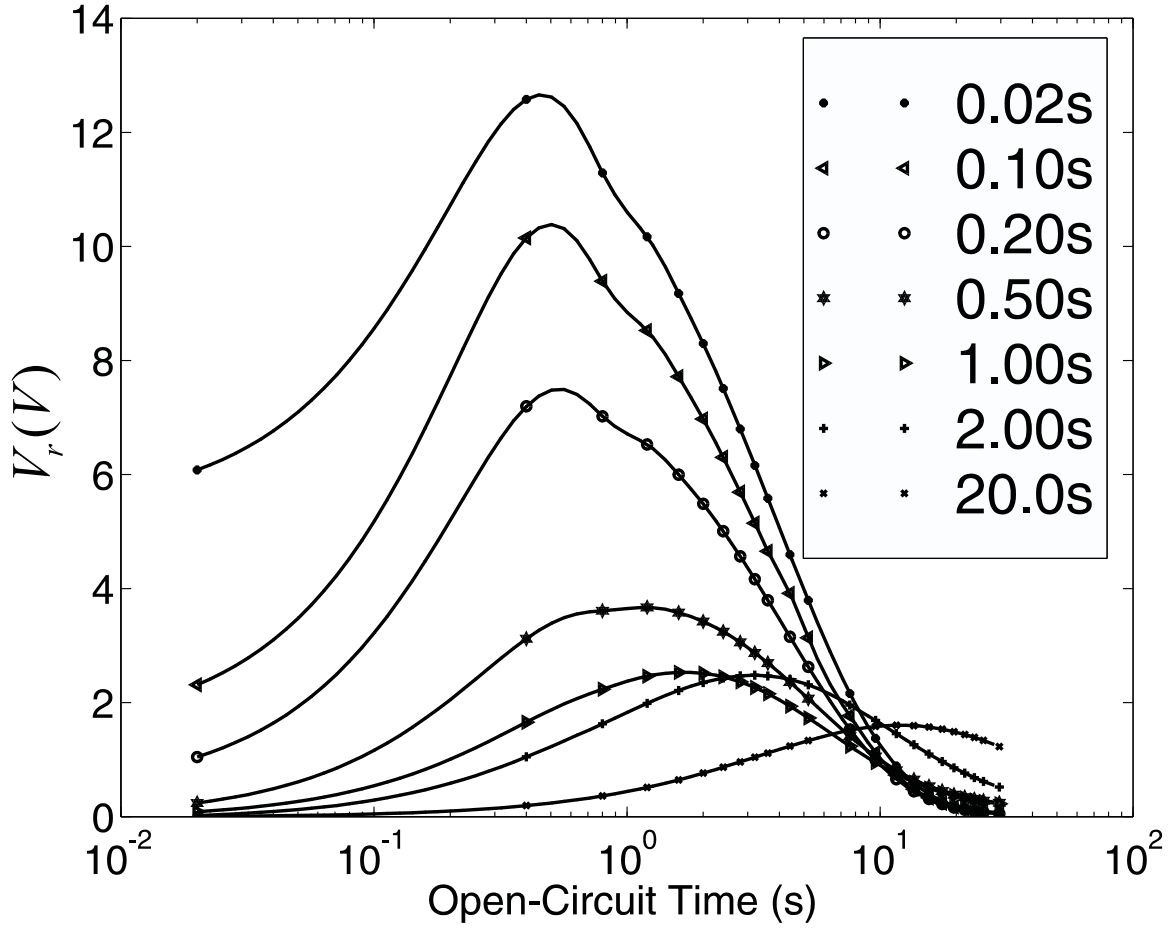

Figure 9.9: The measured recovery voltage with V_c=200 V as a function of open circuit time with $t_c/t_d = 2$ for a lab-aged pressboard and oil layered structure for various charging times at room temperature. With the increase of the charging time, the time at which the recovery voltage reaches maximum shifts to the right because the fast polarization components have decayed away during the longer discharge period.

9.3 Couette Facility Measurements

9.3.1 Excitation Voltage

Return voltage measurements using the Tettex Recovery Voltage Meter with the Couette Facility for various charging voltages with layered oil and pressboard insulation at 70°C is shown in Figure 9.10 with charging time t_c=0.02 s and discharging time t_d=0.01 s. It is replotted in Figure 9.11 as a ratio of return voltage over the charging voltage. Although due to some non-linearity the curves do not completely overlap, the absolute value of the recovery voltage as a function of the excitation voltage does not influence the dominant time constant. A higher excitation provides better signal-to-noise ratio, but it should not exceed the insulation rating voltage.

9.3.2 Charging Characteristics

Recovery voltage for layered oil and paper insulation in the Couette Facility as a function of open circuit time for different charging times at 70°C with $V_c = 200$ V and $t_c = 2t_d$ is shown in Figure 9.12.

9.3.3 Temperature Effects

Recovery voltage measurements with V_c=200 V, t_c=0.2 s, and t_d=0.5t_c=0.1 s, at various temperatures for layered oil and paper insulation in the Couette Facility are shown in Figure 9.13. With an increase of temperature, the conductivity of the paper and oil increases. Therefore the dielectric relaxation time constant reduces and the peak of the return voltage shifts to the left as shown in Figure 9.13.

Charging characteristics for (a) aged oil and pressboard in the parallel-plate sensor at room temperature, (b) oil and pressboard in the Couette Facility at 70°C, and (c) layered oil and pressboard in the Couette Facility at 30°C are shown in Figure 9.14. The aged oil shows two peaks which is a general signature for aged insulation.

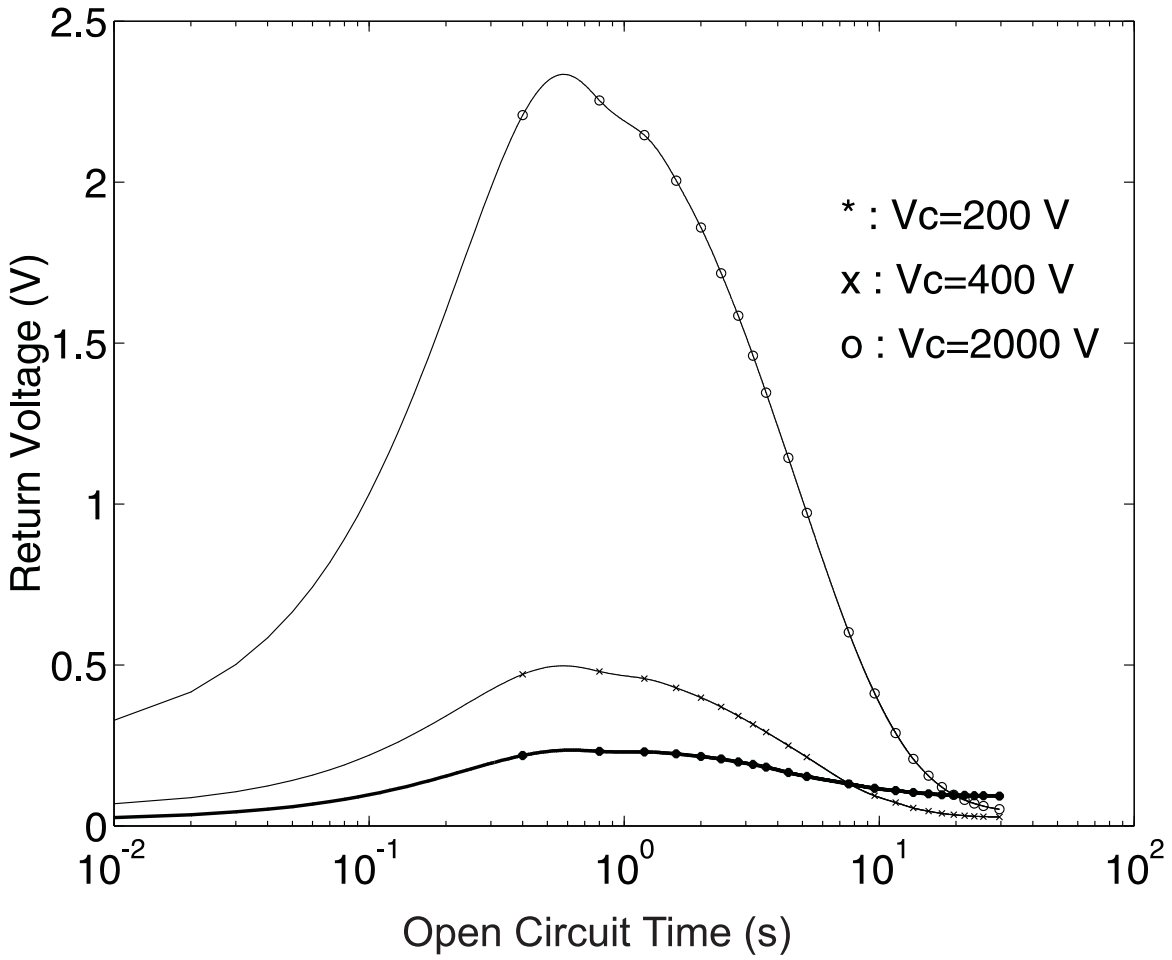

Figure 9.10: Measured return voltage measurements using the Tettex Recovery Voltage Meter with the Couette Facility for various charging voltages with layered oil and pressboard insulation at 70° C. The charging time is t_c=0.02 s and the discharging time is t_d =0.01 s.

9.4 Summary

The results of recovery voltage measurements are presented. The time domain response for aging and temperature effects is qualitatively consistent with the results obtained in the frequency response results discussed in previous chapters. More quantitative analysis and transformation between time and frequency domain responses need to be done for exact comparison.

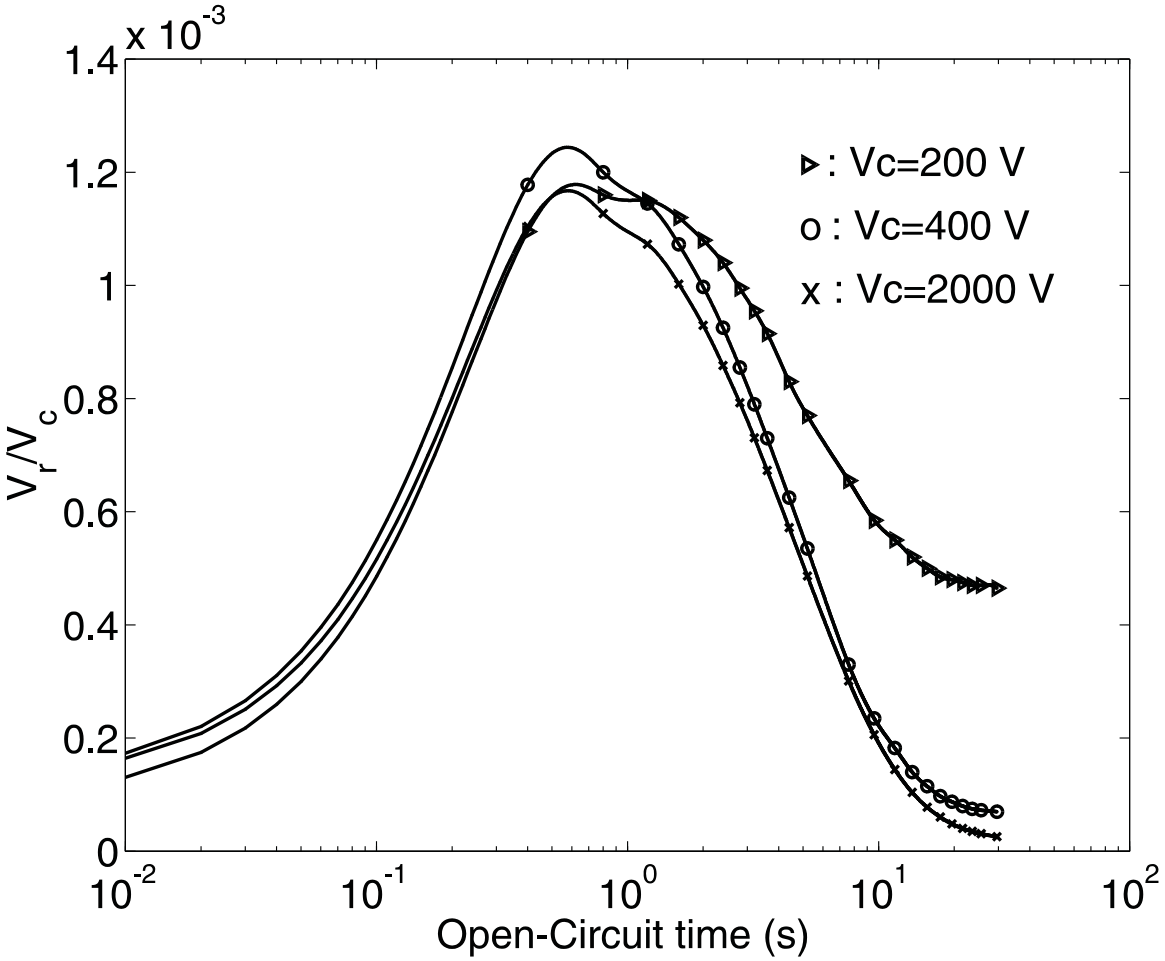

Figure 9.11: Replot of the measured recovery voltage of Figure 9.10 as a ratio of return voltage over the charging voltage.

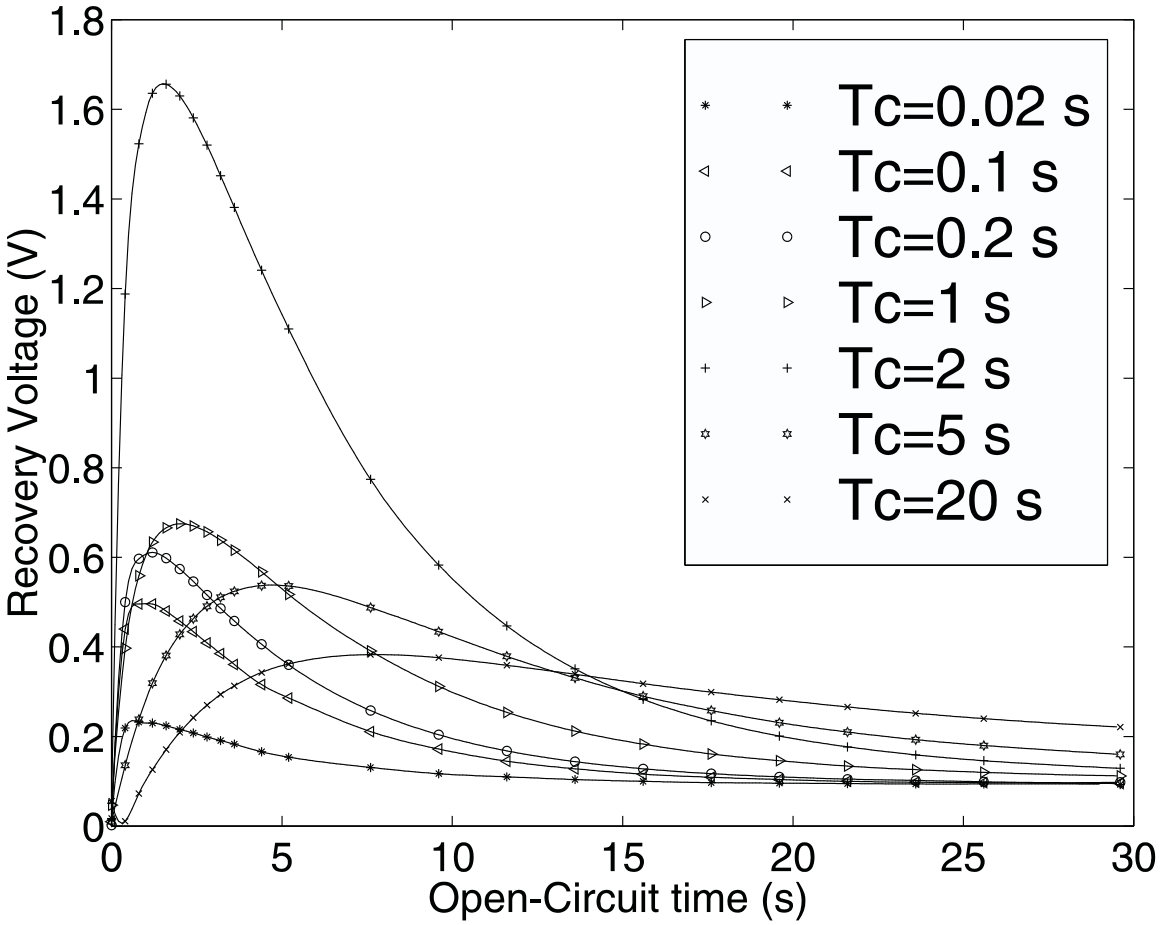

Figure 9.12: Measured recovery voltage for layered oil and paper insulation in the Couette Facility as a function of open circuit time for different charging times at 70° C with $V_c = 200\ V$ and $t_c = 2t_d$.

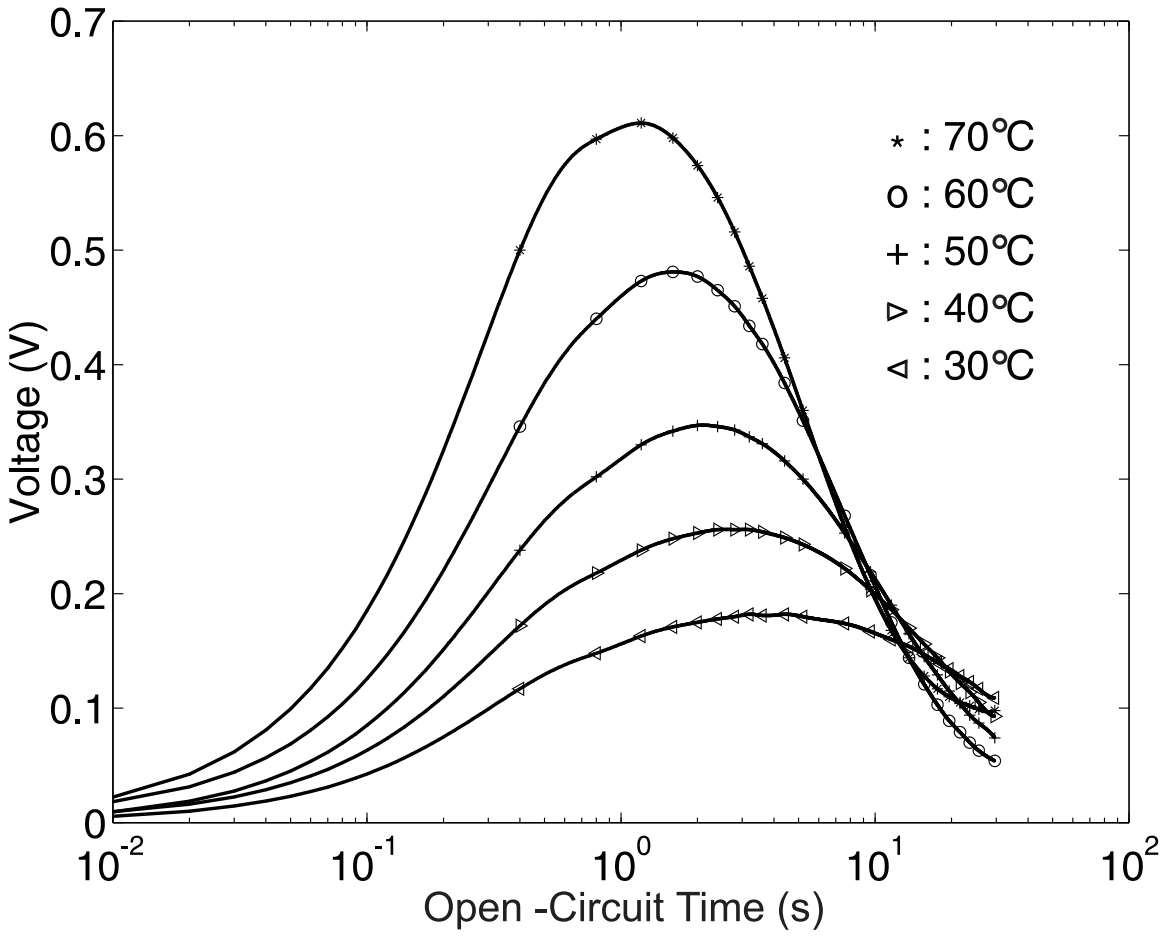

Figure 9.13: Measured return voltage measurements using the Tettex Recovery Voltage meter in the Couette Facility for various temperatures with layered oil and pressboard insulation with $V_c = 200$ V, t_c=0.2 s, and $t_d = 0.1$ s.

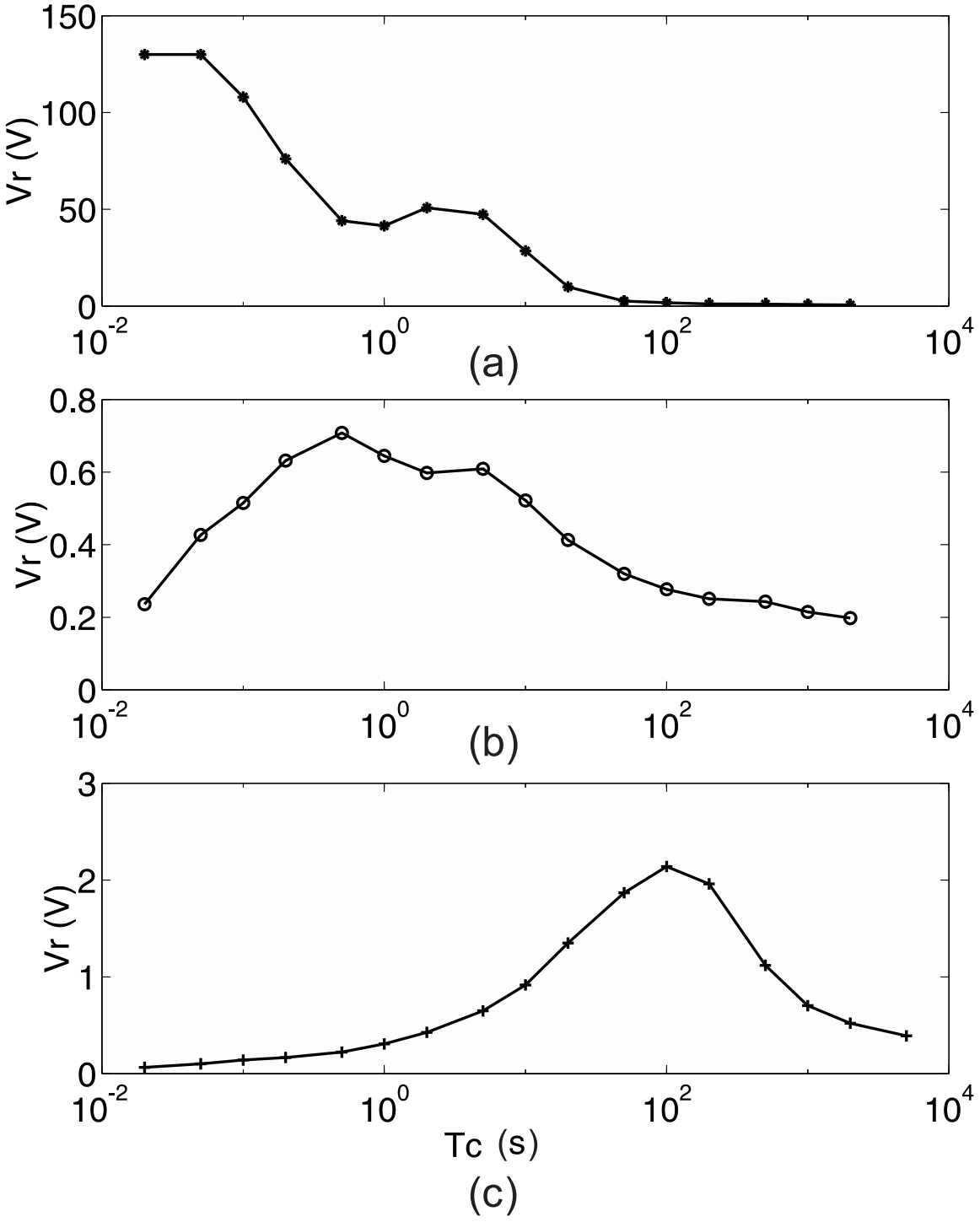

Figure 9.14: Measured charging characteristics for (a) aged oil and pressboard in a parallel-plate electrode structure at room temperature, (b) oil and pressboard in the Couette Facility at 70° C, and (c) layered oil and pressboard in the Couette Facility at 30° C with $V_c = 200\ V$ and $t_c = 2t_d$.

Chapter 10

Conclusions

The presence of moisture in a transformer deteriorates the transformer insulation by decreasing its electrical, mechanical, and thermal strength. Therefore it is important to monitor the moisture condition in both liquid and solid insulation to assure transformer performance. There are commercially available sensors to measure the moisture in oil. When the transformer system is in equilibrium, moisture partitioning curves for the oil-paper system can be used to find the moisture in paper from the oil measurement. A comprehensive survey was performed for existing methodologies to measure moisture in oil and paper transformer insulation. Chapter 3 summarizes this effort. Several sets of classic moisture equilibrium curves were studied and a comparison is given for each method. Historical mistakes were corrected, and all relevant concepts were clarified. A new set of curves was constructed based on the best method which covers the range of zero moisture to saturation moisture levels. This is a useful tool for utilities and power system monitoring manufacturers.

A measurement technique exploiting the linearity between the relative humidity of the oil and the moisture content of the oil to indirectly measure the oil solubility was developed. Solubility tests were performed for differently conditioned oils: Fresh Shell Diala AX oil, lab-aged Shell Diala A oil, used oil from Ramapo Substation, and used oil from Texas Utilities. Results show that aging under normal operation at service temperature is not very likely to significantly change the water solubility.

When the system is not in equilibrium, the moisture curves are not applicable and the three-wavelength interdigital dielectrometry sensor developed at the MIT Laboratory for Electromagnetic and Electronic Systems is a unique way to measure the spatial profile of the moisture distribution in transformer pressboard.

As a first step to relate measurable dielectric properties to absorbed moisture, the moisture and temperature effects on the dielectric spectrum of oil-free pressboard were measured using a parallel-plate geometry sensor for nine moisture levels and five temperature levels. A dielectric model for biological tissue is adopted here for cellulose structured pressboard. A universal curve was found relating dielectric properties to moisture concentration and temperature by fitting the data to the model. Preliminary measurements of oil-impregnated pressboard show similar characteristics. Chapter 4 covers this subject.

Preliminary measurements of oil and pressboard (oil-free and oil-impregnated) using the interdigital dielectrometry sensor are given in Chapters 5. A joint research group effort led to development of an improved design of the three-wavelength sensor and interface box circuitry which reduces the problems associated with the previous design and simplifies the inversion algorithm to convert the electrical signal to dielectric properties. This thesis focuses on the design and implementation of experimental studies based on interdigital dielectrometry using the new three-wavelength sensor. Chapters 6 and 7 elaborate on the results of this work.

An improved bench-top apparatus was designed to implement various moisture measurements using interdigital dielectrometry sensors. Diffusion processes in oil-free pressboard were monitored at five different temperatures using the interdigital dielectrometry sensor technology. Improved sensing techniques provided better quality signals and results. Sensor measurements agreed well with theoretical analysis for effects of pressboard thickness and temperature. The ability of the interdigital sensor to measure the moisture distribution was demonstrated via the bench-top experimental results.

Real-time on-line measurement of the moisture diffusion process is achieved in this

research project. For the first time, the time evolution of the moisture spatial profile in oil-free transformer pressboard has been estimated non-destructively. The moisture diffusion profiles have been obtained using the three-wavelength interdigital sensor with a fast algorithm suitable for on-line monitoring with real time display of results. The understanding of moisture-related processes in power transformers can be enhanced with this methodology.

There is no analytical solution of the time dependent moisture profiles in a sample with finite thickness for moisture diffusion coefficient as a function of temperature and moisture concentration. Numerical algorithms for solving the non-linear diffusion equation were derived. The calculated results extend the existing small database of diffusion studies. Literature results of the diffusion coefficient for cellulose insulation were compared and analyzed. The estimated diffusion coefficient is much smaller than the value reported by Foss, but is close to that of Quarshie at University of Nottingham. Numerical inconsistencies were found in Foss' study.

The interdigital sensor setup was also combined in a transformer oil convective flow Couette Facility for studying temperature and moisture transients in pressboard as presented in Chapter 8. This facility minimizes the shortcomings of the bench-top apparatus and provides a better test model for transformer applications. Measurements of moisture diffusion in oil-free pressboard and dynamics for oil-impregnated pressboard due to a temperature step change were performed. The diffusion coefficient for the non-clamped oil-free pressboard in the Couette Facility is about 4.5 times that of a clamped sample in the bench-top apparatus. This project along with the Flow Electrification Project funded by EPRI helps to understand the mechanism of catastrophic failures of power transformers due to moisture dynamics and flow electrification.

Finally, as detailed in Chapter 9, a newly promoted in-situ time-domain measurement technique using the recovery voltage measurements with the Tettex Recovery Voltage Meter was implemented. Time domain measurements are qualitatively compared with frequency domain measurements for both a parallel-plate electrode geometry and a coaxial cylinder electrode geometry (the Couette Facility). The results for

temperature and aging effects show good agreement with theory.

Suggested future work includes application of the sensor to real transformers, especially to monitor the flow electrification hazard; integration of moisture measurements with other transformer diagnostic techniques; improvement of the computer algorithm to invert the electrical signal to dielectric, moisture, and other physical properties for inhomogeneous materials; development of an algorithm to transform the recovery voltage measurement results to the dielectric spectrum in the frequency domain; and identification of other applications of interdigital dielectrometry sensors for non-destructive evaluation of materials.

Appendix A

Instructions for Using the Bench-Top Apparatus

For the bench-top apparatus shown in Figure 6.7 and experiments described in Chapter 6 and 7, some of the operations are under pressure and high temperature, so safe operation of the system is very important. Because the top of the reservoir is not bolted down to the body and it has a large surface area, a small pressure will create a large force that could lift the top. Therefore, it is important to always remember the following: no pressure for the reservoir. For each function, the procedures as well as the order of operations are as follows and must be followed exactly. Visualization of the flow direction helps to operate the system. All the valves are labeled in the system. "Off" means turn the valve to the closed position and "on" means to open the valve. For a three-way valve, "a" and "b" are used to indicate which way the valve opens to.

1. Vacuum test chamber free of oil

V3 off; V4 off; V5 off; V7 off; V1 to vacuum; V10 off; V12 on; vacuum pump on. Other valves are not directly associated with this operation and should be positioned in accordance with the function of the rest of the system. This applies to the following operations as well.

2. Vacuum test chamber with oil without circulation

V3 off; V4 off; V5 off; V7 off; V1 to vacuum; V10 off; V12 off; vacuum pump on;

V12 on gradually according to the degassing condition to avoid oil being sucked into the moisture trap.

3. Vacuum test chamber with oil circulation within test chamber only

V1 to vacuum; V3 to a; V4 off; V5 to a; V7 off; V12 off; V10 off; vacuum pump on; V12 on gradually according to the degassing condition to avoid oil being sucked into the moisture trap; circulation pump on after system stabilizes under vacuum.

4. Vacuum reservoir with oil

V6 off; V5 off or to a; V4 off; V3 off or a; V11 off; V8 off; vacuum pump on; V2 to vacuum gradually according to the degassing condition. Magnetic stirrer on to allow thorough diffusion after oil stabilizes under vacuum.

5. Get oil from outside into vacuumed test chamber

After vacuum, oil in/outlet port to oil source by plastic tube, V3 off, V4 off, V5 off, V12 off, V1 off, vacuum pump off, V7 on.

6. Transport oil from reservoir into vacuumed test chamber

After vacuum, turn off magnetic stirrer, V4 off, V7 off, V2 to air/nitrogen, V8 off, V11 to vent, V1 off, vacuum pump off, V12 off, V3 to a, V5 to b. Turn light on for observation.

7. Transport oil from reservoir to test chamber by circulation pump

V1 to air, V2 to air, V3 to a, V4 off, V5 to b, V6 off, V7 off, V8 off, V10 to vent, V11 to vent, V12 on, circulation pump on.

8. Get oil from outside into reservoir after vacuum

After vacuum, V3 off or a, V4 off, V5 off or to a, V8 off, V11 off, the oil in/outlet near V6 connected to oil source by plastic tube, V2 off, vacuum pump off, V6 on.

9. Transport oil from test chamber to reservoir by circulation pump

V1 to air, V2 to air, V3 to b, V4 off, V5 to a, V6 off, V7 off, V8 off, V10 to vent, V11 to vent, V12 on, circulation pump on.

10. Get oil out of test chamber by gravitation

V1 to air, V3 off, V4 off, V5 off, V10 to vent, V12 on.

11. Get oil out of test chamber with nitrogen pressure

Bolt down the feed-through with SMA adapters, V1 to air/nitrogen, V12 on, V10 to nitrogen, V3 off, V4 off, V5 off, V7 on, pressure on.

12. Get oil out of reservoir by circulation pump

Connect the oil in/outlet near V6 to container with plastic tube, V2 to air, V3 to b, V4 off, V5 to b, V8 off, V6 on, circulation pump on.

13. Circulate oil within test chamber with system sealed

V1 off, V3 to a, V4 off, V5 to A, V6 off, V7 off, V10 off, circulation pump on.

14. Circulate oil between reservoir and test chamber with system sealed

Bolt down the feed-through, V1 off, V2 off, V3 to a, V4 on, V5 to b, V6 off, V7 off, V8 off, V9 off, V10 off, V11 off, V12 on, circulation pump on.

15. Bubbling moist air to reservoir

Connect pressure source (either nitrogen cylinder or pressure pump) to the gas source with pressure off, V2 to air, V3 off, V4 off, V5 off, V6 off, V7 off, V8 on, V9 on, V11 to air, turn the pressure on.

16. Bubbling moist air to test chamber

Connect pressure source (either nitrogen cylinder or pressure pump) to the gas source with pressure off, V1 to air, V2 off, V3 off, V4 on, V5 off, V6 off, V7 off, V8 on, V9 on, V10 to vent, V11 off, V12 on, turn the pressure on.

17. Pressurize test chamber

V1 to nitrogen, V2 off, V11 off, V9 off, V5 off, V4 off, V3 off, V12 on, and V10 to nitrogen.

18. Bubbling moist air while circulating oil between reservoir and test chamber Bolt down the feedthrough top. V1 off, V2 to air, V3 to a, V4 on, V5 to b, V6 closed, V7 closed, V8 open, V9 open, V10 to vent, V11 off, V12 off, and turn bubbler on.

Appendix B

New Interface Box

This appendix is for the new interface box described in Chapter 6.

B.1 Interface Box Circuitry

Graduate student Darrell Schlicker of the MIT High Voltage Research Lab is the principal designer for the interface box. This thesis work contributed to the implementation of the circuit board layout, manufacturing, and box assembly. All information is included here for future reference. The original designer if other than the thesis author is indicated whenever possible.

The interface box circuitry is composed of three parts: digital expansion board; drive board; and sensing board.

The schematic of the digital expansion part is shown in Figure B.1 and the board layout is shown in Figure B.2 and Figure B.3. The major function is to enable the interface box to run three channels individually and can switch the integration capacitors for different test impedances. The zero-ohm resistors are placed for possible future applications with finite resistances.

The schematic of the drive board is shown in Figure B.4 and the board layout is shown in Figure B.5 and Figure B.6. Its function is to amplify the one volt peak sinusoidal signal from the controller box to 10 volts.

The schematic of the sense board is shown in Figure B.7 and the board layout is shown in B.8 and Figure B.9. Each box has three identical boards for three wavelengths except with different integration capacitor values.

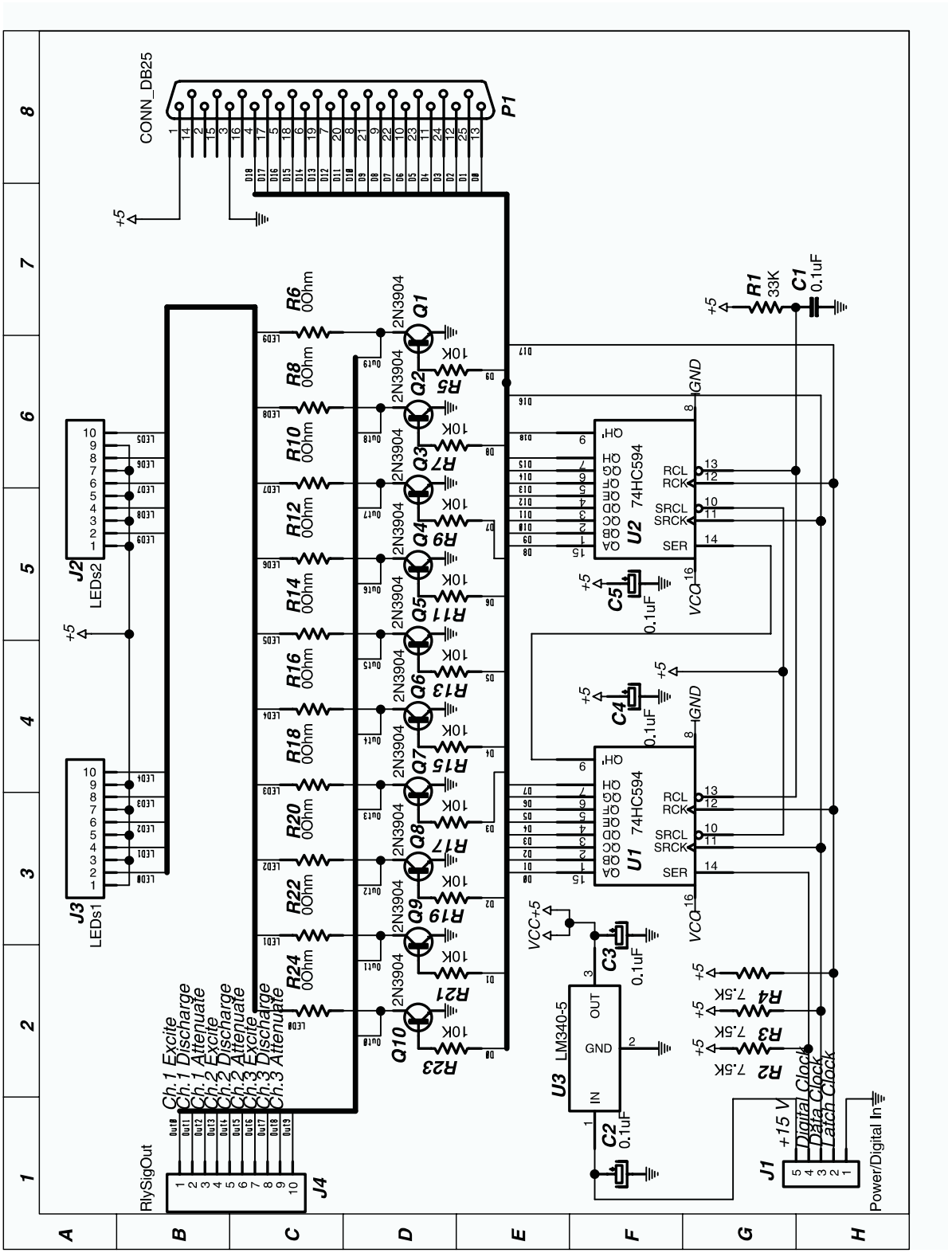

Figure B.1: Schematic of the digital expansion board of the interface box circuitry, mainly laid out by D. E. Schlicker at MIT.

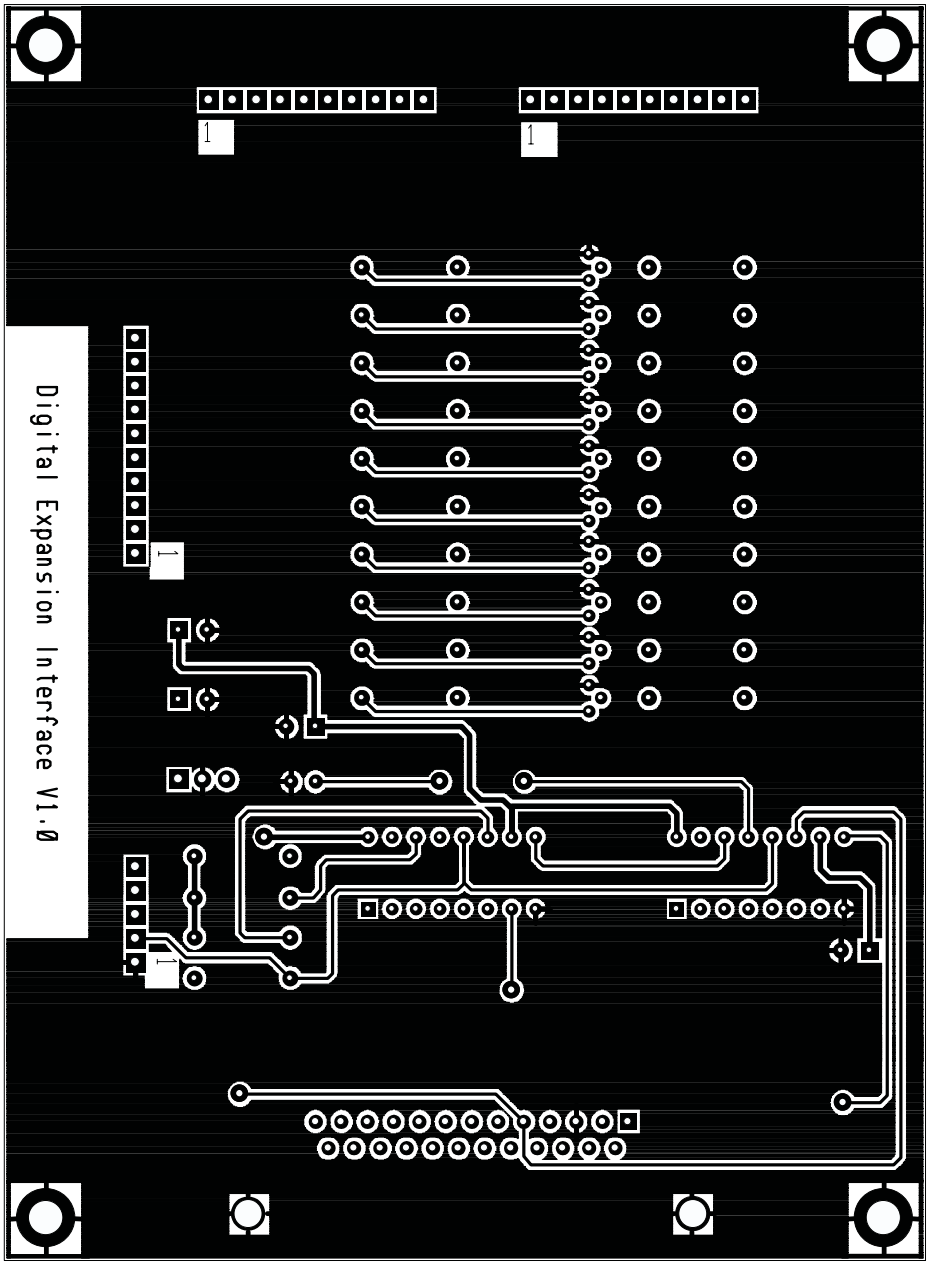

Figure B.2: Component side of the digital expansion board of the interface box circuitry.

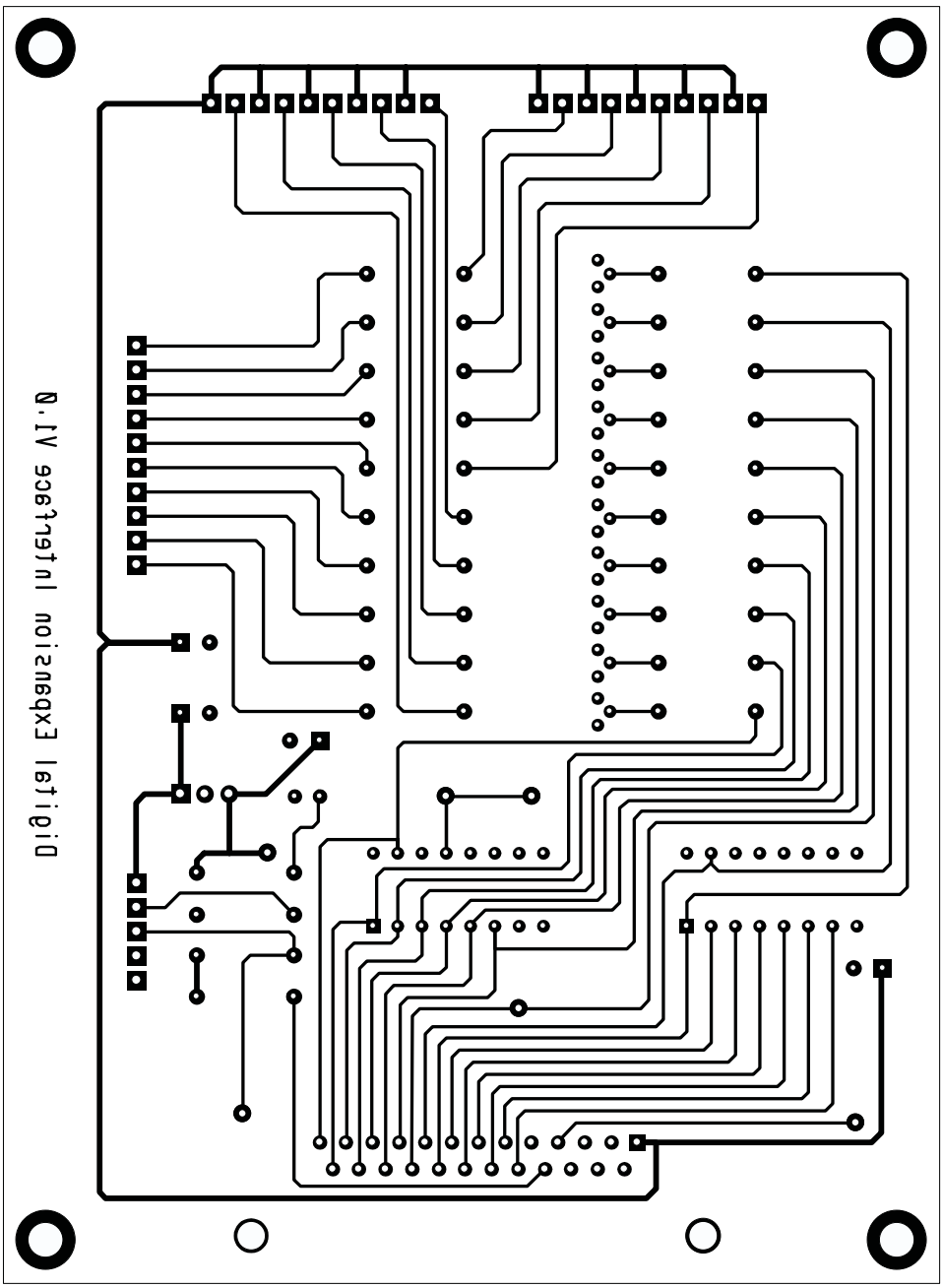

Figure B.3: Solder side of the digital expansion board of the interface box circuitry.

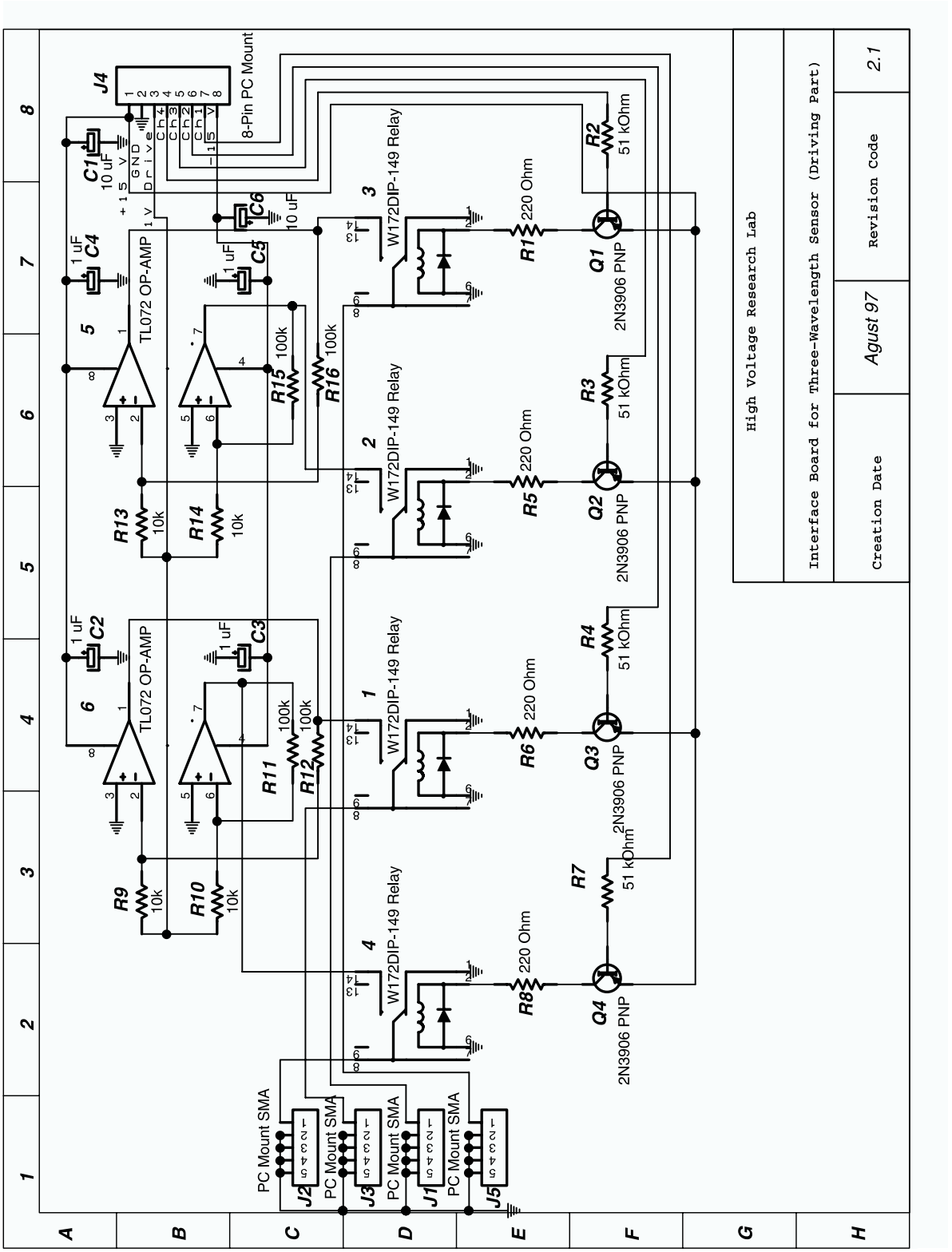

Figure B.4: Schematic of the drive board of the interface box circuitry.

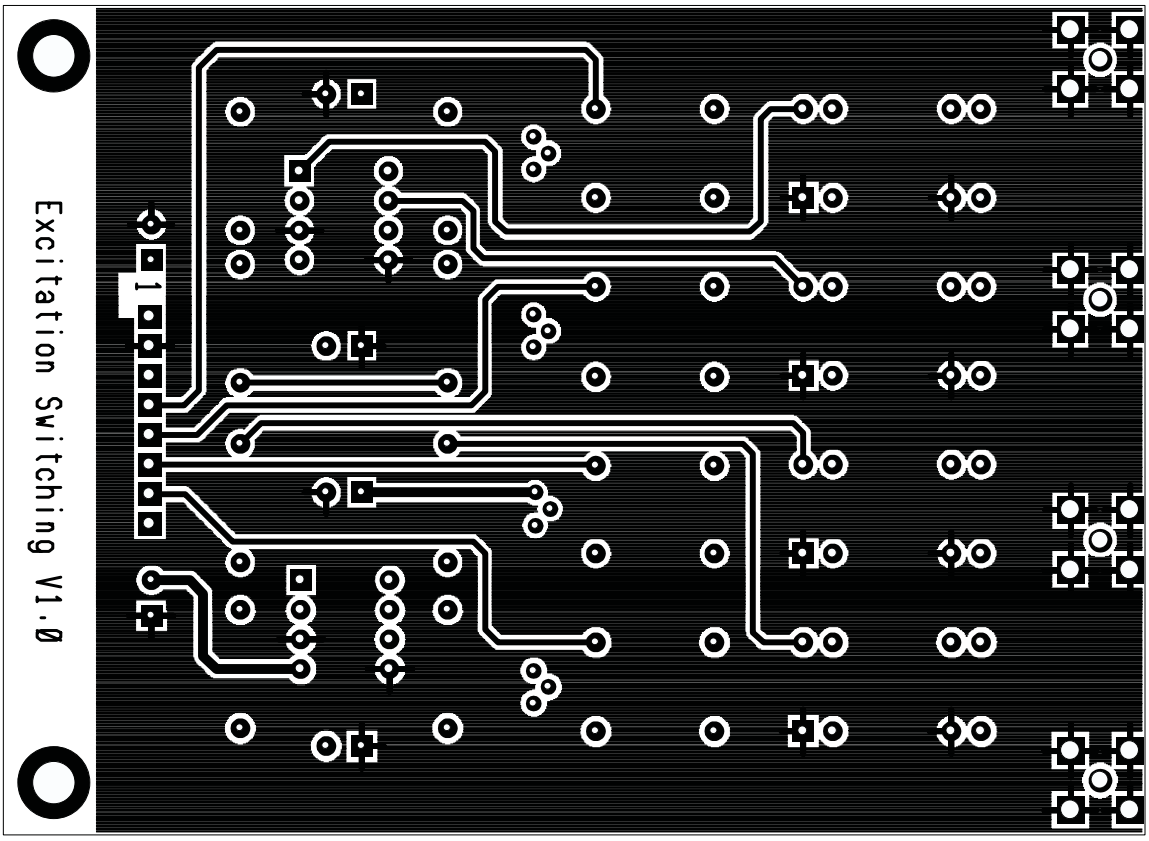

Figure B.5: Component side of the drive board of the interface box circuitry.

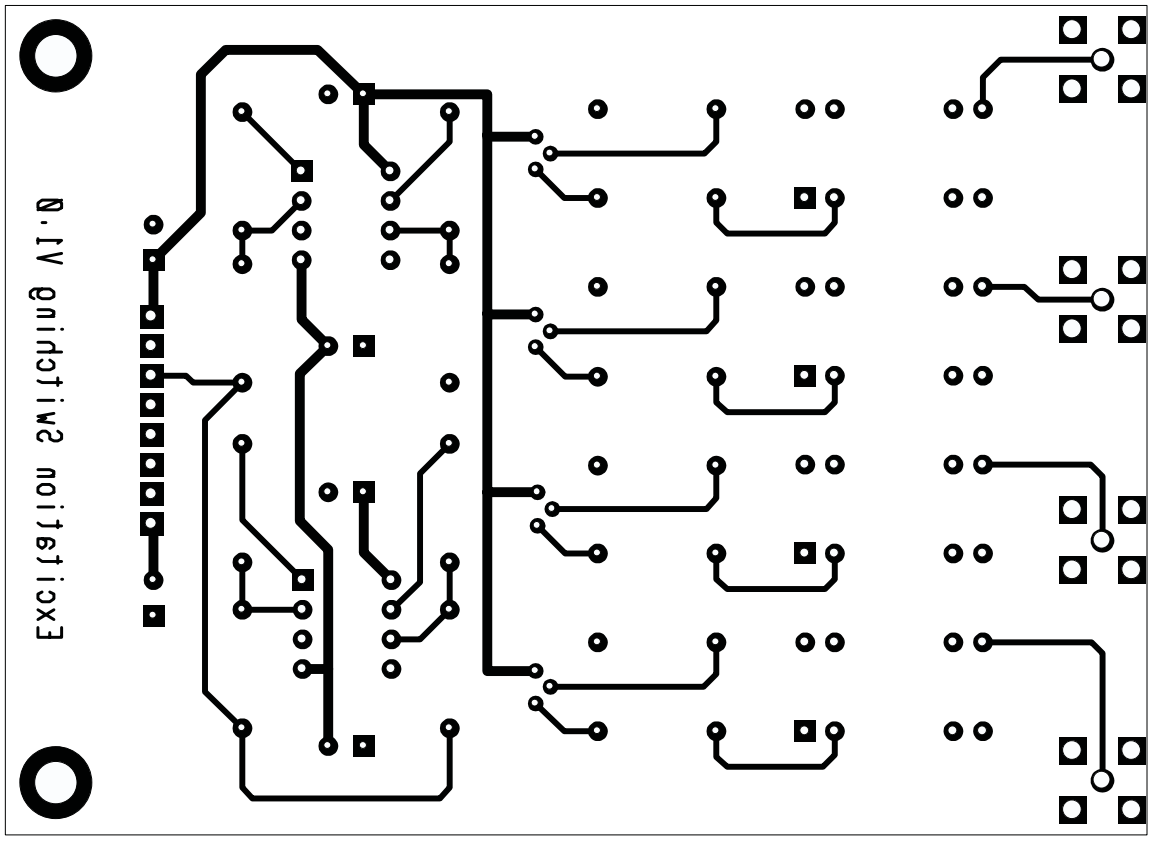

Figure B.6: Solder side of the drive board of the interface box circuitry.

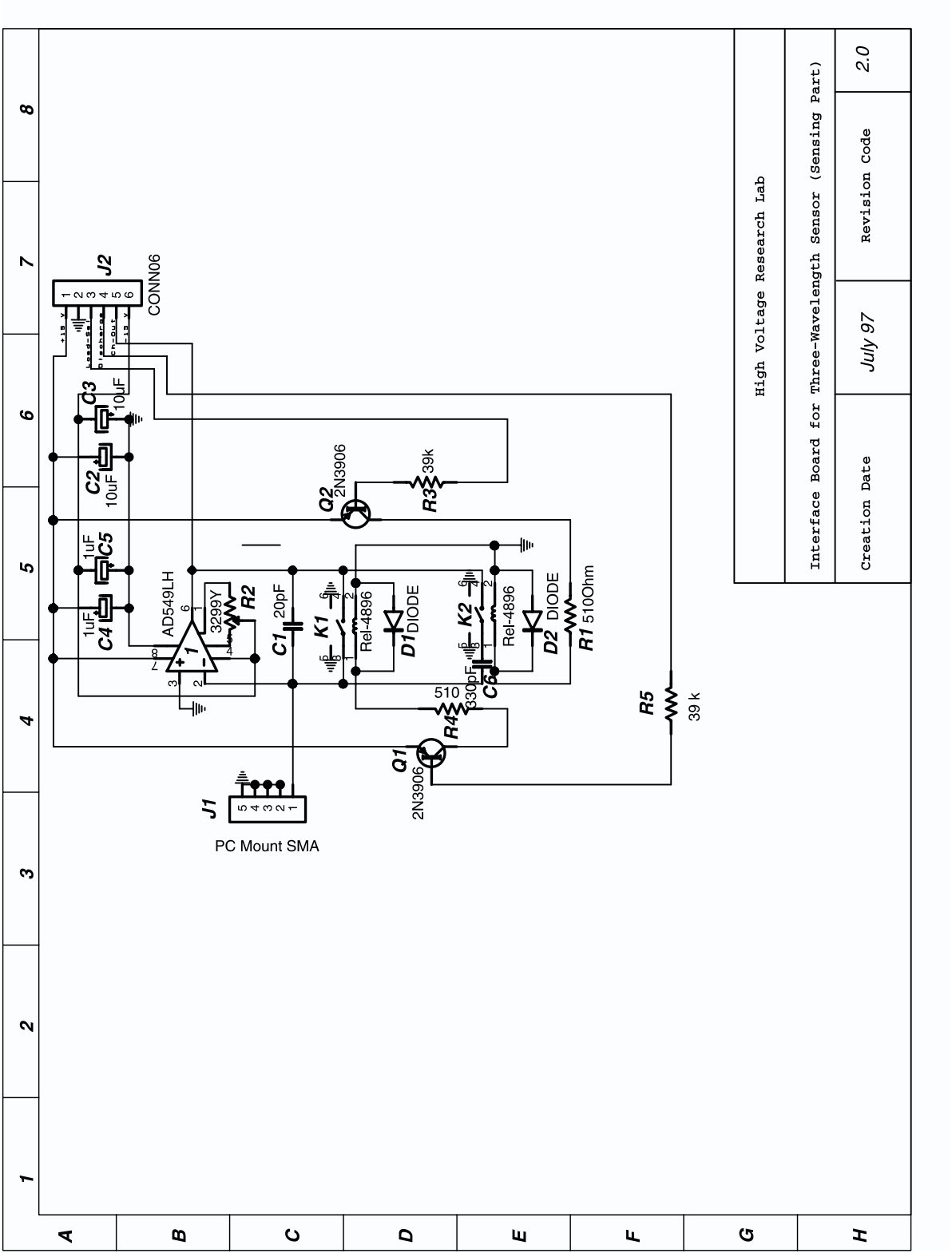

Figure B.7: Schematic of the sense board of the interface box circuitry.

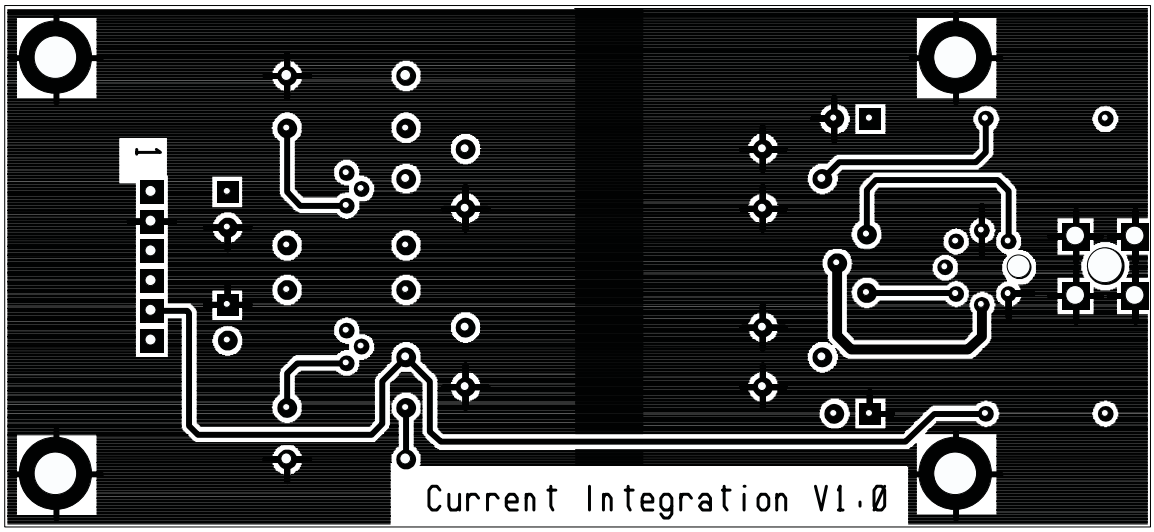

Figure B.8: Component side of the sense board of the interface box circuitry.

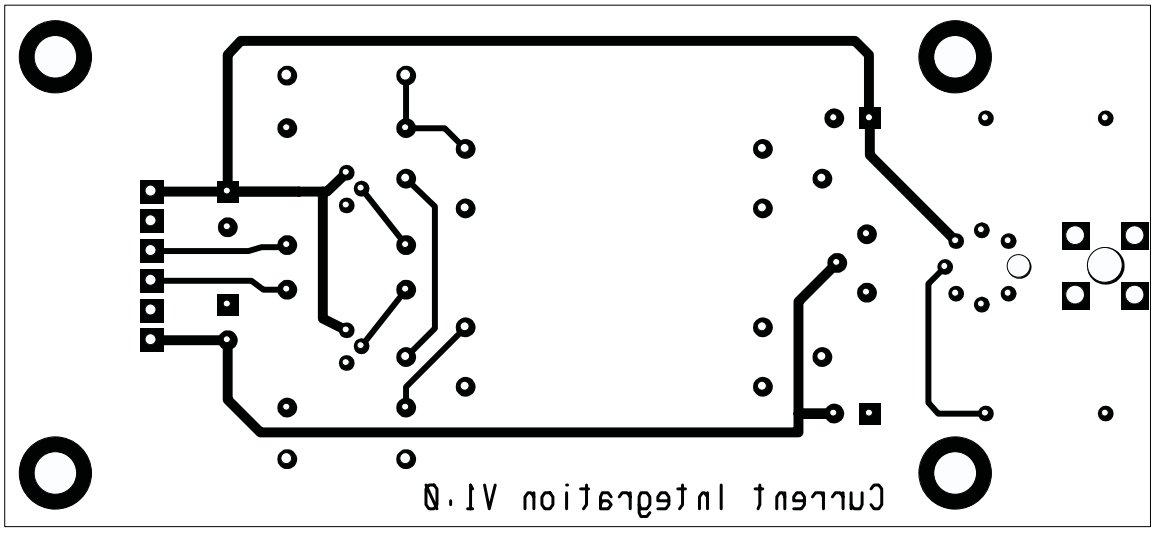

Figure B.9: Solder side of the sense board of the interface box circuitry.

Name	Qua.	Part Number	Supplier	Manufacturer
Connectors:				
Female PC Mount SMA	3	J569-ND	Digi-Key	Johnson Comp.
8-Pin Single Row PC Mount	1	WM4906-ND	Digi-Key	Waldon
8-Pin Single Row Female	1	WM2906-ND	Digi-Key	Waldon
Female Pins for Single Row	8	WM2512	Digi-Key	Waldon
Relays:				
Dip Reed Relay, 12 V SPDT	3	87F237	Newark	Magneraft
Integrated Circuits:				
PNP Transistors	3	2N3906-ND	Digi-Key	National Semi
Resistors:				
51 K, 1/4 W, 5% ,200pkg	0.015	51KQBK-ND	Digi-Key	Yageo
220 Ω, 1/4 W, 5% ,200pkg	0.015	220QBK-ND	Digi-Key	Yageo
10k Ω, 1/4 W, 1% ,200pkg	0.015	10KXBK-ND	Digi-Key	Yageo
100k Ω, 1/4 W, 1% ,200pkg	0.015	100KXBK-ND	Digi-Key	Yageo
Capacitors:				
Tantulum 1uF, 35 WVDC	1	81F4051	Newark	Mallory
Op-Amp				
Dual op-amp	2	LF412CN	Texas Instrument	Texas Instrument

Table B.1: Components list for the drive board.

B.2 Interface Box Assembly

B.2.1 Materials to Begin with

Before starting the interface box assembly, make sure the following materials are available:

- Instruction package including these assembly instructions, circuit schematics, PCB layout, bill of materials (shown in Tables B.1, B.2, B.3, B.4), pinout connections, and box machining template.
- All circuit parts assorted in cabinet.
- Circuit boards.

Name	Qua.	Part No.	Supplier	Manufacturer
Integrated Circuits:				
Shift Register w/ Latch	2	SN74HC594	Arrow Elec.	Texas Instr.
NPN Transistors	10	2N3904-ND	Digi-Key	National Semi
+5 V Regulator	1	LM340T-5.0	Digi-Key	National Semi
Connectors:				
5-Pin Single Row PC Mount	1	WM4903-ND	Digi-Key	Waldon
5-Pin Single Row Female	1	WM2903-ND	Digi-Key	Waldon
10-Pin Single Row PC Mount	1	WM4908-ND	Digi-Key	Waldon
10-Pin Single Row Female	1	WM2908-ND	Digi-Key	Waldon
Female Pins for Single Row	15	WM2512	Digi-Key	Waldon
DB-25 PC Mount 90	1	325F-ND	Digi-Key	Nor Comp
Mounting Hardware	1	A9005-ND	Digi-Key	AMP
10-Pin IDC Single Row .1	2	A1905-ND	Digi-Key	AMP
10-Pin IDC Single Row .1 Header	2	A1920-ND	Digi-Key	AMP
1/4 Watt, 0 Ω Jumper, 200pkg	0.05	0.0QBK_ND	Digi-Key	YAGEO
Indicators:				
Pannel Mt. LED(Red)	3	L10021	Digi-Key	Industrial Devices
Pannel Mt. LED(Amber)	3	L10023	Digi-Key	Industrial Devices
Pannel Mt. LED(Green)	3	L10025	Digi-Key	Industrial Devices
Resistors:				
10 K, 1/4 W, 5% ,200pkg.	0.05	10KQBK-ND	Digi-Key	Yageo
33K Ω, 1/4 W, 5% ,200pkg	0.005	33KQBK-ND	Digi-Key	Yageo
7.5K Ω, 1/4 W, 5% ,200pkg.	0.015	7.5KQBK-ND	Digi-Key	Yageo
Capacitors:				
Tantulum 0.1uF, 50 WVDC	4	81F4062	Newark	Mallory
Ceramic 0.1 uF, 50WVDC	1	95F4960	Newark	Kemet

Table B.2: Components list for digital board.

Name	**Qua.**	**Part No.**	**Supplier**	**Manufacturer**
Connectors:				
Female PC Mount SMA	3	J569-ND	Digi-Key	Johnson Comp.
6-Pin Single Row PC Mount	3	WM4904-ND	Digi-Key	Waldon
6-Pin Single Row Female	3	WM2904-ND	Digi-Key	Waldon
Female Pins for Single Row	36	WM2512	Digi-Key	Waldon
Relays:				
High Contact Impedance Rlys	6		Crydom	Douglas-Randall
Integrated Circuits:				
Electrometer	3	AD549LH	Newark	Analog Devices
Rectifier Diodes	6	1N4001GICT-ND	Digi-Key	General Instr.
PNP Transistors	6	2N3906-ND	Digi-Key	National Semi
Resistors:				
10 K, 25 Turn Trimmer	3	3299Y-103-ND	Digi-Key	Bourns
39 K, 1/4 W, 5%, 200pkg.	0.03	39KQBK-ND	Digi-Key	Yageo
510 Ω, 1/4 W, 5%, 200pkg.	0.03	510QBK-ND	Digi-Key	Yageo
Capacitors:				
Tantulum 1uF, 35 WVDC	6	81F4051	Newark	Mallory
Tantulum 10 uF, 35 WVDC	2	60F3880	Newark	Mallory
20pF, 160V polystyrene	3	20F174	Newark	Mallory

Table B.3: Components list for the sense board.

Name	Qua.	Part No.	Supplier	Manufacturer
Controller-Interface Cable				
8-Cond Shielded 7/30 Stranded	0.1	W508-100-ND	Digi-Key	Carol
RG 179B/U-75 (9179B)	0.4	37F2084	Newark	Alpha
DB-15 Female(solder pot)	1	115F-ND	Digi-Key	Nor-Comp
DB-15 Male(solder pot)	1	115M-ND	Digi-Key	Nor-Comp
DB-15 Metal Hoods	1	915Z-ND	Digi-Key	Nor-Comp
Mounting Hardware	1	A9005-ND	Digi-Key	AMP
Pins for Amp Connector	0.15	96F7936	Newark	AMP
Standard 9 position plug	1	44F8388	Newark	AMP
Shell Size 13 Cable Clamp	1	44F8395	Newark	AMP
Standard 16 position plug	1	44F8390	Newark	AMP
Shell Size 17 Cable Clamp	1	44F8396	Newark	AMP
20-Cond unshielded 7/30 Str.,100ft.	0.02	W131-X-ND	Digi-Key	Carol
Sensor Connection				
Male SMA	6	J525-ND	Digi-Key	Johnson Comp.
Case				
Cast Box (5x 6 x 4)	1	91F718	Newark	Bud
Bumpons(36)	0.11111	SJ5523-0-ND	Digi-Key	3M
Hex Thr. Spacers,6-32, 0.5, 100pkg	0.04	J178-ND	Digi-Key	Johnson Comp.
Rnd. Thr. Spacers,4-40, 0.5, 100pkg	0.04	J241-ND	Digi-Key	Johnson Comp.
4 pole double throw switches	1	CKN1038-ND	Digi-Key	C&K Comp.

Table B.4: Additional parts of the interface box

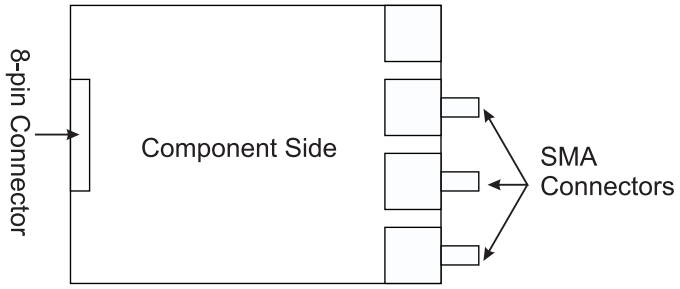

Figure B.10: SMA connections for the drive board.

B.2.2 Board Preparation

Cut individual boards from the raw board carefully using the sheet metal cutter at the LEES machine shop. Need to put paper towel on both sides of the board to protect the surface of the board while cutting.

B.2.3 Interface Board Assembly

Other than regular board soldering cautions, such as the polarity of the capacitor, diodes, and transistors, there are also special places that need extra attention:

1. Sense Boards

• The SMA connectors and the OP-AMP are soldered on the solder side.

• The center pin of the SMA connector, pin 2 of OP-AMP, pin 3 of upper relay and two caps' pins are connected in air without touching the board to avoid a leakage path.

• The SMA should be soldered in such a way that the connector is perpendicular to the board edge. Recommended technique is to solder the pins of SMA diagonally.

2. Drive Board

Only three channels are used for now. So only three SMA connectors are connected as shown in Figure B.10.

3. Digital Board

The 10-pin headers used for LED is IDC (Insulation Displacement Connector), white color, different from that used for the Relay Signal. The designated pin order is

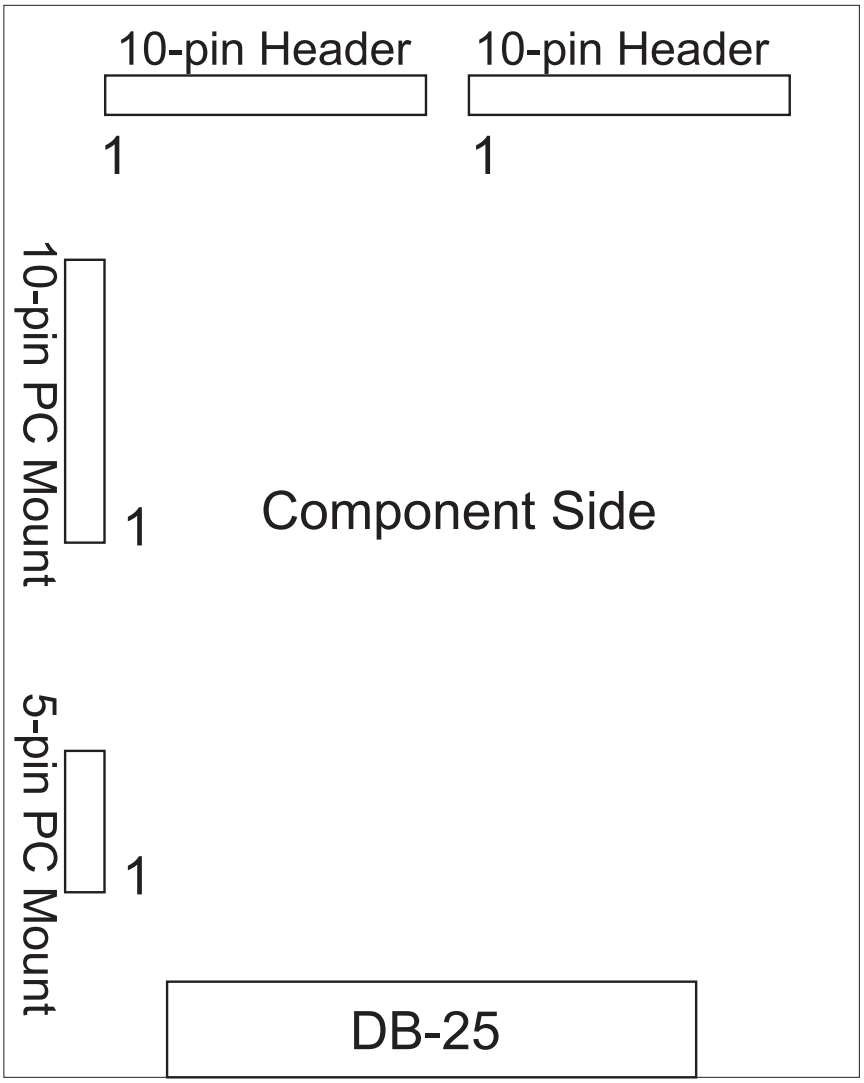

Figure B.11: Connectors for the digital board.

opposite to the header label. The proper pin order is shown in Figure B.11.

B.2.4 Interface Box Assembly

First machine the box following the machine templates shown in Figures B.12– B.16. The templates are all drawn in real size.

- Sense boards are at the bottom and up-side down.
- The SMAs in the front, from left to right, are Channels 1, 2, and 3, respectively; so the sense boards are also designated this way.

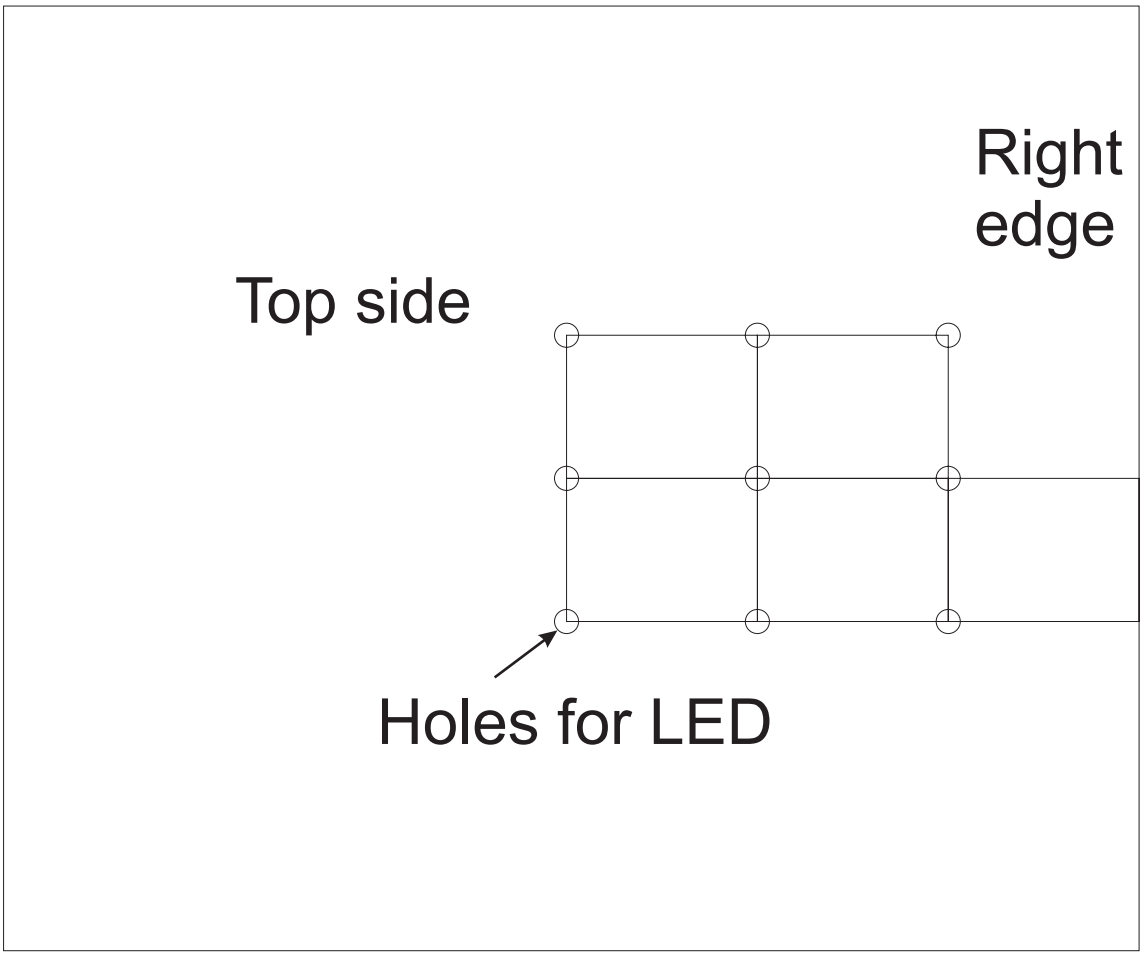

Figure B.12: Machine template for the top of the box for LED connections.

• Sense boards are connected to the bottom side of the Aluminum shielding plate through standoffs. The center board only has three mounting holes on the aluminum plate. Attention must be paid to the orientation of the aluminum plate as indicated in the template.

• Above the aluminum shielding plate is the drive board which has component side up and bolted through stands to the shielding piece.

• The top layer is the digital expansion board and it is component side up. It is mounted to the box through the DB-25 connector. Two porcelain standoffs (about 1 and 3/4" long, such that it touches the aluminum shielding plate; if existing standoff is not long enough, use nylon washers to increase the length) are mounted at the opposite

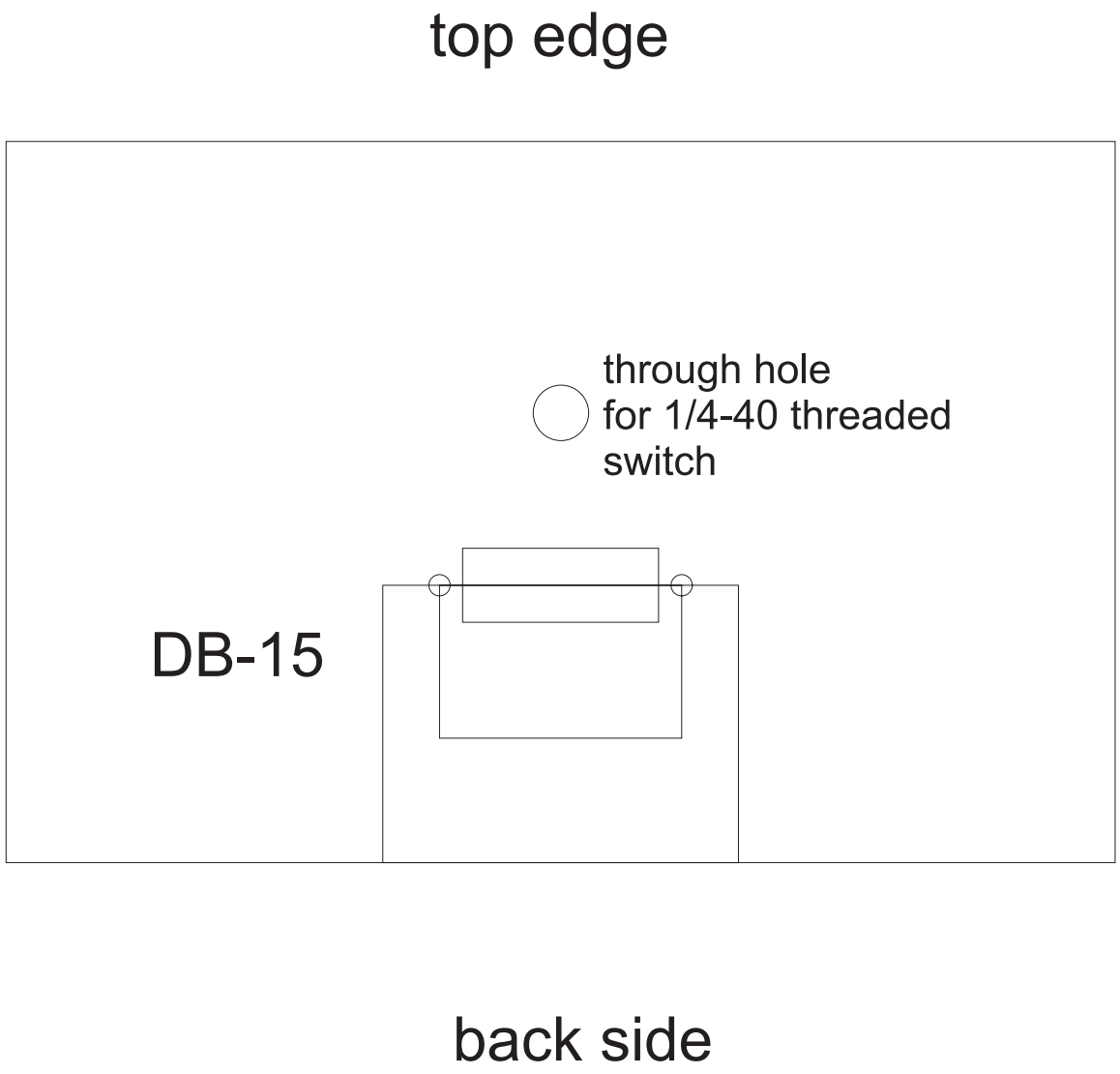

Figure B.13: Machine template for DB 15 connector on the back of the box.

two corners to avoid the digital board touching other places when it is pushed by the LED wires. Without the standoffs, the board could touch the SMA connectors and short circuit, and the two shift registers could be easily burnt out.

• The 4-pole double throw switch is mounted in such a way that looking from the back side of the interface box, the C&K label is at the left. Each pin is defined as shown in Figure B.17.

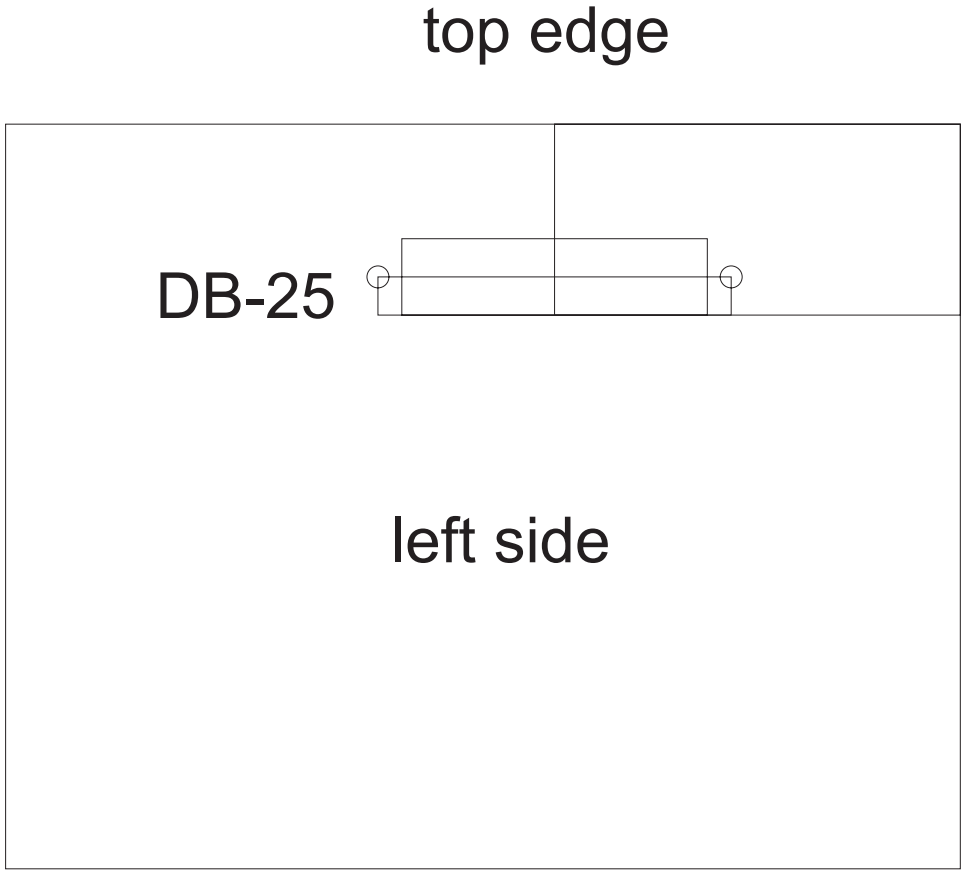

Figure B.14: Machine template for DB 25 connector on the left side of the box.

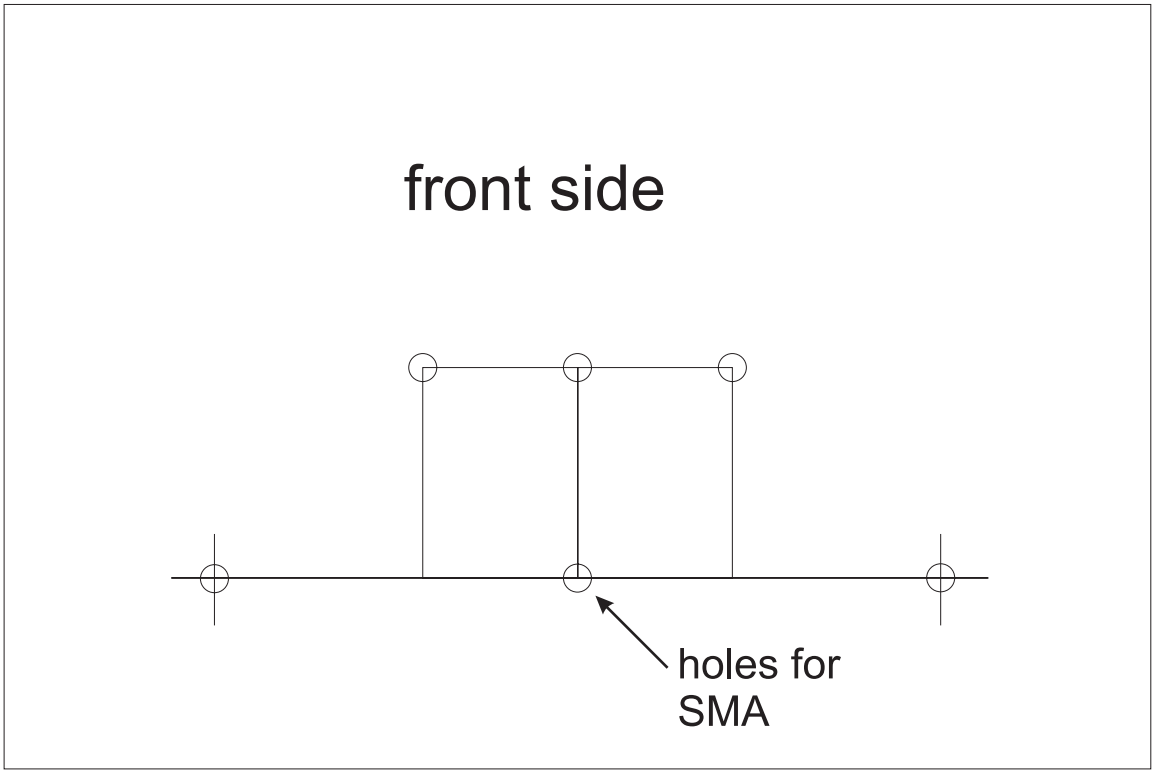

Figure B.15: Machine template for SMA connectors on the front of the box.

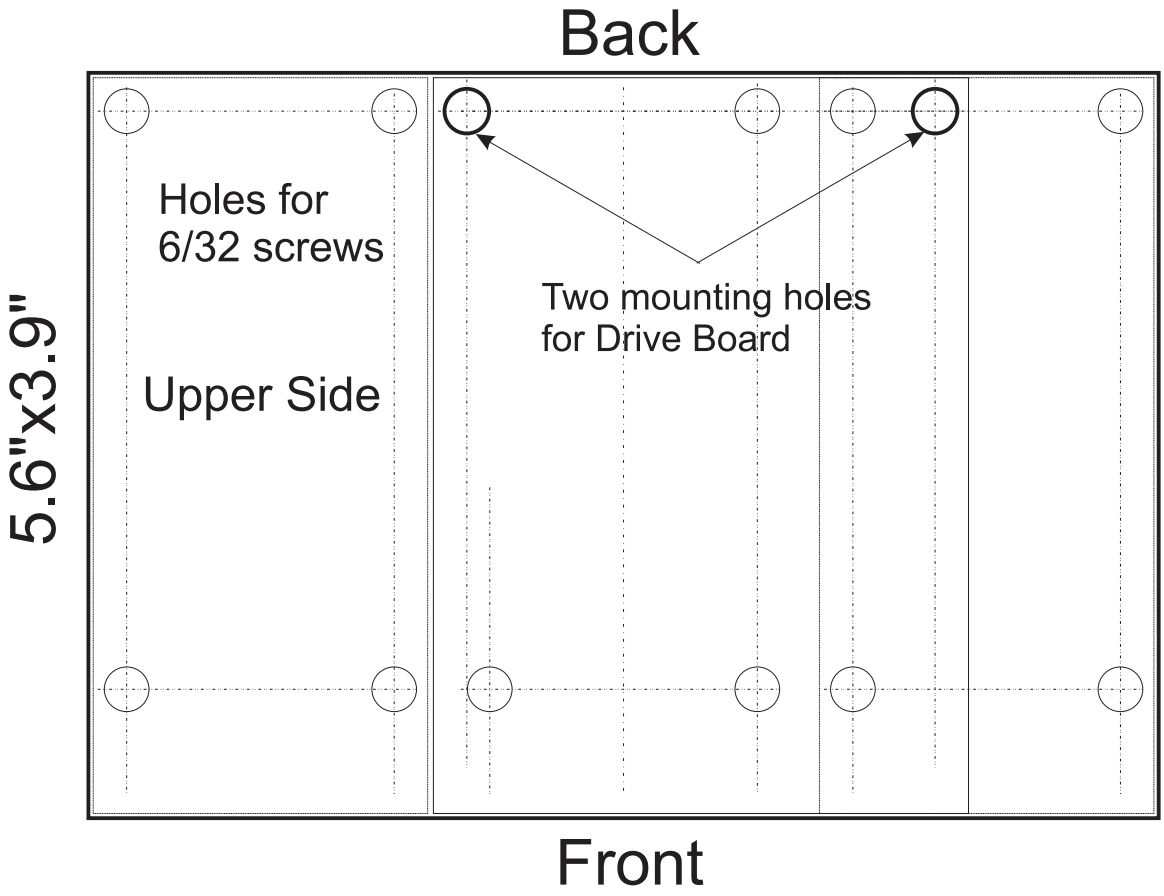

Figure B.16: Machine template for the shielding and separating aluminum plates.

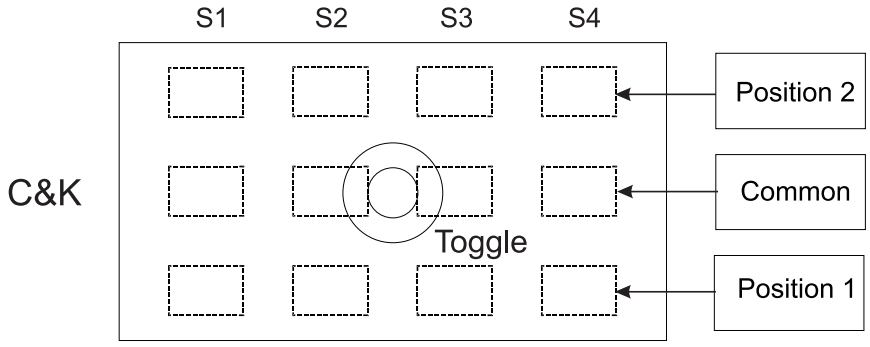

Figure B.17: Numbering and positioning of the four-pole double-throw C&K switch for the relay signal.

Function	Cable	Color Code	DB-15 Pin
1V Excitation	Coax-1	1-Center, 9-Shield	1,9
Channel 1 Signal	Coax-2	2-Center, 10-Shield	2,10
Channel 2 Signal	Coax-3	3-Center, 11-Shield	3,11
Channel 3 Signal	Coax-4	4-Center, 12-Shield	4,12
Mode 0 Discharge	Multi-Conductor	White/Black	5
+15 V	Multi-Conductor	Red, Red/Black	6
Data Clock	Multi-Conductor	White	7
Digital Data	Multi-Conductor	Blue	8
Ground	Multi-Conductor	Green, Bare (cable shield)	13
-15 V	Multi-Conductor	Black	14
Output Latch Strobe	Multi-Conductor	Orange	15

Table B.5: Connection from one end of the multi-conductor cable to DB-15 connector of the interface box.

Function	Cable	Color Code	9-pin CPC
+15 V	Multi-Conductor	Red,Red/Black	1
Mode 0 Discharge	Multi-Conductor	White/Black	2
			3
Excitation	Coax-1	Center	4
GND	Multi-Conductor	Green, Bare(cabel shield)	5
Channel 1	Coax-2	Center	6
Channel 2	Coax-3	Center	7
-15 V	Multi-Conductor	Black	8
Channel 3	Coax-4	Center	9

Table B.6: Connection from the other end of the multi-conductor cable to 9-pin CPC connector of the controller box

B.2.5 Wiring

All wires should be soldered, not just crimped.

• Wiring for Cable Connecting Interface to Controller

The two-end connections for the multi-conductor cables connecting the interface box to the controller box are shown in Tables B.5, B.6, and B.7.

One side of the multi-conductor cable is connected to the DB-15 connector; the majority of wires of the other side of the cable goes to the 9-pin CPC connector while three wires: white, blue, and orange, need to go to the 16-pin CPC connector to the

Function	**Cable**	**Color Code**	**16-pin CPC**
Data Clock	Multi-Conductor	white	12
Digital Data	Multi-Conductor	blue	13
Output Latch Strobe	Multi-Conductor	orange	14

Table B.7: Connection from the other end of the multi-conductor cable to 16-pin connector mate with the controller box 16-pin connector.

controller box. For this purpose, the multi-conductor cable needs to be peeled back about 10 inches to allow enough wires to go to the 16-pin connector.

Pins 9,10,11,12, and 13 of the DB-15 female part should be connected to GND.

• LED Connections

Looking from the component side, the 10-pin IDC header #2 (LEDs1) is at the left side, and 10-pin header #3 is the one on the right side. Pin order is 1 to 10 from left to right. LED connections are listed in Table B.8.

• Board Wiring

Shown in Table B.9 are the wiring charts for DB-15 connectors to board headers and switch: a. DB-15 pin; b. Drive board 8-pin Header; c. Digital board 10-pin Header #1; d. Digital board 5-pin Header e. Sense board Ch.1 6-pin Header; f. Sense board Ch.2 6-pin Header; g. Sense board Ch3. 6-pin Header; h. 4-pole Double Throw Switch. All the PC mount headers on the drive board and sense boards are in reverse pin order, i.e. the arrow in the header indicates the last pin, instead of pin 1. The two PC mount headers in the Digital Board are in the right order, i.e. the arrow indicates Pin 1.

10-Pin Header #2:	**Pin**	**Function**		**Color**
IDC Connectors	1	+5 V	Ch. 1 Excite (green) LED +	Red
	2	D0	Ch. 1 Excite (green) LED -	White
	3	+5 V	Ch. 1 Discharge (red) LED +	Red
	4	D1	Ch. 1 Discharge (red) LED -	White
	5	+5 V	Ch. 1 Attenuate (amber) LED +	Red
	6	D2	Ch. 1 Attenuate (amber) LED -	White
	7	+5 V	Ch. 2 Excite (green) LED +	Red
	8	D3	Ch. 2 Excite (green) LED -	White
	9	+5 V	Ch. 2 Discharge (red) LED +	Red
	10	D4	Ch. 2 Discharge (red) LED -	White
10-Pin Header #3:	**Pin**	**Function**		**Color**
IDC Connector	1	NA		
	2	NA		
	3	+5 V	Ch. 3 Attenuate (amber) LED +	Red
	4	D5	Ch. 3 Attenuate (amber) LED -	White
	5	+5 V	Ch. 3 Discharge (red) LED +	Red
	6	D6	Ch. 3 Discharge (red) LED -	White
	7	+5 V	Ch. 3 Excite (green) LED +	Red
	8	D7	Ch. 3 Excite (green) LED -	White
	9	+5 V	Ch. 2 Attenuate (amber) LED +	Red
	10	D8	Ch. 2 Attenuate (amber) LED -	White

Table B.8: Connections for the LEDs on the top of the interface box to the digital board.

Function	**Wire Color**	**a**	**b**	**c**	**d**	**e**	**f**	**g**	**h**
1. 1V Excitation	White/Black	1	3						
2. Ch. 1 Signal	Blue/Black	2				5			
3. Ch. 2 Signal	Green/White	3					5		
4. Ch. 3 Signal	White/Red	4						5	
5. Mode 0 Discharge	Red/Black	5							1 of all
6. +15 V	Red	6	1		5	1	1	1	
7. Data Clock	Blue/Red	7			3				
8. Digital Data	Red/Green	8			4				
9. Excitation Shield	Black	9							
10. Ch.1 Signal Shield	Black	10							
11. Ch.2 Signal Shield	Black	11							
12. Ch.3 Signal Shield	Black	12							
13. Ground	Black	13	2		1	2	2	2	
14. -15 V	White	14	8			6	6	6	
15. Latch Clock	Orange/Red	15			2				
16. Ch. 1 Excite	Green		7	1					
17. Ch. 1 Discharge	Orange/Black					4			Com. of S1
18. Ch. 1 Discharge (Mode 1)	Orange/Black			2					2 of S1
19. Ch. 1 Attenuate	Green/Black			3		3			
20. Ch. 2 Excite	Orange		6	4					
21. Ch. 2 Discharge	Red/White						4		Com. of S2
22. Ch. 2 Discharge (Mode 1)	Red/White			5					2 of S2
23. Ch. 2 Attenuate	Black/White			6			3		
24. Ch. 3 Excite	Blue		5	7					
25. Ch. 3 Discharge	Black/Red							4	Com. of S3
26. Ch. 3 Discharge (Mode 1)	Black/Red			8					2 of S3
27. Ch. 3 Attenuate	Blue/White			9				3	

Table B.9: Board wiring for DB-15 connectors to board headers and switch.

Appendix C

Moisture Content in Wood Pulp

Jeffries reported data for the moisture content in wood pulp versus ambient relative humidity as a function of temperature in [50]. Oommen [23] drew a group of equilibrium curves from Jeffries' data which can be used to find the moisture content in the pressboard at the boundary when the air relative humidity is monitored. At each temperature each curve is fitted with a 6th-order polynomial (the highest order of *Excel* trendline function) to be conveniently used in the algorithm

$$y = a_6x^6 + a_5x^5 + a_4x^4 + a_3x^3 + a_2x^2 + a_1x + a_0, \tag{C.1}$$

where x is the air relative humidity in percent and y is the moisture in paper in percent by weight. The coefficients in (C.1) are shown in Table C.1. The moisture equilibrium curves reconstructed from the 6-th order polynomial are shown in Figure C.1.

T (°C)	**30**	**40**	**50**	**60**	**70**
$a_6(\times 10^{-11})$	-9.3468655	-3.8729882	9.5319144	7.4380470	16.252499
$a_5(\times 10^{-8})$	4.2446633	2.5228351	-1.1755019	- 0.75286519	- 3.3218692
$a_4(\times 10^{-6})$	-6.3395879	-4.2926236	-0.37397578	- 0.57129397	2.2473555
$a_3(\times 10^{-4})$	4.3831525	3.2448905	1.2731316	1.1731076	- 0.27101029
$a_2(\times 10^{-3})$	- 14.929696	-11.950117	-7.2850779	-6.2300223	- 2.7797731
$a_1(\times 10^{-1})$	3.2828657	2.9079147	2.4316118	2.1359436	1.7762623
$a_0(\times 10^{-1})$	2.4131270	1.6954583	1.0483257	1.3978572	0.7441865

Table C.1: Polynomial fitting parameters for partition curves for ambient air relative humidity and moisture in paper for various temperatures.

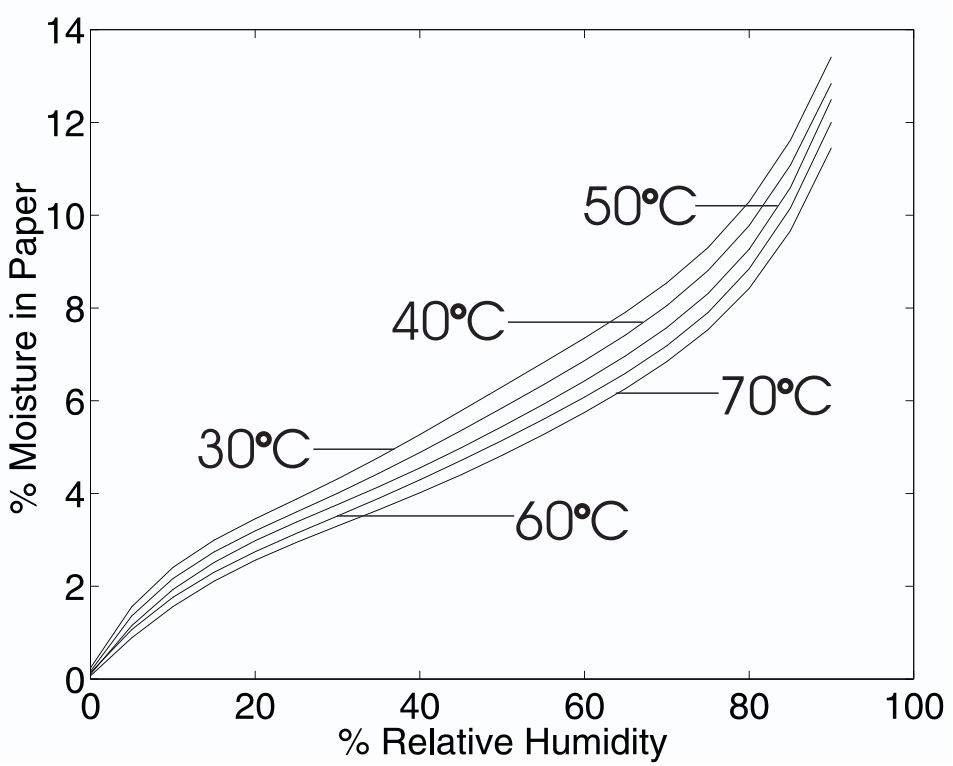

Figure C.1: Moisture in wood pulp as a function of ambient relative humidity curves reconstructed from the 6-th order polynomial fit to Jeffries' [50] data that is plotted in Figure 3.4.

Appendix D

Couette Experiment Check List

The monitoring and control instruments are shown in Figure D.1. Valves are all labeled in the Couette Facility.

D.1 Pre-Check

Before starting any measurement, check the following:

1. Make sure there is enough coolant in the cooling system.

2. Turn on Air-conditioner, Dehumidifier, and wait for the hood to stabilize in temperature.

3. Thermal probe: if there is no transformer oil in the Couette Charger, connect the probe on the side of the cylinder to the plug on the hood labeled as "top"; if there is oil in the Charger, connect the top probe to the "top" plug, and the side probe to the "side" plug.

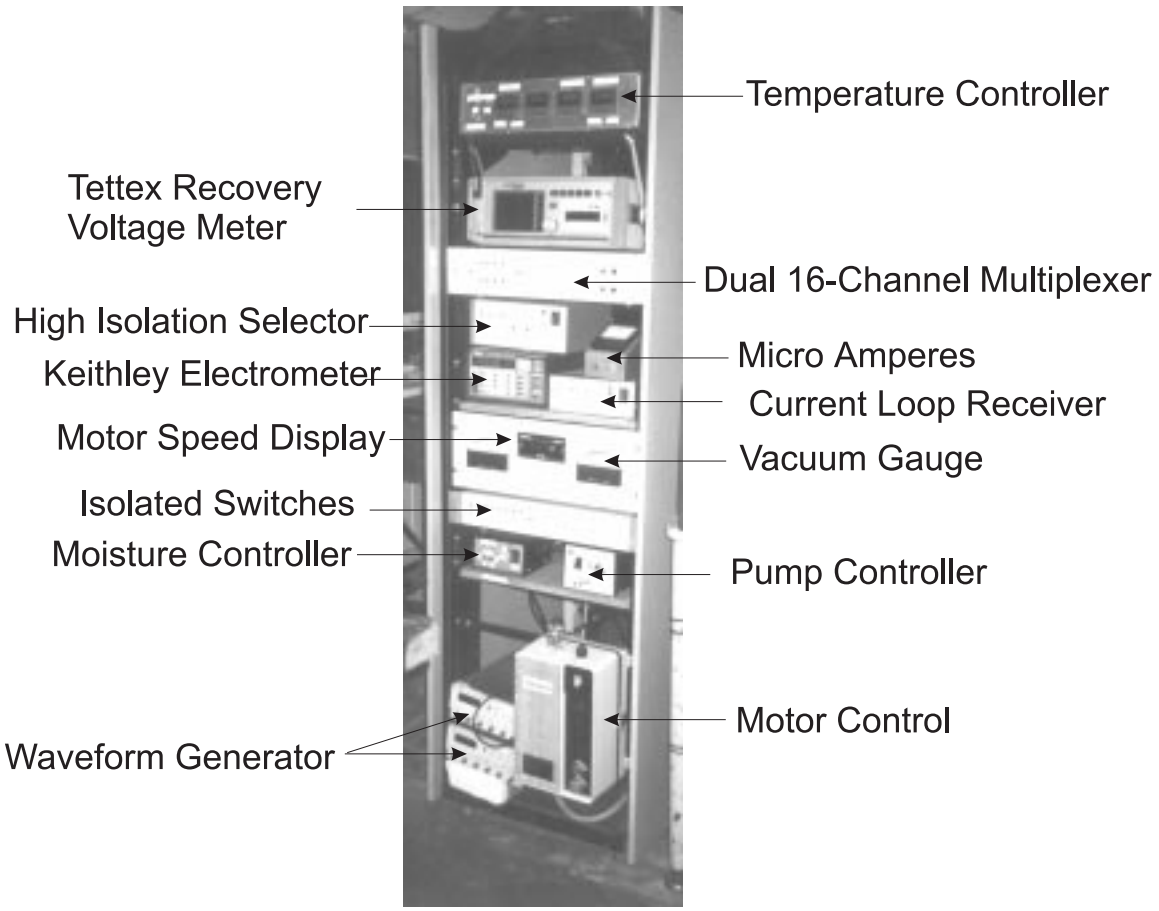

Figure D.1: The instrument rack of the Couette Facility.

D.2 Manual Operation before Starting the Computer Controlled Experiment

The following operations need to be done manually before computer controlled experiment, from top to bottom of the instrument rack:

1. Power on for Heating/Cooling controller. Set both pumps to 'Auto'. Adjust and set temperatures, manually turn on the cooling system. Couette temperature should be stabilized.

2. Power on and set 'Auto' for Dual 16 Channel Multiplexer.

3. Set 'Auto' for High Isolation 1 of 3 Selector.

4. Power on and set 'Volts, Auto, Meter and Zero correct' for Keithley Electrometer.

5. Power on for Current Loop Receiver, verify that indicators are illuminated for each installed moisture meter.

6. Power on for DC MicroAmperes for measuring of the oil level in the reservoir.

7. Power on for Computer Controlled Isolated Switches.

8. Power on and set 'Auto' for both Moisture Controllers.

9. Power on and set 'Auto' for Pump Control.

10. Motor Control power on, turn the speed all the way down (no rotation), push the run button.

Now you are ready to use Darrell Schlicker's fully automated Window's software *SPIN* [89]!

D.3 To Fill Oil in Couette Charger

To introduce dry oil to the Couette Charger (CC) by N_2 pressure when CC is in vacuum:

1. Get flash light, V6 off, V7 off;

2. Turn on N_2;

3. V4 to N_2;

4. V3 to N_2;

5. V15 close;

6. V7 to 'b';

7. V8 on, V9 to 'a';

8. V11 on, V12 off;

9. Shine flash light and watch top when oil is close to top level;

10. Close V14 when oil is close to the top. Do not wait until the oil touches the top because oil will be sucked into the vacuum pipe path;

11. V13 to 'a'.

D.4 To Push Oil from Couette Charger to Reservoir

To push oil from the CC to the Reservoir by nitrogen pressure:

1. Stop vacuum;
2. V2 to N_2;
3. V1 to N_2;
4. V9 to 'a';
5. V8 on;
6. V7 to 'b';
7. V6 off;
8. V3, V4 to air;
9. V14 on.

D.5 To Vacuum Couette Charger

To vacuum CC:

1. V11 off;
2. V13 off;
3. V1 to Vacuum;
4. Turn the vacuum pump on;
5. V14 slowly on to avoid oil being sucked into the vacuum path.

D.6 To Wet Oil in Couette

To moisten the oil in CC:

1. Turn off V14;
2. Stop Vacuum;
3. Connect air pump;

4. V11 on;
5. Push more oil into CC by vacuum;
6. Open to V1,V2,V3 and V4;
7. V9 to 'a';
8. V8 off;
9. V7 to 'b';
10. V13 to 'b';
11. V6 on;
12. Turn air pump on;
13. V5 on;
14. Run bubbler by $SPIN$ software;
15. Turn oil circulating pump on.

Caution: when raising temperature of oil, make sure valve 13 turns to mini-reservoir 'a'.

(This appendix was jointly prepared by D.E. Schlicker, S. H. Kang, and Y. Du)

Appendix E

Data Processing Code

E.1 Diffusion Analysis

```
function C=fick(C1,D,hour)

%Function fick plot the spatial profile of moisture for constant
%diffusion coefficient D and boundary condition C1 at 2-hour interval
%for a total of time of "hour" using Fick's second law of diffusion.

C0=0;
x=0:10^(-5):1.5*10^(-3);
xx=1.5*10^(-3):-10^(-5):0;
l=1.5*10^(-3);
n=0:20;

for t=2*3600:2*3600:hour*3600

for k=1:length(x)
a=(-1).^n./(2*n+1);
b=exp(-D*10^(-12)*(2*n+1).^2*pi^2*t/4/l^2);
c=cos((2*n+1)*pi*x(k)/2/l);
intermediate=a.*b.*c;
C(k)=C0+(C1-C0)*(1-4/pi*sum(intermediate));
end

a=plot(xx*1000,C,'-.');
hold on
end
```

```
function Csim= DiffImpl(D0,k,Ea,T,CompHours,C1,l)
        % This function plots the spatial profile of diffusion process
% with diffusion coefficient a function of concentration and temperature.
% D0 is actual D0*10^12,Ea is actual Ea/1000. T is in C, CompHours
% is in hours, each hour that want to be ploted are stored in column for
% each temperature, C1 is in percent, l is m.
% Implicit Method


%time steps in an hour
TimeSteps=400;
XSteps=150;

q=0;

for n=1:length(T)
dt=max(CompHours(:,n))*3600/TimeSteps;
ll=2*l(n);
x=0:ll/XSteps:ll;
dx=ll/XSteps;
b=dt/dx^2;

%Boundary Condition
C(1)=C1(n);
C(XSteps+1)=C1(n);
%Initial Condition
C(2:XSteps)=0;
Cp=C;
m=XSteps-1;
dimen=2:m-1;
for o=1:length(CompHours(:,n))-1
for t=CompHours(o,n)*3600:dt:CompHours(o+1,n)*3600
         D=D0*1e-12*exp(k*C+Ea*1000*(1/298-1/(273+T(n))));
 Z=D/k;
         Diag1=(-b*D(2:XSteps))';
 Diag2=(1+2*D(2:XSteps)*b)';
 Diag3=(-b*D(2:XSteps))';
 A=spdiags([Diag1 Diag2 Diag3],-1:1,m,m);
 B(1)=b*D(1)*C(1)+C(2)+b*(Z(3)-C(3)*D(3)-2*Z(2)+2*C(2)*D(2)...
+Z(1)-C(1)*D(1));
 B(dimen)=C(dimen+1)+b*(Z(dimen+2)-C(dimen+2).*D(dimen+2)-...
  2*Z(dimen+1)+2*C(dimen+1).*D(dimen+1)+Z(dimen)-C(dimen).*D(dimen));
 B(m)=b*D(1)*C(1)+C(XSteps)+b*(Z(1)-C(1)*D(1)-2*Z(XSteps)...
   +2*C(XSteps)*D(XSteps)+Z(m)-C(m)*D(m));
 Cp(2:XSteps)=A\B';
         C=Cp;
      end
plot(x*1000,C,'r')
hold on
Csim_intermediate(o)=C(XSteps/2+1);
   end
set(gca,'FontSize',20)
```

```
xlabel('Pressboard thickness, mm','FontSize',20);
ylabel('Moisture concentration, %','FontSize',20);
axis([0 1.5 0 C1(n)])

Csim(q+1:q+length(CompHours(:,n))-1)=Csim_intermediate;
q=length(Csim);
end
```

```
          function diff = LsqImpl(D,CompHours,C1,Cexp,T,l)
          % This function is called by leastsq.
          % D is a vector which contains the coefficients of the
          % equation.  For finding the parameters for the D for all temperature data.
  % Use implicit method
  % Y. Du 6/22/98
D0=D(1);
k=D(2);
Ea=D(3);


%time steps in an hour
TimeSteps=60;
dt=3600/TimeSteps;
XSteps=100;

q=0;

for n=1:length(T)
ll=2*l(n);
dx=ll/XSteps;
b=dt/dx^2;

%Boundary Condition
C(1)=C1(n);
C(XSteps+1)=C1(n);
%Initial Condition
C(2:XSteps)=0;
Cp=C;
m=XSteps-1;
dimen=2:m-1;
for o=1:length(CompHours(:,n))-1
for t=CompHours(o,n)*3600:dt:CompHours(o+1,n)*3600
         D=D0*1e-12*exp(k*C+Ea*1000*(1/298-1/(273+T(n))));
 Z=D/k;
         Diag1=(-b*D(2:XSteps))';
 Diag2=(1+2*D(2:XSteps)*b)';
 Diag3=(-b*D(2:XSteps))';
 A=spdiags([Diag1 Diag2 Diag3],-1:1,m,m);
 B(1)=b*D(1)*C(1)+C(2)+b*(Z(3)-C(3)*D(3)-2*Z(2)+2*C(2)*D(2)...
+Z(1)-C(1)*D(1));
 B(dimen)=C(dimen+1)+b*(Z(dimen+2)-C(dimen+2).*D(dimen+2)-...
  2*Z(dimen+1)+2*C(dimen+1).*D(dimen+1)+Z(dimen)-C(dimen).*D(dimen));
 B(m)=b*D(1)*C(1)+C(XSteps)+b*(Z(1)-C(1)*D(1)-2*Z(XSteps)...
   +2*C(XSteps)*D(XSteps)+Z(m)-C(m)*D(m));
 Cp(2:XSteps)=A\B';
         C=Cp;
      end
Csim_Intermediate(o)=C(XSteps/2+1);
end
leng=length(CompHours(:,n));
```

```
Csim(q+1:q+leng-1)=Csim_Intermediate;
q=length(Csim);
end

        diff = Csim- Cexp;
```

```
%Process.m processs the data from newsys97/newint5(30C),8(50C),9(60C),...
% 10(70C),11(40C) for diffusion coefficient
% using the new algorithm of implicit method

Cexp= [ 0.7343, 4.9731, 7.0233,...
0.3198, 1.5261, 3.9067,...
0.3610    1.1857    2.9841 ...
0.2940    1.2938    2.8914 ...
0.5087    1.1251    1.7721]
CompHours=[0       0    0   0    0;
       4.1697  10.3467  6.7314  5.1719   4.6603 ;
       11.2903 24.0158  13.8311 11.9792  9.9106;
       17.2122 44.5989 25.9631 22.3219  17.7275];
T=[30 40 50 60 70];
l=[1e-3 1.5e-3 1.5e-3 1.5e-3 1.5e-3];
C1=[7.8372 4.7156 3.3823 2.9424 1.8712];

%Using Least Square Fit to find D
Opt(1)=0;
Opt(2)=1e-8;
Opt(3)=1e-8;
Opt(4)=1e-8;

tic
Dini=[0.5 0.5 7];
D=leastsq('LsqImpl',Dini,Opt,[],CompHours,C1,Cexp,T,l);
toc
```

E.2 General Three-Wavelength Sensor Data Processing

```
function ngpimpVc(DatFileName,filebegin,fileend,ttl,fno,Num,CL1mm, CL2mm,CL5mm,
VoltageBoostOrNot)

% Function ngpimpVc plots  raw data of all frequency
% data in a multi-frequency measurement in one figure using the
% time in the Head, given the frequency started at 10^fmax, ended
% at 10^fmin and the relative humidity using the new interface box.
% Data collected using Code NA*SIN1C.e
% It also computes C12 and G12.
% VoltageBoostOrNot=0, means 1 volt excitation
% VoltageBoostOrNot=1, means 10 volts boost

% Data aquisition by D.E. Schlicker
% Data process by Y. Du
% 11/11/97

% open data file

%no. of data in one measurement (between each time header
dno=2;
col=0;
fileno=fileend-filebegin+1;

for file=filebegin:fileend
file
    if (fileno==1) DatID=fopen(DatFileName,'rt');
else if(file<=9)  DatID = fopen([DatFileName '00' num2str(file) '.gpd'],'rt');
     else if(file<=99) DatID= fopen([DatFileName '0' num2str(file) '.gpd'],'rt');
else DatID=fopen([DatFileName '1' num2str(file) '.gpd'],'rt');
     end
    end
    if (DatID == -1)
disp(' ');
error('Error Opening Data File!');
    end;
    for k=1:Num*3*fno
Head(:,k+col) = fscanf(DatID,'[GH,%f,%i,%i,%i,%i,%i,%i]',7);
      Data(:,col*dno+(k-1)*dno+1:col*dno+(k-1)*dno+dno)=fscanf(DatID,...
         '[GD,%i,%f,%f,%f,%f,%i]',[6,dno]);
    end

    fclose(DatID);
    [row col]=size(Head);
    end
end
col=col/fno;
```

```
dno=dno*fno;

for k=1:fno
Gain1(k,:)=Data(3,k*2-1+dno*2:dno*3:col*dno-1);
Gain25(k,:)=Data(3,k*2-1+dno:dno*3:col*dno-1);
Gain5(k,:)=Data(3,k*2-1:dno*3:col*dno-1);

Offset1(k,:)=Data(5,k*2-1+dno*2:dno*3:col*dno-1);
Offset25(k,:)=Data(5,k*2-1+dno:dno*3:col*dno-1);
Offset5(k,:)=Data(5,k*2-1:dno*3:col*dno-1);
Amp1(k,:)=Data(6,k*2-1+dno*2:dno*3:col*dno-1);
Amp25(k,:)=Data(6,k*2-1+dno:dno*3:col*dno-1);
Amp5(k,:)=Data(6,k*2-1:dno*3:col*dno-1);

Phase1(k,:)=Data(4,k*2-1+dno*2:dno*3:col*dno-1);
Phase1(k,:)=Phase1(k,:)+360*(Phase1(k,:)<0)*(VoltageBoostOrNot==0);
Phase25(k,:)=Data(4,k*2-1+dno:dno*3:col*dno-1);
Phase25(k,:)=Phase25(k,:)+360*(Phase25(k,:)<0)*(VoltageBoostOrNot==0);
Phase5(k,:)=Data(4,k*2-1:dno*3:col*dno-1);
Phase5(k,:)=Phase5(k,:)+360*(Phase5(k,:)<0)*(VoltageBoostOrNot==0);

%RH for oil
RH(k,:)=(Data(5,k*4:dno*3:col*dno)-1)/4*100-2.575;

Freq(k,:)=10.^(Data(2,k*2-1+dno*2:dno*3:col*dno-1));
end


%Determine the relative time

T1=Head(3,1)*30*24+Head(4,1)*24+Head(5,1)+Head(6,1)/60+Head(7,1)/3600;
T22=T1;
for k=1:col/3
kk=k*3*fno-8;
T2=Head(3,kk)*30*24+Head(4,kk)*24+Head(5,kk)+Head(6,kk)/60+Head(7,kk)/3600;
time(k)=T2-T1;
end


%Impedance calculation
Gr1mm = 10.^(Gain1./20);
Fi1mm = Phase1*pi/180;

Gr25mm = 10.^(Gain25./20);
Fi25mm = Phase25*pi/180;

Gr5mm = 10.^(Gain5./20);
Fi5mm = Phase5*pi/180;

% Recalculate into real and imaginary parts of gain
Gre1 = Gr1mm.*(cos(Fi1mm));
Gim1 = Gr1mm.*(sin(Fi1mm));
```

```
cGain1=Gre1+j*Gim1;


Gre2 = Gr25mm.*(cos(Fi25mm));
Gim2 = Gr25mm.*(sin(Fi25mm));
cGain25=Gre2+j*Gim2;

Gre5 = Gr5mm.*(cos(Fi5mm));
Gim5 = Gr5mm.*(sin(Fi5mm));
cGain5=Gre5+j*Gim5;

for k=1:fno

Omega = Freq (k,1)*2*pi;
   Y12m1(k,:)=(-1)^((VoltageBoostOrNot==0))*cGain1(k,:)*j*Omega*CL1mm/...
      (1+9*VoltageBoostOrNot);
GG12m1(k,:)=real(Y12m1(k,:));
CC12m1(k,:)=imag(Y12m1(k,:))/Omega;

   Y12m25(k,:)=(-1)^((VoltageBoostOrNot==0))*cGain25(k,:)*j*Omega*CL2mm/...
      (1+9*VoltageBoostOrNot);
GG12m25(k,:)=real(Y12m25(k,:));
CC12m25(k,:)=imag(Y12m25(k,:))/Omega;

   Y12m5(k,:)=(-1)^((VoltageBoostOrNot==0))*cGain5(k,:)*j*Omega*CL5mm/...
      (1+9*VoltageBoostOrNot);
GG12m5(k,:)=real(Y12m5(k,:));
CC12m5(k,:)=imag(Y12m5(k,:))/Omega;
end

for k=1:fno
figure('PaperPosition',[0.25 0.75 8 9.5])
subplot(3,2,1), plot(time, Gain1(k,:))
xlabel('Time(hours)')
ylabel('Gain of 1.0mm (dB)')
ax=axis;
axis([0 max(time) ax(3) ax(4)]);

subplot(3,2,2), plot(time, Phase1(k,:))
xlabel('Time(hours)')
ylabel('Phase of 1.0mm (deg)')
ax=axis;
axis([0 max(time) ax(3) ax(4)]);


subplot(3,2,3) ,plot(time, Gain25(k,:))
xlabel('Time(hours)')
ylabel('Gain of 2.5mm (dB)')
ax=axis;
axis([0 max(time) ax(3) ax(4)]);

subplot(3,2,4) ,plot(time, Phase25(k,:))
```

```
xlabel('Time(hours)')
ylabel('Phase of 2.5mm (deg)')
ax=axis;
axis([0 max(time) ax(3) ax(4)]);

subplot(3,2,5), plot(time, Gain5(k,:))
xlabel('Time(hours)')
ylabel('Gain of 5.0mm (dB)')
ax=axis;
axis([0 max(time) ax(3) ax(4)]);

text('String',ttl,'Fontsize',18,'HorizontalAlignment','center','Units','Inches',...
'Position',[3 8.5])
text('String', [ num2str(Head(3)) '/' num2str(Head(4)) '/' num2str(Head(2)) ' ' ...
num2str(Head(5)) ':' num2str(Head(6)) ],'Fontsize',10,'HorizontalAlignment',...
'left','Units','Inches','Position',[5 8.2] )
text('String',  ['f= ' num2str(Freq(k)) ''] ,'Fontsize',10,...
'HorizontalAlignment','left','Units','Inches','Position',[5 8.05] )
text('String', ['File:' DatFileName ],'Fontsize',10,'HorizontalAlignment','left',...
'Units','Inches','Position',[5 7.9] )

subplot(3,2,6), plot(time, Phase5(k,:))
xlabel('Time(hours)')
ylabel('Phase of 5.0mm (deg)')
ax=axis;
axis([0 max(time) ax(3) ax(4)]);

%************************************** Plot Impedance
figure('PaperPosition',[0.25 0.75 8 9.5])
subplot(3,2,1), plot(time, CC12m1(k,:))
xlabel('Time(hours)')
ylabel('C12 of 1.0mm (pF)')
ax=axis;
axis([0 max(time) ax(3) ax(4)]);

subplot(3,2,2), plot(time, GG12m1(k,:))
xlabel('Time(hours)')
ylabel('G12 of 1.0mm (pS)')
ax=axis;
axis([0 max(time) ax(3) ax(4)]);


subplot(3,2,3) ,plot(time, CC12m25(k,:))
xlabel('Time(hours)')
ylabel('C12 of 2.5mm (pF)')
ax=axis;
axis([0 max(time) ax(3) ax(4)]);

subplot(3,2,4) ,plot(time, GG12m25(k,:))
xlabel('Time(hours)')
ylabel('G12 of 2.5mm (pS)')
ax=axis;
```

```
axis([0 max(time) ax(3) ax(4)]);

subplot(3,2,5), plot(time, CC12m5(k,:))
xlabel('Time(hours)')
ylabel('C12 of 5.0mm (pF)')
ax=axis;
axis([0 max(time) ax(3) ax(4)]);

text('String',ttl,'Fontsize',18,'HorizontalAlignment','center','Units','Inches',...
'Position',[3 8.5])
text('String', [ num2str(Head(3)) '/' num2str(Head(4)) '/' num2str(Head(2)) ' ' ...
num2str(Head(5)) ':' num2str(Head(6)) ],'Fontsize',10,'HorizontalAlignment',...
'left','Units','Inches','Position',[5 8.2] )
text('String',  ['f= ' num2str(Freq(k)) ''] ,'Fontsize',10,...
'HorizontalAlignment','left','Units','Inches','Position',[5 8.05] )
text('String', ['File:' DatFileName ],'Fontsize',10,'HorizontalAlignment','left',...
'Units','Inches','Position',[5 7.9] )

subplot(3,2,6), plot(time, GG12m5(k,:))
xlabel('Time(hours)')
ylabel('G12 of 5.0mm (pS)')
ax=axis;
axis([0 max(time) ax(3) ax(4)]);
end



figure
plot(time,RH(1,:))
ax=axis;
axis([0 max(time) ax(3) ax(4)])
xlabel('Time (hours)')
ylabel('%')
ax=axis;
if ((ax(4)-ax(3))<3) ax(4)=ceil((ax(4)-ax(3))/2+ax(3)+2);
ax(3)=floor((ax(4)-ax(3))/2+ax(3)-2);
elseif (max(RH(k,:))-min(RH(k,:))>10)
ax(4)=ceil(max(RH(k,:)));
ax(3)=floor(min(RH(k,:)));
end
axis([0 max(time) ax(3) ax(4)]);
text('String','','Fontsize',18,'HorizontalAlignment','center','Units','Inches',...
'Position',[3 6.5])
text('String', [ num2str(Head(3)) '/' num2str(Head(4)) '/' num2str(Head(2)) ' ' ...
num2str(Head(5)) ':' num2str(Head(6)) ],'Fontsize',10,'HorizontalAlignment',...
'left','Units','Inches','Position',[5 5.8] )
text('String', ['File:' DatFileName ],'Fontsize',10,'HorizontalAlignment','left',...
'Units','Inches','Position',[5 5.5] )
```

E.3 Reconstruction of Jeffries' Curves

```
%Function Jeff calculates the moisture concentration at the boundary of the
%pressboard by ambient Relative Humidy rh at temperature T using Jeffries' data.
% 4/28/98 Yanqing Du

x=0:5:90;

for T=30:10:70
if T==70
y = 1.62524996E-10*x.^6 - 3.32186925E-08*x.^5 + 2.24735555E-06*x.^4 ...
 - 2.71010293E-05*x.^3 - 2.77977314E-03*x.^2 + 1.77626234E-01*x + 7.44186563E-02;

elseif T==60
y = 7.43804707E-11*x.^6 - 7.52865191E-09*x.^5 - 5.71293970E-07*x.^4 ...
+1.17310767E-04*x.^3-6.23002235E-03*x.^2+2.13594361E-01*x+1.39785727E-01;

elseif T==50
y = 9.53191441E-11*x.^6 - 1.17550191E-08*x.^5 - 3.73975784E-07*x.^4 ...
+1.27313164E-04*x.^3-7.28507799E-03*x.^2+2.43161186E-01*x+1.04832578E-01;



elseif T==40
y = -3.87298823E-11*x.^6 + 2.52283515E-08*x.^5 - 4.29262362E-06*x.^4 ...
+3.24489057E-04*x.^3-1.19501173E-02*x.^2+2.90791470E-01*x+1.69545834E-01;

elseif T==30
y = -9.34686547E-11*x.^6 + 4.24466336E-08*x.^5 - 6.33958786E-06*x.^4 ...
+4.38315253E-04*x.^3-1.49296958E-02*x.^2+3.28286566E-01*x+2.41312699E-01;

end

plot(x,y)
hold on

end

set(gca,'FontSize',20)
xlabel('% Relative Humidity','FontSize',20);
ylabel(' % Moisture in Paper','FontSize',20);
axis([0  100 0 14])
```

E.4 Couette Facility Data Processing

```
function rhtempCF(DataFileName, ttl)
%************************************************************************
% for ploting data of Moisture and Temprature for the Couette Facility
% Data obtained by SPIN software
% Data for TEM 3 (Couette Charger), TEM 4 (Hood) and MST 2(Couette Charger)
% Ploting : CC temprature, hood temprature, CC RH, and CC PPM
% S.H. Kang and Y. Du
% 11/3/98
%************************************************************************
%Read the data file
fid = fopen(DataFileName,'r');
j=1;
while feof(fid)~=1
   A=fgetl(fid);
   [dummy,d_leng]=size(A);
   if d_leng>=22
      %******Read Temprature in CC and Hodd ********************
      if A(1:3)=='TEM' & A(5)=='3' & A(7)=='R';
         if d_leng==23
            time_t(j)=str2num(A(9))*3600*10+str2num(A(10))*3600*1+...
               str2num(A(12))*60*10+str2num(A(13))*60*1+...
               str2num(A(15))*10+str2num(A(16))*1;
            T_hood(j)=str2num(A(18))*10+str2num(A(19))+str2num(A(21))*0.1...
               +str2num(A(22))*0.01;
         else
            time_t(j)=str2num(A(9))*3600*100+str2num(A(10))*3600*10+...
               str2num(A(11))*3600+...
               str2num(A(13))*60*10+str2num(A(14))*60*1+...
               str2num(A(16))*10+str2num(A(17))*1;
            T_hood(j)=str2num(A(19))*10+str2num(A(20))+str2num(A(22))*0.1...
               +str2num(A(23))*0.01;
         end
      end

      if A(1:3)=='TEM' & A(5)=='4' & A(7)=='R';
         if d_leng==23
            T_CC(j)=str2num(A(18))*10+str2num(A(19))+str2num(A(21))*0.1...
               +str2num(A(22))*0.01;
         else T_CC(j)=str2num(A(19))*10+str2num(A(20))+str2num(A(22))*0.1...
               +str2num(A(23))*0.01;
         end
      end

      %******Read %Relative Humidity in CC*********

      if A(1:3)=='MST' & A(5)=='2' & A(7)=='R'
         %******Change '-' to 0 *************************
         if(exist('-'))
            A=strrep(A,'-','0');
            %disp(A);
```

```
         end
         %*******Read %Relative Humidity and PPM Moisture in CC********
         if A(11)==':'
            if d_leng==34
               RH(j)=str2num(A(18))+str2num(A(20))*0.1+str2num(A(21))*0.01;
               PPM(j)=str2num(A(23))+str2num(A(25))*0.1+str2num(A(26))*0.01...
                  +str2num(A(27))*0.001;
elseif d_leng==35
               RH(j)=str2num(A(18))+str2num(A(20))*0.1+str2num(A(21))*0.01;
               PPM(j)=str2num(A(23))*10+str2num(A(24))...
                  +str2num(A(26))*0.1+str2num(A(27))*0.01...
                  +str2num(A(28))*0.001;
else
               RH(j)=str2num(A(18))*10+str2num(A(19))+str2num(A(21))*0.1+...
                  str2num(A(22))*0.01;
               PPM(j)=str2num(A(24))*10+str2num(A(25))+str2num(A(27))*0.1...
                  +str2num(A(28))*0.01+str2num(A(29))*0.001;
            end
         else
            if d_leng==35
               RH(j)=str2num(A(19))+str2num(A(21))*0.1+str2num(A(22))*0.01;
               PPM(j)=str2num(A(24))+str2num(A(26))*0.1+str2num(A(27))*0.01...
                  +str2num(A(28))*0.001;
            elseif d_leng==36
               RH(j)=str2num(A(19))+str2num(A(21))*0.1+str2num(A(22))*0.01;
               PPM(j)=str2num(A(24))*10+str2num(A(25))...
                  +str2num(A(27))*0.1+str2num(A(28))*0.01...
                  +str2num(A(29))*0.001;
            else
               RH(j)=str2num(A(19))*10+str2num(A(20))+str2num(A(22))*0.1+...
                  str2num(A(23))*0.01;
               PPM(j)=str2num(A(25))*10+str2num(A(26))+str2num(A(28))*0.1...
                  +str2num(A(29))*0.01+str2num(A(30))*0.001;
            end
         end
          j=j+1;
      end
     end
  end

  fclose(fid);

 %Save data for plotting
 save time_t time_t
 save RH RH
 save T_hood T_hood
 save T_CC T_CC
 save PPM PPM

%*********Plot Temperature, Relative Humidity, and PPM of Charger ***********

figure('PaperPosition', [.25 .75 8 9.5])
```

```
set(gca,'FontSize',18)

subplot(3,1,1)
plot(time_t/3600,T_CC);
ylabel('Temperature in CC (^oC)')

subplot(3,1,2)
plot(time_t/3600,RH);
ylabel('RH in CC (%)')

subplot(3,1,3)
plot(time_t/3600,PPM)
ylabel('Moisture in Oil (PPM)')
xlabel('Time (hour)')
title(ttl)

%********* Plot Temperature of Hood ***********
figure
subplot(2,1,1)
plot(time_t/3600,T_hood);
ylabel('Temperature in Hood(^oC)')
title(ttl)
```

Appendix F

Forward Simulation Input File

(a) The following input file is used for the simulation of moisture profile using *diff.c* during the wetting process at 60°C in Section 8.2.1.

```
outputfile o60CF5f01 /* specify the name of the output file
NHMCS 100 /* Number of harmonics
outputs 10 2340 1 2 3 4 5 6 7 8 9 10 /* specify times at which to print output
/* outputs #points scaling t1 t2 ...
/* scaling is in seconds. The example
/* at the left prints out every 2340 seconds for
/* ten such intervals. (initial time also printed)
measured diff60CF.boundary /* "measured" specifies that the boundary
/* conditions (moisture and temperature)
/* are specified in the file diff.boundary
/* Other option is "simmoist" which
/* simulates with a mass balance constraint.
freq 0.1 /* frequency (Hz)
wavelength 5000E-6 /* sensor wavelength (m)
C1 9804.6 /* feedback capacitor (pF)
samplewidth 1.15E-3 /* sample thickness (m)
distoil 2.54e-2 /* thickness of layer above sample (m)
```

sigoil 0.0 /* relative conductivity simga/e0 of the layer above sample

epsoil 1 /* relative permittivity of the layer above sample

D0 3E-12 /* base diffusion coefficient

Ea 7646 /* diffusion coefficient

dx 10E-6 /* spatial discretization (m)

dt 0.1 /* temporal discretization (s)

(b) The following input file is used for the simulation of temperature transients in Section 8.3.2.

outputfile oTinc5f01

NHMCS 100

outputs 150 360 1 2 3 4 5 6 7 8 9 10 11 12 13 14 15 16 17 18 19 20 21 22 23 24 25 26 27 28 29 30 31 32 33 34 35 36 37 38 39 40 41 42 43 44 45 46 47 48 49 50 51 52 53 54 55 56 57 58 59 60 61 62 63 64 65 66 67 68 69 70 71 72 73 74 75 76 77 78 79 80 81 82 83 84 85 86 87 88 89 90 91 92 93 94 95 96 97 98 99 100 101 102 103 104 105 106 107 108 109 110 111 112 113 114 115 116 117 118 119 120 121 122 123 124 125 126 127 128 129 130 131 132 133 134 135 136 137 138 139 140 141 142 143 144 145 146 147 148 149 150

sampleprofile 2.7275

measured diffTinc.boundary

freq 0.1

wavelength 5000E-6

C1 19617

samplewidth 1.18E-3

distoil 2.54E-2

sigoil 1

epsoil 2.2

D0 6.44E-14

Ea 7700

dx 10E-6

dt 0.6

Bibliography

[1] M. C. Zaretsky, *Parameter Estimation Using Microdielectrometry with Application to Transformer Monitoring*. PhD thesis, Department of Electrical Engineering and Computer Science, Massachusetts Institute of Technology, Cambridge, MA, Nov. 1987.

[2] P. A. von Guggenberg, *Application of Interdigital Dielectrometry to Moisture and Double Layer Measurements in Transformer Insulation*. PhD thesis, Department of Electrical Engineering and Computer Science, Massachusetts Institute of Technology, Cambridge, MA, June 1993.

[3] Y. K. Sheiretov, "Dielectrometry measurements of moisture dynamics in oil-impregnated pressboard," Master's thesis, Department of Electrical Engineering and Computer Science, Massachusetts Institute of Technology, Cambridge, MA, May 1994.

[4] "The Origins of the IEEE", IEEE website: http://www.ieee.org.

[5] G. M. Urbani and R. S. Brooks, "Using the recovery voltage method to evaluate aging in oil-paper insulation," in *Proceedings of the 1998 IEEE 6th International Conference on Conduction and Breakdown in Solid Dielectrics*, (Vasteras, Sweden), pp. 93–97, June 1998.

[6] V. D. Houhanessian, *Measurement and Analysis of Dielectric Response in Oil-Paper Insulation Systems*. PhD thesis, High Voltage Laboratory, Swiss Federal Institute of Technology, Zurich, Switzerland, 1998.

[7] A. Helgeson, "Dielectric properties of machine insulation studied with dielectric response," Master's thesis, Department of Electric Power Engineering, Kungliga Tekniska Hogskolan, Stockholm, Sweden, May 1997.

[8] Thomas A. Prevost, Technical Manager, EHV-Weidmann Industries, Inc., One Gordon Mills Way, P.O. Box 903, St. Johnsbury, VT 05819-0903 USA, personal communication.

[9] A. V. Mamishev, Y. Du, and M. Zahn, "Measurement of dielectric property distributions using interdigital dielectrometry sensors," in *IEEE Conference on*

Electrical Insulation and Dielectric Phenomena, (Virginia Beach, VA), pp. 309–312, Oct. 1995.

[10] Y. Du, M. Zahn, A. V. Mamishev, , and D. E. Schlicker, "Moisture dynamic measurements of transformer board using a three-wavelength dielectrometry sensor," in *IEEE International Symposium on Electrical Insulation*, (Montreal, Quebec, Canada), pp. 53–56, June 1996.

[11] A. Washabaugh, A. V. Mamishev, Y. Du, and M. Zahn, "Dielectric measurements of semi-insulating liquids and solids," in *International Conference on Conduction and Breakdown in Dielectric Liquids*, (Rome, Italy), pp. 381–384, July 1996.

[12] Y. Du, B. C. Lesieutre, and M. Zahn, "Dielectrometry measurements of effects of moisture and anti-static additive on transformer board," in *IEEE Conference on Electrical Insulation and Dielectric Phenomena*, (Minneapolis, MN), pp. 226–229, Oct. 1997.

[13] A. V. Mamishev, Y. Du, B. C. Lesieutre, and M. Zahn, "Measurement of stratified distributions of dielectric properties and dependent physical parameters," in *Fall Meeting of Materials Research Society*, (Boston, MA), Dec. 1997.

[14] A. V. Mamishev, Y. Du, B. C. Lesieutre, and M. Zahn, "Development and applications of multi-wavelength interdigital dielectrometry sensors and parameter estimation algorithms," in *Joint Symposium on Electrostatics*, (San Francisco, CA), pp. 169–181, June 1998.

[15] A. V. Mamishev, C. Lin, B. C. Lesieutre, Y. Du, , and M. Zahn, "Improvement of algorithms for on-line interdigital dielectrometry measurement of material properties," in *IEEE International Symposium on Electrical Insulation*, (Washington, D.C.), pp. 444–447, June 1998.

[16] Y. Du, A. V. Mamishev, B. C. Lesieutre, and M. Zahn, "Measurements of moisture diffusion in transformer pressboard," in *IEEE Conference on Electrical Insulation and Dielectric Phenomena*, (Atlanta, GA), pp. 341–344, Oct. 1998.

[17] A. V. Mamishev, Y. Du, B. C. Lesieutre, and M. Zahn, "Measurement of moisture spatial profiles in transformer pressboard," in *IEEE Conference on Electrical Insulation and Dielectric Phenomena*, (Atlanta, GA), pp. 323–326, Oct. 1998.

[18] Y. Du, M. Zahn, B. C. Lesieutre, A. V. Mamishev, and S. Lindgren, "Moisture equilibrium in transformer paper-oil systems," *IEEE Electrical Insulation Magazine*, vol. 15, pp. 11–20, Jan. 1999.

[19] A. V. Mamishev, Y. Du, B. C. Lesieutre, and M. Zahn, "Development and applications of fringing field dielectrometry sensors and parameter estimation algorithms," *Journal of Electrostatics*, 1999.

[20] Y. Du, A. V. Mamishev, B. C. Lesieutre, M. Zahn, and S. H. Kang, "Measurements of moisture solubility for differently conditioned transformer oils," in *13th International Conference on Dielectric Liquids*, (Nara, Japan), July 1999.

[21] M. C. Zaretsky, L. Mouayad, and J. R. Melcher, "Continuum properties from interdigital electrode dielectrometry," *IEEE Transactions on Electrical Insulation*, vol. 23, pp. 897–917, Dec. 1988.

[22] J. Fabre and A. Pichon, "Deterioration processes and products of paper and oil. Application to transformers," in *Proceedings of the International Conference on Large High Voltage Electric Systems (CIGRÉ)*, (Paris, France), June 15–25, 1960. Paper No. 137.

[23] T. V. Oommen, "Moisture equilibrium in paper-oil insulation systems," in *Proceedings of the 16th Electrical/Electronics Insulation Conference*, (Chicago, IL), pp. 162–166, Oct. 3–6, 1983.

[24] P. J. Griffin, C. M. Bruce, and J. D. Christie, "Comparison of water equilibrium in silicone and mineral oil transformers," in *Minutes of the Fifty-Fifth Annual International Conference of Doble Clients*, 1988. Paper No. 10-9.

[25] "Standard test method for A-C loss characteristics and permittivity (dielectric constant) of solid electrical insulating materials (ASTM D 150-81)." *Annual Book of ASTM Standards,* 10.01, 1987.

[26] "Standard test method for A-C loss characteristics and relative permittivity (dielectric constant) of electrical insulating liquids (ASTM D 924-82b)." *Annual Book of ASTM Standards,* 10.03, 1987.

[27] Tettex Instruments, AG, "Polarization spectrum analysis for diagnosis of insulation systems," Information 29, TI 29-d/e-04.92.

[28] K. S. Cole and R. H. Cole, "Dispersion and absorption in dielectrics. ii. direct current characteristics," *Journal of Chemical Physics*, vol. 10, pp. 98–105, 1942.

[29] A. van Roggen and H. Zhou, "Data analysis in dielectric time-domain spectroscopy," in *Annual Report of Conference on Electrical Insulation and Dielectric Phenomena*, (Piscataway, NJ), pp. 322–327, Oct. 1992.

[30] P. J. Griffin and J. D. Christie, "Effects of water and benzotriazole on electrostatic charge generation in mineral oil/cellulose systems," in *Proceedings: Static Electrification in Power Transformers*, June 1993. Project 1499-99.

[31] T. O. Rouse, "Mineral insulating oil in transformers," *Electrical Insulation Magazine*, vol. 14, no. 3, pp. 6–16, 1998.

[32] "Relative Humidity," *Britannica Online*, 1994-1997 Encyclopedia Britannica, Inc., URL: http://www.britannica.com/.

[33] H. P. Moser, *Transformerboard*. St. Johnsbury, Vermont: Special print of Scientia Electrica, translated by EHV-Weidmann Lim., 1979.

[34] G. Beer, G. Gasparini, F. Osimo, and F. Rossi, "Experimental data on the drying-out of insulation samples and test coil for transformers," in *Proceedings of the International Conference on Large High Voltage Electric Systems (CIGRÉ)*, vol. II, (Paris, France), June 8–18, 1966. Paper No. 135.

[35] R. Neimanis, "Dielectric diagnostics of oil-paper insulated current transformers," Master's thesis, School of Electrical and Computer Engineering, Chalmers University of Technology, Goteborg, Sweden, 1997.

[36] S. Itahashi, H. Mitsui, T. Sato, and M. Sone, "State of water in hydrocarbon liquids and its effect on conductivity," *IEEE Transactions on Dielectrics and Electrical Insulation*, vol. 2, pp. 1117–1122, Dec. 1995.

[37] W. A. Fessler, W. J. McNutt, and T. O. Rouse, "Bubble formation in transformers," Tech. Rep. EL-5384, EPRI, Palo Alto, CA, Aug. 1987.

[38] F. M. Clark, "Factors affecting the mechanical deterioration of cellulose insulation," *Transactions of Electrical Engineering*, vol. 61, pp. 742–749, Oct. 1942.

[39] A. J. Morin, M. Zahn, and J. R. Melcher, "Fluid electrification measurements of transformer pressboard/oil insulation in a Couette charger," *IEEE Transactions on Electrical Insulation*, vol. 26, pp. 870–901, Oct. 1991.

[40] A. P. Washabaugh, P. A. von Guggenberg, M. Zahn, and J. R. Melcher, "Temperature and moisture transient flow electrification measurements of transformer pressboard/oil insulation using a Couette facility," in *Proceedings of The 3rd International Conference on Properties and Applications of Dielectric Materials*, vol. 2, (Tokyo, Japan), pp. 867–870, July 8–12, 1991.

[41] "Standard test methods for water in insulating liquids (Karl Fischer reaction method (ASTM D 1533-86)." *Annual Book of ASTM Standards,* 10.03, 1987.

[42] "Standard test method for moisture content of oil-impregnated cellulosic insulation (ASTM D 3277-85)." *Annual Book of ASTM Standards,* 10.03, 1987.

[43] B. Fallou, "Summary of work done at l.c.i.e. on the paper-oil complex," *Internal Report of Laboratoire Centre des Industries Electriques, France.*

[44] S. M. Islam, P. R. S. Jota, and M. Stace, "Detection of oil-paper equilibrium moisture content in power transformer using hybrid intelligent interpretation of polarization spectrums from recovery voltage measurements," in *IEEE International Symposium on Electrical Insulation*, (Arlington, VA), June 1998.

[45] R. B. Kaufman, E. J. Shimanski, and K. W. McFaydynen, "Gas and moisture equilibrium in transformer oil," *Communication and Electronics*, pp. 312–318, July 1955.

[46] D. N. Ewart, "Laboratory and factory measurements of moisture in power transformers," *GE TIS report 60PT44*, Aug. 1960.

[47] E. T. Norris, "High-voltage power-transformer insulation," *Proceedings of The Institution of Electrical Engineers*, vol. 110, pp. 428–440, Feb. 1963.

[48] J. K. Nelson, "Electrical field distribution in transformer oil," *IEEE Electrical Insulation Magazine*, vol. 10, no. 3, pp. 16–28, 1994.

[49] A. G. Schlag, "The recovery voltage method for transformer diagnosis," *Tettex Instruments booklet*.

[50] R. Jeffries, "The sorption of water by cellulose and eight other textile polymers," *Journal of the Textile Institute Transactions*, vol. 51, no. 9, pp. 339–374, 1960.

[51] J. Reason, "Cost-effective transformer maintenance," *Electrical World*, pp. 17–30, Oct. 1997.

[52] Handbook of Chemistry and Physics, D-94, 46th Edition, the Chemical Rubber Co., Cleveland, Ohio, 1966.

[53] J. D. Piper, "Moisture equilibrium between gas space and fibrous materials in enclosed electric equipment," *Transactions of the American Institute of Electrical Engineers (AIEE)*, vol. 65, pp. 791–797, Dec. 1946.

[54] A. R. Urquhart and A. M. Williams, "The moisture relations of cotton, the effect of temperature on the absorption of water by soda-boiled cotton," *Journal, Textile Institute*, vol. 15, p. T559, Oct. 1924.

[55] S. M. Neale and W. A. Stringfellow, "The primary sorption of water by cotton," *Transactions, Faraday Society*, vol. 37, p. 525, 1941.

[56] C. C. Houtz and D. A. McLean, "Adsorption of water by papers at elevated temperatures," *Journal of Physical Chemistry*, vol. 43, pp. 309–321, 1939.

[57] L. M. Pidgeon and O. Maass, "The adsorption of water by wood," *Journal, American Chemical Society*, vol. 52, p. 1053, 1930.

[58] W. W. Guidi and H. P. Fullerton , "Mathematical methods for prediction of moisture take-up and removal in large power transformers," *Proceedings of IEEE Winter Power Meeting*, no. C-74, pp. 242–244, 1974.

[59] T. V. Oommen, "Moisture equilibrium charts for transformer insulation drying practice," *IEEE Transaction on Power Apparatus and Systems*, vol. PAS-103, pp. 3063–3067, Oct. 1984.

[60] S. Glasstone, *Textbook of Physical Chemistry*, ch. XIV. Cambridge, MA: D. Van Nostrand Co., 1946.

[61] T. V. Oommen, E. M. Petrie, and S. R. Lindgren, "Bubble generation in transformer windings under overload conditions," *Minutes of the Sixty-Two Annual International Conference of Doble Clients*, pp. 16–28, Mar. 1995.

[62] S. D. Foss, "Power transformer drying model," Tech. Rep. DS-002-87, Dynamic Systems, Pittsfield, MA, Oct. 1987. Prepared for General Electric Company, Large Transformer Operation, Pittsfield, MA, and Consolidated Edison Corporation, New York, NY.

[63] P. F. Ast, "Movement of moisture through a50p281 kraft paper (dry and oil-impregnated)," Tech. Rep. Test report HV-ER-66-41, General Electric, June 1966.

[64] E. K. Steele, "Moisture redistribution in simulated transformer paper-oil systems," Tech. Rep. Memo report MATL 70-37, General Electric, Nov. 1970.

[65] Shell Oil Company, One Shell Plaza, 900 Louisiana Street, Houston, Texas 77002, (800) 231-6950, *Shell Diala Oils.* Shell Lubricants Technical Bulletin SOC: 39-95.

[66] "Transformers use edible seed-oil-based fluid," *IEEE Power Engineering Review*, vol. 19, p. 34, Feb. 1999.

[67] "Standard test methods for estimation of solubility of water in hydrocarbon and aliphatic ester lubricants (ASTM D 4056-92(1997))." *Annual Book of ASTM Standards,* 05.02, 1998.

[68] Harley Moisture Sensor, Model CT-880-BN-H-(0–100%)-X, J. W. Harley Inc., Monitoring Products Group, 9177 Dutton Drive, Twinsburg, OH 44087, (800) 635-3030.

[69] Test report by Doble Engineering Company, Report No. 30187, Nov. 11, 1996, 85 Walnut Street, Watertown, MA 02172-4037.

[70] "Standard test methods for ASTM color of petroleum products (ASTM color scale (ASTM D 1500-82)." *Annual Book of ASTM Standards,* 10.03, 1987.

[71] Test report by Doble Engineering Company, Report No. C36545, Mar. 8, 1999, 85 Walnut Street, Watertown, MA 02172-4037.

[72] R. T. Conley, *Infrared Spectroscopy.* 2nd Edition, Allyn and Bacon, Inc., Boston, 1972.

[73] G. D. Golovan', T. B. Zhilyaev, A. I. Panchenko, and V. S. Kriven'kaya, "Water solubility in transformer oils with various hydrocarbon compositions," *Chemistry and Technology of Fuels and Oils*, vol. 20, pp. 387–391, July 1984.

[74] W. Kennedy, "Resistivity of oil and pressboard insulation and their effect on transformer design," in *Third EPRI Static Electricfication Workshop*, Jan. 1992.

[75] Y. K. Sheiretov and M. Zahn, "Dielectrometry measurements of moisture dynamics in oil-impregnated pressboard," *IEEE Transactions on Dielectrics and Electrical Insulation,*, vol. 2, pp. 329–335, June 1995.

[76] A. K. Jonscher, *Dielectric Relaxation in Solids.* Chelsea Dielectrics Press, London, 1983.

[77] B. Nettelblad, "Effect of moisture content on the dielectric properties of cellulose," in *Nordic Insulation Symposium NORD-IS 92*, June 1992.

[78] N. Altamirano, "Effects of moisture and temperature on dielectric spectroscopy of transformer pressboard," *MIT Advanced Undergraduate Projects final report*, Dec. 1998.

[79] H. P. Moser and V. Dahinden, *Transformerboard II.* Rapperswil, CH 8640: H. Weidmann AG, 1987.

[80] T. B. Jones, "Dielectric measurements on packed beds," Tech. Rep. Technical Information Series 79CRD131, General Electric, June 1979.

[81] Technical support from William A. Phelps and Christopher Stankowski, Senior Technical Services Engineers, EHV-Weidmann Industries, Inc., One Gordon Mills Way, P.O. Box 903, St. Johnsbury, VT 05819-0903 USA.

[82] B. A. Barry, *Errors in practical measurement in science, engineering, and technology*, ch. 6. New York: John Wiley & Sons, Inc., 1978.

[83] Omega Series CN 310/320 Solid State Temperature Controllers, Operator's Manual, Omega Engineering, Inc., an OMEGA group company, One Omega Drive, Box 4047, Stamford, Connecticut 06907-0047.

[84] A. K. Jonscher, *Universal Relaxation Law.* Chelsea Dielectrics Press, London, 1996.

[85] S. Westerlund, "Capacitor theory," *IEEE Transactions on Dielectrics and Electrical Insulation,*, vol. 1, pp. 826–839, Oct. 1994.

[86] U. Gafvert, S. M. Gubanski, and A. Helgeson, "Calculations of thermally stimulated depolarisation current from isothermal dielectric response data," in *Proceedings of International Symposium on Electrical Insulating Materials*, (Tokyo, Japan), pp. 55–60, Sept. 1995.

[87] R. M. Hill, L. A. Dissado, J. Pugh, M. G. Broadhurst, C. K. Chiang, and K. J. Wahlstrand, "The dielectric response of portulacaceae (jade) leaves over an extended frequency range," *Journal of Biological Physics*, vol. 14, no. 4, pp. 133–135, 1987.

[88] Matlab Optimization Toolbox, The MathWorks, Inc., 1996.

[89] D. E. Schlicker, "Flow electrification of aged transformer oils," Master's thesis, Department of Electrical Engineering and Computer Science, Massachusetts Institute of Technology, Cambridge, MA, Sept. 1996.

[90] M. C. Zaretsky and J. R. Melcher, "Complex permittivity measurements of thin films using microdielectrometry," in *Conference on Electrical Insulation and Dielectric Phenomena*, (Claymont, DE), pp. 462–471, Nov. 1986.

[91] Y. K. Sheiretov and M. Zahn, "Dielectrometry measurements of moisture dynamics in oil-impregnated pressboard," in *IEEE International Conference on Properties and Applications of Dielectric Material*, (University of Queensland, Brisbane, Australia), pp. 33–36, July 1994.

[92] B. C. Lesieutre, A. V. Mamishev, Y. Du, E. Keskiner, G. Verghese, and M. Zahn, "Forward and inverse parameter estimation algorithms of interdigital dielectrometry sensors," in *Electrostatics Society of America 27th Annual Conference*, (Boston, MA), June 1999. Accepted.

[93] URL: http://power.mit.edu/SENSORS/.

[94] A. V. Mamishev and M. Zahn, "Techniques for semi-empirical characterization of material and sensor properties in interdigital dielectrometry," in *IEEE International Symposium on Electrical Insulation*, (Montreal, Quebec, Canada), pp. 486–489, June 1996.

[95] A. V. Mamishev, B. C. Lesieutre, and M. Zahn, "Parameter estimation using an interdigital dielectrometry sensor with finite-element software," in *IEEE Conference on Electrical Insulation and Dielectric Phenomena*, (Minneapolis, MN), pp. 234–237, Oct. 1997.

[96] D. R. Day, D. D. Shepard, and K. J. Craven, "A microdielectric analysis of moisture diffusion in thin epoxy/amine films of varying cure state and mix ratio," *Polymer Engineering and Science*, vol. 32, pp. 524–528, Apr. 1992.

[97] A. V. Mamishev, *Interdigital Dielectrometry Sensor Design and Parameter Estimation Algorithms for Non-Destructive Materials Evaluation*. PhD thesis, Department of Electrical Engineering and Computer Science, Massachusetts Institute of Technology, Cambridge, MA, May 1999.

[98] W. H. Press, S. A. Teukolsky, W. T. Vetterling, and B. P. Flannery, *Numerical Recipes in C: The Art of Scientific Computing*, ch. 19. Cambridge: Cambridge University Press, 1992.

[99] J. Quarshie, "Diffusion of moisture through cellulose insulation," Master's thesis, Department of Electrical and Electronic Engineering, University of Nottingham, Oct. 1977.

[100] H. Fujita, "The exact pattern of a concentration-dependent diffusion in a semi-infinite medium, Part I," *Textile Research Journal*, vol. 22, pp. 757–760, 1952.

[101] H. Fujita, "The exact pattern of a concentration-dependent diffusion in a semi-infinite medium, Part II," *Textile Research Journal*, vol. 22, pp. 823–827, 1952.

[102] J. R. Philip, "A very general class of exact solutions in a concentration dependent diffusion," *Nature*, p. 233, Jan. 1960.

[103] H. P. Fullerton, "Determination of moisture diffusion coefficient of oil-free A50P260A paper," Tech. Rep. Technical Information Series DF71ESP-23, General Electric, Jan. 1972.

[104] D. J. Lyon, J. R. Melcher, and M. Zahn, "Couette charger for measurement of equilibrium and energization flow parameters: Application to transformer insulation," *IEEE Transactions on Electrical Insulation*, vol. 23, pp. 159–176, Feb. 1988.

[105] A. P. Washabaugh and M. Zahn, "A study of flow electrification using a couette flow facility," *IEEE Transactions on Dielectrics and Electrical Insulation*, vol. 3, pp. 161–181, Apr. 1996.

[106] J. Castrillon, MIT Internal Report, June 6, 1997.

[107] U. Gafvert and B. Nettelblad, "Measurement techniques for dielectric response characterization at low frequencies," in *NORD-IS-90*, 1990.

[108] G. C. A. Bognar and I. Hamos, "Comparing various methods for the dielectric diagnostics of oil-paper insulation systems in the range of low frequencies or long time constants," in *Proceedings of 8th International Symposium on High Voltage Engineering*, (Yokohama), p. 21.01, Aug. 1993.

[109] A. Bognar, L. Kalocsai, G. Csepes, E. Nemeth, and J. Schmidt, "Diagnostic tests of high voltage oil-paper insulating systems (in particular transformer insulation) using DC dielectrometrics," in *CIGRE*, pp. 15/33–08, Aug. 1990.

[110] U. P. Tharning, P. Holmgren, "High voltage dielectric response analyser for cable diagnostics," in *IEEE Annual Report of Conference on Electrical Insulation and Dielectric Phenomena*, (Pocono Manor, PA), pp. 745–750, Oct. 1993.

[111] U. Gafvert and E. Ildstad, "Modelling return voltage measurements of multi-layer insulation systems," in *Proceedings of the 4th International Conference on Properties and Applications of Dielectric Materials*, (Brisbane Australia), pp. 123–126, July 1994.

[112] B. H. A. Kozlovski, R. Neimanis and S. M. Gubanski, "Diagnostic measurements of oil-paper insulation in current transformers," in *Proceedings of Nordic Insulation Symposium*, (Bergen, Norway), pp. p.131–138, June 1996.

[113] R. E. B. Holmgren, P. Werelius and U. Gafvert, "Dielectric measurements for diagnosis of XLPE cable insulation," in *Proceedings of 14th Biennial International Conference and Exhibition on Electricity Distribution*, (Birmingham, UK), pp. 11/1–4, June 1997.

Biography

Yanqing Du was born in Hangzhou, the People's Republic of China in 1971. She graduated from Hangzhou Number Two Middle School, China, in 1989. She received a Bachelor of Science degree in Electrical Engineering in 1993, and a Master of Science degree in Electrical Engineering in 1994, both from the Northwestern Polytechnical University (NPU) in Xi'an, China; and Master of Science and Electrical Engineer degrees from the Massachusetts Institute of Technology in 1999.

From 1992 to 1994, Yanqing Du was a research assistant at the NPU Laboratory of Electrical Drives and Automation; in Fall 1992, she was the lecturer for junior and senior courses: English for Science and Technology. From 1994 to 1999, she was a research assistant at the MIT Laboratory for Electromagnetic and Electronic Systems; in Fall 1996, she was the head teaching assistant for the MIT Department of Electrical Engineering and Computer Science undergraduate core course: 6.013 Electromagnetic Fields and Energy. Her research interests include interdigital sensor measurements, moisture diffusion phenomena, electromagnetism, and signal processing for dielectric relaxation measurements.

During her graduate studies in the United States, she received the following awards (in reverse chronological order): An Wang Graduate Fellowship from MIT Graduate Education Office (1998); Spring and Fall term Travel Grant from MIT Graduate Student Council (1998); Demonstration of Energy-Efficient Developments Scholarships from American Public Power Association (APPA)(1998, 1996, 1995); IEEE Conference on Electrical Insulation and Dielectric Phenomena student travel scholarship (1998); Honorable Mention in IEEE Student Poster Contest at Power Engineering Society Winter Meeting (1998); Graduate Student Award paper finalist in the Material Research Society Fall Meeting (1997); IEEE Conference on Electrical Insulation and Dielectric Phenomena student travel scholarship (1997); IEEE International Symposium on Electrical Insulation student travel scholarship (1996); Wang Tiwu Fellowship for excellent students studying at top universities in the United States (1994). She also received numerous awards and honors during undergraduate and graduate studies in China (1989-1994), including Honor of the most outstanding university graduate in Shaanxi Province from Shaanxi Province Education Committee (1994) and Second Prize in the Physics Experiment category of the China Aeronautics and Astronautics Ministry's Second Annual University Contest of Experimental Skills and Science Invention (1992).

Yanqing Du was the Secretary of the MIT Graduate Student Council and Editor-in-Chief of the Graduate Student News for the academic year of 1997.

Du is a co-author of 15 technical papers published in archival journals and at international conferences, including one invited paper. She has made many industrial and conference presentations and prepared three technical reports.

Yanqing Du is a member of Sigma Xi, and of the Dielectrics and Electrical Insulation Society and Power Engineering Society of the Institute of Electrical and Electronic Engineers.